Faculty of Sciences
Department of Analytical Chemistry
Research group “Atomic & Mass Spectrometry”

Development and application of analytical methods based on ICP – mass spectrometry for spatially resolved, elemental, and Fe, Ni isotopic analysis of metal and silicate meteoritic material

Thesis submitted in fulfillment of the requirements for the degree of
Doctor of Science: Chemistry
by
Stepan M. Chernonozhkin
Academic year 2015-2016

Supervisor: Prof. Dr. Frank Vanhaecke
Supervisor: Prof. Dr. Philippe Claeys

For my family
and my wife

Contents

Goals

Understanding the formation and early evolution of planetesimals and planetary embryos in our Solar System is a major scientific challenge. In particular the processes of planetary accretion and differentiation, whereby an unsorted mass of primitive meteoritic material evolves into a body with a silicate mantle and metallic core, remain poorly understood. Space programs of multiple countries are oriented at probing the Solar System objects by remote orbiters or landers (*e.g.* the European Rosetta and ExoMars missions), but technological constraints limit the analytical capabilities of the remote measurements, and return missions require enormous financial resources. However, meteorites represent easily accessible extraterrestrial material which (1) covers a diverse range of parent bodies/sampling locations and (2) also stems from deep interiors of parent bodies, making them the largest and most precise source of knowledge of the Solar System evolution. Among the various groups of meteorites, iron and stony-iron meteorites are particularly interesting for the study of planetary differentiation. Differentiated meteorites represent the deep interiors of their parent asteroids, i.e. cores and core-mantle boundaries, not accessible on Earth or any other non-destructed planet (except, perhaps, parent bodies of silicate-bearing iron meteorites, which were “frozen” at an earlier stage of their metal core formation). Iron and stony-iron meteorite parent bodies therefore provide a natural laboratory that can be used to study core formation and differentiation, the compositional evolution of mantles and crusts these planetesimals through time, processes with direct bearing on discrete accretion of terrestrial planets, and, ultimately, the formation of habitable planets such as our own. The distribution of trace elements and stable isotope variations in extraterrestrial material provide an improved insights into the processes taking place during the evolution of the Solar System. These chemical and isotope fingerprints can be used to study a number of processes critical to answer general questions of evolution of asteroid and planetary bodies, also applicable to the formation of our own planet, such as parent body melting, metal-silicate fractionation, core formation and thermal evolution of the parent bodies of meteorites.

Cosmochemistry is continuously seeking for new developments in modern analytical chemistry in terms of sensitivity, accuracy, precision and lateral resolution. The overall aim of this work was to contribute to the development of ICP-mass spectrometry (ICP-MS) – based techniques for elemental and high-precision isotopic analysis (Fe, Ni) for cosmochemical applications, including the application of *in situ* laser ablation (LA) micro-sampling, which provides capabilities for spatially resolved analysis. In particular, the present research was focused on an evaluation of the capabilities of LA-ICP-MS to provide 2-dimensional distribution maps for trace to major elements, which involved an assessment of quantification approaches, matrix effects, requirements imposed on reference materials and detection limits of the methods. It is shown how 2D elemental mapping of the metal phase of iron meteorites and silicate material of pallasites can contribute to the knowledge of processes that occurred in the meteorite parent bodies. A second focus of this work was an evaluation of the capability of multicollector (MC) ICP-MS for high-precision isotopic analysis of Fe and Ni, two major elements composing differentiated meteorites. The element isolation procedure and MC-ICP-MS measurement protocol for the study of stable isotope ratio variations of nickel needed to be carefully evaluated in order to provide accurate and precise data. The ability to measure natural variations of the Fe isotopic composition with high-precision is one of the biggest breakthroughs in geo- and cosmochemistry during the last decade. This became possible due to the development of analytical methods for Fe isotope ratio measurements via MC-ICP-MS. This work reports a systematic evaluation of the effect of cold plasma conditions on the spectral interferences, hampering Fe isotopic analysis, and instrumental mass discrimination, both being inherent pitfalls of MC-ICP-MS isotope ratio measurements. Isotopic analysis of Ni is promising when applied in conjunction to that of Fe, because these elements possess nearly similar chemical properties, except for their oxidation states in nature. Particularly, this work applied stable isotopic analysis of Fe and Ni to reveal the thermal evolution of the parent bodies of iron and stony-iron meteorites, in which these two elements became distributed between multiple mineral phases during the evolution of the meteorite parent bodies. Of special interest are methods of *in situ* high precision isotopic analysis, e.g. LA-MC-ICP-MS, which can (1) directly determine isotopic compositions of accessory minerals, which help to reconstruct equilibration conditions of the mineral assemblages, and (2) provide lateral isotope profiles of diffusion or overgrowth within individual minerals, invaluable for reconstruction of cooling histories of meteorites.

In second half of 20th century instrumental neutron activation analysis (INAA) was established as a standard tool for trace and ultra trace bulk elemental analysis of planetary materials, which led to a significant breakthrough in the understanding of cosmochemical processes in the early Solar System. However, as INAA is being gradually decommissioned worldwide the last decade, bulk trace elemental analysis of planetary materials has been typically performed using pneumatic nebulization ICP-MS. At the same time, there is an ever-growing request for *in situ* minimally invasive, laterally resolved, sensitive, accurate and precise methods of trace element analysis for cosmochemical applications. Chapter 2 evaluates the capabilities and limitations of nanosecond LA-ICP-MS for spatially resolved (2-dimensional mapping) and bulk elemental analysis of iron meteorites. To assess the performance of this analytical approach, the data obtained were compared to those obtained (1) via multi-element solution ICP-MS (after digestion) relying on external calibration and (2) high-accuracy determination of selected platinum group elements using solution ICP-MS after target element isolation by anion exchange chromatography and deploying isotope dilution for quantification. The occurrence of matrix effects during nanosecond LA of metallic meteoritic material requires special attention. It was demonstrated that careful quantification using a set of matrix-matched reference materials and sum normalization to 100 % as a means of internal standardization permits ns-LA-ICP-MS to be used for fast and quasi non-destructive analysis of iron meteorites, not only of homogeneous ataxites and hexahedrites, but also of more heterogeneous ones. In the context of elemental mapping, multivariate analysis was demonstrated to be a powerful tool that can provide valuable information on the sub-solidus fractionation of the elements in the cores of differentiated parent bodies. Chapter 3 describes the application of two microbeam techniques, i.e. LA-ICP-MS and micro-X-ray fluorescence spectrometry (μXRF), for major and trace element mapping of pallasite olivines. It is discussed how, in contrast to bulk analytical methods, laterally resolved mapping techniques allow one to discriminate non-olivine inclusions mathematically, permitting establishment of average concentration values for “pure olivine”. The element mapping approach revealed complex zoning in pallasite olivines, which can potentially be explained by evolutional histories of the pallasite parent bodies and the crystal chemistry of olivine. Multivariate analysis of the laterally resolved multi-element concentration data of different pallasite olivines yielded slight differences in their clustering in factor score space, potentially providing an independent measure of the genetic relationships that exist between the different pallasites and their parent bodies.

Another benefit of ICP-MS, highly requested in analytical cosmochemistry, is its ability to measure isotope ratios with a precision that suffices to resolve the tiny natural variations of isotopic compositions. Proper chemical sample preparation procedures and measurement protocols are necessary to ensure accurate and precise isotope ratio measurements. In chapter 4, the development of an isolation procedure and measurement protocol relying on MC-ICP-MS for high-precision Ni isotopic analysis in metal and silicate matrixes is reported on. In studies of Ni isotope systematics, mass-dependent variations in the isotopic composition of Ni are often bypassed because of the challenges associated with the sample preparation. At the level of natural variation studied, Ni isotope ratio measurements are extremely sensitive to spectral interference, to artificial on-column isotope fractionation and possibly even to the mass bias correction model applied. Due to the difficulties affecting chemical isolation of Ni from multiple elements (Cr, Ti, alkali metals), a laborious double spike technique was previously preferred to address Ni stable isotope signatures in silicate matrices. The recognition of the small natural variations in the isotopic composition of Fe resulting from geological processes is one of the biggest breakthroughs in geosciences of the last decade. This accomplishment results from widespread application of MC-ICP-MS. Chapter 5 evaluates the capabilities of cold plasma conditions in combination with the standard and high-transmission interfaces and dry/wet plasma conditions for high-precision isotopic analysis of Fe by multi-collector ICP-MS. Cold plasma conditions were once widely used in ICP-MS to suppress Ar-based spectral interferences, and most often they were used to offer a solution for the overlap of the signals of $^{40}Ar^{16}O^+$ and $^{56}Fe^+$. However, after widespread application of high-resolution instruments and collision/reaction cells, the approach became nearly forgotten. Although cold plasma was successfully used in the context of isotope ratio measurements of Fe, Li and Cr via MC-ICP-MS, the possibility of using higher mass resolution provided by the new generation of MC-ICP-MS instruments is typically preferred for resolving spectral interferences. Chapter 5 presents an experimental evaluation of the effects of the plasma RF power, different plasma interfaces, and wet/dry plasma conditions on the level of the spectral interferences in high-precision isotopic analysis of Fe by MC-ICP-MS. Critically, this chapter sheds more light onto not yet completely understood processes leading to instrumental mass discrimination, which jeopardize the precision and, especially, the accuracy of isotope ratio measurements. It is demonstrated that careful selection of the instrumental parameters allows to decrease the magnitude of instrumental mass discrimination between the Fe isotopes.

Chapter 6 describes the application of the isolation and measurement protocols developed for Ni isotopic analysis to the determination of the Ni isotopic composition (together with that of Fe) in various iron and stony-iron meteorites in an attempt to further constrain the planetary differentiation processes that shifted these isotope ratios and to shed light on the formational history and evolution of selected achondrite parent body asteroids. Emphasis is placed on spatially resolved isotopic analysis of iron meteorites and on the isotopic characterization of adjacent metal and silicate phases. High-precision Ni isotopic signatures and the 3-isotope method revealed the kinetic nature of the process underlying the formation of the Widmanstätten pattern. It is also shown that the Fe isotopic signatures of iron meteorites and the metal phases of pallasites correlate with their Ir content, revealing a dependence of the bulk Fe isotopic composition on the fractional crystallization of an asteroidal metal core. The heavier Fe isotope ratios for the metal and lighter values for the corresponding olivines are interpreted to reflect later-stage Fe isotopic re-equilibration between these phases, rather than a pristine record of mantle-core differentiation. It is shown that for mesosiderites and silicate-bearing iron meteorites, the isotopic signatures of Ni and Fe likely result from solid-state diffusion.

In the last chapter, the *in situ* measurement of Fe and Ni isotopic signatures in individual mineral phases of iron meteorites and pallasites via femtosecond LA-MC-ICP-MS is reported on. The isotopic signatures are determined in individual sub-mm sized phosphide and sulphide minerals. Additionally, isotopic profiles across olivines of main group pallasites, large troilite, and Fe-Ni metal phases were measured with a spatial resolution of 30-80 μm. It is demonstrated that in general, laterally resolved Fe-Ni stable isotopic signatures reveal efficient thermal equilibration of mineral phases formed at higher temperatures (olivine, troilite, schreibersite), and an equilibrium-driven isotope fractionation between the phases. In particular, the confirmed equilibrium-controlled isotope fractionation of Fe in olivine-bulk metal system permits to use the Fe isotopic composition as an isotope geothermometer. At the same time, kamacite-taenite Fe-Ni metal, formed below ≈800 ^{o}C displays diffusive Fe and Ni isotopic profiles, confirming previous suggestions of kinetic-driven isotope fractionation. By comparison with patterns theoretically calculated for kamacite-taenite sub-solidus diffusive isotopic profiles, the experimentally determined patterns of the laterally resolved isotopic signatures allow discriminating between higher (650 ^{o}C) and lower (250, 450 ^{o}C) temperatures at which the cooling of the cores of the parent bodies occurred.

Inzicht verschaffen in de vorming en vroege evolutie van planetesimalen en planetaire embryos in ons Zonnestelsel vormt een belangrijke wetenschappelijke uitdaging. In het bijzonder blijft het huidige inzicht in planetaire accretie en differentiatieprocessen, waarbij een onveranderde massa van primitief meteoritisch materiaal evolueert in een lichaam met een silicaat-rijke mantel en metallische kern, beperkt. De ruimteprogramma's georganiseerd door verschillende landen zijn erop gericht verschillende objecten in het Zonnestelsel beter te karakteriseren door gebruik te maken van orbiters of landers (bv. de Europese Rosetta en ExoMars missies), maar technologische restricties beperken de analytische mogelijkheden op basis van afstandswaarneming, en return missions vereisen enorme financiële middelen. In tegenstelling daarmee stellen meteorieten gemakkelijk toegankelijk extraterrestrisch materiaal voor dat (1) een brede diversiteit aan moederlichamen/staalname locaties vertegenwoordigt en (2) ook uit de diepste binnenzijde van meteoritische moederlichamen afkomstig is, hetgeen hen de grootste en meest precieze bron van kennis over de evolutie van het Zonnestelsel maakt. Gedifferentieerde meteorieten stellen het binnenste gedeelte van hun moederasteroïden voor, d.w.z. de kern en kern-mantel overgang, niet toegankelijk in het geval van Aarde of de andere planeten. De moederlichamen van ijzer en steenijzermeteorieten stellen daarom een natuurlijk laboratorium voor dat gebruikt kan worden om kernvorming en differentiatie, de evolutie in de samenstelling van de mantels en korsten van planetesimalen doorheen de tijd, processen die directe informatie over de discrete accretie van de terrestrische planeten opleveren, en, uiteindelijk, de vorming van bewoonbare planeten, zoals de onze, te bestuderen. De verdeling van spoorelementen en stabiele isotopische variaties in extraterrestrisch materialen kan verbeterde inzichten opleveren in de processen die zich afspeelden tijdens de evolutie van het Zonnestelsel. Deze chemische en isotopische vingerafdrukken kunnen gebruikt worden om een aantal processen te bestuderen, die kritisch zijn om algemene vragen over de evolutie van asteroïden en planetaire lichamen te beantwoorden en toepasbaar zijn op de vorming van onze eigen planeet. Onder deze processen nemen de opsmelting van het moederlichaam, metaal-silicaat fractionering, kernvorming en thermische evolutie van het meteoritisch moederlichaam een bijzonder plaats in.

Cosmochemie is voortdurend op zoek naar nieuwe ontwikkelingen in moderne analytische scheikunde in termen van sensitiviteit, accuratesse, precisie en laterale resolutie. Het uiteindelijke doel van dit werk is om een bijdrage te leveren in de ontwikkeling van op ICP-massaspectrometrie (ICP-MS) gebaseerde technieken voor de bepaling van element concentraties en hoge-precisie isotopenverhoudingen (Fe, Ni) in cosmochemische toepassingen. Hiertoe behoort ook de toepassing van in situ laser ablatie (LA) staalname op een microscopisch niveau, waardoor een ruimtelijke dimensie aan de verzamelde informatie wordt toegevoegd. Dit onderzoek focusseerde zich in het bijzonder op een evaluatie van de mogelijkheden van LA-ICP-MS om de 2-dimensionale (2D) verdeling van spoor- en hoofdelementen in kaart te brengen, waarbij verschillende kwantificatiestrategieën, matrixeffecten, referentiemateriaaleigenschappen en methodologische detectielimieten werden geëvalueerd. Er werd aangetoond hoe 2D elementverdelingen in de metaalfase van ijzermeteorieten en silicaatmateriaal van pallasieten kunnen bijdragen tot een beter begrip van de processen die zich voordeden in de moederlichamen van meteorieten. Een tweede focus in dit werk was een evaluatie van de mogelijkheden van "multicollector" (MC) ICP-MS voor hoge-precisie isotopische analyse van ijzer (Fe) en nikkel (Ni), twee elementen waaruit gedifferentieerde meteorieten voornamelijk zijn opgebouwd. De procedure voor de isolatie van deze elementen en het MC-ICP-MS meetprotocol voor de studie van variaties in de stabiele isotopenverhoudingen van nikkel dienden nauwkeurig te worden geëvalueerd om accurate en precieze data te verkrijgen.

Het vermogen om natuurlijke variaties in de Fe isotopenverhouding met een hoge precisie vormt een van de grootste doorbraken in de geo- en cosmochemie in het laatste decennium. Deze omwenteling werd mogelijk gemaakt door de ontwikkeling van analytische methodes om Fe isotopenverhoudingen te bepalen via MC-ICP-MS. Dit voorgestelde werk stelt een systematische evaluatie voor van het effect van "cold plasma" condities op spectrale interferenties, die de analyse van Fe isotopenverhoudingen verstoren, en op instrumentele massadiscriminatie, beide hindernissen bij het meten van isotopenverhoudingen met behulp van MC-ICP-MS. De bepaling van de verhouding van de hoeveelheid van de isotopen van Ni is vooral beloftevol wanneer deze gecombineerd kan worden met de isotopenanalyse van Fe, omdat deze elementen sterk vergelijkbare chemische eigenschappen vertonen, met uitzondering van hun in de natuur voorkomende oxidatietoestanden. De analyse van de stabiele isotopen van Fe en Ni werd in dit werk uitdrukkelijk toegepast om de thermische evolutie van de moederlichamen van ijzer en steen-ijzer meteorieten te duiden, waarbij deze twee elementen, tijdens de evolutie van de moederlichamen van deze meteorieten, werden verdeeld over meerdere mineraalfasen. Er werd in het bijzonder aandacht besteed aan methoden die hoge-precisie in situ isotopenanalyse toelaten, zoals LA-MC-ICP-MS, om (1) op directe wijze de isotopische samenstelling van accessorische mineralen te bepalen, hetgeen toelaat om de condities voor evenwichtsinstelling in mineraalassemblages te reconstrueren, (2) laterale isotopische profielen ten gevolge van diffusie of “overgrowth” binnen individuele mineralen te bepalen, hetgeen zeer waardevol is om de afkoelingsgeschiedenis van meteorieten te achterhalen.

In de tweede helft van de 20ste eeuw heeft instrumentele neutron activeringsanalyse (INAA) zich onderscheiden als de standaardmethode voor de analyse van spoor- en ultraspoorelementen in planetaire materialen, hetgeen leidde tot belangrijke doorbraken in het begrip van cosmochemische processen in het vroege Zonnestelsel. Aangezien INAA geleidelijk aan uit routine wordt genomen sinds de laatste 10 jaar, worden bulk spoorelementanalysen van planetaire materialen gewoonlijk uitgevoerd met behulp van ICP-MS voorzien van pneumatische verstuivers. Tegelijkertijd bestaat er een immer-groeiende nood aan accurate en precieze in situ methodes, die leiden tot minimale invasie en optimale laterale beeldvorming, voor cosmochemische toepassingen. Hoofdstuk 2 evalueert de mogelijkheden en beperkingen van nanoseconde LA-ICP-MS voor ruimtelijke beeldvorming (2-dimensionele elementverdelingen) en elementanalyse van de bulk van ijzermeteorieten. Om de prestaties van deze analytische benadering door te lichten werd de data vergeleken met de resultaten verkregen via (1) multi-element oplossing ICP-MS (na digestie) met behulp van externe kalibratie en (2) hoge-accuratesse concentratiebepaling van geselecteerde platinagroep-elementen met behulp van oplossing ICP-MS na isolatie van de beoogde elementen via anion-uitwisselingschromatografie en gebruik makend van isotopendilutie als kwantificatiemethode.

De aanwezigheid van matrixeffecten tijdens nanoseconde LA op metallisch meteorietmateriaal vereist bijzondere aandacht. Er werd aangetoond dat zorgvuldige kwantificatie met behulp van een set referentiematerialen met vergelijkbare matrices en de toepassing van som-normalisatie tot 100% als interne normalisatieprocedure van ns-LA-ICP-MS een snelle en quasi niet-destructieve methode maakt voor de analyse van ijzermeteorieten, niet enkel homogene ataxieten en hexahedrieten, maar ook heterogenere types. In de context van 2-dimensionele elementverdelingen werd aangetoond dat multivariate analyse een krachtig werktuig vormt dat waardevolle informatie oplevert over de sub-solidus fractionering van elementen in de kern van gedifferentieerde moederlichamen. Hoofdstuk 3 beschrijft de toepassing van twee “microprobe” technieken, met name LA-ICP-MS en micro-X-straal fluorescentiespectrometrie (µXRF), om de 2D-verdeling van hoofd- en spoorelementen in olivijnen van pallasieten in kaart te brengen. Er werd beschreven hoe, in tegenstelling tot bulk analytische methoden, beeldvormingstechnieken toelaten om niet-olivijn inclusies mathematisch te onderscheiden, waardoor gemiddelde concentratiewaarden voor “zuivere olivijn” konden worden bepaald. De elementverdelingen duidden op een complexe zonering in de olivijnen van pallasieten, wat mogelijk verklaard kan worden door de evolutionaire geschiedenis van de moederlichamen van de pallasieten en de kristalchemie van olivijn. Multivariate analyse van de “laterally resolved” multi-element concentratiedata verkregen voor olivijnen van verschillende pallasieten leverden kleine verschillen op in hun clustering in de factor score ruimte wat mogelijk een onafhankelijke maat oplevert voor de genetische verbanden te onthullen tussen verschillende pallasieten en hun moederlichamen.

Een ander voordeel van ICP-MS, vaak gezocht in analytische cosmochemie, is het vermogen om isotopenverhoudingen te meten met een precisie die toelaat om de kleine natuurlijke variaties in isotopische samenstellingen te onderscheiden. Gepaste chemische staalvoorbereidingsprocedures en meetprotocols zijn nodig voor accurate en precieze metingen van isotopenverhoudingen. In hoofdstuk 4 wordt de ontwikkeling van een isolatieprocedure en meetprotocol gebaseerd op MC-ICP-MS voor de hoge-precisie isotopische analyse van Ni in metaal en silicaatmatrices beschreven. In studies met betrekking tot de isotopensystematiek van Ni worden massa-afhankelijke afwijkingen in de isotopische samenstelling van Ni vaak vermeden omwille van de uitdagingen die geassocieerd zijn met de staalvoorbereiding. Op het niveau van de bestudeerde natuurlijke variaties zijn de metingen van Ni isotopenverhoudingen extreem gevoelig voor spectrale interferenties, voor artificiële isotopenfractionering op de chromatografische kolom en mogelijk zelfs voor het toegepaste mathematisch model ter correctie van de “mass bias”. Omwille van de moeilijkheden bij de chemische afscheiding van Ni van verschillende elementen (Cr, Ti, alkalimetalen) werd voorheen vaak geopteerd om de stabiele isotopensignaturen van Ni in silicaatmatrices te bepalen met behulp van een arbeidsintensieve “double spike” techniek. De erkenning van het voorkomen van kleine natuurlijke variaties in de isotopische samenstelling van Fe als gevolg van geologische processen vormt een van de belangrijkste doorbraken in de geowetenschappen van het laatste decennium. Deze prestatie resulteert van het wijdverspreide toepassen van MC-ICP-MS.

Hoofstuk 5 evalueert de mogelijkheden van “cold plasma” condities in combinatie met standaard en hoge-transmissie “interfaces” en natte/droge plasmacondities voor hoge-precisie isotopische analyse van Fe met behulp van multicollector ICP-MS. “Cold plasma” condities werden in het verleden toegepast in ICP-MS om Ar-gebaseerde spectrale interferenties te onderdrukken, en het vaakst werd deze specifieke toestand van het plasma gebruikt om een oplossing te bieden voor de overlap tussen de 40Ar16O+ en 56Fe+ signalen. Na de wijdverspreide ingebruikname van hoge-resolutie instrumenten en collisie/reactiecellen, raakte deze benadering echter in ongebruik. Hoewel een “cold plasma” succesvol werd gebruikt in de context van de meting van Fe, Li, en Cr isotopenverhoudingen via MC-ICP-MS, wordt de mogelijkheid om de hogere massaresolutie te gebruiken in de nieuwste generatie MC-ICP-MS instrumenten vaak verkozen om spectrale interferenties aan te pakken. Hoofdstuk 5 stelt een experimentele evaluatie voor van de effecten van het plasma RF-vermogen, verschillende types plasma “interfaces”, en natte/droge plasmacondities op het niveau van de spectrale interferenties tijdens de hoge-precisie isotopische analyse van Fe met behulp van MC-ICP-MS. In het bijzonder legt dit hoofdstuk zich toe op de nog niet volledig begrepen processen die leiden tot instrumentele massadiscriminatie, die de precisie, maar ook vooral de accuratesse tijdens metingen van isotopenverhoudingen in het gedrang brengt. Er wordt aangetoond dat een voorzichtige keuze van de instrumentele parameters de omvang van de instrumentele massadiscriminatie tussen de Fe isotopen significant kan doen afnemen.

Hoofdstuk 6 beschrijft de toepassingen van de isolatie- en meetprotocols ontwikkeld voor de isotopische analyse van Ni voor de bepaling van de Ni isotopische samenstelling (samen met die van Fe) van verschillende ijzer en steen-ijzer meteorieten, in een poging om de planetaire differentiatieprocessen die leidden tot veranderingen in deze isotopenverhoudingen en de vormingsgeschiedenis en evolutie van geselecteerde achondritische moederlichaamasteroïden beter toe te lichten. De nadruk werd gelegd op de combinatie van ruimtelijke beeldvorming en isotopische analyse van ijzermeteorieten en op de isotopische karakterisering van nabij elkaar gelegen metaal- en silicaatfasen. De hoge-precisie Ni isotopische signaturen en 3-isotopenmethode duidden op de kinetisch aard van het proces dat aan de basis ligt van de vorming van het Widmanstätten patroon. Er werd ook aangetoond dat de Fe isotopische signaturen van ijzermeteorieten en de metaalfasen van pallasieten correleren met hun Ir inhoud, hetgeen erop wijst dat de bulk Fe isotopische samenstelling afhangt van fractionele kristallisatie in de metallische asteroïdekern. De zwaardere Fe isotopenverhoudingen van het metaal en de lichtere waarden voor de overeenkomstige olivijn worden geïnterpreteerd het gevolg te zijn van een Fe isotopische herverdeling tussen deze fasen in een later ontwikkelingsstadium, eerder dan een ongewijzigde opname van de mantel-kern differentiatie. Dit werk toont aan dat de Ni en Fe isotopische signaturen van mesosiderieten en silicaat-bevattende ijzermeteorieten waarschijnlijk het gevolg zijn van “solid-state” diffusie.

Het laatste hoofdstuk rapporteert over de in situ meting van de Fe en Ni isotopische signaturen van individuele mineraalfasen in ijzermeteorieten en pallasieten bepaald via femtoseconde LA-MC-ICP-MS. De isotopische vingerafdrukken werden bepaald in individuele sub-mm fosfide en sulfide mineralen. Bovendien werden isotopische profielen met een ruimtelijke resolutie van 30-80 μm bepaald doorheen olivijnkristallen van “main group” pallasieten, grote troiliet en Fe-Ni metaalfasen. Er werd aangetoond dat “laterally resolved” Fe-Ni stabiele isotopische signaturen over het algemeen wijzen op een efficiënte thermische evenwichtsinstelling tussen mineraalfasen die gevormd werden bij hogere temperaturen (olivijn, troiliet, schreibersiet), en een door evenwichts-gedreven isotopenfractionering tussen de fasen. In het bijzonder laat de bevestigde evenwichts-gedreven isotopenfractionering van Fe in het olivijn-bulk metaalsysteem toe om de Fe isotopische samenstelling te gebruiken als een isotopische geothermometer. Tezelfdertijd vertoont kamaciet-taeniet Fe-Ni metaal dat gevormd wordt bij temperaturen onder ≈800 ˚C diffusieve Fe en Ni isotopische profielen, hetgeen een kinetisch gedreven isotopenfractionering bevestigt. Door de vergelijking met patronen die theoretische werden berekend voor kamaciet-taeniet sub-solidus diffusieve isotopische profielen, laten de experimenteel bepaalde patronen van de “laterally resolved” isotopische signaturen toe om het onderscheid te maken tussen hogere (650 ˚C) en lagere (250, 450 ˚C) temperaturen waarbij de afkoeling van de moederlichamen plaatsgreep.

The impact of my PhD research is reflected in publications in peer-reviewed scientific journals:

1. Stepan M. Chernonozhkin, Steven Goderis, Stephen Bauters, Bart Vekemans, Laszlo Vincze, Philippe Claeys and Frank Vanhaecke, 2014. Evaluation of pneumatic nebulization and ns-laser ablation ICP-MS for bulk elemental analysis and 2-dimensional element mapping of iron meteorites. J. Anal. At. Spectrom., 29 (6), 1001–1016. doi:10.1039/c3ja50387a (Chapter 2).
2. Stepan M. Chernonozhkin, Steven Goderis, Lara Lobo, Philippe Claeys and Frank Vanhaecke, 2015. Development of an isolation procedure and MC-ICP-MS measurement protocol for the study of stable isotope ratio variations of nickel. J. Anal. At. Spectrom., 30 (7), 1518–1513. doi: 10.1039/c5ja00080g (Chapter 4).
3. Stepan M. Chernonozhkin, Steven Goderis, Marta Costas-Rodríguez, Philippe Claeys and Frank Vanhaecke, 2016. Effect of parent body evolution on equilibrium and kinetic isotope fractionation: a combined Ni and Fe isotope study of iron and stony-iron meteorites. Geochimica et Cosmochimica Acta 186, 168–188. doi:10.1016/j.gca.2016.04.050 (Chapter 6).

The scientific outcomes of my PhD were also presented in a number of conference proceedings:

1. Stepan M. Chernonozhkin, Steven Goderis, Lara Lobo, Philippe Claeys and Frank Vanhaecke, 2015. Development of an isolation method and MC-ICP-MS measurement protocol for studying mass-dependent isotope fractionation of nickel. European Winter Conference on Plasma Spectrochemistry, Münster, Germany, February 22–26, abstact# IS1-OP03 (Chapter 4).
2. Stepan M. Chernonozhkin, Steven Goderis, Philippe Claeys and Frank Vanhaecke, 2015. Fe and Ni isotope fractionation in magmatic and non-magmatic iron meteorites. Goldschmidt 2015, Prague, Czech Republic, August 16–21, abstract# 3801 (Chapter 6).

Additional manuscripts within the context of this PhD are currently in preparation, these include, but not limited to:

1. Stepan M. Chernonozhkin, Seann J. McKibbin, Stijn J. M. Van Malderen, Steven Goderis, Philippe Claeys and Frank Vanhaecke. Quantitative laser ablation ICP-MS and µXRF element mapping of zoned olivines of main group pallasites (Chapter 3).
2. Stepan M. Chernonozhkin, Marta Costas-Rodríguez, Philippe Claeys and Frank Vanhaecke. Evaluation of the use of cold plasma conditions for Fe isotopic analysis via MC-ICP-MS: effect on spectral interferences and instrumental mass discrimination (Chapter 5).
3. Stepan M. Chernonozhkin, Mona Weyrauch, Steven Goderis, Martin Oeser, Seann J. McKibbin, Ingo Horn, Lutz Hecht, Stefan Weyer, Philippe Claeys and Frank Vanhaecke. Thermal equilibration of iron meteorite and pallasite parent bodies recorded at the mineral scale by Fe and Ni isotope systematics (Chapter 7).

Chapter 1

General Introduction

"Since it is a close analogue of the ordinary spectrograph and gives a "spectrum" depending upon mass alone, the instrument is called a "mass spectrograph" and the spectrum it produces a "mass spectrum"."

Francis William Aston
Nobel Lecture 1922

1. Meteorites and their parent bodies

Meteorites are solid fragments of silicate or iron originating from outer space, which survived the passage through the atmosphere and fell to Earth, and they are currently the largest and most precise source of knowledge on the chemistry and composition of the Solar System. Currently, meteorites are classified into multiple classes, groups and sub-groups depending on their chemical properties. This classification aims to separate the meteorites on the basis of their genesis in different parent bodies, currently still existing in the Solar System or disrupted with only partial asteroids and meteorites remaining. All meteorites are traditionally identified as falls or finds, depending whether they are recovered after observation when passing through the atmosphere or not, respectively. The parent bodies of some meteorites are defined based on the petrographic, mineralogical and geochemical *in situ* observations by remote landers and orbiters or laboratory analyses of samples available from return missions. For instance, 244 meteorites with a total mass of more than 138 kg, found in arid deserts of Africa and in Antarctica, are recognized to come from the Moon, based on the comparison with samples returned by the Apollo and Luna missions. With a total mass exceeding 136 kg, 162 meteorites are currently believed to originate from Mars. The last group of meteorites with an identified currently complete parent body is the HED clan, consisting of 1699 known members with total mass over 1600 kg. Based on the data collected by the Dawn space probe, HED meteorites are thought to have formed in the crust of asteroid 4 Vesta. Apart from these 3 groups of known genesis, other meteorites are believed to originate from a variety of parent bodies of which the remnants can be traced in the asteroid belt. Today (2016), the Meteoritical Bulletin Database contains 53181 approved meteorites, 77.7 % (41327) of which were recovered in Antarctica, and 18.5 % (9816) in arid deserts of North Africa, Australia, Chile, and the Arabian Peninsula. The amount of meteorites available is rapidly increasing through dedicated meteorite recovery missions to Antarctica and arid deserts. For instance, the total mass of lunar meteorites that were recently recovered equals the total amount of material returned from the Moon by manned and un-manned missions. At the same time, lunar meteorites obviously cover more differential sampling locations than the returned material, although the latter are accompanied by geological contexts.

1.1. Classification of meteorites

Meteorites are traditionally divided into the major groups “chondrites” and “non-chondritic meteorites” based on their chemical and mineralogical composition. Depending on the degree of fractionation experienced in their parent body, the latter are separated into primitive and differentiated achondrites, further sub-divided into smaller groups. The achondrites include, for example, Lunar, Martian, stony iron and iron meteorites (Figure 1-1). Following sections present the description of various meteorite groups, with emphasis made on iron and stony-iron meteorites, as these form a major part of present PhD thesis.

Chondrites are the most abundant type of meteorite found on Earth, accounting for 91.8 % (48845) of the meteorites present in collections worldwide. They are believed to stem from the most primitive solid materials in the Solar System, which underwent significantly less melting and differentiation than differentiated achondrites. Chondrites are composed of fine unequilibrated assortments of mineral grains, mostly silicates, oxides, metals and sulfides, most of which formed in the Solar nebula. Apart from this matrix, chondrites are principally composed of chondrules – round grains of sub-millimeter size, which are interpreted to represent partially molten droplets formed in interplanetary space before accretion. The volumetrical abundance of chondrules varies among chondrite groups and can reach up to 80 % (for O- and E-types of chondrites (Brearley and Jones, 1998). Chondrules exhibit a variety of textures and are composed primarily of olivine and pyroxene crystals set in fine-grained or glassy matrices. Refractory inclusions form another important component of chondrites, i.e., calcium- and aluminum-rich inclusions (CAIs), amoeboid olivine aggregates (AOAs) and pre-solar grains (McSween and Huss, 2010). The fine mineral grains composing chondrites are thought to most closely resemble the primary minerals composing the Solar Nebula – the gas/dust/plasma cloud surrounding the young Sun from which the Solar System objects later formed. During the early evolution of the nebula, these minerals condensed, accreted and compacted to form parent bodies of chondrites – primitive undifferentiated asteroids.

The chondrites are classified into clans and subdivided into smaller chemical groups based on their mineralogy, bulk chemical and isotopic composition: the carbonaceous chondrites (C), ordinary chondrites (O), enstatite chondrites (E) and the more rare Rumuruti (R) and Kakangari (K) chondrites.

Ordinary chondrites are the most abundant type of meteorites, accounting for 86.8 % of all classified meteorites (46155), 894 of which are falls. Ordinary chondrites are subdivided into 3 chemical groups depending on their bulk Fe content: H (≈27 % Fe by mass), L (≈22 % Fe by mass) and LL (≈21 % Fe by mass) (Scott and Krot, 2014). The chemical compositions of ordinary chondrites are characterized by several distinct patterns, known as Prior’s rules:

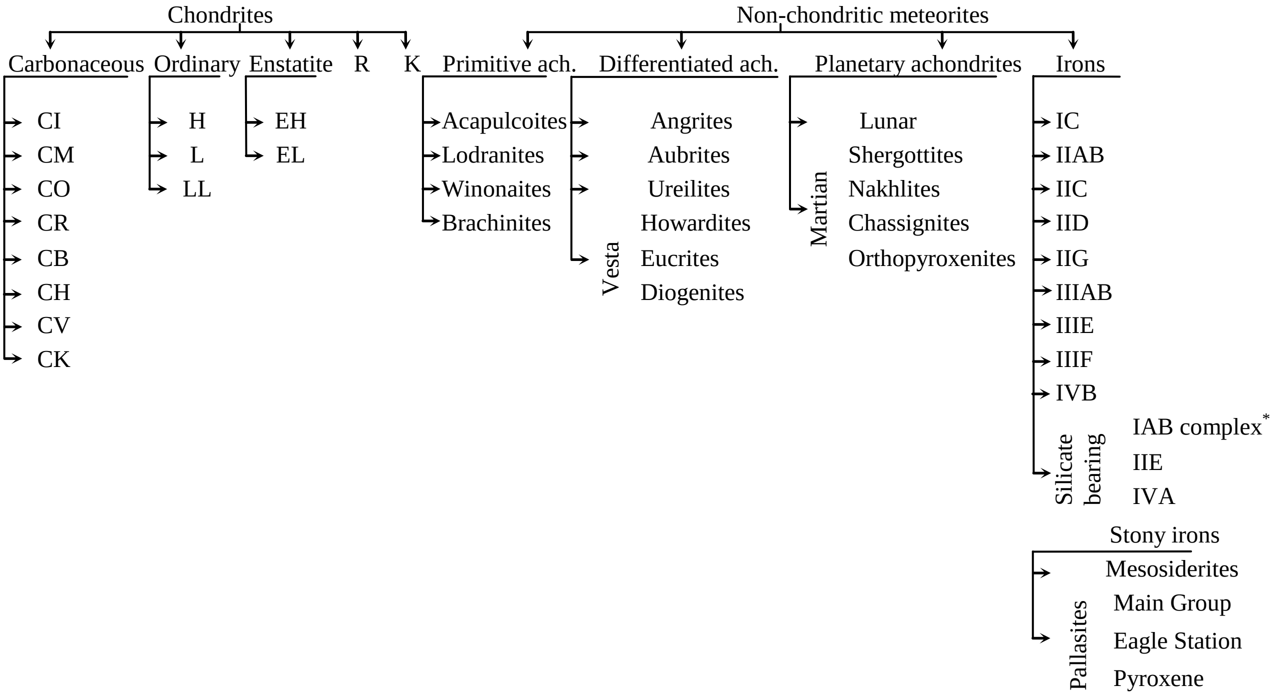

Figure 1-1. Classification of meteorites adopted from Krot, 2014 (Krot et al., 2014). * IAB complex includes former IAB and IIICD groups.

(a) chondrites with low metal content have high Ni concentrations in the metal, (b) chondrites with low metal content have silicates with higher FeO abundances. Additionally, Urey and Creig revealed that ordinary chondrites cluster into 2 separate groups when the Fe content of their silicate fraction is plotted versus the Fe content in the metal plus the Fe content in the sulfide fraction. These groups correlate with the H and L+LL chemical groups, defined based on the bulk Fe content. The LL chemical group can be distinguished from the L group by a higher ferrosilite content in the pyroxene and a higher fayalite content in the olivine.

Carbonaceous chondrites are rarer than ordinary chondrites and make up 3.7 % (1948) of all meteorites. They contain large amounts of the volatile elements C, N, H and exhibit generally higher Mg/Si and Ca/Si ratios than measured for other chondrite clans. The clan of carbonaceous chondrites is subdivided into 8 chemical groups, which show a large variety in chemical composition and petrography: Ivuna type (CI), Murchison type (CM), Vigarano type (CV), Ornans type (CO), Keroonda type (CK), Renazzo type (CR), high metal type CH and Bencubbin type CB. All the groups except for the CH groups are named after the characteristic first member. Abundance ratios of Na, Cr, Mn and S are characteristic for each subgroup (Lodders and Fegley, 2011). Carbonaceous chondrites are thought to be essentially the least fractionated clan of chondrites, and the CI group, consisting of a fine-grained matrix almost entirely free of refractory inclusions, metal and chondrules, is traditionally used as a reference for the bulk element composition of the solid Solar System because it contains elements in proportions similar to the abundances of the Sun. All the chondrite groups are depleted in volatile elements relative to CI, *e.g.,* Zn and S. CM, CV, CK and CO chondrites are enriched in refractory Al compared to CI chondrites. Such relations are explained by fractionation processes, experienced by meteorite parent bodies. Based on overall the chemical composition, mineralogy and petrology, the clan of C chondrites consists of meteorite groups that are relatively less related to each other, compared with the other chondrite clans (Scott and Krot, 2014).

Enstatite chondrites are a rare group of chondrites, forming 1.1 % (575) of classified meteorites. Enstatite chondrites are formed under strongly reducing conditions, which is reflected by the atypical mineralogy of silicates and unusual metal and sulfide phases. Most Fe is contained in metal and sulfides, reflected by low Fe contents for all silicate minerals. In particular, the Mg-end member of pyroxene, enstatite $MgSiO_3$, is abundant. Other indications of the

Mineral	Comment	Formula
	Native elements	
Kamacite	α-iron (*bcc*), Ni-poor, ≈ 5 % Ni	Fe-Ni alloy
Taenite	γ-iron (*fcc*), Ni-rich, ≈ 10-70 % Ni	Fe-Ni alloy
	Silicates	
Olivine	Mg^{2+} silicate (forsterite) and Fe^{2+} silicate (fayalite) make up olivine solid solution series	$Mg_2SiO_4 – Fe_2SiO_4$
Pyroxene	Low Ca pyroxenes make up solid solution series between Mg (enstatite) and Fe-rich (ferrosilite) end members	$Mg_2Si_2O_6 – Fe_2Si_2O_6$
	High Ca pyroxenes make up solid solution between Mg (diopside) and Fe-rich (hedenbergite) end members, including intermedium Mg-Fe augite.	$CaMgSi_2O_6 – CaFeSi_2O_6$, $Ca(Mg,Fe)Si_2O_6$
	Pigeonite is intermediate in composition between enstatite and diopside.	$(Ca,Mg)(Mg,Fe)Si_2O_6$
Feldspar	Na-rich albite and Al-rich anorthite end members make up plagioclase feldspars solid solution series	$NaAlSi_3O_8 – CaAl_2Si_2O_8$
	Na-rich albite and K-rich orthoclase / microcline end members make up alkali feldspars solid solution series	$NaAlSi_3O_8 – KAlSi_3O_8$
Serpentine	Group of layered magnesium-iron hydrous silicate minerals abundant in some meteorites	$(Mg,Fe)_6Si_4O_{10}(OH)_8$
	Oxides	
Spinel		$MgAl_2O_4$
Chromite		$(Mg,Fe)Cr_2O_4$
Ilmenite		$FeTiO_3$
	Sulfides, phosphides and phosphates	
Troilite		FeS
Schreibersite		$(Fe,Ni)_3P$
Merrillite	Extraterrestrial hydrogen-free member of variety of whitlockites $Ca_9(MgFe^{2+})(PO_4)_6PO_3OH$	$Ca_{18}Na_2Mg_2(PO_4)_{14}$
Stanfieldite		$Ca_4(Mg,Fe^{2+},Mn)_5(PO_4)_6$
Farringtonite		$Mg_3(PO_4)_2$

Table 1-1. Some of minerals found in extraterrestrial materials and their formula.

reducing conditions under which the E chondrites were formed are the large abundance (1-3 wt%) of Si in the metal phases, the presence of Mg and Ca sulfides, and the occurrence of nitrogen minerals (osbornite TiN and sinoite Si_2N_2O) (Brearley and Jones, 1998). Compared to the other types of chondrites, enstatite chondrites have the lowest Mg/Si ratio (although some CH chondrites can have comparable Mg/Si values) (Lodders and Fegley, 2011). Similar to ordinary chondrites, E chondrites are divided into the EH and EL groups, based on the overall Fe content. The bulk compositional differences in non-volatile major elements between EH and EL were established by nebular rather than planetary processes (Keil, 1989). Additionally, EH can be differentiated from EL chondrites by higher bulk contents of Na, S, Mn, Zn and Au.

Rumuruti and Kakangari chondrites are 2 minor groups of meteorites, with 164 and 4 known members, respectively (0.3 and < 0.1 % of total classified meteorites). K-type chondrites most closely resemble particular carbonaceous chondrites, although the chemical and isotopic signatures are sufficiently distinct to separate them as a group. The Rumuruti chondrites contain 58-75 vol % of essentially equilibrated olivine, with high Fe contents (fayalite number of olivine $Fa = FeO / [FeO + MgO] \cdot 100 = 37\text{-}40$ at maximums of olivine composition frequency distribution histograms) (Brearley and Jones, 1998). This high Fe content in olivine reflects the highly oxidizing conditions at which the R chondrites formed. Compared to the ordinary chondrite groups, R chondrites have lower bulk Mg/Si and Ca/Si, but higher Ca/Si ratios (Lodders and Fegley, 2011).

Petrologic types of chondrites. Additionally to chemical groups, chondrites are classified into six petrologic types, designated by the arabic numbers 1 to 6, following the symbol of the chemical meteorite. The petrologic type indicates the degree of thermal metamorphism or aqueous alteration. Many chondrite parent bodies with originally pristine compositions suffered different degrees of chemical and mineralogical alteration by later heating (thermal metamorphism), resulting in various degrees of equilibration of mineral assortments or aqueous alteration, reflected by the occurrence of hydrous phases. The most pristine meteorites are referred to as type 3 (sometimes called “unequilibrated chondrites”). The petrologic types 4 to 6 group (some authors also distinguish petrologic type 7) indicate increasing degrees of sub-solidus thermal metamorphism, which leads to (a) compacting of the material by sintering, (b) erasing of the profiles in initially zoned minerals, (c) a reduction in the initially broad range of mineral compositions, e.g. fayalite numbers of olivines, (d) metamorphic changes of minerals, expressed in the disappearance and formation of new minerals, e.g., the formation of phosphate from schreibersite, (e) disappearance of pre-solar grains, and (f) vanishing of chondrules. Fractions can be used to distinguish smaller degrees of metamorphism between types 3 and 4. The petrologic types 1 and 2 indicate increasing degrees of aqueous alteration expressed in (a) the oxidation of iron, (b) the precipitation of sulfate and the occurrence of carbonate veins and (c) the alteration of the matrix to serpentine. Aqueous alteration does not change the overall bulk element compositions of chondrites (Lodders and Fegley, 2011; McSween and Huss, 2010; Scott and Krot, 2014).

Clan	Chemical group	Aqueous alteration		Thermal metamorphism			
Petrologic type		1	2	3	4	5	6
Carbonaceous	CI	CI1					
	CM	CM1	CM2				
	CR	CR1	CR2	CR3			CR6*
	CB			CB3			
	CH			CH3			
	CV			CV3			
	CO			CO3			
	CK			CK3	CK4	CK5	CK6
Ordinary	H			H3	H4	H5	H6
	L			L3	L4	L5	L6
	LL			LL3	LL4	LL5	LL6
Enstatite	EH			EH3	EH4	EH5	EH6
	EL			EL3	EL4	EL5	EL6
Rumuruti				R3	R4	R5	R6
Kakangari				K3	K4		
Metamorphic T, °C				400-600	600-700	700-800	800-950

Table 1-2. Classification of the petrologic types of chondrites. The petrologic types observed for the existing chemical groups of chondrites are indicated. Approximate metamorphic temperatures are indicated in the bottom row. *NWA 7317 and NWA 6921 meteorites are classified as CR6.

Primitive achondrites (acapulcoites-lodranites, winonaites, brachinites) are stony meteorites, which underwent moderate degrees of igneous planetary fractionation (melting and crystallization) of the initially chondritic precursor. Mineral compositions indicate compositional equilibration, mineral textures point to metamorphic episodes, while the bulk element compositions are only moderately fractionated from nebular. Primitive achondrites are believed to derive from chondritic materials as melt-depleted ultramafic rocks. The refractory siderophile element/Ni and chalcophile/siderophile element ratio signatures, as well as the presence of metal-sulfide veins (Mittlefehldt et al., 1998) are interpreted as indicators of melting. Acapulcoites have bulk chemical compositions similar to those of H ordinary chondrites, reflecting moderate metal/silicate fractionation. Some acapulcoites contain relict chondrules, which indicates that the degrees of experienced melting are not extensive. Lodranites are closely related to acapulcoites, but their textures, mineralogies and bulk compositions show higher degrees of differentiation (Mittlefehldt, 2014). The removal of metal and silicate partial melts in lodranites is indicated by depletion in troilite and plagioclase (Mittlefehldt et al., 1998). The elevated content of trapped noble gas is a definitive feature, genetically differentiating the acapulcoites-lodranites from ordinary chondrites. As many as 138 (0.26 % of the total amount of classified meteorites) acapulcoites-lodranites are currently known (april 2016), with nearly equal amounts in each group. Winonaites form another rare type (29 representative members) of primitive achondrites, often referred to as a single clan combined with the silicate inclusions found in IAB-complex iron meteorites (see below) based on their similarities. Winonaites can contain relict chondrules and combined observations indicate partial melt removal from initially chondritic material (Ruzicka, 2014). Brachinites (38 records in the Meteoritical bulletin catalogue) form another meteorite class, sometimes included in the primitive achondrites because of their chondritic abundances of lithophile and siderophile elements, and trapped noble gases (Mittlefehldt et al., 1998). However, brachinites do not exhibit a strictly chondritic mineralogy, which, together with the presence of melt inclusions, indicates a history of high-temperature partial melting. The brachinites formation history remains debated, with high temperature partial melting of chondritic material, coupled with metamorphism and oxidation (Nehru et al., 1996, 1992, 1983) and accumulation from magma (Mittlefehldt, 2014) as an alternative. The latter places brachinites among the differentiated achondrites.

Differentiated achondrites (ureilites, angrites, aubrites, HEDs) are stony meteorites representing crust of differentiated asteroids that formed either as solidified silicate melts or cumulates from crystallizing magma under relatively oxidizing conditions. Their parent magma is suggested to form from chondritic material, but the elemental abundances, highly fractionated from chondritic, indicate melting and fractional crystallization (McSween and Huss, 2010). Ureilites are ultramafic rocks composed predominately of olivine and pyroxene, while minor phases include carbon-rich materials, typically graphite, and diamond/lonsdaleite inclusions (Mittlefehldt et al., 1998). The carbon content of ureilites suggests possible genetic links to carbonaceous chondrites. The lithophile elements are highly fractionated from chondritic abundances, but the relatively high contents of siderophile elements are more typical for primitive meteorites (Mittlefehldt, 2014). The formation history of ureilites remains debated, as they possess features characteristic for both primitive and differentiated achondrites. As such, ureilites most likely formed as ultramafic igneous cumulates or as partial melt residues (Goodrich, 1992). Ureilites form one of the largest achondrite groups, consisting of 416 classified members to date, which is equal to 0.78 % of official meteorites. Angrites are basaltic rocks, enriched in incompatible lithophile elements, with an unusual SiO_2-poor, Ca, Al, Ti-rich mineralogy. Angrites are depleted in alkali elements, with at the same time nearly chondritic abundances of other volatile elements (e.g. Se, Zn, In, Cd) (Mittlefehldt et al., 1998). Angrites contain characteristic, unusual minerals, such as aluminan–titanian–diopside and calcium-rich olivine (kirschsteinite) (Keil, 2012; Mittlefehldt, 2014; Mittlefehldt et al., 1998). Angrites are extremely rare, with only 24 classified group members. Aubrites, as opposed to angrites, are stony meteorites with an origin derived from asteroidal crust with signatures of extremely reductive conditions in their mineralogy and element abundances. The silicates are essentially FeO free, and the dominant silicate is enstatitic orthopyroxene. Aubrites also contain metallic iron, and sulfides of lithophile elements, confirming reducing conditions. Bulk elemental abundances are characterized by low Ca/Si and Al/Si ratios and depleted siderophile elements (Mittlefehldt, 2014). The degree of reduction indicates that aubrites and E chondrites were probably formed in the same region of the Solar System (Keil, 2010). In total, 72 aubrites are known, according to the Meteoritical Bulletin Database (0.14 % of the meteorite records). Howardites, eucrites and diogenites (HED meteorites) compose the largest sample suit of differentiated asteroid crustal rocks, and remain the most studied group of achondrites, the only group with a possibly identified parent body – the asteroid 4 Vesta or several smaller Vesta-like asteroids (Burbine et al., 2001; McSween et al., 2013, 2011). The HED group consists of

1699 recognized members (322 howardites, 965 eucrites and 412 diogenites), making up 3.2 % of all classified meteorites. The HED meteorites are depleted in volatile- and in siderophile elements. The HED group includes basaltic lavas (eucrites), cumulate gabbros (cumulate eucrites), orthopyroxenites (diogenites) and impact mixtures of diogenite and eucrite clasts (howardites), representing melting, differentiation, impact- and crustal igneous processes on the differentiated parent asteroid (McSween et al., 2011; Mittlefehldt, 2014).

Planetary achondrites (lunar and Martian meteorites) are rocks differentiated in the Moon or Mars, excavated from the surface by late-stage impacts that were energetic enough to accelerate the ejecting fragments to escape velocities, and later entered Earth-crossing orbits. Currently, 244 lunar and 162 Martian meteorites with a total mass of 138 and 136 kg, respectively are officially known. Depending on their origin from the surface of the Moon, lunar meteorites are divided into 2 subgroups, representing the ancient highlands or the younger maria. Highland rocks are distinguished by high Al/Si ratios and lower Ti content. The most distinct mineral of lunar mare basalts is ilmenite, having a high Ti bulk content (Warren and Taylor, 2014). Martian meteorites (“SNC” for shergottite, nakhlite, chassignite, plus several rare orthopyroxenites and basaltic breccias) are recognized by their young crystallization ages inconsistent with igneous activity on asteroids (however, some Martian meteorites are 4 Ga old (Bouvier et al., 2005), due to (a) the large size of the parent body and associated prolonged igneous activity, and (b) a sampling bias linked to the impact excavation, undersampling the geologically older crust. SNC are basalts, clinopyroxenes, dunites or ultramafic cumulates (McSween and McLennan, 2014).

Iron meteorites are the remains of Fe-Ni metal cores from catastrophically disrupted differentiated asteroids. Some groups of iron meteorites are, however, believed to have formed on less fractionated parent bodies during early stages of core formation. Iron meteorites are relatively widespread (1129 official members, or 2.12% of all classified meteorites), not only because of their resistance to weathering and a higher survival rate during atmospheric entry, but also because of the higher likelihood that these will be recognized as unusual objects. Such bias will probably change with the rapidly increasing proportion of meteorites found in arid and Antarctic deserts, where this recognition and weathering bias is less pronounced. Iron meteorites fall into 13 major chemical groups, based on their bulk abundances of particular siderophile elements, mainly Ga, Ge, As, Ir, Ni and Au (Krot et al., 2014). The compositional differences between the groups (cores of the parent bodies) indicate that the parent bodies were formed under significantly diverse conditions in the early solar system (Benedix et al., 2014). At the same time, the compositional differences within most iron meteorite groups preserve chemical trends consistent with fractional crystallization, implying that each group formed from a single molten metallic pool or core (Scott, 1972). Highly compatible elements, such as Ir, tend to enrich in solidifying metal, while incompatible elements, such as S, are concentrated in evolving melt, ultimately forming Fe-Ni-S eutectic melts. Fractional crystallization is not the governing mechanism for the formation of the silicate-bearing iron meteorite groups (IIE and IAB complex, including former IIICD group), with textures and poorly defined elemental trends that suggest that impact mixed molten metal and silicates, and that neither group formed from a single isolated metallic melt (Goldstein et al., 2009). During slow cooldown of the iron meteorite parent bodies below approximately 900 ˚C, Ni-poor kamacite (bcc α-iron) nucleates and grows out of Ni-rich taenite (fcc γ-iron), forming the characteristic Widmanstätten pattern. The lamellae growth is controlled by solid-state diffusion, and absolute cooling rates can be elucidated by various metallographic techniques (Goldstein et al., 2014).

The IIAB, IIIAB and IVA irons are the three largest groups with distinct well-defined fractional crystallization patterns (formerly known as magmatic), with 124, 305 and 83 members to date, respectively. Low Ni contents, the absence of phosphates and the presence of graphite in IIAB irons indicate their formation from reduced material. In contrast, IIIAB irons probably have the highest abundance of phosphates, suggesting formation from oxidized material. The non-uniform metallographic cooling rates of IIIABs suggest that the parent body core was (partially) exposed deprived of mantle during cooling due to a hit-and-run collision. Similarly, distinct metallographic cooling rates for IVA irons may be interpreted as the result of a hit-and-run collision, which stripped off the silicate mantle from the core, or even as an indication of a catastrophic breakup and reassembly event (Benedix et al., 2014).

Silicate-bearing iron meteorites differ from other iron meteorite groups in that they contain variable amounts of enclosed silicates and in the observation that the minor element composition of the metal portions of most silicate-bearing iron meteorites does not indicate trends of fractional crystallization (this is why they were formerly known as the non-magmatic irons). The largest silicate-bearing groups of iron meteorites are the IAB complex (including former IAB and IIICD groups, 282 official members in total) and the IIE group (22 known members). The IAB complex irons are rich in the volatile elements C, S, and P, similar to carbonaceous chondrites. The silicates in IAB complex irons consist of a fine mixture of minerals with chondritic mineralogy, and the properties of their silicates suggest partial melting and melt migration. The IIE iron meteorites have a restricted range in metal compositions, suggesting formation on a H-chondrite-like parent asteroid. The IIE irons vary in the degree of fractionation of their silicate inclusions from felsic minerals to nearly chondritic mineralogies similar to H chondrites. The formation models of the silicate-bearing iron meteorites are heavily debated and remain unclear. Some authors suggest endogenic models, which involve interior heating of parent asteroids and the resulting incomplete segregation of metal melt and solid silicates to different degree. But such a mechanism would lead to a correlation between metal separation degree and the degree of differentiation of the silicates embedded in inclusions, which is not observed for IIE meteorites. In contrast, exogenic formation models involve impact heating as the main process, which formed molten metal pools in impact craters on the surface of a parent asteroid. However, impact heating would lead to at least partial melting of the silicates, and silicates of different melting degree would be simultaneously present as a result, which is not the case for IAB (containing only undifferentiated chondritic inclusions) and some IIE irons (containing only fractionated silicates). Another group of formation models involves a combination of endogenic and exogenic processes, either by mixing variably differentiated crust with molten metal (of external origin or from the same parent body), or via collisional disruption and re-accretion of partially differentiated asteroids (Ruzicka, 2014).

Stony-iron meteorites, consisting of pallasites and mesosiderites, are closely related to iron meteorites. There are only 106 and 220 classified members of the pallasite and mesosiderite groups, respectively. Both meteorite groups are similarly composed of nearly equal parts of metal, derived from the metal core of a differentiated asteroid, and a silicate counterpart. This silicate is made up of mantle-derived olivine crystals in the case of pallasites, or brecciated remains of basaltic minerals of predominantly crustal origin in the case of mesosiderites. Besides the observation that the parent bodies of both meteorite groups show evidence for processes related to impact and collision, there is no data to support a common origin from the same parent body (Greenwood et al., 2015, 2006).

Pallasites are stony-iron meteorites that are composed of nearly equal parts of metal, derived from the molten metal core of a differentiated planetesimal, and a mantle-derived silicate (olivine) counterpart, along with a number of accessory mineral phases (including chromites, sulfides, schreibersites and phosphates). The majority of pallasites originates from a single parent body, as evident from the limited range of trace element compositions (Wasson and Choi, 2003) and restricted oxygen isotope signatures (Greenwood et al., 2015, 2006), and is classified accordingly, as the Main Group Pallasites (PMG). Significant differences in isotopic signatures, mineral and metal compositions indicate that a number of pallasites derive from separate parent bodies, each with only one or a few representative members. Unique pallasites include the Eagle Station group (Clayton and Mayeda, 1978), Milton (Jones et al., 2003), and two pyroxene-pallasites sources (Boesenberg et al., 2000; Bunch et al., 2005).

The trace element contents of PMG metal indicate a possible link with the IIIAB iron meteorite parent body (Franchi et al., 2013; Wasson and Choi, 2003). Element contents in IIIAB iron meteorites are known to follow fractional crystallization sequences, with concentrations of Ir (and particular other elements) decreasing as the crystallization proceeds. The compositions of PMGs (*e.g.*, Au-As trends) are broadly compatible with late-stage crystallization of a core with IIIAB-like composition, suggesting a possible genetic relationship (Wasson, 2016). However, the PMGs are scattered around the IIIAB crystallization trend without showing any fractional crystallization sequence of their own (Scott, 1977a, 1977b; Wasson, 2016; Wasson and Choi, 2003).

There are currently several arguments in favor of and against a shared origin for PMGs and IIIAB iron meteorites. A key argument for the formation on a single parent body relates to the determined cosmic ray exposure ages (Voshage, 1967; Voshage and Feldmann, 1979). Potential evidence for a common origin of IIIAB and pallasite metal also includes the similar oxygen isotopic signatures for pallasites and chromite inclusions in particular IIIAB irons, with exception of the IIIAB iron Cape York with distinct oxygen isotope ratios (Franchi et al., 2013). Similarly, the Mo isotopic signatures for the metal phases (Dauphas et al., 2002) and the Hf-W short-lived isotopic decay system (Quitté et al., 2005) suggest a common origin for IIIAB and PMG meteorites. On the other hand, the Re-Os isotope chronometer has produced a whole-rock pallasite isochron distinct from those of iron meteorites, indicating that iron meteorites underwent fractional crystallization processes ~60 Myr later than pallasite metals (Chen et al., 2002). Metallographic studies of metal phases imply that below 975 K, IIIAB irons experienced faster cooling rates than pallasites and that different pallasites cooled at disparate rates, probably because this cooling took place at different depths in the parent body (Goldstein et al., 2014; Yang et al., 2010). Earlier suggestions of faster cooling of silicate at high temperature and slower cooling at lower temperatures following the metal-olivine mixing event (Tomiyama and Huss, 2005) have recently been supported by Mn-Cr isotopic work (McKibbin et al., 2016). Although the range of non-mass-dependent W isotopic signatures within the IIIAB iron group is narrower than for the iron meteorites as a whole (Markowski et al., 2006), which makes the genetic link between pallasites and IIIAB iron meteorites elusive, the mass-dependent W isotopic compositions of IIIAB and pallasites fall on the same mass-dependent isotope fractionation line (Fukami et al., 2010). Negative correlation of W isotope fractionation to Ir suggests that W stable isotopes in IIIAB and pallasites fractionated during fractional crystallization of liquid metal (Fukami et al., 2010).

The exact formation mechanism of pallasites remains heavily debated. The most rudimentary model of their formation near the quiescent core-mantle boundary of the pallasite parent body is based on their metal element composition, which is compatible with the late fractional crystallization of the pallasite parent body core, in combination with the presence of olivine, which represents either the residue of high degree partial melting or the first cumulate phase from a magma ocean. However, the angular shapes and minor compositional zoning of pallasite olivine (McKibbin et al., 2013), the dispersion of PMG compositions away from the IIIAB fractional crystallization trend, together with the observation that olivine would rapidly separate from the molten metal as the result of differences in buoyancy (Wasson, 2016), imply that additional processes are needed to explain this quiescent core-mantle boundary PMG formation model (Benedix et al., 2014). Additionally, such model requires the crystallization of the metal core on PMG differentiated parent body from the inside out, which has previously been disputed (*e.g.* see (Wasson, 2016) for discussion).

To account for the deviation of the PMG compositions from the main IIIAB fractional crystallization trend, mixing between late fractionated metallic melt and earlier crystallized metal has been proposed (Scott, 1977b; Ulff-Moller et al., 1997). To further constrain this model, Wasson (Wasson, 2016) suggests a catastrophic impact that mixed the mantle olivine and crystallized blocks from the upper part of the metal core with more evolved molten metal from deeper parts of the metal core. Part of the solid metal was re-melted during this impact and contaminated the metal magma, shifting the metal composition away from the fractional crystallization trend (Wasson, 2016). The presence of colder solid metal blocks explains the absence of a fractional crystallization trend among PMGs by fast crystallization through heat exchange and may potentially explain the disturbance of cooling rates between PMGs and IIIABs.

Another model, involving collision with a substantially molten parent body, which separated a partially solidified core and mantle containing olivine and silicate melt, remains a compelling possibility (Ruzicka, 2014). In a “hit and run” impact scenario, molten metal and silicate mantle material from the core-mantle boundary would be mixed and re-accreted (Yang et al., 2010).

Although there is little doubt that the pallasite components formed deep on the differentiated parent asteroid, near the core-mantle boundary, impact mixing of partially molten metal and silicates is needed in the formation model of pallasites. What the relation of PMG to IIIAB iron meteorites might be and how exactly the pallasite silicates were formed remain unresolved questions.

Mesosiderites have enigmatic formation histories, and most models suggest that they formed by mixing material from two different parent bodies. Silicate clasts of mesosiderites indicate their derivation from the evolved crust of a differentiated asteroid (Greenwood et al., 2015; Haack et al., 2003; Stewart et al., 1994), potentially linking these to the crust of asteroid 4 Vesta and HED meteorites (cf. above; (McSween et al., 2013, 2011). Mesosiderites have a restricted range in metal compositions, suggesting that the metal did not undergo fractional crystallization and was melted when mixed with the colder silicates (Hassanzadeh et al., 1990). The compositional range for the metallic portions of mesosiderites suggests that mesosiderite metal may have crystallized from a core with an original composition similar to IIIAB and H-group chondrite metal (Wasson et al., 1974). The differences between slow metallographic cooling rates at 500 ˚C (Goldstein et al., 2014) and fast cooling of pyroxene clasts at peak metamorphic temperatures above 800 ˚C (Ruzicka et al., 1994; Schwandt et al., 1998) reflect either the equilibration of mixed hot and cold fragments or a change in cooling regime when mesosiderites were buried deep in a re-accreted parent body after a collision event (Bogard and Garrison, 1998). A competing hypothesis for mesosiderite formation envisions mixing of brecciated basaltic/pyroxenic silicates (Ruzicka et al., 1994)derived from igneous differentiated asteroid crust/regolith with asteroidal core fragments upon impact (Hassanzadeh et al., 1990; Wasson and Rubin, 1985).

1.2. Triple-oxygen isotope ratios

The oxygen isotope ratios $^{18}O/^{16}O$ and $^{17}O/^{16}O$ can serve as useful indicators for a shared meteorite origin (Clayton, 2003; Clayton et al., 1976, 1973). The oxygen isotopic signatures of meteorites and terrestrial samples are determined by various processes in the solar nebular and subsequent fractionation processes in the parent bodies of meteorites. Many chemical reactions and physical processes involving oxygen lead to fractionation of its isotopes in a mass-dependent manner (i.e. the magnitude of the resulting isotope ratio shift depends on the mass of the isotopes involved). The resulting difference between the initial (I) and final (II) isotope ratios accompanying the physical process or chemical reaction can thus be written as follows:

$$\frac{(^{17}O/^{16}O)_I}{(^{17}O/^{16}O)_{II}} = \left(\frac{(^{18}O/^{16}O)_I}{(^{18}O/^{16}O)_{II}}\right)^{\beta} \qquad (1-1)$$

As the reaction rate constants and thermodynamic properties of the processes depend on the masses of the isotopes involved, the exponent β is typically around 0.52, as calculated via (although this can vary slightly for different processes):

$$\beta = \frac{1/m_{16} - 1/m_{17}}{1/m_{16} - 1/m_{18}} \qquad (1-2)$$

The resulting differences in the isotope ratios are usually in the order of several per mil, and are conventionally denoted as delta notation relative to Vienna Standard Mean Ocean Water (V-SMOW) in per mil:

$$\delta^{x/16}O = \left[\frac{(^{x}O/^{16}O)_{smp}}{(^{x}O/^{16}O)_{SMOW}} - 1\right] \cdot 1000 \qquad (1-3)$$

Where $x = 17, 18$. Given that these fractionations are relatively small, equation 1-1 can be rearranged to show the following relation:

$$\delta^{17/16}O \approx \beta \cdot \delta^{18/16}O \qquad (1-4)$$

As the result of mass-dependent fractionation processes, the isotope ratios of terrestrial rocks and water form a nearly straight terrestrial fractionation line with slope $\beta \approx 0.52$ on a $^{17}O/^{16}O$ – $^{18}O/^{16}O$ or $\delta^{17}O$ - $\delta^{18}O$ three-isotope plot (Lodders and Fegley, 2011).

However, many extraterrestrial samples do not plot on this terrestrial fractionation line. In fact, almost each meteorite group has a characteristic oxygen isotopic composition, which indicates that they formed from distinct sources of oxygen. The sources of the oxygen with these distinct isotopic compositions in the Solar System is not entirely clear, but it is generally accepted that such oxygen can either be of nucleosynthetic origin, e.g., supernovae input of pure ^{16}O (Clayton et al., 1973), or reflect mass-independent fractionation (MIF) in the Early Solar Nebula (Marcus, 2004). Alternatively, CO photodissociation in the cooler surface region of a turbulent nebula could also be possible (Lyons and Young, 2005; Rumble et al., 2011; Yurimoto and Kuramoto, 2004).

Some terrestrial atmosphere reservoirs, e.g., containing O_3, CO_2 and N_2O do not follow mass-dependent isotope fractionation, and certain meteorites or their composing parts follow similar trends. While mass-dependent isotope fractionation effects are typically explained by the effect of the atomic weights of isotopes on the thermodynamic and kinetic parameters of the process, MIF is explained by the small effects that the atom nuclei exert on the outer electron shells. Differences in the structure of the nuclei result in slight differences in the chemical properties of the molecular species composed of even and odd isotopes of the same element. Two types of MIF have been described: (1) The nuclear field shift effect that occurs because the volume occupied by the nucleus influences the attraction force on the valence electrons. This causes the isotopes with larger nuclei to preferentially partition into chemical species with lower electron density near the nuclei; (2) The nuclear spin effect, which arises from interaction between the spin of the valence electrons and the non-zero nuclear spin, is typically found in chemical reactions involving radical pairs. As a result, radical pairs with a non-zero nuclear spin (odd isotopes) show faster triplet-to-singlet conversion and thus higher recombination rates (Malinovsky and Vanhaecke, 2011).

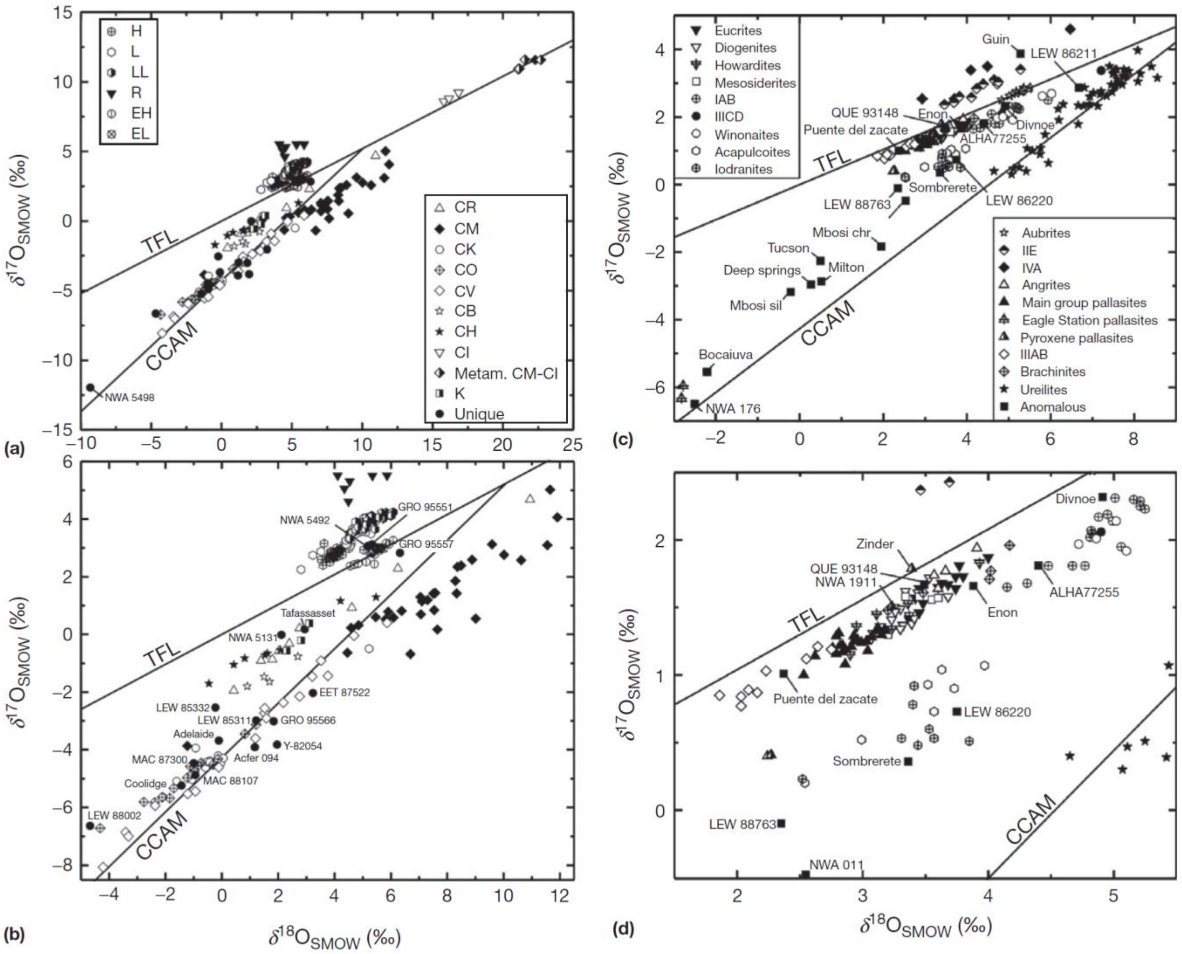

Figure 1-2. a, b) Bulk oxygen isotopic composition of chondrites. c,d) Bulk oxygen isotopic composition of achondrites . The image is adapted from (Krot et al., 2014).

The carbonaceous chondrites are spread under the terrestrial fractionation line (TFL) on a δ^{17}O - δ^{18}O three-isotope plot, along a mass-independent mixing line with a slope of approximately one. The slope on this mass-independent mixing line is in part defined by the calcium-aluminum refractory inclusions (CAIs), and the corresponding line is called CAIs mixing line (CCAM). The H, L and LL chondrite groups have resolvable differences from the TFL and form another mixing line, with R chondrites not plotting far from it. Achondrites can also be distinguished on the basis of their oxygen isotopic compositions. Differentiated and planetary achondrites plot along lines that are parallel to the TFL, but are displaced to either lower (e.g., HED) or higher (e.g., SNCs) values. Aubrites and lunar samples fall close to the TFL, and angrites, PMGs and mesosiderites fall next to the HED fractionation line. The mass-dependent slopes observed for differentiated and planetary achondrites can be explained by efficient melting and homogenization of oxygen with an initial non-terrestrial isotopic composition, followed by planetary mass-dependent fractionation processes. Primitive achondrites, e.g., ureilites, occur scattered along the CCAM line (Clayton, 2003; Lodders and Fegley, 2011; McSween and Huss, 2010). Measurement of the oxygen isotopic compositions of iron meteorites is complicated because of the low abundances of oxygen, but can be accomplished via chromite analysis (Franchi et al., 2013).

2. Isotopic variability in the Solar System

The physical and chemical processes in the Early Solar system that occurred during the formation and evolution of meteorite parent bodies left traces, not only in their element concentration, but also in the isotopic composition of the composing elements. These isotopic signatures can be used to better understand the nature of these processes. Among the known effects that shift isotopic compositions in the Solar System are: (1) stellar nucleosynthesis, coupled with incomplete homogenization of presolar components; (2) radioactive decay of unstable nuclides; (3)

spallation effects by cosmic radiation; (4) MIF (nuclear field shift and nuclear volume effects), known for a limited number of elements and (5) mass-dependent isotope fractionation.

Nucleosynthetic isotope anomalies have been observed for many elements in meteorites and their components (e.g., presolar grains in C chondrites). These isotope anomalies are inherited from various stellar sources with different stellar nucleosynthetic environments. There are three major mechanisms for synthesizing elements heavier than Fe, i.e., slow neutron capture (*s*-process), rapid neutron capture (*r*-process) and proton capture (*p*-process) processes. The *s*-process is a chain reaction of neutron capture (with timescales of several thousand years per single neutron capture event) and β^- decay, which occurs in stars or interior zones of stars with relatively low neutron density. In contrast, the *r*-process is a chain reaction that occurs at higher neutron densities, when neutron capture happens faster than the timescale of β-decay of a generated nucleus. The *p*-process is a chain of proton captures and β^+ decays in proton-rich environments (Yokoyama and Walker, 2016). Different nucleosynthetic mechanisms typically result in different isotopes of the same element, for instance light isotopes of Mo, ^{92,94}Mo are synthesized solely by the *p*-process, ^{95,97,98}Mo by a combination of the *s*- and *r*-processes, ^{96}Mo solely by the *s*-process, and ^{100}Mo solely by the *r*-process (Wieser and Laeter, 2007). As a result, elements with different isotopic compositions are synthesized in stars with different nucleosynthetic environments (neutron/proton flux densities, temperatures, and mass). As a result of incomplete homogenization of the Early Solar Nebula, the nucleosynthetic components, largely contained in pre-solar refractory grains, were re-distributed between the first accreted solids and planetesimals, leading to small, but resolvable differences of their isotopic fingerprints. Alternatively, this isotope inhomogeneity can result through the evolution of the Solar Nebula by “un-mixing” of the grains carrying the isotopic signatures because of the different physical properties of the grains (Trinquier et al., 2009), or through the late-injection into an initially homogeneous molecular cloud, *e.g.,* by supernovae. The nucleosynthetic anomalies found in meteorites are typically on the order of parts per ten thousand (pptt) to parts per million (ppm) in magnitude, but can reach orders of magnitude for single pre-solar grains, and potentially serve as genetic proxies of the meteorite parent bodies. So far, nucleosynthetic anomalies have been described for Mo, Ru, Te, W, Os, Cd, Sn, Ti, Ca, Cr, Ni, Sr, Zr, Ba, Nd, Sm, Ni either on the bulk meteorite scale or for certain specific meteorite components (Birck, 2004; Yokoyama and Walker, 2016).

Radioactive decay of unstable nuclides can shift the isotopic composition of meteorite phases, if the parent and daughter nuclides were (partially) separated from each other by a fractionation process during the lifetime of unstable nuclide. Unstable isotopes undergo spontaneous radioactive decay to stable or unstable daughter nuclides together with the release of particles and radiant energy (Faure and Mensing 2005). The α-, β- and γ- types of decay are distinguished based on the type of emitted rays, with the β-particle being a positron or negatron (electron), the α-particle a nucleus of $^{4}_{2}$He and γ-rays high-frequency electromagnetic radiation (>10^{19} Hz). When the half-life of the unstable nuclide, the current ratio of daughter to parent nuclides in the mineral studied, and the pristine isotopic composition of the daughter element are known, the isotope enrichment of the daughter element in the sample, e.g., a given mineral, can be used to calculate the timing of the closure of that phase. Isotopic decay chronometers include, but are not limited to, the ^{87}Rb-^{87}Sr β^-, ^{147}Sm-^{143}Nd α, and U-Pb chronometers. The isotopic composition of most ancient meteorites indicates that short-lived, now extinct, radioisotopes existed in the Early Solar System. These short-lived decay systems can be used in a similar way as isotopic chronometers, but on a relative basis, in contrast to long-lived isotope decay systems, which provide an absolute timescale but, with exception of the U-Pb chronometer, do not show the required precision needed to discriminate between early solar system events. The ^{41}Ca-^{41}K, ^{26}Al-^{26}Mg, ^{10}Be-^{10}B, ^{60}Fe-^{60}Ni, ^{53}Mn-^{53}Cr, ^{107}Pd-^{107}Ag, ^{182}Hf-^{182}W, ^{129}I-^{129}Xe, ^{244}Pu-Xe and ^{146}Sm-^{142}Nd short-lived decay systems have been demonstrated to occur in the Early Solar System (Goderis et al., 2016; Zinner, 2003).

When not covered by thick layers of screening material (crust, regolith or atmosphere), the meteoroid surface material is irradiated by cosmic rays, *e.g.,* neutrons, leading to transformation of the composing elements into new stable and radionuclides. The abundances of cosmogenic ^{3}He, ^{21}Ne, ^{38}Ar, and ^{83}Kr can be used to calculate cosmic ray exposure ages of meteorites, the time periods between the excavation of a meteoroid from its parent body to the moment when it falls to Earth (Herzog and Caffee, 2013), although other cosmogenic nuclides can obscure the applied isotope chronometer (e.g. cosmogenic ^{60}Ni can be interpreted as a result of short lived ^{60}Fe decay (Quitté et al., 2006). The latter can potentially be corrected for using other cosmogenic isotopes (Kruijer et al., 2013), or avoided by working with isotopes with small neutron capture radii. Cosmic radiation is filtered by the atmosphere of

Earth, but a fraction is still reaching the Earth's surface and gives rise to the production of cosmogenic nuclides on the surface. The occurrence of these cosmogenic nuclides can provide insights into rates and styles of surface processes (Gosse and Phillips, 2001).

Besides oxygen, described in the previous section, only few elements have been reported to experience MIF in extraterrestrial materials. S isotopic compositions of achondrites testify of MIF, which is likely the result of photochemical reactions in the early solar nebula (Rai et al., 2005), and MIF of Hg isotopes linked to radical reactions during evaporation and redeposition during heating of asteroids from primordial radionuclides (mainly due to ^{26}Al decay) and late-stage impact heating (Meier et al., 2016).

However, the effects of nucleosynthetic anomalies, decay of unstable nuclides, spallation and MIF on the bulk meteorite scale are typically smaller than those observed from mass-dependent fractionation of stable isotopes, which can achieve magnitudes on the order of a few percent. Mass-dependent isotope fractionation results from slight differences in the efficiency with which the isotopes of an element participate in physical processes or chemical reactions, as a result of their difference in mass (Vanhaecke and Degryse, 2012). At present, natural mass-dependent isotope fractionation has been shown to affect all elements with ≥2 isotopes, but the extent of the isotope fractionation observed, caused by chemical reaction or phase change, depends on the masses of the isotopes. Generally, differences of the order of ~1 ‰ are observed for isotope ratios on the bulk meteorite scale, with usually even larger effects for lighter elements. Mass-dependent isotope fractionation can be subdivided into equilibrium and kinetic in nature. The distinction between equilibrium and kinetic mass-dependent isotope fractionation is made based on the underlying natural process. Equilibrium mass-dependent isotope fractionation occurs during exchange of the isotopes between compounds (or between phases) as the result of differences in the equilibrium reaction constants for different isotopes, which arise from slightly different vibrational energy levels for the molecules that contain these different isotopes.

For the partitioning of isotopes x_1 and x_2 between compounds a and b at equilibrium,

$$ax_1 + bx_2 \rightleftarrows ax_2 + bx_1 \qquad (1-5)$$

assuming that the internal molecular vibrations behave as harmonic oscillations and relying on the assertion that the vibrational frequencies in the material depend only on the masses of the isotopes themselves, it can be shown for the fractionation factor $\alpha_{2/1}^{a-b} = (\mathrm{x}_2/\mathrm{x}_1)_\mathrm{a}/(\mathrm{x}_2/\mathrm{x}_1)_\mathrm{b}$ (Young et al., 2015, 2002a):

$$\ln \alpha\,_{2/1}^{a-b} = \frac{1}{24}\left(\frac{h}{k_b T}\right)^2 \left(\frac{1}{m_1} - \frac{1}{m_2}\right) \sum_j \left(\frac{K_{j,a} - K_{j,b}}{4\pi^2}\right) \qquad (1-6)$$

Here, h and k_b denote the Planck and Boltzmann constants, T is the temperature, $m_{1,2}$ are the masses of corresponding isotopes, and $K_{j,a}$ and $K_{j,b}$ are bond force constants for the atom of interest and vibrational mode j. As such, isotope fractionation between 2 compounds at equilibrium largely depends on the bonding environment of the atom and the temperature of the governing process. Equation 1-6 shows that the heavier isotopes tend to concentrate in the compound where the average force constant is larger. Young et al. detail that the crystal chemistry constraints on equilibrium isotope fractionation require that: 1) heavy isotopes concentrate in the compound where the coordination number is lower, and 2) heavy isotopes concentrate where the valence is higher (Young et al., 2015). Equation 1-6 shows that the fractionation factor α between 2 compounds varies linearly with $1/T^2$, which allows the use of the isotope ratios of 2 equilibrated minerals as an isotope geothermometer, when the phases are in chemical and mineralogical equilibrium (Hoefs, 2009). To be able to apply an isotope system to a pair of minerals as geothermometer, the isotope system needs to be calibrated via experimental measurement of the mean force constants of the target element in the minerals of interest. The latter can, e.g., be accomplished with Nuclear Resonant Inelastic X-ray Scattering (NRIXS) or Mössbauer spectroscopy (Dauphas et al., 2014, 2012; Polyakov and Mineev, 2000). By expressing the fractionation factor $\alpha_{3/1}^{a-b}$of another isotope pair of the same element in a manner similar to equation 1-6, the isotope fractionation law for mass-dependent isotope partitioning at equilibrium and the corresponding exponent β for equilibrium law can be derived:

$$\alpha_{2/1}^{a-b} = \left(\alpha_{3/1}^{a-b}\right)^{\beta_{eq}};\ \beta_{eq} = \frac{(1/m_1 - 1/m_2)}{(1/m_1 - 1/m_3)} \qquad (1-7)$$

Other phenomena producing mass-dependent isotope fractionation are kinetic processes. In contrast to an equilibrium (thermodynamic) control, kinetic mass-dependent isotope fractionation arises without achieving equilibrium in the system, as a result of the different rates at which the isotopes or isotope-containing species are involved in a process (either physical rates, as in the case of sub-solidus diffusion, or chemical reaction rates). Such effects result from unidirectional processes, such as evaporation/condensation, dissociation reactions or diffusion:

$$ax_1 \overset{k_1}{\rightarrow} bx_1; \text{ and } ax_2 \overset{k_2}{\rightarrow} bx_2 \qquad (1-8)$$

The isotope fractionation factor α can in this case be interpreted as the ratio of the forward rate constants for the couple of isotopes $\alpha_{2/1}^{a-b} = \mathrm{k}_2/\mathrm{k}_1$, which in accordance to the theory of activated transition state provides the expression for isotope fractionation factor under kinetic control (Young et al., 2002a):

$$\alpha_{2/1}^{a-b} = \sqrt{\frac{m_1}{m_2}} \qquad (1-9)$$

When a similar expression is formulated for another isotope ratio of the same element, the kinetic isotope fractionation law and the corresponding exponent β can be derived:

$$\alpha_{2/1}^{a-b} = \left(\alpha_{3/1}^{a-b}\right)^{\beta_{kin}};\ \beta_{kin} = \frac{ln(m_1/m_2)}{ln(m_1/m_3)} \qquad (1-10)$$

A classical example of kinetic isotope fractionation is the irreversible evaporation of an element to vacuum at high temperature, where the rate constants depend on the isotopic masses. For such process, the kinetic isotope fractionation factor can be shown to be similar to equation 1-9, using the Hertz-Knudsen equation for evaporation fluxes (Richter et al., 2009):

$$\alpha_{2/1}^{a-b} = \left(\frac{\gamma_2}{\gamma_1}\right)\sqrt{\frac{m_1}{m_2}} \qquad (1-11)$$

Here, γ_i denotes a condensation coefficient, which is similar for both isotopes at first estimate. Similarly, the isotope ratios of the elements taking part in chemical or thermal diffusion can be affected, as isotopes tend to diffuse at dissimilar rates as a result of differences in their masses (F. M. Richter *et al.*, 2009). More recently, the generalized power law with a flexible fractionation exponent *n* has been defined (Maréchal et al., 1999; Wombacher and Rehkamper, 2003). By varying the fractionation exponent *n*, the law can take on the mathematical form of either the equilibrium (*n* = -1) or the kinetic (*n*→0) fractionation law, or have a mixed nature:

$$\alpha_{2/1}^{a-b} = \left(\alpha_{3/1}^{a-b}\right)^{\beta_{GPL}};\ \beta_{GPL} = \frac{m_1^n - m_2^n}{m_1^n - m_3^n} \qquad (1-12)$$

As a result of mass-dependent isotope fractionation (equations 1-7 and 1-10), the isotope ratios of the same element will fractionate in a manner that depends on the mass differences between the isotopes. Consequently, when knowing one isotope ratio, the other ratio can be predicted through the underlying fractionation law. Mass-dependent isotope ratios are commonly presented in a three-isotope plot ($\delta^{2/1}$ versus $\delta^{3/1}$ axis), where data points plot on a nearly straight fractionation line with a slope (nearly) equal to the exponent β:

$$\frac{(x_2/x_1)_a}{(x_2/x_1)_b} = \alpha_{2/1}^{a-b} = \left(\alpha_{3/1}^{a-b}\right)^{\beta} = \left(\frac{(x_3/x_1)_a}{(x_3/x_1)_b}\right)^{\beta} \qquad (1-13)$$

$$\left(\frac{\delta^{2/1}}{1000} + 1\right) = \left(\frac{\delta^{3/1}}{1000} + 1\right)^{\beta} \qquad (1-14)$$

$$ln\left(\frac{\delta^{2/1}}{1000} + 1\right) = \beta ln\left(\frac{\delta^{3/1}}{1000} + 1\right) \qquad (1-15)$$

Taking the Tailor series of $ln(x+1)$ with the assumption that $|x| \ll 1$, reasonable for the typical magnitudes found for natural isotope fractionation, this translates into:

$$ln\left(\frac{\delta^{2/1}}{1000} + 1\right) = \frac{\delta^{2/1}}{1000} - \left(\frac{\delta^{2/1}}{1000}\right)^2/2 + \left(\frac{\delta^{2/1}}{1000}\right)^3/3 - \ldots \approx \frac{\delta^{2/1}}{1000} \qquad (1-16)$$

The linear relation between the delta-notations can thus be formulated as:

$$\delta^{2/1} = \beta\delta^{3/1} \tag{1 – 17}$$

However, it is necessary to stress that, although this assumption of linearity is true within the modern levels of isotope ratio measurements precision attainable for natural isotope ratio variations on the per mil level, the mathematically precise fractionation line is linear in logarithmic δ` notation three-isotope space, where the δ` notation used is:

$$\delta`^{2/1} = ln\left(\frac{(\mathrm{x}_2/\mathrm{x}_1)_{\mathrm{smp}}}{(\mathrm{x}_2/\mathrm{x}_1)_{\mathrm{std}}}\right) \cdot 1000 \tag{1 – 18}$$

As a result of continuous improvements in the precision of analytical techniques capable of determining isotope ratios, the distinction between kinetic and equilibrium isotope fractionation processes can be made. The exponent β of the natural process, underlying the formation of the species of interest, can be calculated in practice as the slope of the fractionation line in $\delta`^{2/1}$ versus $\delta`^{3/1}$ three-isotope space for the isotope ratios measured (Wombacher et al., 2004; Young et al., 2002a). Another important conclusion is that natural mass-dependent isotope fractionation can be cancelled out (corrected for) from the measured isotope ratio mathematically, relying on the isotope fractionation law, when the abundances for more than two isotopes of the target element are measured. This internal normalization procedure yields the original isotopic composition revealing, e.g., a nucleosynthetic anomaly or the decay of unstable nuclide.

There are many processes that, during the formation and evolution of the protosolar nebula and Solar System, led to mass-dependent fractionation of stable isotopes and resulted in isotopic signatures that can be used to shed light onto the underlying process. Among the processes leading to stable isotope fractionation in the Solar System are: (1) processes in the protosolar nebula, such as condensation of the first solar solids and evaporation processes; (2) physical particle sorting based on refractoriness, mass, size or composition of the particles during the accretion of the first planetesimals; (3) partitioning of the elements between silicate mantles and metal cores of the differentiated asteroids; (4) igneous fractionation in mantle and crust processes via fractional crystallization, partial melting and a variety of diffusion-related effects and (5) impact processes that lead to irreversible evaporation of the material due to impact heat. As an example, the intense heating of initially undifferentiated planetesimals as a result of short-lived β^- isotope decay of ^{26}Al in the Early Solar System led to the differentiation of these bodies with the formation of silicate-dominated mantles and iron-rich cores (Grimm and Mcsween, 1993). These planetary fractionation processes not only affected the major element composition, but also shifted the isotopic compositions of the meteorite parent bodies (Moynier et al., 2007). In the case of iron-rich meteorites, Fe and Ni can experience resolvable equilibrium isotope fractionation in the processes associated with the melting of undifferentiated precursors and subsequent segregation of metal from silicate (Poitrasson, 2007). The degree of the equilibrium isotope fractionation between the co-existing phases depends largely on the temperature at which these processes occurred, and can be used as a thermometer of these processes (Poitrasson et al., 2005). The δ^{29}Si values of Earth and carbonaceous chondrites reflect fractionation that occurred during core segregation on Earth (Rumble et al., 2011). Isotope fractionation due to evaporation is another important process that was used to model the formation of certain components of primitive meteorites – chondrules and CAIs by condensation in the Early Solar nebula (Alexander and Wang, 2001; Rumble et al., 2011; Shahar and Young, 2007). Evaporation due to the catastrophic collision that led to the formation of the Moon was initially proposed to fractionate the originally chondritic Fe isotopic composition on Earth, although more recently mantle and crustal processes, such as partial melting have been invoked to explain the observed isotopic signatures (Weyer, 2008). Evaporation related to impact has been suggested to affect the isotopic composition of Ge in silicate-bearing meteorites (Luais, 2007). In the case of ordinary chondrites, the isotopic variations of Ni, Cu and Zn have been suggested to result from vapor-solid reactions, followed by mineral sorting during accretion (Moynier et al., 2007).

3. Principles of ICP-mass spectrometry and its cosmochemical applications

Inductively coupled plasma-mass spectrometry (ICP-MS) is a technique for elemental and isotopic analysis. In ICP-MS, an introduced sample is converted into atomic (M^+) ions in an inductively coupled argon plasma, the ions thus formed are extracted via an interface and subsequently separated from one another in a mass-separation device, and the isolated ion beam(s) is(are) converted into (an) electrical signal(s) using a detector. After the first coupling of an ICP ion source to a mass spectrometer in 1980 (Houk et al., 1980) and the commercial introduction of the technique

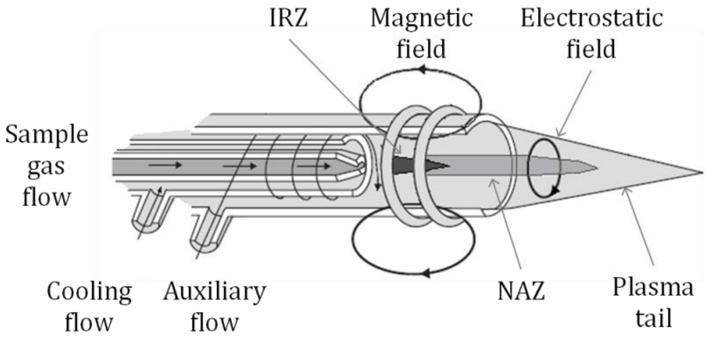

Figure 1-3. Torch and ICP. Adapted from (Vanhaecke and Degryse, 2012)

in 1983, ICP-MS rapidly became widespread due to the high sample throughput, the flexibility of sample introduction and high ionization efficiency of the ICP ion source, which enables multi-element and ultra-trace element determination (limits of detection down to pg g^{-1}), and the wide linear dynamic range (up to 12 orders of magnitude). After the introduction of a multi-collector (MC) version of ICP-MS (Walder and Freedman, 1992), dedicated to high-precision isotopic analysis, the method got a second wind and largely replaced thermal ionization mass spectrometry (TIMS), the former “gold standard” for isotopic analysis. From the appearance of the first commercial instruments on, ICP-MS became a highly popular tool for geochemical applications, which require high-precision elemental concentration and isotope ratio data, often for a larger collection of elements, and it significantly contributed to the current understanding of geological and cosmochemical processes.

3.1. Principle design of ICP-MS

Similar to other types of mass spectrometric instrumentation, an ICP-MS instrument consists of 3 principal components: (1) an ionization source, which provides atomization and ionization of the sample; (2) a mass analyzer, which separates the ions based on their mass-to-charge ratios and (3) a detector, which converts the arriving ions or the entire ion beam into (an) measurable electrical signal(s). While the implemented type of mass separation device and detector can vary, the ICP ion source and plasma interface, extracting the ions from the plasma at ambient pressure into the MS operated under high-vacuum conditions, are the two distinctive components of all ICP-MS instruments.

The ICP ion source is principally a plasma operated at atmospheric pressure formed in the inert atmosphere of a noble gas stream (typically Ar), which is sustained in a quartz torch of which one end is surrounded by a water- or Ar-cooled load coil. This cylindrical torch consists of three concentric quartz tubes, each flushed with an Ar flow: two tangential flows, called the cooling and auxiliary flows, and a sample gas flow, introduced through the co-axial injector into the torch. The sample gas flow contains the aerosol of the sample (figure 1-3). The sample aerosol can be generated in several ways, the most common being pneumatic or ultrasonic nebulization of a sample solution, while the sample aerosol can also be formed via laser ablation of solid sample (see below). When pneumatic nebulization is used, the aerosol is formed using a pneumatic nebulizer (typically a concentric nebulizer, where aerosol is formed by interaction of the sample solution with an accelerated flow of Ar gas), and further conditioned in the spray chamber (Scott-type double pass or cyclonic). The spray chamber is used to remove the larger aerosol particles via impact, gravitation or centrifugal forces to guarantee a stable atomization and ionization in the ICP and, ultimately, a stable signal (Vanhaecke and Degryse, 2012). The toroidal plasma is generated in the flow of the argon at the end of the ICP torch via inductive coupling with the load coil, to which a radiofrequency alternating current is applied. The power of the plasma, transferred from the RF generator through the load coil, is typically around 1-2 kW, and the frequency of the current through the load coil is either 27.12 or 40.68 MHz (radiofrequencies permitted for industrial applications). Under such conditions, the load coil generates an oscillating electromagnetic field inside the torch, with the magnetic field oriented co-axially to the cylindrical torch and the circularly oriented electrical field co-axial to the central axis of the torch. Seeding the argon flow with electrons produced via a high-voltage spark discharge ignites the plasma, as the seeded electrons are accelerated within the electromagnetic field by oscillating vortex trajectories. The accelerated electrons transfer their energies to the Ar gas atoms via a collision process (electron impact ionization, equation 1-19), leading to the formation of more electrons and a self-sustaining plasma. Simultaneously, excited Ar atoms are formed (equation 1-20):

$$Ar + e^- \rightarrow Ar^+ + 2e^- \qquad (1-19)$$

$$Ar + e^- \rightarrow Ar^* + h\nu \qquad (1-20)$$

In most applications, when the ICP is operated under 1.2-1.3 kW, the plasma reaches a gas temperature of 5000-8000 K, the electron temperature attains 8000-10000 K, and the electron density is 1-3 10^{15} cm^{-3} (Becker, 2007). At such temperatures, the sample aerosol introduced with the sample gas via the injector is first desolvated (in case of introduction through pneumatic nebulization), vaporized, as it moves through this axial channel, and subsequently atomized downstream of the torch. The ionization of the atomized analyte (M) in the ICP is achieved by electron impact ionization (equation 1-21), charge transfer ionization (equation 1-22), and/or Penning ionization (equation 1-23) (Becker, 2007):

$$M + e^- \rightarrow M^+ + 2e^- \qquad (1-21)$$

$$M + Ar^+ \rightarrow M^+ + Ar \qquad (1-22)$$

$$M + Ar^* \rightarrow M^+ + Ar + e^- \qquad (1-23)$$

At the same time, electron impact excitation (equation 1-24) and ion-electron radiative recombination (equation 1-25) lead to the formation of excited atoms of the target element (Becker, 2007):

$$M + e^- \rightarrow M^* + e^- \qquad (1-24)$$

$$M^+ + e^- \rightarrow M^* + h\nu \qquad (1-25)$$

The axial channel of plasma is separated into several distinct zones: (1) the initial radiation zone (IRZ, ≈7500 K), which contains abundant molecular species and neutral atoms; (2) the normal analytical zone (NAZ, ≈6500 K), where the atomic analyte ions are most abundant, is located downstream of the IRZ; (3) the plasma tail (≈6000 K) contains abundant recombined molecular ions, doubly charged ions and neutral atoms (Niu and Houk, 1996). Under such conditions most elements are ionized to a high degree in the ICP, as the ionization efficiency depends on the first ionization energy of the element, and elements with ionization energies less than 8 eV are ionized with a nearly 100% yield. Metalloids and non-metals are still ionized to reasonable degree, sufficient to be analyzed with ICP-MS, with ionization efficiencies α of 0.3-0.8 and 0.01-0.3, respectively (Vanhaecke and Degryse, 2012). To avoid secondary electrical discharge between ICP and the other components of the mass spectrometer, a grounded shield is introduced between the ICP and load coil to decouple these. Simultaneously with the singly charged elemental (M^+) ions of the sample constituents and the Ar plasma gas, a variety of other unwanted species are also formed: doubly charged ions, polyatomic ions (consisting of ≥ 2 elements from the solvent, the Ar plasma gas and the air surrounding the ICP and/or the sample itself). These species can interfere with the determination of target elements of a similar mass-to-charge ratio (*m*/*z*) in the mass spectrum, and have to be avoided to guarantee correct analysis results, either via chemical pretreatment of the sample prior to its introduction, or instrumental approaches (higher mass resolution or a collision/reaction cell) or at least corrected for via mathematical approaches. Additionally, the formation of disturbing Ar-containing polyatomic species in the ICP (e.g., ArO^+, $ArOH^+$) can be suppressed by using cold plasma conditions, which are attained at a lower RF power (600-800 W) and relatively high sample gas flow rate (Tanner, 1995). This approach can be used for the interference-free determination of elements with low first ionization energy, such as K and Fe. However, the application of cold plasma conditions is coupled with an elevated formation rate of oxide ions and decreased sensitivities for elements with high ionization energy.

Interface. After the ionization in the ICP, operated at atmospheric pressure (≈10^5 Pa), ions need to be directed into the mass spectrometer, operated under high-vacuum conditions (≈10^{-2} Pa pressure is needed to assure a collision-trajectory for the ion beam inside the mass spectrometer). The interface of the ICP-mass spectrometer plays a central role in the extraction of the analyte ions from the ICP into the mass spectrometer, and was pioneered by a study by Campargue (Campargue, 1984). As such, the interface ensures: (1) continuous extraction of the target element ions from the plasma source under atmospheric pressure with high efficiency, and transmission of the target element ions into the mass spectrometer under high vacuum; (2) a rejection of the main portion of plasma components not related to the sample analyzed (e.g., atomic argon); (3) limiting non-stoichiometric losses of analytes (fractionation) during the transmission and (4) limiting the formation of undesired spectral interferences during the transmission. Interfaces typically consist of 2 (or rarely 3) serially positioned water-cooled metal cones (Ni, Pt and to a lesser extent, Al, are widely used) located downstream of the ICP, co-axial with the central axis of the torch. The space between the 1st and 2nd cone, called sampler and skimmer, respectively, is evacuated with a fore-vacuum pump down to $\approx 10^2$ Pa. Sampler and skimmer cones have small orifices in their tips ($\approx$1 mm magnitude). The tip of the sampler is located into the NAZ of the plasma, and a part of plasma is extracted from the narrow region of the NAZ into the interface as a result of the pressure difference. The extracted plasma gas undergoes supersonic adiabatic expansion. As a result of the rapid expansion regime and short transit time, the ions and electrons practically do not recombine (essentially in the central stream of the expanding plume) and the plasma composition is virtually “frozen” (Niu and Houk, 1996). The central part of the expanding plasma plume is leaving the interface region via the orifice of the skimmer, positioned a few mm downstream from the sampler, into the mass spectrometer through the pressure difference between the interface and the mass spectrometer. A large part of the plasma plume is removed by the vacuum system. At the conditions of the ion sampling from the interface, all ions accelerate to velocities (nearly) similar to that of neutral Ar, composing the main portion of the plasma, such that the kinetic energy of the ions depends on their mass (in case the plasma is grounded and secondary discharges do not provide additional acceleration to the ions during their extraction):

$$E_j = \left(\frac{m_j}{m_{Ar}}\right) E_{Ar} = \frac{5 m_j k T}{2 m_{Ar}} \qquad (1-26)$$

Here the E_j and E_{Ar} stand for the mean or average kinetic energies of the ion with mass m_j and the neutral argon atom with mass m_{Ar} (Niu and Houk, 1996).

Ion optics. Another component of ICP-mass spectrometers, located downstream of the skimmer cone and before the mass separation device is the ion optics assembly. It is sustained under high vacuum conditions of the mass spectrometer and composed of one or several ion lenses, which are metallic plates, barrels, or cylinders at a certain voltage. The extraction lens is typically located just after the skimmer. The high voltage applied to it assures acceleration and extraction of the positive ions from the plasma plume. The functions of the ion optic system are: (1) capturing the ions exiting the interface and transmitting them quantitatively to the mass separation device; (2) reducing mass-dependent losses; (3) selecting positive ions from the plasma plume, rejecting electrons, particulates, neutral species and photons; (4) shaping, accelerating and focusing of the ion beam towards the mass separation device; (5) matching the properties of the ion beam to those desired for the mass separation device; (6) reducing the level of doubly charged and oxide species (Surikov and Pupyshev, 2011).

Mass analyzer. The beam of ions, formed and focused through the ion optics, enters the mass separation device, where the ions are separated according to their m/z ratio. The most popular types of mass separation devices applied in commercial ICP-MS instruments are quadrupole and sector field analyzers, while the less conventional time-of-flight (TOF) mass spectrometer has proven highly valuable in more restricted applications. The performance of mass analyzers is characterized quantitatively by the mass resolution and abundance sensitivity it provides. The mass resolution is a parameter that provides quantitative information on the minimal m/z difference between two neighboring ion beams, which can still be separated by the mass spectrometer. The most commonly used definition of spectral mass resolution (R) is formulated for two equal peaks with masses m_1 and m_2, which have a valley between them equal to 10 % of their peak height. An alternative definition is based on the mass width of a single peak at 5 % of its maximum, $\Delta m_{5\%}$ (Becker, 2007; Vanhaecke and Degryse, 2012):

$$R = \frac{(m_1+m_2)/2}{m_2-m_1} \approx \frac{m}{\Delta m_{5\%}} \qquad (1-27)$$

Abundance sensitivity characterizes scattering of ions inside the mass spectrometer. This effect is critical when a low intensity signal needs to be measured next to an intense peak. Abundance sensitivity is a measure of the effect, which this intense ion beam has on the neighboring mass. Typically m and m+1 masses are used, although the m+2 definition is also common:

$$Abundance\ sensitivity = \frac{Intensity\ at\ m}{Intensity\ at\ m+2} \qquad (1-28)$$

A quadrupole mass filter consists of parallel metal rods, cylindrical or hyperbolic in shape, which have a combination of DC and AC voltage components applied to them. The opposed rods are electrically connected to each other and form an electrode pair, and the voltage applied to the second pair of rods is similar in magnitude but different in sign compared to the first pair of rods, and the AC component shows a phase difference of π between the rod pairs. The ion beam coming from the ion optics is directed into the central channel between the rods, and the ions move along oscillating trajectories as a result of the force applied to them by the AC voltage. The DC and AC voltages are selected in such a way that only the ions of a selected narrow m/z range can pass through the quadrupole filter, and the heavier and lighter ions collide with one of the pairs of rods. The dynamic selection of masses that pass the filter is accomplished by changing the DC and AC voltages in a way that the ratio of their magnitudes remains constant (Becker, 2007; Vanhaecke and Degryse, 2012). The advantage of the quadrupole mass analyzer is its technical simplicity and cost, relatively small volume, which needs to be maintained under high vacuum, and larger tolerance towards the spread of the kinetic energies of ions entering the filter. Although the quadrupole filter does not provide truly simultaneous transmission of the mass spectrum, the scanning rate provided is relatively fast (in the order of ≈100 Hz). The weakness of the quadrupole mass filter is the associated low mass resolution ($M/\Delta M \approx 300$).

In a TOF mass analyzer, a small package of ions is accelerated by an electrical potential V and is subsequently introduced into a field-free flight tube. All the ions acquire similar kinetic energies during the acceleration $E_{kin} = zV$, so the ion speed $v = \sqrt{2zV/m}$ depends only on the mass of the ion m. The mass spectrum of the introduced package of ions is recorded at the end of the flight tube with a detector, which is continuously registering the time-dependent signal: $m = 2zVt^2/L^2$. In some instrument designs, the ions are reflected by an ion mirror to pass the flight tube twice to increase its effective length L and to correct for a spread in kinetic energies. TOF currently demonstrates the fastest acquisition rate among the mass analyzers, an order of 10^4-10^5 spectra per second can be recorded.

In a sector field mass analyzer, the ions composing the entering beam are separated from one another and focused on the detector statically by the Lorentz force in a homogeneous magnetic field. In modern mass spectrometers the magnetic and electrostatic sectors are located sequentially after each other. The ions of mass m and charge z, are first accelerated in the ion optics over an electrical potential difference V, such that they acquire a kinetic energy $E_{kin} = zV$. Subsequentially, they enter the area of a homogeneous magnetic field B in the magnetic sector at speed v, where they experience the effect of the Lorentz force $F = zvB$. The resulting radius r_B of the circular trajectory of the ion will depend on its m/z mass to charge ratio: $r_B = \sqrt{2Vm}/\sqrt{zB^2}$. This effect of separation of ions of different m/z is called prism effect. Additionally, the magnetic sector provides a lens effect, causing mono-energetic ions of the same mass, but with speed vectors slightly deviating from one another, to still be focused at the image point by the magnetic sector. The electrostatic sector is practically a sector of a condenser, consisting of 2 bent circular plates to which a deflecting potential is applied, such that the electrostatic field E is always directed to the center of the sector. The centrifugal force mv^2/r_E, applied to the moving ions is provided by electrostatic force, equal to zE. As a result, the radius r_E of the ion trajectory in the electrical field depends on the initial kinetic energy of the ion: $r_E = 2E_{kin}/(zE)$. If the kinetic energy of the ions is determined solely by the accelerating voltage V in the ion optics, the radius r_E needed to direct the ions to the detector is $r_E = 2V/E$. However, ions of the same mass extracted from the ICP ion source show a dispersion in their initial kinetic energies, which can be up to 10-30 eV (Rehkämper et al., 2001), and the electrostatic sector provides separation of the ions based on their initial kinetic energies. Because such initial energy dispersion can broad the mass peak and degrade the mass resolution of the magnetic sector working solely, several double-focusing mass spectrometers were designed, with magnetic and electrostatic sectors working ”simultaneously”. Both energy and directional focusing to one point can be provided when the energy dispersion of the magnetic sector is compensated by the energy dispersion of the electrostatic sector. This is achieved in several calculated geometries, such as the Nier-Johnson (electrostatic sector of 90^o followed by a co-directionally curved magnetic sector of 90^o), the reversed Nier-Johnson (magnetic sector of 90^o followed by a co-directionally curved electrostatic sector of 90^o) or the Mattauch–Herzog (electrostatic sector of 31.8^o followed by an anti-directionally curved magnetic sector of 90^o) geometry. The latter possesses the additional ability to focus ions of different m/z ratios in one focal plane. In geometries where the electrostatic sector is located after the magnetic sector, only one mass can be focused at the detector at any given time, and the spectrum needs to be measured dynamically, in peak-hopping mode. The actual m/z-ratio reaching a detector at a fixed position can be selected via adapting the magnetic field strength (B-scanning) or the accelerating potential (E-scanning). The sector field mass analyzers are characterized by a higher mass resolution (up to 10000), low abundance sensitivity down to $9\ 10^{-7}$ based on m+2 definition, high ion transmission efficiency and by the ability to generate flat-topped peaks with trapezoidal shape. However, when working in dynamic scanning mode, a sector field instrument is slower than other types of mass analyzers, making it less suited for transient signals (Becker, 2007; Vanhaecke and Degryse, 2012).

Ion detection systems. Modern ICP-MS instruments are equipped with electron multiplying detectors or Faraday cups. The operating principle of an electron multiplier is based on avalanche multiplication of electrons formed when an ion strikes the surface of a conversion electrode. The primary electrons are accelerated towards the back end of the detector via a potential difference, and strike the inner walls of discrete dynodes, leading to a further multiplication of the number of electrons. As a result, each individual ion arriving to the detector produces a pulse of 10^7-10^8 electrons, and the pulses are counted in "pulse counting mode". However, some time is needed before the detector can handle the next ion, which results in a slightly underestimated count rate for an intense ion beam. The correction of the measured count rate $I_{observed}$ for this time, called dead time τ, is fairly easy if the count rate is << 1/ τ (Vanhaecke and Degryse, 2012):

$$I_{true} = \frac{I_{observed}}{1-(I_{observed}\tau)} \qquad (1-29)$$

The Faraday cup is one another type of detector, used when relatively intense ion beams are to be measured accurately. This detector consists of deep bucket, usually of rectangular shape, which collects all the entering ions to enter and deposit their charge. The resulting current flows away from the Faraday cup via high Ohmic resistor, and the voltage is measured. The limiting noise source for Faraday cup is Johnson noise ΔV generated by an Ohmic resistance (R) at a temperature T during an integration time t_{int} (Becker, 2007):

$$\Delta V = \sqrt{\frac{4k_bRT}{t_{int}}} \qquad (1-30)$$

3.2. Multi-collector ICP-MS

Although ICP-MS is capable of distinguishing isotopes, the precision of isotope ratio measurements is limited to RSD ~0.05% (Vanhaecke et al., 1997) when using systems with a single detector, which is sufficient only for limited number of geo- and cosmochemical applications. This is principally due to sequential mode of recording the signal intensities for the isotopes of interest and the short-term signal fluctuations (noise) characteristic to ICP ion source. This can be solved when the signals of the different isotopes are measured simultaneously, most commonly by using a variable multi-collector array, consisting of up to 13 independently moveable or fixed faraday cups or ion counters with a mass spread of up to ~ 15% (Rehkämper et al., 2001). After the first demonstration of a substantially improved precision for isotope ratio measurements and multielement capabilities (Walder and Freedman, 1992), multi-collector ICP-MS (MC-ICP-MS) has aroused a lot of attention due to its capability to measure tiny natural isotope variations for elements with high ionization energy, which was not possible to accomplish with other techniques available those days. For instance elements with a first ionization energy >7 eV are difficult to analyze by TIMS at sufficiently high precision, and the mass spectrometric techniques based on other ion sources are not capable of providing the continuous signal needed for precise isotope ratio measurement. Moreover, TIMS is associated with low sample throughput and practically no multielement capabilities. The introduction of MC-ICP-MS led to a dramatic broadening of the set of elements subjected to isotopic analysis in geo- and cosmochemical applications and the establishment of new isotopic chronometers (e.g., based on decay systems of a short lived isotope from a siderophile element, e.g., ^{107}Pd-^{107}Ag, ^{182}Hf-^{182}W). Critically, stable isotope systems which were impossible to address with TIMS either due to high first ionization energy of the target element or due to necessity of using the double-spike technique with its associated principal limitations, can be addressed by MC-ICP-MS when using an element of nearby atomic mass as internal isotopic standard (see below). Additionally, when equipped with LA, MC-ICP-MS provides possibilities for *direct* high-precision isotopic analysis of solid samples with a lateral resolution down to some μm (see below), making it competitive with *in situ* techniques, such as secondary ion mass spectrometry (SIMS).

All the current MC-ICP-MS instruments are based on a double-focusing sector field analyzer to provide flat-topped peaks and "pseudo-high resolution" (up to M/ΔM=10000, 5 – 95 % on plateau notation, see Vanhaecke and Moens, 2004) and static separation of ion beams (the Micromass IsoProbe employed a single-focusing mass analyzer preceded by a hexapole collision cell used for thermalization, reduction in the spread of kinetic energies of the ion beam). The instruments are typically equipped with movable faraday cups equipped with 10^{10} - 10^{13} Ω amplifiers. Faraday cups are preferred for their linearity, robustness and accuracy (Vanhaecke and Degryse, 2012). Ion counters pre-installed for selected isotope systems are sometimes used for measurement of extremely low ion currents in pulse-counting mode.

The fundamental limit of precision attainable for isotope ratio measuring arise from particulate nature of matter and random character of ions arrival to the detector, described by Poisson probability distribution:

$$P(Q) = \frac{(It)^Q e^{-It}}{Q!} \qquad (1-31)$$

Here *P(Q)* is the probability to count $Q=It$ ions in t seconds. I (counts s^{-1}) is the mean count rate of the Poisson distribution, while the standard deviation of the distribution is $\sigma = \sqrt{Q}$. The variance u^2 of the isotope abundance ratio I_1/I_2 can be calculated using the uncertainty propagation (Baxter et al., 2012a; Vanhaecke et al., 1997, 1996):

$$u(I_1/I_2) = \frac{t_1}{t_2}\frac{I_1}{I_2}\sqrt{\frac{1}{Q_2}+\frac{1}{Q_1}} \qquad (1-32)$$

Instrumental mass discrimination is a significant feature of ICP-MS, which needs to be taken care of in order to provide accurate isotope ratio results. Instrumental mass discrimination is a phenomenon of non-stoichiometric transfer of isotopes through the spectrometer. In the overwhelming majority of cases, the resulting artificial fractionation of isotopes is mass-dependent in nature, and can be described by well-known laws (see the previous chapter) and, as such, corrected for, but cases of mass-independent instrumental mass discrimination were also reported (Newman et al., 2009). The difference between the true and measured isotope ratio affected by instrumental discrimination can reach up to several % per mass unit for MC-ICP-MS instruments (*e.g.* see Andren et al., 2004), which is much larger than that for TIMS. At the same time, the time-dependent functional part of the instrumental mass discrimination of MC-ICP-MS is more stable than in TIMS, where it is characterized by an exponential increase of the fractionation magnitude during the process of sample resistive vaporization from the filament into vacuum (see figure 1-4). The main source of instrumental mass discrimination in TIMS is the preferential vaporization of the lighter isotope. The sources of MC-ICP-MS instrument discrimination are less understood. Among the main sources described are: (1) Coulomb repulsion of positive ions constituting a non electrically neutral ion beam, which leads to preferential displacement of lighter ions to the periphery of the beam and resulting in a more efficient transport of the heavier isotope to the detector (space-charge effects) (Kivel et al., 2012; Rehkämper et al., 2001); (2) Supersonic expansion of the plasma plume in the interface after the sampler and extraction of only its central part by the skimmer, which leads to a more efficient sampling of the heavier isotope into the mass spectrometer (nozzle effect) (Albarède et al., 2015; Andren et al., 2004).

3.3. Correction for instrumental mass discrimination

Instrumental mass discrimination is mass-dependent in nature (with rare exceptions, *e.g.*, see (Newman et al., 2009; Yang et al., 2011). Hence, the measured target isotope ratio can be corrected for mathematically based on an assumed underlying isotope fractionation law and the measurements of an isotope pair with known ratio.

The simplest model of instrumental mass discrimination correction is measurement of the target isotope ratio of the element itself in a reference material, in which the isotope ratio is known (preferably, a certified isotopic reference material or gravimetrically prepared isotope mixture) in a sample-standard bracketing (SSB) sequence to determine the so-called K-factor, subsequently used to correct the measured target isotope ratio of the sample:

$$R_{x,smp} = K r_{x,smp}; K = \frac{R_{x,RM}}{r_{x,RM}} \qquad (1-33)$$

Here *R* and *r* indicate the corrected and measured isotope ratios, respectively, and indexes *x* and *IS*, *RM* and s*mp* denote whether the isotope ratio is related to the target isotopes or the isotopes of an internal standard (IS), reference material (RM) or sample (smp) respectively. Although the method does not assume any underlying mass-dependent isotope fractionation law and requires matching of matrix and concentration between sample and reference solutions in order to assure similar instrumental mass discrimination, it is often preferred for its simplicity.

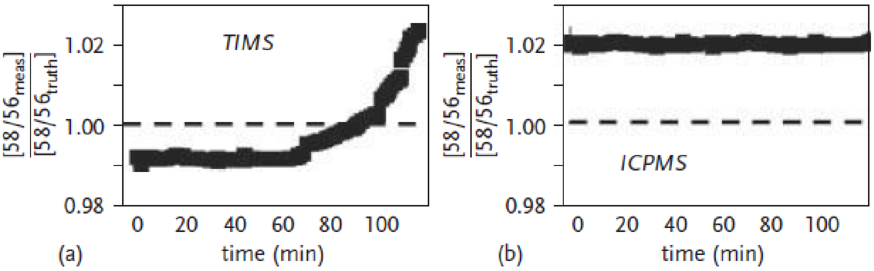

Figure 1-4. Comparison of instrumental mass discrimination observed for (a) TIMS and (b) ICP-MS. Adapted from Vanhaecke and Degryse, 2012

Another classical method, initially adopted from TIMS, is using a second isotope pair of the analyte to correct the target isotope ratio for instrumental mass discrimination; this approach is called internal standardization. Natural variation in the reference isotope ratio of the element has to be irrelevant in nature and precisely known. This naturally imposes a restriction to the model that the target element needs to have at least 3 isotopes. This model not only corrects for instrumental mass discrimination, but also cancels out any natural mass-dependent isotope fractionation of the target isotope ratio, and is especially useful when nucleosynthetic anomalies or radioisotope decay systems are studied, when natural mass-dependent fractionation of isotopes can obscure the information aimed for (Yang, 2009).

MC-ICP-MS, due to its multielement capabilities, also permits internal standardization using another element. Isotopes with known abundances of another element, added to the sample as an internal standard (IS), can be used to correct the target element isotope ratios for instrumental mass discrimination, eliminating the limitations of intra-element internal correction. The power law, generalized power law, kinetic (exponential) law, or equilibrium (thermodynamic) mathematical formulation of the mass-dependence of the mass discrimination can be used for calculating the K-factor (Wombacher and Rehkamper, 2003). The exponential mathematical description of the mass-dependent isotope fractionation (equation 1-10) is most widely preferred, and the corresponding correction is often referred to as Russell's law (Russell et al., 1978). According to equation 1-10, the mathematical formulation of K-factor can be presented using the masses of the target (m_1, m_2) and IS (m_3, m_4) element isotopes and the kinetic exponent β:

$$R_{x,smp} = r_{x,smp}\left(\frac{m_2}{m_1}\right)^{f_x};\ R_{IS,smp} = r_{IS,smp}\left(\frac{m_4}{m_3}\right)^{f_{IS}};\ f_{IS} = \frac{ln\left(R_{IS,smp}/r_{IS,smp}\right)}{ln(m_4/m_3)} \qquad (1-34)$$

Although some early correction models relied on the fact that the fractionation coefficient f for the target isotope ratio and the IS (either intra-element or for an admixed element) are linked in a mass-dependent manner as a first approximation, later various relations between the correction factors were explored in practice. It is particularly due to the fact that the instrumental mass bias is not constant and drifts in time with changing parameters and composition of the plasma, slightly drifting mass spectrometer settings and changing conditions of the environment where the unit is installed. As such, the K-factor, in addition to mass-dependent functional part, should also include a mass-independent functional part which varies in time (Meija et al., 2009). To account for this, Woodhead proposed to determine the fractionation coefficient f_x of the target isotope ratio from that of IS and a linear regression of a reference data in f_x –f_{IS} plot (Woodhead, 2002). Such plot is built using the daily SSB measurements of reference materials of the target element doped with IS with known isotope ratio (or using a second isotope ratio of the same element when intra-element internal correction is used). Further updating the model, Baxter and co-workers have shown that when the formulations of fractionation coefficients f for the target isotope ratio and that of IS (equation 1-34) are divided by one another, it provides a linear relation between the logarithms of their measured ratios (Baxter et al., 2006):

$$lnr_{x,RM} = a + blnr_{IS,RM};\text{where } a = lnR_{x,RM} - blnR_{IS,RM} \text{ and } b = \frac{f_x\ln{(m_2/m_1)}}{f_{IS}\ln{(m_4/m_3)}} \qquad (1-35)$$

and when the a and b parameters are measured from the regression line based on SSB measurements of a reference material of the target element and using another isotope ratio of the dame element or the isotope ratio of an admixed other element, the true ratio can be shown to be (Baxter et al., 2006):

$$R_{x,smp} = r_{x,smp}\cdot\frac{R_{x,RM}}{e^{a}\cdot\left(r_{IS,smp}\right)^{b}} \qquad (1-36)$$

The regression line can be defines using the common least squares method or the mathematically more correct regression of York (York, 1966). Differently to the regression model of Woodhead, the revised exponential model of Baxter does not require knowledge of the isotopic composition of the IS, and only needs it to be similar in the sample and the bracketing calibrator. The ''regression'' internal standardization method appears more favorable as both matrix- induced mass bias and temporal mass bias drift can be corrected for (Yang, 2009).

Another method, originally developed for correction for the isotope fractionation in TIMS, is the double spike approach. In this approach, an isotopically enriched spike of the target element, with 2 enriched isotopes, is added to the sample. The isotopic composition of the spike and the amount (mass) of spike added to the sample must be known precisely (Dodson, 1970; Galer, 1999). To define the extent of instrumental mass discrimination, the spiked and unspiked samples are measured in 2 separate runs. The disadvantages of this correction method are the costs of isotopically enriched materials, the low sample throughput and the high laboriousness and the requirement for the target element to have at least 4 isotopes. However, this method is capable of providing highly precise and accurate isotope ratio data, and, critically, after isotope equilibration of the spike and the sample is established in the mixture, any losses of the sample during the chemical pretreatment leading to artificial isotope fractionation would not affect the result. Due to the latter, the double spike approach is often a method of choice for the stable isotopes of elements which require complex chemical isolation associated with incomplete recoveries (e.g. Ni (Gueguen et al., 2013) or Cr (Schoenberg et al., 2008).

3.4. Spectral interference and matrix effects

The signals of target element isotopes in the mass spectrum can be overlapped by those of other species of similar mass (the same nominal mass at low mass resolution), deteriorating the results. First of all, such a species may be an isobar (a nuclide of the same atomic mass but from another element). For instance, the nuclides ^{74}Se and ^{76}Se suffer from overlap from the signals of ^{74}Ge and ^{76}Ge, and the nuclides ^{78}Se, ^{80}Se, and ^{82}Se from the signals of ^{78}Kr, ^{80}Kr, and ^{82}Kr. Unfortunately, an ICP-MS mass spectrum also shows signals from polyatomic ions with an m/z ratio potentially similar to that of the target nuclides, interfering with the measurement of the target element, *e.g.*, ^{40}Ar^{40}Ar$^+$ can interfere with the monitoring of ^{80}Se$^+$. Doubly charged ions, extracted from plasma, with a mass equal to twice that of target nuclide would have similar m/z ratio, thus also resulting in a spectral interference, *e.g.*, the measurement of ^{77}Se$^+$ can be interfered by the occurrence of ^{154}Sm^{2+}. The most critical interferences originate from constituents of the plasma, solvent, entrained air, and elements composing the matrix of the sample. Interference-free conditions are critically important for isotopic analysis of natural samples, when tiny differences in isotope ratios are of interest. Additionally, the matrix of the sample can affect the results of ICP-MS in non-spectral manner, by changing the plasma conditions and the Coulomb repulsion within the ion beam. Matrix effects in ICP-MS are typically addressed by internal standardization when trace element concentrations are measured. However, the matrix effects can cause critical changes in the extent of instrumental mass discrimination when tiny natural variations of isotope ratios are measured with MC-ICP-MS (Albarède et al., 2004). It leads to the requirement of matrix and analyte concentration matching between the samples and isotopic calibrators, and, ultimately, to the necessity of sample matrix removal or analyte isolation prior to isotopic analysis via MC-ICP-MS.

Although every element in the periodic table (except for In) has at least 1 isotope free from isobaric interference, several approaches to avoid interference due to the occurrence of polyatomic and doubly charged ions are used in ICP-MS. Higher mass resolution provided by sector field instruments (up to $M/\Delta M=10000$) is in many cases sufficient to resolve overlap by distinguishing between ions showing a slight difference in mass, resulting from the mass defect, thus providing interference-free conditions. However, many types of interferences, *e.g.*, hydrides cannot be resolved by means of the higher mass resolution provided by commercially available mass spectrometers.

Collision/reaction cell technology was introduced in ICP-MS instrumentation (Tanner et al., 2002) to resolve spectral interferences by means of gas phase ion-molecule processes. A collision/reaction cell is an enclosed cell pressurized with (a) collision/reaction gas(es), containing a multipole under radio frequency potential, placed between the interface of the mass spectrometer and the mass analyzer. Selective ion-chemical reactions of the interfering ion with the reaction gas in the cell eliminate its contribution to the spectrum, by neutralizing it or by changing its m/z ratio (charge transfer from an interfering ion to the gas molecule or exothermic transformation of the interfering molecule with an associated mass change). The unwanted species, formed in the cell as a result of side reactions, can be eliminated either via the mass-filtering capabilities of the cell multipole, or by kinetic energy discrimination using a deceleration voltage. As an alternative, the analyte ion can be involved in a selective ion-molecule reaction, converting it into a reaction product ion that can be measured interference-free at another m/z ratio. Polyatomic species in the ion beam can alternatively be discriminated against by using a deceleration potential after slowing them down to a larger extent than the atomic ions in the collision/reaction cell filled with an inert collision gas (He) due their higher collision cross-section compared to monoatomic ions.

Cold plasma conditions suppress the formation of Ar-based ions in the plasma and can be used effectively to eliminate spectral interferences for several elements, *e.g.*, ^{40}Ar^{16}O$^+$ for ^{56}Fe$^+$ (Tanner, 1995). When the species overlapping with the target element in the spectrum originate from the solvent (*e.g.*, oxide ions or Cl-containing ions), desolvation of the aerosol can be used to reduce the overall amount of oxygen or chlorine introduced into the plasma and to limit the formation of the aforementioned species. The same effect is achieved when a dry aerosol of the sample is introduced by laser ablation (see paragraph 3.6).

3.5. Ion exchange chromatography for isotopic analysis

The ultimate way to eliminate matrix effects and the majority of spectral interferences (except those originating from the plasma constituents) is chemical isolation of the target element from the matrix prior to ICP-MS analysis. For the majority of MC-ICP-MS applications, target element isolation is a prerequisite for high-precision isotopic analysis. Ion exchange column chromatography is a flexible approach for target element isolation prior to MC-ICP-MS analysis, and is often preferred over other separation methods (*e.g.*, solvent extraction or sublimation (Van Hoecke et al., 2014) due to (1) low procedural blanks; (2) the flexibility owing to the availability of various types of chromatographic resins; (3) the fact that there is no need of using organic solvents and reagents, associated with elevated metal blanks and severe matrix effects in ICP-MS, and (4) relative technical simplicity.

A pitfall associated with ion exchange chromatography is the mass-dependent isotope fractionation accompanying the ion exchange process between the resin and mobile phase (Maréchal and Albarède, 2002). However, similar isotope fractionation is expected for any other element isolation method in which the target element is distributed between phases. The magnitude of the artificial on-column isotope fractionation depends on the efficiency of the column for the target element (number of theoretical plates) (Malinovsky and Vanhaecke, 2014). On-column isotope fractionation is avoided in those cases where the target element itself is not bound to the resin and simply passes through the column. In such cases, matrix and/or unwanted interfering elements obviously have to be retained on the resin to achieve isolation. If the target element shows retention on the ion exchange resin, (nearly) quantitative recovery has to be aimed for to avoid on-column fractionation, because any material lost from the tail of the chromatographic peak is isotopically enriched. If nearly 100% recovery after isolation cannot be assured, use of the double spike correction approach is recommended, because when the spike is added to the sample prior to isolation, it will correct not only for instrumental mass discrimination, but also for artificial on-column mass-dependent isotope fractionation. Similarly, 100% recoveries are not needed when non-mass dependent variations are of interest (*e.g.*, nucleosynthetic anomalies or radioisotope decay systems) and internal intra-element correction (using a pair of isotopes of the target element unaltered in nature) is applied for correction for instrumental mass discrimination. Additionally, organic material stripped from the resin can cause matrix effects when introduced into the ICP and affect the results of isotope ratio measurements significantly (Pietruszka and Reznik, 2008).

The lowest possible procedural blanks during sample preparation for high-precision isotopic analysis have to be assured when (1) the target element is present in the samples in trace concentrations only and is prone to contamination or/and (2) the variation in the isotope ratio(s) of interest is (are) extremely small. All the reagents used for chemical preparation of the samples (digestion and target element isolation) have to meet high purity requirements for trace element contents.

To assure the lowest possible contents of trace elements (and organic molecules), ultra-pure water, used in the laboratory, is purified in specialized water purification systems in multiple steps up to ≥18.2 MΩ cm at 25°C, and the inorganic acids, used for acid digestion and/or ion exchange isolation, are (double-) distilled just before use from commercially available *pro analysis* (*p.a.*) grade acids in a sub-boiling apparatus made from quartz or Teflon. The glassware (sample recipients, consumables) used throughout the chemical preparation prior to high-precision isotopic analysis also needs to meet special requirements: the material of the container (1) should not generate contaminating metal species; (2) not be prone to memory effects and (3) rule out or limit adsorption losses of the target element on the surface. Special high-density low-porosity Teflon or perfluoroalkoxy alkane (PFA) are preferred for trace element and high-precision isotopic analysis applications.

Once contamination from reagents and recipients are ruled out or limited to the largest possible extent, the last source of contamination is the ubiquitous airborne dust. Room air can contain several millions of particles larger than 1 μm per cubic meter, potentially polluting the sample. Special clean laboratories (clean room or clean laboratory) are designed to provide optimum conditions for metal-free sample preparation. Chemical laboratories with levels up to 10 particles larger than 1 μm per cubic foot are available (class 10 according to the US FED STD 209E standard, or < 83 particles per cubic meter, equivalent to the ISO 4 class according to ISO 14644-1). Several technical solutions are used to ensure a metal-free environment. First of all, the clean laboratory is supplied with purified air, filtered from naturally present airborne dust particles in an air filtering system with a stack of filters with decreasing pore size, including high-efficiency particulate air (HEPA) filter units. The air provided is conditioned and maintained at constant humidity and temperature. The laboratory is maintained under overpressure to avoid non-conditioned air from entering. The entrances and sample transfer ports are additionally equipped with airlocks, and often a room-in-room design is used to provide higher levels of cleanness. Secondary, all clean laboratory components (fume hoods, furniture with accessories, doors and hinges, ventilation, water pipes and sinks) have metal-free designs, so that they can’t generate metal particles as a result of friction when used. Special polymers like TRESPA and acrylic glass are used for furniture and fume hoods, polyvinylidene fluoride and polypropylene for screws, furniture accessories and sinks, and polytetrafluorethylene for sliding rods, hotplates and door hinges. Additionally, generation of a laminar top-down air flow inside the clean laboratory provides fast and predictable removal of generated potentially contaminating particles towards the floor. The air stream entering the clean laboratory is distributed homogeneously among the laboratory in a diffusive manner through a polymer textile filter stretched underneath the ceiling. The air is extracted near the floor of the laboratory to provide laminar unidirectional flow. Finally, special suits have to be worn inside the controlled environment to prevent contamination from the clothes, skin and hair of the users. Regular cleaning, air filters maintenance, and quality control are important to maintain a high cleanliness level inside the clean laboratory.

The class 10 clean laboratories of A&MS group at Ghent University are used for sample preparation of multiple isotopic systems prior to high-precision MC-ICP-MS analysis. Table 1-2 lists several examples of isotope systems which require sample pretreatment in the controlled environment of clean laboratories, either due to the very low concentration of the target element (e.g., Pb in Antarctic snow samples), or because of the small magnitude of the isotope ratio variation studied (e.g., Cl in sea water samples). Some elements, *e.g.*, Zn and Fe, are very prone to contamination because they are ubiquitous in the environment, so the strictest precautions are needed to provide the lowest blanks and reliable results.

3.6. Laser ablation *in-situ* sample introduction

Laser ablation (LA) is an approach of *in situ* material sampling for (MC-)ICP-MS analysis from the solid or liquid target by means of laser radiation. In many cases it allows to avoid digestion and chemical processing of the sample, at the same time providing possibilities for laterally and depth resolved elemental and isotopic analysis. A monochromatic and, critically, high intensity short (20 ns to 100 fs) laser pulse is focused onto a small spot (down to 1 μm in diameter) on the surface of sample, which leads to formation of a partly ionized vapor, solid fragments and melted droplets of the target material. Evolution of this plasma plume in a stream of Ar or He leads to the formation of sample aerosol, which is transferred with sample gas via a transport tube and introduced into the ICP for ionization and analysis. The main mechanisms of material removal under the effect of laser beam are: (1) evaporation from the melted surface, as described by the Hertz-Knudsen equation; (2) the fast decomposition of metastable overheated liquid to form vapor and liquid droplets of melted material, called phase explosion (Bulgakova and Bulgakov, 2001; Martynyuk, 1977; Miotello and Kelly, 1999); (3) displacement and spraying of the melted material (Bleiner, 2005; Bleiner and Bogaerts, 2006; Körner et al., 1996). If the laser impulses are shorter than a few picoseconds, local thermal equilibrium between the electrons and the lattice of the target material, as well as thermal and mechanical relaxations cannot be achieved. Mechanical tension caused by fast thermal expansion of the surface layer of the target material leads to (4) photomechanical fragmentation (Anisimov et al., 2003; Perez and Lewis, 2002; Povarnitsyn et al., 2007). Co-existence of different mechanisms of aerosol formation leads to multimodality of particle size and compositional distribution (Bleiner and Bogaerts, 2006).

One of significant pitfalls of LA sampling is element fractionation, typically expressed as non-stoichiometric sampling of the target material, aerosol transport and atomization/ionization in ICP. The degree of element fractionation is affected by both the operating parameters of laser: fluence, wavelength, pulse duration and pulse frequency, and the properties of the target material: heat capacity, thermal conductivity, melting and boiling temperatures, transparency of the material at the wavelength of the laser. Preferential vaporization can fractionate the elemental composition of the sampled aerosol when thermal mechanisms, *e.g.*, evaporation from the surface, dominate aerosol formation (Mao et al., 1998). These effects are typically less significant when UV lasers with shorter wavelength (Guillong et al., 2003; Motelica-Heino et al., 2001) and homogenized “flat-topped” beam energy profile (Guillong et al., 2002) are used for ablation. Transfer losses of the aerosol of multimodal composition (Kovacs and Günther, 2008) and incomplete vaporization/ionization of the larger fraction of the aerosol in the ICP (Aeschliman et al., 2003; Kuhn et al., 2004) can also lead to non-stoichiometric effects. Spraying of melted material, coupled with formation of large μm-sized droplets, which are not fully vaporized and ionized in ICP, is characteristic for laser ablation of metals (Bleiner et al., 2006; Motelica-Heino et al., 2001). LA by femtosecond lasers is found to result in less sample melting (Chichkov et al., 1996; Povarnitsyn et al., 2007; Yang et al., 2006) and to produce a more homogeneous aerosol (Možná et al., 2006), providing less element fractionation than systems with nanosecond pulses. This is especially critical in case of LA-ICP-MS analysis of metals. Such dependence of the characteristics of nanosecond LA sampling brings about the necessity of using matrix-matched standards for reliable

Element	Application, sample matrix	Chemical pretreatment provided in the clean laboratory	The lowest concentration of the target element	The smallest isotope ratio variation, which can be measured	Reference
Fe	Biomedical applications (blood, tissues)	Hot-plate digestion, Anion exchange column target element isolation	≈1 μg g^{-1} in human serum	$\delta^{56/54}$Fe < 0.07 ‰ (2 s, period of 1 year, *n*=25)	(Anoshkina et al., 2015; Van Heghe et al., 2012)
Cu	Biomedical applications (blood, tissues), Archaeometric applications (ancient glasses, bronzes and ores)	Hot-plate digestion; Anion exchange column target element isolation	≈1 μg g^{-1} in human serum 0.05 wt% in glass	$\delta^{65/63}$Cu = 0.07 ‰ (2 s, period of 1 year, *n*=28)	(Costas-Rodríguez et al., 2015; Lobo et al., 2014; Van Heghe et al., 2012)
Zn	Biomedical applications (blood, tissues)	Hot-plate digestion; Anion exchange column target element isolation	≈1 μg g^{-1} in human serum	$\delta^{66/64}$Zn = 0.05 ‰ (2 s, period of 1 year, *n*=30)	(Van Heghe et al., 2012)
Sb	Archaeometric applications (ancient glasses and ores)	Hot-plate digestion; Combination of cation and anion-exchange column target element isolation	> 0.05 wt% in glass	$\delta^{123/121}$Sb = 0.1 ‰ (1 s)	(Lobo et al., 2014, 2012)
Li	Geochemical applications (clays, carbonates)	Cation exchange column target element isolation	0.1-1 μg g^{-1} in carbonates	$\delta^{7/6}$Li = 0.2 ‰ (2 SE, *n*=15)	(Van Hoecke et al., 2015)
B	Archaeometric applications (ancient glasses and fluxes)	Hot-plate digestion; Anion exchange target element isolation; or target element isolation based on microsublimation	> 100 μg g^{-1} in glass > 6 μg g^{-1} in natron samples	$\delta^{11/10}$B = 0.3 ‰ (2 s, *n*=140)	(Devulder et al., 2014, 2013; Van Hoecke et al., 2014)
Cl	Environmental applications, (sea water, snow)	Cation exchange column separation of Na$^+$	≈ 70 μg g^{-1} in sea water	1s (^{37}Cl/^{35}Cl) ≈ 0.07 ‰, n = 3	(de Gois et al., 2016a)
Br	Environmental applications, (aea water, snow)	Cation exchange column separation of Na$^+$	≈ 70 μg g^{-1} in sea water	1s (^{81}Br/^{79}Br) ≤ 0.08 ‰	(de Gois et al., 2016b)
Sn	Archaeometric applications (ancient bronzes)	Hot-plate digestion; Extraction chromatographic column target element isolation	≈ 5 wt% in bronze	$\delta^{122/116}$Sn = 0.06-0.16 ‰ (2 s, period of 1 month, *n*=42)	(Balliana et al., 2013)
Hg	Biogeochemical applications (natural waters, biological samples, sediments)	Hot-plate digestion	≈ 1 ng g^{-1} in water samples	$\delta^{202/198}$Hg ≤ 0.06 ‰ (1 s, 18 months, n = 250)	(Rua-Ibarz et al., 2016)
Pb	Environmental applications (Antarctic snow), archaeometric applications (bones)	Target element preconcentration *via* freeze-drying, or target element isolation using extraction chromatography	5 pg g^{-1}	1s (^{207}Pb/^{206}Pb) = 0.16 ‰	(Bazzano et al., 2015)
Sr	Archaeometric applications (ancient glasses)	Hot-plate digestion; Extraction chromatographic column target element isolation	≈ 10 μg g^{-1} in glass	2s (^{87}Sr/^{86}Sr) = 0.06 ‰	(Brems et al., 2013a; De Muynck et al., 2009)
Nd	Archaeometric applications (ancient glasses)	Hot-plate digestion; Sequential ion exchange chromatographic target element isolation	≈ 1-10 μg g^{-1} in glass	2s (^{143}Nd/^{144}Nd) = 0.04 ‰	(Brems et al., 2013b; Ganio et al., 2012)

Table 1-2. Examples of isotope systems for which chemical preparation in class 10 clean laboratories was done prior to MC-ICP-MS isotope ratio measurements in the A&MS research group.

calibration. A large variety of synthetic glass certified reference materials from the National Institute of Standards and Technology (NIST, USA) (Jochum et al., 2011), and reference glasses of natural rock compositions from the United States Geologic Survey (USGS) (Jochum et al., 2005) or from the Max Planck Institut für Chemie (MPI-DING) (Jochum et al., 2000) are currently available for quantification of the results of silicate rock analysis. LA systems with femtosecond pulse duration are less prone to the laser-induced matrix effects (Jochum et al., 2014).

Additionally to element fractionation, LA sampling is also a source of isotope fractionation, predominantly due to preferential volatilization of the lighter isotope and incomplete aerosol ionization in ICP (Jackson and Günther, 2003). Taking into account the tiny magnitude of natural stable isotope fractionation for heavy elements which are typically determined by LA-MC-ICP-MS, application of femtosecond LA systems is highly desirable, especially for metallic samples.

Laser ablation *in situ* sampling, when coupled to ICP-MS not only eliminates the need of chemical digestion of the solid sample, which is often laborious and associated with application of dangerous chemical agents at high temperatures and pressures, but also opens the possibility of quantitative laterally resolved elemental and isotopic analysis, with a spatial resolution down to 1 μm, when the ablation cell is combined with computer-controlled stages and a suitable optical system. The latter, first of all, allows analysis of small inclusions, which are difficult or impossible to extract physically for further digestion. Finally, quantitative elemental and isotopic mapping (or imaging) can be performed, *e.g.*, by rastering focused laser beam on the surface of interest and simultaneously recording the temporally resolved signal.

3.7. Complementary techniques

After its first introduction in the early 1980s, ICP-MS became widespread and was abundantly used for geochemical and cosmochemical applications. When used for (multi-)elemental analysis, ICP-MS nearly fully replaced neutron activation analysis techniques, formerly broadly used in field of geo-applications. At nearly similar detection capabilities, ICP-MS is incomparably advantageous to NAA in terms of cost associated with running the nuclear reactor. At the same time, when combined with LA, ICP-MS complemented and extended the detection and spatial resolution capabilities of X-ray fluorescence (XRF) and electron probe micro analysis (EPMA). Speaking of high-precision isotopic analysis, MC-ICP-MS largely replaced TIMS (see paragraph 3.3.), and its application field partially overlaps with that of SIMS, when LA sample introduction is used. The most important techniques complementary to ICP-MS, used for element abundance and isotope ratio determination in geo- and cosmochemical applications are briefly described below.

TIMS is one of the oldest mass spectrometry techniques used for high-precision isotopic analysis with a precision better than 0.01 % RSD and is utilizing the thermal ionization effect (Becker, 2007). A small volume of aqueous analyte solution (1-10 μl, containing a minimum of about 1 ng of analyte) is placed on the resistively heated (to 1000 – 2500 K) metal filament (e.g., Re) under high vacuum conditions. The analyte is first desorbed from the surface and its atoms are spontaneously ionized. In the double filament approach, sample evaporation and ionization are separated, which provides more flexibility and control of the process. The thermal ionization ion source is characterized by low energy dispersion (0.1–0.2 eV), which allows a single-focusing magnetic sector mass analyzer to be used. The ion source generates both positively and negatively charged ions. Negative ions can be used for isotopic analysis of elements with high electron affinity (*e.g.*, Cl, Br). Comparatively to ICP-MS, the thermal ionization ion source is characterized by lower ionization efficiency, exponential instrumental mass discrimination, complicating the correction (see figure 1-4), and practically no multielement capabilities. Because of the limited ionization efficiency of the ion source, TIMS is mostly useful for high-precision isotopic analysis of elements with low first ionization energy < 7 eV, but is reported to be applied successfully for nearly all elements in periodic table (Heumann et al., 1995). Absence of multi-element capabilities limits application of the technique to isotope dilution quantification for highly accurate and precise element concentration determination, and restricts the available instrumental discrimination correction methods to intra-element normalization or the double spike approach (Becker, 2007).

SIMS is a mass spectrometry technique for *direct* analysis of solid samples, utilizing a secondary ionization source. The primary ion beam is generated in a primary ion source, such as a duoplasmatron or electron ionization source (to generate, *e.g.*, Ar^+, Xe^+, O^-, O_2^-, SF_5^- ions), via surface ionization (Cs^+) or using a liquid metal ion gun (*e.g.*, Ga^+, Au^+, Bi_n^+). The beam of primary ions is subsequently accelerated to 0.2-40 keV and focused to a spot with a size down to several nm. The components of the solid sample are sampled by bombardment of its surface by a primary ion beam under high vacuum conditions. This leads to the kinetic energy of accelerated primary ions being transferred to the atoms of sample, generating sputtered neutrals and ions. Secondary ions are ejected and directed to the mass analyzer. The yields and relative sensitivity factors of secondary ions highly depend on the sample matrix and properties of the primary ion beam, requiring matrix-matched standards for quantification (Becker, 2007). SIMS is capable of *in situ* determination of element concentrations and high-precision isotopic analysis with high associated lateral resolution, including mapping. SIMS was recently used for in-situ high-precision (typical reproducibility obtained for $\delta^{56/54}$Fe is 0.2 – 0.4 ‰ at 2 SD) isotopic analysis of Fe (Kita et al., 2011; Marin-Carbonne et al., 2011; Sio et al., 2013) and Ni (Watson et al., 2016) in silicate and metal matrices with 15 – 50 µm lateral resolution. Although SIMS provides slightly superior lateral resolution compared to that typical for in-situ isotopic analysis of Fe via LA-MC-ICP-MS (Horn et al., 2006; Horn and von Blanckenburg, 2007), it demonstrates an overall lower reproducibility in isotope ratio measurements. Notably, SIMS measurements of Fe and Ni isotope ratios were reported to be prone to matrix effects, which required application of a matrix-matched standard or of mathematical correction (Sio et al., 2013; Watson et al., 2016). This is not the case for femtosecond LA sampling, which opens the way to truly matrix-independent *in-situ* isotopic analysis (Horn et al., 2006). Nanoscale SIMS (nano SIMS) was recently used for *in-situ* measurement of nucleosynthetic anomalies in the isotopic composition of Fe and Ni in presolar grains (Marhas et al., 2008).

X-ray emission detection based techniques, XRF and EPMA are techniques used for determination of elemental concentrations in solid (more rarely, liquid) samples based on analysis of the spectrum of characteristic X-rays emitted from the sample under primary X-ray excitation (XRF) or excitation by an electron beam (EPMA). The primary beam in XRF can be generated in an X-ray tube or synchrotron radiation can be used. EPMA relies on an accelerated beam of electrons as an excitation source. When atoms of the sample are exposed to the primary (X-ray or electron) beam, the electrons from inner orbitals of the atom are expelled. Such electron configuration is unstable, and electrons from higher energy levels tend to fill the vacant position. When the electron is transferred to the vacant orbital from the higher energy levels, a photon can be emitted. The energy of the emitted photon is equal to the difference between the energy levels of the transition involved, making the wavelength of the secondary X-ray emission characteristic to the atoms contained in the sample. The energy levels with principal quantum numbers 1, 2, 3 are traditionally termed K, L, M in X-ray spectroscopy, and the transitions L→K, M→K and M→L, together with corresponding lines in spectrum are called K_α, K_β and L_α respectively. The characteristic secondary X-ray spectrum is recorded using either wavelength-dispersive spectroscopy or energy-dispersive spectroscopy, based on various types of semiconductor detectors.

The X-ray based techniques are characterized by superior lateral resolution, making it complementary to LA-ICP-MS in terms of elemental analysis. However, LA-ICP-MS provides lower detection limits, making it suitable for trace element geochemical applications at mineral scale, when extreme lateral resolution is not needed. Additionally, the X-ray based techniques do not possess isotope ratio capabilities.

4. List of references

Aeschliman, D.B., Bajic, S.J., Baldwin, D.P., Houk, R.S., 2003. High-speed digital photographic study of an inductively coupled plasma during laser ablation: comparison of dried solution aerosols from a microconcentric nebulizer and solid particles from laser ablation. J. Anal. At. Spectrom. 18, 1008–1014. doi:10.1039/b302546m

Albarède, F., Albalat, E., Télouk, P., 2015. Instrumental isotope fractionation in multiple-collector ICP-MS. J. Anal. At. Spectrom. 30, 1736–1742. doi:10.1039/C5JA00188A

Albarède, F., Telouk, P., Blichert-Toft, J., Boyet, M., Agranier, A., Nelson, B., 2004. Precise and accurate isotopic measurements using multiple-collector ICPMS. Geochim. Cosmochim. Acta 68, 2725–2744. doi:10.1016/j.gca.2003.11.024

Alexander, C.M.O., Wang, J., 2001. Iron isotopes in chondrules: Implications for the role of evaporation during chondrule formation. Meteorit. Planet. Sci. 36, 419–428. doi:10.1111/j.1945-5100.2001.tb01883.x

Andren, H., Rodushkin, I., Stenberg, A., Malinovsky, D., Baxter, D.C., 2004. Sources of mass bias and isotope ratio variation in multi-collector ICP-MS: optimization of instrumental parameters based on experimental observations. J. Anal. At. Spectrom. 19, 1217–1224. doi:10.1039/b403938f

Anisimov, S.I., Zhakhovskii, V. V., Inogamov, N.A., Nishihara, K., Oparin, A.M., Petrov, Y. V., 2003. Destruction of a solid film under the action of ultrashort laser pulses. J. Exp. Theor. Phys. Lett. 77, 606–610.

Anoshkina, Y., Costas-Rodríguez, M., Vanhaecke, F., 2015. High-precision Fe isotopic analysis of whole blood for biomedical purposes without prior isolation of the target element. J. Anal. At. Spectrom. 30, 1816–1821. doi:10.1039/C5JA00209E

Balliana, E., Aramendía, M., Resano, M., Barbante, C., Vanhaecke, F., 2013. Copper and tin isotopic analysis of ancient bronzes for archaeological investigation: development and validation of a suitable analytical methodology. Anal. Bioanal. Chem. 405, 2973–2986. doi:10.1007/s00216-012-6542-1

Baxter, D.C., Rodushkin, I., Engström, E., 2012. Isotope abundance ratio measurements by inductively coupled plasma-sector field mass spectrometry. J. Anal. At. Spectrom. 27, 1355–1381. doi:10.1039/c2ja30153a

Baxter, D.C., Rodushkin, I., Engström, E., Malinovsky, D., 2006. Revised exponential model for mass bias correction using an internal standard for isotope abundance ratio measurements by multi-collector inductively coupled plasma mass spectrometry. J. Anal. At. Spectrom. 21, 427–430. doi:10.1039/b517457k

Bazzano, A., Latruwe, K., Grotti, M., Vanhaecke, F., 2015. Lead isotopic analysis of Antarctic snow using multi-collector ICP-mass spectrometry. J. Anal. At. Spectrom. 30, 1322–1328. doi:10.1039/C4JA00484A

Becker, J.S., 2007. Inorganic mass spectrometry Principles and applications. John Wiley & Sons Ltd, The Atrium, Southern Gate, Chichester, West Sussex PO19 8SQ, England.

Benedix, G.K., Haack, H., McCoy, T.J., 2014. Iron and Stony-Iron Meteorites, in: Treatise on Geochemistry. Volume 1: Meteorites, Comets, and Planets. Elsevier, pp. 267–285. doi:10.1016/B978-0-08-095975-7.00109-1

Birck, J.L., 2004. An Overview of Isotopic Anomalies in Extraterrestrial Materials and Their Nucleosynthetic Heritage. Rev. Mineral. Geochemistry 55, 25–64. doi:10.2138/gsrmg.55.1.25

Bleiner, D., 2005. Mathematical modelling of laser-induced particulate formation in direct solid microanalysis. Spectrochim. Acta Part B At. Spectrosc. 60, 49–64. doi:10.1016/j.sab.2004.10.005

Bleiner, D., Bogaerts, A., 2006. Multiplicity and contiguity of ablation mechanisms in laser-assisted analytical micro-sampling. Spectrochim. Acta Part B At. Spectrosc. 61, 421–432. doi:10.1016/j.sab.2006.02.007

Bleiner, D., Chen, Z., Autrique, D., Bogaerts, A., 2006. Role of laser-induced melting and vaporization of metals during ICP-MS and LIBS analysis, investigated with computer simulations and experiments. J. Anal. At. Spectrom. 21, 910–921. doi:10.1039/b602800d

Boesenberg, J.S., Davis, A.M., Prinz, M., Weisberg, M.K., Clayton, R.N., Mayeda, T.K., 2000. The pyroxene pallasites, Vermillion and Yamato 8451: Not quite a couple. Meteorit. Planet. Sci. 35, 757–769. doi:10.1111/j.1945-5100.2000.tb01460.x

Bogard, D.D., Garrison, D.H., 1998. 39Ar- 40Ar ages and thermal history of mesosiderites. Geochim. Cosmochim. Acta 62, 1459–1468.

Bouvier, A., Blicherttoft, J., Vervoort, J., Albarede, F., 2005. The age of SNC meteorites and the antiquity of the Martian surface. Earth Planet. Sci. Lett. 240, 221–233. doi:10.1016/j.epsl.2005.09.007

Brearley, A.J., Jones, R.H., 1998. Chondritic meteorites, in: Papike, J.J. (Ed.), Reviews in Mineralogy. Vol 36: Planetary Materials. Mineralogical Society of America, pp. 3–01–3–398.

Brems, D., Ganio, M., Latruwe, K., Balcaen, L., Carremans, M., Gimenio, D., Silvestri, A., Vanhaecke, F., Muchez, P., Degryse, P., 2013a. Isotopes on the beach, part 1: Strontium isotope ratios as a provenance indicator for lime raw materials used in Roman galss-making. Archaeometry 55, 214–234. doi:10.1111/j.1475-4754.2012.00702.x

Brems, D., Ganio, M., Latruwe, K., Balcaen, L., Carremans, M., Gimeno, D., Silvestri, A., Vanhaecke, F., Muchez, P., Degryse, P., 2013b. Isotopes on the beach, part 2: Neodymium isotopic analysis for the provenancing of roman glass-making. Archaeometry 55, 449–464. doi:10.1111/j.1475-4754.2012.00701.x

Bulgakova, N.M., Bulgakov, A.V., 2001. Pulsed laser ablation of solids: transition from normal vaporization to phase explosion. Appl. Phys. A Mater. Sci. Process. 73, 199–208. doi:10.1007/s003390000686

Bunch, T.E., Rumble, D., I., Wittke, J.H., Irving, A.J., 2005. Pyroxene-rich Pallasites Zinder and NWA 1911: Not Like the Others, in: 68th Annual Meeting of the Meteoritical Society. Gatlinburg, Tennessee, p. 5219.

Burbine, T.H., Buchanan, P.C., Binzel, R.P., Bus, S.J., Hiroi, T., Hinrichs, J.L., Meibom, A., Mccoy, T.J., 2001. Vesta, Vestoids, and the howardite, eucrite, diogenite group: Relationships and the origin of spectral differences. Meteorit. Planet. Sci. 36, 761–781. doi:10.1111/j.1945-5100.2001.tb01915.x

Campargue, R., 1984. Progress in overexpanded supersonic jets and skimmed molecular beams in free-jet zones of silence. J. Phys. Chem. 88, 4466–4474. doi:10.1021/j150664a004

Chen, J.H., Papanastassiou, D.., Wasserburg, G.., 2002. Re-Os and Pd-Ag systematics in Group IIIAB irons and in pallasites. Geochim. Cosmochim. Acta 66, 3793–3810. doi:10.1016/S0016-7037(02)00952-3

Chichkov, B.N., Momma, C., Nolte, S., Alvensleben, F., Tünnermann, A., 1996. Femtosecond, picosecond and nanosecond laser ablation of solids. Appl. Phys. A Mater. Sci. Process. 63, 109–115. doi:10.1007/BF01567637

Clayton, R.N., 2003. Oxygen Isotopes in Meteorites, in: Davis, A.M. (Ed.), Treatise on Geochemistry. Volume 1: Meteorites, Comets, and Planets. Elsevier, pp. 129–142. doi:10.1016/B0-08-043751-6/01063-X

Clayton, R.N., Grossman, L., Mayeda, T.K., 1973. A Component of Primitive Nuclear Composition in Carbonaceous Meteorites. Science (80-.). 182, 485–488. doi:10.1126/science.182.4111.485

Clayton, R.N., Mayeda, T.K., 1978. Genetic relations between iron and stony meteorites. Earth Planet. Sci. Lett. 40, 168–174. doi:10.1016/0012-821X(78)90087-0

Clayton, R.N., Onuma, N., Mayeda, T.K., 1976. A classification of meteorites based on oxygen isotopes. Earth Planet. Sci. Lett. 30, 10–18. doi:10.1016/0012-821X(76)90003-0

Costas-Rodríguez, M., Anoshkina, Y., Lauwens, S., Van Vlierberghe, H., Delanghe, J., Vanhaecke, F., 2015. Isotopic analysis of Cu in blood serum by multi-collector ICP-mass spectrometry: a new approach for the diagnosis and prognosis of liver cirrhosis? Metallomics 7, 491–498. doi:10.1039/c4mt00319e

Dauphas, N., Marty, B., Reisberg, L., 2002. Molybdenum Evidence for Inherited Planetary Scale Isotope Heterogeneity of the Protosolar Nebula. Astrophys. J. 565, 640–644. doi:10.1086/324597

Dauphas, N., Roskosz, M., Alp, E.E., Golden, D.C., Sio, C.K., Tissot, F.L.H., Hu, M.Y., Zhao, J., Gao, L., Morris, R.V., 2012. A general moment NRIXS approach to the determination of equilibrium Fe isotopic fractionation factors: Application to goethite and jarosite. Geochim. Cosmochim. Acta 94, 254–275. doi:10.1016/j.gca.2012.06.013

Dauphas, N., Roskosz, M., Alp, E.E., Neuville, D.R., Hu, M.Y., Sio, C.K., Tissot, F.L.H., Zhao, J., Tissandier, L., Médard, E., Cordier, C., 2014. Magma redox and structural controls on iron isotope variations in Earth's mantle and crust. Earth Planet. Sci. Lett. 398, 127–140. doi:10.1016/j.epsl.2014.04.033

de Gois, J.S., Costas-Rodríguez, M., Vallelonga, P., Borges, D.L.G., Vanhaecke, F., 2016a. A simple method for high-precision isotopic analysis of chlorine via pneumatic nebulization multi-collector inductively coupled plasma-mass spectrometry. J. Anal. At. Spectrom. 31, 537–542. doi:10.1039/C5JA00408J

de Gois, J.S., Vallelonga, P., Spolaor, A., Devulder, V., Borges, D.L.G., Vanhaecke, F., 2016b. Bromine isotope ratio measurements in seawater by multi-collector inductively coupled plasma-mass spectrometry with a conventional sample introduction system. Anal. Bioanal. Chem. 408, 409–416. doi:10.1007/s00216-015-8820-1

De Muynck, D., Huelga-Suarez, G., Van Heghe, L., Degryse, P., Vanhaecke, F., 2009. Systematic evaluation of a strontium-specific extraction chromatographic resin for obtaining a purified Sr fraction with quantitative recovery from complex and Ca-rich matrices. J. Anal. At. Spectrom. 24, 1498–1510. doi:10.1039/b908645e

Devulder, V., Degryse, P., Vanhaecke, F., 2013. Development of a Novel Method for Unraveling the Origin of Natron Flux Used in Roman Glass Production Based on B Isotopic Analysis via Multicollector Inductively Coupled Plasma Mass Spectrometry. Anal. Chem. 85, 12077–12084. doi:10.1021/ac403176c

Devulder, V., Vanhaecke, F., Shortland, A., Mattingly, D., Jackson, C., Degryse, P., 2014. Boron isotopic composition as a provenance indicator for the flux raw material in Roman natron glass. J. Archaeol. Sci. 46, 107–113. doi:10.1016/j.jas.2014.03.009

Dodson, M.H., 1970. Simplified equations for double-spiked isotopic analyses. Geochim. Cosmochim. Acta 34, 1241–1244. doi:10.1016/0016-7037(70)90060-8

Franchi, I.A., Greenwood, R.C., Scott, E.R.D., 2013. The IIIAB-pallasite relationship revisited the oxigen isotope perspective, in: 76th Annual Meteoritical Society Meeting. p. 5326.

Fukami, Y., Kimura, J., Irisawa, K., Yokoyama, T., Hirata, T., 2010. Mass-dependent fractionation of tungsten isotopes in IIIAB iron meteorites, in: 41st Lunar and Planetary Science Conference. p. 1649.

Galer, S.J.G., 1999. Optimal double and triple spiking for high precision lead isotopic measurement. Chem. Geol. 157, 255–274. doi:10.1016/S0009-2541(98)00203-4

Ganio, M., Latruwe, K., Brems, D., Muchez, P., Vanhaecke, F., Degryse, P., 2012. The Sr–Nd isolation procedure for subsequent isotopic analysis using multi-collector ICP-mass spectrometry in the context of provenance studies on archaeological glass. J. Anal. At. Spectrom. 27, 1335–1341. doi:10.1039/c2ja30154g

Goderis, S., Chakrabarti, R., Debaille, V., Kodolányi, J., 2016. Isotopes in cosmochemistry: recipe for a Solar System. J. Anal. At. Spectrom. 31, 841–862. doi:10.1039/C5JA00411J

Goldstein, J.I., Scott, E.R.D., Chabot, N.L., 2009. Iron meteorites: Crystallization, thermal history, parent bodies, and origin. Chemie der Erde - Geochemistry 69, 293–325. doi:10.1016/j.chemer.2009.01.002

Goldstein, J.I., Yang, J., Scott, E.R.D., 2014. Determining cooling rates of iron and stony-iron meteorites from measurements of Ni and Co at kamacite–taenite interfaces. Geochim. Cosmochim. Acta 140, 297–320. doi:10.1016/j.gca.2014.05.025

Goodrich, C.A., 1992. Ureilites: A critical review. Meteoritics 27, 327–352. doi:10.1111/j.1945-5100.1992.tb00215.x

Gosse, J.C., Phillips, F.M., 2001. Terrestrial in situ cosmogenic nuclides: theory and application. Quat. Sci. Rev. 20, 1475–1560. doi:10.1016/S0277-3791(00)00171-2

Greenwood, R.C., Barrat, J.-A., Scott, E.R.D., Haack, H., Buchanan, P.C., Franchi, I.A., Yamaguchi, A., Johnson, D., Bevan, A.W.R., Burbine, T.H., 2015. Geochemistry and oxygen isotope composition of main-group pallasites and olivine-rich clasts in mesosiderites: Implications for the “Great Dunite Shortage” and HED-mesosiderite connection. Geochim. Cosmochim. Acta 169, 115–136. doi:10.1016/j.gca.2015.07.023

Greenwood, R.C., Franchi, I.A., Jambon, A., Barrat, J.A., Burbine, T.H., 2006. Oxygen isotope variation in stony-iron meteorites. Science 313, 1763–1765. doi:10.1126/science.1128865

Grimm, R.E., Mcsween, H.Y., 1993. Heliocentric zoning of the asteroid belt by aluminum-26 heating, in: Lunar and Planetary Science Conference XXIV. pp. 577–578.

Gueguen, B., Rouxel, O., Ponzevera, E., Bekker, A., Fouquet, Y., 2013. Nickel Isotope Variations in Terrestrial Silicate Rocks and Geological Reference Materials Measured by MC-ICP-MS. Geostand. Geoanalytical Res. 37, 297–317. doi:10.1111/j.1751-908X.2013.00209.x

Guillong, M., Horn, I., Günther, D., 2003. A comparison of 266 nm, 213 nm and 193 nm produced from a single solid state Nd:YAG laser for laser ablation ICP-MS. J. Anal. At. Spectrom. 18, 1224–1230. doi:10.1039/B305434A

Guillong, M., Horn, I., Günther, D., 2002. Capabilities of a homogenized 266 nm Nd:YAG laser ablation system for LA-ICP-MS. J. Anal. At. Spectrom. 17, 8–14. doi:10.1039/B107823M

Haack, H., Bizzarro, M., Backer, J.A., Rosing, M., 2003. Early thermal evolution and sizes of the HED and mesosiderite parent bodies new constraints from Lu-Hf chronology, in: Lunar and Planetary Science XXXIV. p. 1317.

Hassanzadeh, J., Rubin, A.E., Wasson, J.T., 1990. Compositions of large metal nodules in mesosiderites: Links to iron meteorite group IIIAB and the origin of mesosiderite subgroups. Geochim. Cosmochim. Acta 54, 3197–3208. doi:10.1016/0016-7037(90)90134-7

Herzog, G.F., Caffee, M.W., 2013. Cosmic-Ray Exposure Ages of Meteorites, in: Treatise on Geochemistry. Volume 1: Meteorites, Comets, and Planets. Elsevier Ltd., pp. 419–454. doi:10.1016/B978-0-08-095975-7.00110-8

Heumann, K.G., Eisenhut, S., Gallus, S., Hebeda, E.H., Nusko, R., Vengosh, A., Walczyk, T., 1995. Recent developments in thermal ionization mass spectrometric techniques for isotope analysis. A review. Analyst 120, 1291–1299. doi:10.1039/an9952001291

Hoefs, J., 2009. Stable Isotope Geochemistry, 6th ed. Springer-Verlag, Berlin Heidelberg.

Houk, R.S., Fassel, V.A., Flesch, G.D., Svec, H.J., Gray, A.L., Taylor, C.E., 1980. Inductively coupled argon plasma as an ion source for mass spectrometric determination of trace elements. Anal. Chem. 52, 2283–2289. doi:10.1021/ac50064a012

Horn, I., von Blanckenburg, F., Schoenberg, R., Steinhoefel, G., Markl, G., 2006. In situ iron isotope ratio determination using UV-femtosecond laser ablation with application to hydrothermal ore formation processes. Geochim. Cosmochim. Acta 70, 3677–3688. doi:10.1016/j.gca.2006.05.002

Horn, I., von Blanckenburg, F., 2007. Investigation on elemental and isotopic fractionation during 196 nm femtosecond laser ablation multiple collector inductively coupled plasma mass spectrometry. Spectrochim. Acta Part B At. Spectrosc. 62, 410–422. doi:10.1016/j.sab.2007.03.034

Jackson, S.E., Günther, D., 2003. The nature and sources of laser induced isotopic fractionation in laser ablation-multicollector-inductively coupled plasma-mass spectrometry. J. Anal. At. Spectrom. 18, 205–212. doi:10.1039/b209620j

Jochum, K.P., Dingwell, D.B., Rocholl, A., Stoll, B., Hofmann, A.W., Becker, S., Besmehn, A., Bessette, D., Dietze, H.-J., Dulski, P., Erzinger, J., Hellebrand, E., Hoppe, P., Horn, I., Janssens, K., Jenner, G.A., Klein, M., McDonough, W.F., Maetz, M., Mezger, K., Müker, C., Nikogosian, I.K., Pickhardt, C., Raczek, I., Rhede, D., Seufert, H.M., Simakin, S.G., Sobolev, A.V., Spettel, B., Straub, S., Vincze, L., Wallianos, A., Weckwerth, G., Weyer, S., Wolf, D., Zimmer, M., 2000. The Preparation and Preliminary Characterisation of Eight Geological MPI-DING Reference Glasses for In-Situ Microanalysis. Geostand. Geoanalytical Res. 24, 87–133. doi:10.1111/j.1751-908X.2000.tb00590.x

Jochum, K.P., Stoll, B., Weis, U., Jacob, D.E., Mertz-Kraus, R., Andreae, M.O., 2014. Non-Matrix-Matched Calibration for the Multi-Element Analysis of Geological and Environmental Samples Using 200 nm Femtosecond LA-ICP-MS: A Comparison with Nanosecond Lasers. Geostand. Geoanalytical Res. 38, 265–292. doi:10.1111/j.1751-908X.2014.12028.x

Jochum, K.P., Weis, U., Stoll, B., Kuzmin, D., Yang, Q., Raczek, I., Jacob, D.E., Stracke, A., Birbaum, K., Frick, D.A., Günther, D., Enzweiler, J., 2011. Determination of Reference Values for NIST SRM 610-617 Glasses Following ISO Guidelines. Geostand. Geoanalytical Res. 35, 397–429. doi:10.1111/j.1751-908X.2011.00120.x

Jochum, K.P., Willbold, M., Raczek, I., Stoll, B., Herwig, K., 2005. Chemical Characterisation of the USGS Reference Glasses GSA-1G, GSC-1G, GSD-1G, GSE-1G, BCR-2G, BHVO-2G and BIR-1G Using EPMA, ID-TIMS, ID-ICP-MS and LA-ICP-MS. Geostand. Geoanalytical Res. 29, 285–302. doi:10.1111/j.1751-908X.2005.tb00901.x

Jones, R.H., Wasson, J.T., Larson, T., Sharp, Z.D., 2003. Milton: A New, Unique Pallasite, in: 34th Annual Lunar and Planetary Science Conference. League City, Texas, p. 1683.

Keil, K., 2012. Angrites, a small but diverse suite of ancient, silica-undersaturated volcanic-plutonic mafic meteorites, and the history of their parent asteroid. Chemie der Erde - Geochemistry 72, 191–218. doi:10.1016/j.chemer.2012.06.002

Keil, K., 2010. Enstatite achondrite meteorites (aubrites) and the histories of their asteroidal parent bodies. Chemie der Erde - Geochemistry 70, 295–317. doi:10.1016/j.chemer.2010.02.002

Keil, K., 1989. Enstatite meteorites and their parent bodies. Meteoritics 24, 195–208. doi:10.1111/j.1945-5100.1989.tb00694.x

Kita, N.T., Hurberty, J.M., Kozdon, R., Beard, B.L., Valley J.W., 2010. High-precision SIMS oxygen, sulfur and iron stable isotope analyses of geologicalmaterials: accuracy, surface topography and crystal orientation. Surface and Interface Analysis 43 (1–2), 427–431. doi:10.1002/sia.3424

Kivel, N., Günther-Leopold, I., Vanhaecke, F., Günther, D., 2012. Isotope fractionation during ion beam formation in multi-collector inductively coupled plasma mass spectrometry. Spectrochim. Acta Part B At. Spectrosc. 76, 126–132. doi:10.1016/j.sab.2012.06.045

Körner, C., Mayerhofer, R., Hartmann, M., Bergmann, H.W., 1996. Physical and material aspects in using visible laser pulses of nanosecond duration for ablation. Appl. Phys. A Mater. Sci. Process. 63, 123–131. doi:10.1007/BF01567639

Kovacs, R., Günther, D., 2008. Influence of transport tube materials on signal response and drift in laser ablation-inductively coupled plasma-mass spectrometry. J. Anal. At. Spectrom. 23, 1247–1252. doi:10.1039/b803789b

Krot, A.N., Keil, K., Scott, E.R.D., Goodrich, C.A., Weisberg, M.K., 2014. Classification of Meteorites and Their Genetic Relationships, in: Treatise on Geochemistry. Volume 1: Meteorites, Comets, and Planets. Elsevier, pp. 1–63. doi:10.1016/B978-0-08-095975-7.00102-9

Kruijer, T.S., Fischer-Gödde, M., Kleine, T., Sprung, P., Leya, I., Wieler, R., 2013. Neutron capture on Pt isotopes in iron meteorites and the Hf–W chronology of core formation in planetesimals. Earth Planet. Sci. Lett. 361, 162–172. doi:10.1016/j.epsl.2012.10.014

Kuhn, H.-R., Guillong, M., Günther, D., 2004. Size-related vaporisation and ionisation of laser-induced glass particles in the inductively coupled plasma. Anal. Bioanal. Chem. 378, 1069–74. doi:10.1007/s00216-003-2346-7

Lobo, L., Degryse, P., Shortland, A., Eremin, K., Vanhaecke, F., 2014. Copper and antimony isotopic analysis via multi-collector ICP-mass spectrometry for provenancing ancient glass. J. Anal. At. Spectrom. 29, 58–64. doi:10.1039/C3JA50303H

Lobo, L., Devulder, V., Degryse, P., Vanhaecke, F., 2012. Investigation of natural isotopic variation of Sb in stibnite ores via multi-collector ICP-mass spectrometry – perspectives for Sb isotopic analysis of Roman glass. J. Anal. At. Spectrom. 27, 1304–1310. doi:10.1039/c2ja30062a

Lodders, K., Fegley, B., 2011. Chemistry of the Solar System. Royal Society of Chemistry, Cambridge.

Luais, B., 2007. Isotopic fractionation of germanium in iron meteorites: Significance for nebular condensation, core formation and impact processes. Earth Planet. Sci. Lett. 262, 21–36. doi:10.1016/j.epsl.2007.06.031

Lyons, J.R., Young, E.D., 2005. CO self-shielding as the origin of oxygen isotope anomalies in the early solar nebula. Nature 435, 317–320. doi:10.1038/nature03557

Malinovsky, D., Vanhaecke, F., 2014. Molybdenum isotope enrichment by anion-exchange chromatography. J. Anal. At. Spectrom. 29, 1090–1097. doi:10.1039/c4ja00013g

Malinovsky, D., Vanhaecke, F., 2011. Mass-independent isotope fractionation of heavy elements measured by MC-ICPMS: a unique probe in environmental sciences. Anal. Bioanal. Chem. 400, 1619–1624. doi:10.1007/s00216-011-4856-z

Mao, X.L., Ciocan, A.C., Russo, R.E., 1998. Preferential Vaporization during Laser Ablation Inductively Coupled Plasma Atomic Emission Spectroscopy. Appl. Spectrosc. 52, 913–918.

Marcus, R.A., 2004. Mass-independent isotope effect in the earliest processed solids in the solar system: a possible chemical mechanism. J. Chem. Phys. 121, 8201–8211. doi:10.1063/1.1803507

Maréchal, C., Albarède, F., 2002. Ion-exchange fractionation of copper and zinc isotopes. Geochim. Cosmochim. Acta 66, 1499–1509. doi:10.1016/S0016-7037(01)00815-8

Maréchal, C.N., Télouk, P., Albarède, F., 1999. Precise analysis of copper and zinc isotopic compositions by plasma-source mass spectrometry. Chem. Geol. 156, 251–273. doi:10.1016/S0009-2541(98)00191-0

Marhas, K.K., Amari, S., Gyngard, F., Zinner, E., Gallino, R., 2008. Iron and Nickel Isotopic Ratios in Presolar SiC Grains. Astrophys. J. 689, 622–645. doi:10.1086/592599.

Markowski, A., Quitté, G., Halliday, A., Kleine, T., 2006. Tungsten isotopic compositions of iron meteorites: Chronological constraints vs. cosmogenic effects. Earth Planet. Sci. Lett. 242, 1–15. doi:10.1016/j.epsl.2005.11.048

Martin-Carbonne, J., Rollion-Bard, C., Luais, B., 2011. In-situ measurements of iron isotopes by SIMS: MC-ICP-MS intercalibration and application to a magnetite crystal from the Gunflint chert. Chem. Geol. 285 (1–4), 50–61. doi:10.1016/j.chemgeo.2011.02.019

Martynyuk, M.M., 1977. Phase explosion of a metastable fluid. Combust. Explos. Shock Waves 13, 178–191. doi:10.1007/BF00754998

McKibbin, S.J., Ireland, T.R., Holden, P., O'Neill, H.S.C., Mallmann, G., 2016. Rapid cooling of planetesimal core-mantle reaction zones from Mn-Cr isotopes in pallasites. Geochemical Perspect. 2, 68–77. doi:10.7185/geochemlet.1607

McKibbin, S.J., O'Neill, H.S.C., Mallmann, G., Halfpenny, A., 2013. LA-ICP-MS mapping of olivine from the Brahin and Brenham meteorites: Complex elemental distributions in the pallasite olivine precursor. Geochim. Cosmochim. Acta 119, 1–17. doi:10.1016/j.gca.2013.05.031

McSween, H.Y., Binzel, R.P., De Sanctis, M.C., Ammannito, E., Prettyman, T.H., Beck, A.W., Reddy, V., Le Corre, L., Gaffey, M.J., McCord, T.B., Raymond, C.A., Russell, C.T., 2013. Dawn; the Vesta-HED connection; and the geologic context for eucrites, diogenites, and howardites. Meteorit. Planet. Sci. 48, 2090–2104. doi:10.1111/maps.12108

McSween, H.Y., McLennan, S.M., 2014. Mars, in: Treatise on Geochemistry. Volume 2: Planets, Asteriods, Comets and The Solar System. Elsevier, pp. 251–300. doi:10.1016/B978-0-08-095975-7.00125-X

McSween, H.Y., Mittlefehldt, D.W., Beck, A.W., Mayne, R.G., McCoy, T.J., 2011. HED Meteorites and Their Relationship to the Geology of Vesta and the Dawn Mission. Space Sci. Rev. 163, 141–174. doi:10.1007/s11214-010-9637-z

McSween, H.Y.J., Huss, G.R., 2010. Cosmochemistry. Cambridge University press, Cambridge.

Meier, M.M.M., Cloquet, C., Marty, B., 2016. Mercury (Hg) in meteorites: Variations in abundance, thermal release profile, mass-dependent and mass-independent isotopic fractionation. Geochim. Cosmochim. Acta 182, 55–72. doi:10.1016/j.gca.2016.03.007

Meija, J., Yang, L., Sturgeon, R., Mester, Z., 2009. Mass bias fractionation laws for multi-collector ICPMS: assumptions and their experimental verification. Anal. Chem. 81, 6774–6778. doi:10.1021/ac9008435

Miotello, A., Kelly, R., 1999. Laser-induced phase explosion: new physical problems when a condensed phase approaches the thermodynamic critical temperature. Appl. Phys. A Mater. Sci. Process. 69, S67–S73. doi:10.1007/s003399900296

Mittlefehldt, D.W., 2014. Achondrites, in: Treatise on Geochemistry. Volume 1: Meteorites, Comets, and Planets. Elsevier, pp. 235–266. doi:10.1016/B978-0-08-095975-7.00108-X

Mittlefehldt, D.W., McCoy, T.J., Goodrich, C.A., Kracher, A., 1998. Non-chondritic meteorites from asteroidal bodies, in: Papike, J.J. (Ed.), Reviews in Mineralogy. Vol 36: Planetary Materials. Mineralogical Society of America, pp. 4–01–4–195.

Motelica-Heino, M., Le Coustumer, P., Donard, O.F.X., 2001. Micro- and macro-scale investigation of fractionation and matrix effects in LA-ICP-MS at 1064 nm and 266 nm on glassy materials. J. Anal. At. Spectrom. 16, 542–550. doi:10.1039/B010154K

Moynier, F., Blichert-Toft, J., Telouk, P., Luck, J.-M., Albarède, F., 2007. Comparative stable isotope geochemistry of Ni, Cu, Zn, and Fe in chondrites and iron meteorites. Geochim. Cosmochim. Acta 71, 4365–4379. doi:10.1016/j.gca.2007.06.049

Možná, V., Pisonero, J., Holá, M., Kanický, V., Günther, D., 2006. Quantitative analysis of Fe-based samples using ultraviolet nanosecond and femtosecond laser ablation-ICP-MS. J. Anal. At. Spectrom. 21, 1194–1201. doi:10.1039/B606988F

Nehru, C.E., Prinz, M., Delaney, J.S., Dreibus, G., Palme, H., Spettel, B., Wänke, H., 1983. Brachina: A new type of meteorite, not a chassignite. J. Geophys. Res. 88, B237–B244. doi:10.1029/JB088iS01p0B237

Nehru, C.E., Prinz, M., Weisberg, M.K., Ebihara, M., Clayton, R.N., Mayeda, T.K., 1992. Brachinites: A New Primitive Achondrite Group. Meteoritics 27, 267.

Nehru, C.E., Prinz, M., Weisberg, M.K., Ebihara, M.E., Clayton, R.N., Mayeda, T.K., 1996. A New Brachinite and Petrogenesis of the Group, in: Lunar and Planetary Science XXVII. pp. 943–944.

Newman, K., Freedman, P.A., Williams, J., Belshaw, N.S., Halliday, A.N., 2009. High sensitivity skimmers and non-linear mass dependent fractionation in ICP-MS. J. Anal. At. Spectrom. 24, 742–751. doi:10.1039/b819065h

Niu, H., Houk, R.S., 1996. Fundamental aspects of ion extraction in inductively coupled plasma mass spectrometry. Spectrochim. Acta Part B At. Spectrosc. 51, 779–815. doi:10.1016/0584-8547(96)01506-6

Perez, D., Lewis, L.J., 2002. Ablation of solids under femtosecond laser pulses. Phys. Rev. Lett. 89, 255504–1–255504–4. doi:10.1103/PhysRevLett.89.255504

Pietruszka, A.J., Reznik, A.D., 2008. Identification of a matrix effect in the MC-ICP-MS due to sample purification using ion exchange resin: An isotopic case study of molybdenum. Int. J. Mass Spectrom. 270, 23–30. doi:10.1016/j.ijms.2007.11.001

Poitrasson, F., 2007. Does planetary differentiation really fractionate iron isotopes? Earth Planet. Sci. Lett. 256, 484–492. doi:10.1016/j.epsl.2007.01.039

Poitrasson, F., Levasseur, S., Teutsch, N., 2005. Significance of iron isotope mineral fractionation in pallasites and iron meteorites for the core–mantle differentiation of terrestrial planets. Earth Planet. Sci. Lett. 234, 151–164. doi:10.1016/j.epsl.2005.02.010

Polyakov, V.B., Mineev, S.D., 2000. The use of Mössbauer spectroscopy in stable isotope geochemistry. Geochim. Cosmochim. Acta 64, 849–865. doi:10.1016/S0016-7037(99)00329-4

Povarnitsyn, M.E., Itina, T.E., Sentis, M., Khishchenko, K. V., Levashov, P.R., 2007. Material decomposition mechanisms in femtosecond laser interactions with metals. Phys. Rev. B 75, 235414–1–235414–5. doi:10.1103/PhysRevB.75.235414

Quitté, G., Birck, J.-L., Allègre, C.J., 2005. Stony-iron meteorites: History of the metal phase according to tungsten isotopes. Geochim. Cosmochim. Acta 69, 1321–1332. doi:10.1016/j.gca.2004.07.035

Quitté, G., Meier, M., Latkoczy, C., Halliday, A., Gunther, D., 2006. Nickel isotopes in iron meteorites–nucleosynthetic anomalies in sulphides with no effects in metals and no trace of 60Fe. Earth Planet. Sci. Lett. 242, 16–25. doi:10.1016/j.epsl.2005.11.053

Rai, V.K., Jackson, T.L., Thiemens, M.H., 2005. Photochemical mass-independent sulfur isotopes in achondritic meteorites. Science 309, 1062–1065. doi:10.1126/science.1112954

Rehkämper, M., Schönbächler, M., Stirling, C.H., 2001. Multiple Collector ICP-MS: Introduction to Instrumentation, Measurement Techniques and Analytical Capabilities.

Geostand. Geoanalytical Res. 25, 23–40. doi:10.1111/j.1751-908X.2001.tb00785.x

Richter, F., Dauphas, N., Teng, F., 2009. Non-traditional fractionation of non-traditional isotopes: Evaporation, chemical diffusion and Soret diffusion. Chem. Geol. 258, 92–103. doi:10.1016/j.chemgeo.2008.06.011

Rua-Ibarz, A., Bolea-Fernandez, E., Vanhaecke, F., 2016. An in-depth evaluation of accuracy and precision in Hg isotopic analysis via pneumatic nebulization and cold vapor generation multi-collector ICP-mass spectrometry. Anal. Bioanal. Chem. 408, 417–29. doi:10.1007/s00216-015-9131-2

Rumble, D., Young, E.D., Shahar, A., Guo, W., 2011. Stable Isotope Cosmochemistry and the Evolution of Planetary Systems. Elements 7, 23–28. doi:10.2113/gselements.7.1.23

Russell, W.A., Papanastassiou, D.A., Tombrello, T.A., 1978. Ca isotope fractionation on the Earth and other solar system materials. Geochim. Cosmochim. Acta 42, 1075–1090. doi:10.1016/0016-7037(78)90105-9

Ruzicka, A., 2014. Silicate-bearing iron meteorites and their implications for the evolution of asteroidal parent bodies. Chemie der Erde - Geochemistry 74, 3–48. doi:10.1016/j.chemer.2013.10.001

Ruzicka, A., Boynton, W. V., Ganguly, J., 1994. Olivine coronas, metamorphism, and the thermal history of the Morristown and Emery mesosiderites. Geochim. Cosmochim. Acta 58, 2725–2741. doi:10.1016/0016-7037(94)90140-6

Schoenberg, R., Zink, S., Staubwasser, M., von Blanckenburg, F., 2008. The stable Cr isotope inventory of solid Earth reservoirs determined by double spike MC-ICP-MS. Chem. Geol. 249, 294–306. doi:10.1016/j.chemgeo.2008.01.009

Schwandt, C.S., Cygan, R.T., Westrich, H.R., 1998. Magnesium self-diffusion in orthoenstatite. Contrib. to Mineral. Petrol. 130, 390–396. doi:10.1007/s004100050373

Scott, E.R.D., 1977a. Geochemical relationships between some pallasites and iron meteorites. Mineral. Mag. 41, 265–272.

Scott, E.R.D., 1977b. Pallasites—metal composition, classification and relationships with iron meteorites. Geochim. Cosmochim. Acta 41, 349–360. doi:10.1016/0016-7037(77)90262-9

Scott, E.R.D., 1972. Chemical fractionation in iron meteorites and its interpretation. Geochim. Cosmochim. Acta 36, 1205–1236. doi:10.1016/0016-7037(72)90046-4

Scott, E.R.D., Krot, A.N., 2014. Chondrites and Their Components, in: Treatise on Geochemistry. Volume 1: Meteorites, Comets, and Planets. Elsevier, pp. 65–137. doi:10.1016/B978-0-08-095975-7.00104-2

Shahar, A., Young, E.D., 2007. Astrophysics of CAI formation as revealed by silicon isotope LA-MC-ICPMS of an igneous CAI. Earth Planet. Sci. Lett. 257, 497–510. doi:10.1016/j.epsl.2007.03.012

Sio, C.K.I., Dauphas, N., Teng., F.-Z., Chaussidon, M., Helz., R.T., Roskosz., M., 2013., Discerning crystal growth from diffusion profiles in zoned olivine by in situ Mg–Fe isotopic analyses., Geochim. Cosmochim. Acta 123., 302–231. doi:10.1016/j.gca.2013.06.008

Stewart, B.W., Papanastassiou, D.A., Wasserburg, G.J., 1994. Sm-Nd chronology and petrogenesis of mesosiderites. Geochim. Cosmochim. Acta 58, 3487–3509. doi:10.1016/0016-7037(94)90100-7

Surikov, V.T., Pupyshev, A.A., 2011. Input ion optics of inductively coupled plasma qadrupole mass spectrometers. Part I. Systems with cylinder symmetry and straight-line axis (In russian). Anlytika i Kontrol 15, 256–280.

Tanner, S.D., 1995. Characterization of ionization and matrix suppression in inductively coupled "cold" plasma mass spectrometry. J. Anal. At. Spectrom. 10, 905–921. doi:10.1039/ja9951000905

Tanner, S.D., Baranov, V.I., Bandura, D.R., 2002. Reaction cells and collision cells for ICP-MS: a tutorial review. Spectrochim. Acta Part B At. Spectrosc. 57, 1361–1452. doi:10.1016/S0584-8547(02)00069-1

Tomiyama, T., Huss, G.R., 2005. Minor element behavior of pallasite olivine: understandidng pallasite thermal history and chronology, in: 36th Lunar and Planetary Science Conference. p. 2071.

Trinquier, A., Elliott, T., Ulfbeck, D., Coath, C., Krot, A.N., Bizzarro, M., 2009. Origin of Nucleosynthetic Isotope Heterogeneity in the Solar Protoplanetary Disk. Science (80-.). 324, 374–376. doi:10.1126/science.1168221

Ulff-Moller, F., Tran, J., Choi, B.-G., Haag, R., Rubin, A.E., Wasson, J.T., 1997. Esquel: Implications for Pallasite Formation Processes Based on the Petrography of a Large Slab. 28th Lunar Planet. Sci. Conf. 1342.

Van Heghe, L., Engström, E., Rodushkin, I., Cloquet, C., Vanhaecke, F., 2012. Isotopic analysis of the metabolically relevant transition metals Cu, Fe and Zn in human blood from vegetarians and omnivores using multi-collector ICP-mass spectrometry. J. Anal. At. Spectrom. 27, 1327–1334. doi:10.1039/c2ja30070b

Van Hoecke, K., Belza, J., Croymans, T., Misra, S., Claeys, P., Vanhaecke, F., 2015. Single-step chromatographic isolation of lithium from whole-rock carbonate and clay for isotopic analysis with multi-collector ICP-mass spectrometry. J. Anal. At. Spectrom. 30, 2533–2540. doi:10.1039/C5JA00165J

Van Hoecke, K., Devulder, V., Claeys, P., Degryse, P., Vanhaecke, F., 2014. Comparison of microsublimation and ion exchange chromatography for boron isolation preceding its isotopic analysis via multi-collector ICP-MS. J. Anal. At. Spectrom. 29, 1819–1826. doi:10.1039/C4JA00111G

Vanhaecke, F., Degryse, P. (Eds.), 2012. Isotopic Analysis Fundamentals and Applications Using ICP-MS. WILEY-VCH Verlag GmbH & Co. KGaA, Weinheim, Germany.

Vanhaecke, F., Moens, L., 2004. Overcoming spectral overlap in isotopic analysis via single- and multi-collector ICP-mass spectrometry. Anal. Bioanal. Chem. 378, 232–240. doi:10.1007/s00216-003-2175-8

Vanhaecke, F., Moens, L., Dams, R., Papadakis, I., Taylor, P., 1997. Applicability of High-Resolution ICP−Mass Spectrometry for Isotope Ratio Measurements. Anal. Chem. 69, 268–273. doi:10.1021/ac960740j

Vanhaecke, F., Moens, L., Dams, R., Taylor, P., 1996. Precise Measurement of Isotope Ratios with a Double-Focusing

Magnetic Sector ICP Mass Spectrometer. Anal. Chem. 68, 567–569. doi:10.1021/ac9507247

Voshage, H., 1967. Cosmic-ray exposure ages and origin of iron meteorites, in: Radioactive Dating and Methods of Low-Level Counting. International atomic energy agency, Vienna, Monaco, pp. 281–298.

Voshage, H., Feldmann, H., 1979. Investigations on cosmic-ray-produced nuclides in iron meteorites, 3. Exposure ages, meteoroid sizes and sample depths determined by mass spectrometric analyses of potassium and rare gases. Earth Planet. Sci. Lett. 45, 293–308. doi:10.1016/0012-821X(79)90131-6

Walder, A.J., Freedman, P.A., 1992. Communication. Isotopic ratio measurement using a double focusing magnetic sector mass analyser with an inductively coupled plasma as an ion source. J. Anal. At. Spectrom. 7, 571–575. doi:10.1039/ja9920700571

Warren, P.H., Taylor, G.J., 2014. The Moon, in: Treatise on Geochemistry. Volume 2: Planets, Asteriods, Comets and The Solar System. Elsevier, pp. 213–250. doi:10.1016/B978-0-08-095975-7.00124-8

Wasson, J.T., 2016. Formation of the Treysa quintet and the main-group pallasites by impact-generated processes in the IIIAB asteroid. Meteorit. Planet. Sci. 51, 773–784. doi:10.1111/maps.12635

Wasson, J.T., Choi, B.-G., 2003. Main-group pallasites: Chemical composition, relationship to IIIAB irons, and origin. Geochim. Cosmochim. Acta 67, 3079–3096. doi:10.1016/S0016-7037(03)00306-5

Wasson, J.T., Rubin, A.E., 1985. Formation of mesosiderites by low-velocity impacts as a natural consequence of planet formation. Nature 318, 168–170.

Wasson, J.T., Schaudy, R., Bild, R.W., Chou, C.-L., 1974. Mesosiderites—I. Compositions of their metallic portions and possible relationship to other metal-rich meteorite groups. Geochim. Cosmochim. Acta 38, 135–149. doi:10.1016/0016-7037(74)90199-9

Watson, H.C., Richter, F., Liu., A., Huss., G.R., 2016. Iron and nickel isotope fractionation by diffusion, with applications to iron meteorites. Earth and Planetary Science Letters 451, 159–167. doi:10.1016/j.epsl.2016.06.030

Weyer, S., 2008. Geochemistry: What Drives Iron Isotope Fractionation in Magma? Science (80-.). 320, 1600–1601. doi:10.1126/science.1160204

Wieser, M., Laeter, J., 2007. Absolute isotopic composition of molybdenum and the solar abundances of the p-process nuclides Mo92,94. Phys. Rev. C 75, 055802–1–055802–8. doi:10.1103/PhysRevC.75.055802

Wombacher, F., Rehkamper, M., 2003. Investigation of the mass discrimination of multiple collector ICP-MS using neodymium isotopes and the generalised power law. J. Anal. At. Spectrom. 18, 1371–1375. doi:10.1039/b308403e

Wombacher, F., Rehkämper, M., Mezger, K., 2004. Determination of the mass-dependence of cadmium isotope fractionation during evaporation. Geochim. Cosmochim. Acta 68, 2349–2357. doi:10.1016/j.gca.2003.12.013

Woodhead, J., 2002. A simple method for obtaining highly accurate Pb isotope data by MC-ICP-MS. J. Anal. At. Spectrom. 17, 1381–1385. doi:10.1039/b205045e

Yang, J., Goldstein, J.I., Scott, E.R.D., 2010. Main-group pallasites: Thermal history, relationship to IIIAB irons, and origin. Geochim. Cosmochim. Acta 74, 4471–4492. doi:10.1016/j.gca.2010.04.016

Yang, J., Zhao, Y., Zhu, X., 2006. Transition between nonthermal and thermal ablation of metallic targets under the strike of high-fluence ultrashort laser pulses. Appl. Phys. Lett. 88, 094101–1–094101–3. doi:10.1063/1.2168513

Yang, L., 2009. Accurate and precise determination of isotopic ratios by MC-ICP-MS: a review. Mass Spectrom. Rev. 28, 990–1011. doi:10.1002/mas

Yang, L., Mester, Z., Zhou, L., Gao, S., Sturgeon, R.E., Meija, J., 2011. Observations of large mass-independent fractionation occurring in MC-ICPMS: implications for determination of accurate isotope amount ratios. Anal. Chem. 83, 8999–9004. doi:10.1021/ac201795v

Yokoyama, T., Walker, R.J., 2016. Nucleosynthetic Isotope Variations of Siderophile and Chalcophile Elements in the Solar System. Rev. Mineral. Geochemistry 81, 107–160. doi:10.2138/rmg.2016.81.03

York, D., 1966. Least-sqares fitting of a straight line. Can. J. Phys. 44, 1079–1086. doi:10.1139/p66-090

Young, E.D., Galy, A., Nagahara, H., 2002. Kinetic and equilibrium mass-dependent isotope fractionation laws in nature and their geochemical and cosmochemical significance. Geochim. Cosmochim. Acta 66, 1095–1104. doi:10.1016/S0016-7037(01)00832-8

Young, E.D., Manning, C.E., Schauble, E.A., Shahar, A., Macris, C.A., Lazar, C., Jordan, M., 2015. High-temperature equilibrium isotope fractionation of non-traditional stable isotopes: Experiments, theory, and applications. Chem. Geol. 395, 176–195. doi:10.1016/j.chemgeo.2014.12.013

Yurimoto, H., Kuramoto, K., 2004. Molecular Cloud Origin for the Oxygen Isotope Heterogeneity in the Solar System. Science (80-.). 305, 1763–1766. doi:10.1126/science.1100989

Zinner, E., 2003. Planetary science. An isotopic view of the early solar system. Science (80-.). 300, 265–267. doi:10.1126/science.1080300

Chapter 2

Evaluation of pneumatic nebulization and ns-laser ablation ICP-MS for bulk elemental analysis and 2-dimensional element mapping of iron meteorites

based on publication by
Stepan M. Chernonozhkin, Steven Goderis, Stephen Bauters, Bart Vekemans, Laszlo Vincze, Philippe Claeys and Frank Vanhaecke, 2014. Journal of Analytical Atomic Spectrometry, Vol. 29, Issue 6, P. 1001-1016

S.Ch. designed and carried out the experiments, processed the raw data, delivered and analysed the results, wrote the manuscript and took part in the discussion.

"The secret of getting ahead is getting started."

Mark Twain

1. Abstract

The capabilities and limitations of nanosecond laser ablation ICP – mass spectrometry for bulk and spatially resolved (elemental mapping) analysis of iron meteorites were assessed. The quantitative data obtained were compared to those obtained via multi-element solution ICP-MS (after digestion) relying on external calibration and high-accuracy determination of selected platinum group elements using solution ICP-MS after target element isolation using anion exchange chromatography and deploying isotope dilution. Results generated by the different methods described show good agreement. Significant matrix effects were observed to affect the results of the ns-LA-ICP-MS analysis of iron meteorites, making quantification via a matrix-matched standard a prerequisite. Careless use of intensity distribution maps without proper correction for laser-solid coupling efficiency can lead to incorrect interpretation of the element maps. ns-LA-ICP-MS was shown to be suitable for fast and quasi-nondestructive analysis of iron meteorites, not only homogeneous ataxites and hexahedrites, but also more heterogeneous ones, when considering ablated areas of a sufficient size. In the context of elemental mapping using LA-ICP-MS, Pearson's product-moment correlation analysis was demonstrated to be a powerful tool that can provide valuable information on the fractionation of the elements in the parent bodies of meteorites.

2. Introduction

The continuously improving sensitivity, precision and spatial resolution of modern analytical techniques, applied to a diversity of (extra-)terrestrial materials, constantly refine our view on the cosmochemical history of the early solar system and even lead to a deeper understanding of the processes taking place before its formation (MacPherson and Thiemens, 2011; Zinner et al., 2011).

Extraterrestrial materials are available from various sources, with meteorites being the most common, falling in great numbers on the surface of the Earth. Of these, iron meteorites are the most widespread, not only because of their resistance to weathering and a higher survival rate during atmospheric entry, but also because of the higher likelihood that these will be recognized as unusual objects. Iron meteorites fall into 14 major chemical groups (Goldstein et al., 2009), with chemical trends within most iron meteorite groups consistent with fractional crystallization, implying that each group formed from a single molten metallic pool or core. This is not the case for the silicate-bearing iron meteorite groups (IAB and IIE), with textures and poorly defined elemental trends that suggest that impact mixed molten metal and silicates and that neither group formed from a single isolated metallic melt (Goldstein et al., 2009). The chemical classification of iron meteorites is based on the contents of and ratios between particular elements, mainly Ga, Ge, As, Ir, Ni, and Au.

Bulk concentrations of several elements in iron meteorites are used to reveal the crystallization history of their parent bodies. Except for the elements mentioned above, together with a few others, such as Pt, Os, and Au, the pool of analytical data for particular elements in iron meteorites is rather small. Among the elements for which information is scarce, Ru, Rh, Pd and Pt are the most interesting. Nichiporuk and Brown (Nichiporuk and Brown, 1965) found that iron meteorites fall into 3 major groups with regard to their Ru-Rh concentrations, and these groups correlate with the Ga-Ge groups found by previous researchers. More detailed data on fractionation of Rh in iron meteorites were presented by Ryan et al.(Ryan et al., 1990). In both studies, Ru, Rh, Ir, and Pt were found to correlate positively with each other. Hoashi et al. (Hoashi et al., 1993) show that the combination of concentration data for several platinum group elements (PGEs) can provide a more powerful tool for taxonomic classification of iron meteorites than the more common approach with Ir alone. At the same time, Pd concentrations span a range of about one order of magnitude and show negative correlation with Ru, Rh, Ir, and Pt. Unlike the other PGEs, Pd correlates positively with Ni (Hoashi et al., 1993; Ryan et al., 1990). This exceptional fractionation behavior must result from the non-refractory nature of Pd (Palme, 2008).

ICP-mass spectrometry (ICP-MS) is the most sensitive technique for (ultra)trace elemental analysis. While in its standard configuration, an ICP-MS instrument is intended for analysis of aqueous solutions, use of laser ablation (LA) as a means of sample introduction permits the direct analysis of solid samples as well. In addition, laser ablation – ICP – mass spectrometry (LA-ICP-MS) gives access to the spatial distribution of elements inside the iron meteorites studied. Spatially resolved chemical analysis of extraterrestrial materials can give invaluable data on presolar grains, dust and refractory inclusions (Davis, 2011). Element diffusion profiles across the lamellae of iron meteorites provide information on the crystallization of molten metal and cooling rates of the meteorite parental bodies (Andrew J Campbell and Humayun, 1999). Together with Re, Mo and W, the PGEs (with exception of Pd) have condensation temperatures above that of Fe-Ni alloy, leading to the formation of refractory nuggets (fremdlinge) in chondritic material during nebula solidification (Palme, 2008). Spatially resolved determination of Re and Os also improves the understanding of their fractionation mechanisms between mineral phases, applicable to building potential isochrones basing on Os isotope ratio measurements of individual phases (Hirata and Nesbitt, 1997). Although there is a lot of data available on the bulk concentrations of several elements in iron meteorites, their lateral distribution remains largely unstudied. It is mostly because EPMA and SEM-EDX, the most commonly applied methods for such spatially resolved analysis, do not show sufficiently low limits of detection for these elements. Moreover, the analytical techniques mentioned above are scarcely used for two-dimensional element imaging, and are only applied for spot analysis or one-dimensional profiling. However, two-dimensional element imaging in combination with data correlation analysis is a promising tool to reveal the fractionation behavior of the elements inside the parent bodies of iron meteorites.

Next to elemental analysis, isotopic analysis of meteorites is an attractive tool to shed light onto history of early Solar System and astrophysical processes. Variation in the isotopic composition of particular elements can serve as a sensitive tracer of stellar nucleosynthesis and as a tracer of heterogeneity of the solar nebula (MacPherson and Boss, 2011; Yin et al., 2002; Zinner, 2003). Isotopic analysis can yield chronological constrains on the formation of the first objects in the Solar System, when applied to several short- and long-lived isotopic decay systems in extraterrestrial material (Amelin and Ireland, 2013; Lee and Halliday, 1995; Palme, 2008; Smoliar et al., 1996; Woodland et al., 2005). Although the capabilities of LA-ICP-MS for direct isotopic analysis are compromised by the co-presence of elements causing spectral interference, LA systems have been coupled to multi-collector-ICP-MS and used for high precision isotopic analysis of Mg, Si and Fe in meteorites (Horn et al., 2006; Young et al., 2005). Importantly, LA-ICP-MS can provide fast and quasi-nondestructive analysis of iron meteorites for their elemental composition, an essential first stage for the subsequent investigation of isotopic systems of interest.

In view of the above, further assessment of the capabilities of LA-ICP-MS, a technique for high-resolution spatially resolved analysis with a potential of chemical and isotopic analysis, will likely contribute to our understanding of the solar system formation. Previous works have focused on the comparison of the precision, accuracy and consistency of ns-LA-ICP-MS data for iron meteorites with data obtained via instrumental neutron activation analysis (INAA) and isotope dilution mass spectrometry (IDMS) (Andrew J Campbell and Humayun, 1999; Petaev and Jacobsen, 2004). In this work, we compare the LA-ICP-MS approach with other ICP-MS based techniques: pneumatic nebulization (PN) ICP-MS, discussed in detail by Folco et al. (D'Orazio and Folco, 2003), and ID-PN-ICP-MS in combination with target element isolation using anion exchange chromatography. Special attention is paid to element mapping with LA-ICP-MS, widely used in geological applications to build element distribution maps (Ulrich et al., 2009). Matrix effects, appearing due to interaction of the nanosecond laser pulse with iron phases showing different properties and their possible effect on the element distribution maps are also discussed.

3. Experimental

3.1. Reagents, certified reference materials (CRMs) and samples. Only high-purity reagents and acids were used throughout the experiments. Pro analysis grade nitric (65%, Chem-Lab, Belgium) and hydrochloric (37%, Chem-Lab, Belgium) acids were additionally purified by sub-boiling in a PFA and quartz apparatus, respectively. Water was purified (18.2 MΩ·cm) in a Direct-Q 3 water purification system (Millipore, France).

The 1000 $\mu g \cdot ml^{-1}$ single-element stock solutions used for external calibration originated from Merck (Darmstadt, Germany), PlasmaCAL (Quebec, Canada), Inorganic ventures (Virginia, USA) and Alfa Aesar GmbH (Karlsruhe, Germany). High purity Pt and Pd standards of natural isotopic composition, used for reverse ID-ICP-MS determination of the spike concentrations, were NBS 680 Pt (National Institute of Standards and Technology, Maryland, USA) and 99.9+%, Pd (Aldrich Chem Co) metals. Isotopically enriched Ru, Pd, Ir and Pt powdered metals were obtained from Oak Ridge National Laboratory (Tennessee, USA). Isotopic abundances are 97.70%, 98.86%, 99.59%, and 91.46% for ^{101}Ru, ^{108}Pd, ^{193}Ir and ^{194}Pt, respectively (Compernolle et al., 2012). Certified reference materials used for LA-ICP-MS are listed in details in the appendix (see electronic supplementary information).

Seven iron meteorite specimens (4 from Russia, 1 from Kazakhstan, 1 from Australia, and 1 from the USA) were obtained from different sources (see table 2-1). For two of these (Sikhote-Alin and Canyon-Diablo), the

Name	Type	Place found	Origin
Chinga	IVB-an	Tyva Republic, Russia	CSGM IGM SB RAS^1
Sikhote-Alin	IIB	Primorsky Krai, Russia	CSGM IGM SB RAS^1
Cheder	IID	Tyva Republic, Russia	CSGM IGM SB RAS^1
Elga	IIE	Sakha (Yakutia) Republic, Russia	CSGM IGM SB RAS^1
Darinskoe	IIC	Uralsk, Kazakhstan	CSGM IGM SB RAS^1
Canyon-Diablo	IAB-MG	Arizona, USA	Specimen 1: RBINS^2 Specimen 2: Ordered from meteorite market (Alaska, USA)
Miles	IIE	Queensland, Australia	RBINS^2

Table 2-1. List of the iron meteorites studied. ^{1} - CSGM IGM SB RAS stands for Central Siberian Geological Museum, V.S. Sobolev Institute of Geology and Mineralogy Siberian Branch of Russian Academy of Sciences, Novosibirsk, Russia. ^{2} - RBINS stands for Royal Belgian Institute of Natural Sciences.

concentrations of several elements of interest have been published earlier, providing reference data for the validation of our results. The other meteorites have not been studied in detail via modern analytical methods.

3.2. Determination of the relative sensitivity factors in iron-matrix. CRMs Steel CRMs were polished with silicon carbide sandpaper (P4000 grit size, i.e. 2.5 μm median particle diameter). A New Wave Research UP193HE ArF* excimer-based LA-system (New Wave Research, CA, USA) coupled to a quadrupole-based XSeries II ICP-mass spectrometer (Thermo Fisher Scientific, Germany) was used to measure the signal intensities of the elements contained in the iron and glass CRMs selected (see appendix for instrument settings used). Pre-ablation was always applied to avoid possible contamination (400 μm beam diameter, 20 μm·s^{-1} lateral scanning speed, 5 J·cm^{-2} energy fluence). Relative sensitivity factors (RSFs) of the elements were calculated relative to Cu according to the equation:

$$RSF_x = \frac{I_x \cdot C_{Cu}}{C_x \cdot I_{Cu}} \cdot \frac{A_{Cu}}{A_x} \qquad (2-1)$$

where I_x, I_{Cu} are the intensities for the nuclide of interest and for ^{63}Cu, C_x and C_{Cu} are the concentrations of the element of interest and of Cu in the CRM, and A_x and A_{Cu} are the relative isotopic abundances of the nuclide measured and of ^{63}Cu, respectively.

3.3. Bulk LA-ICP-MS. Thick sections of the iron meteorites were polished with silicon carbide sandpaper (grit size P4000) and lightly etched in a 4% v/v nital (HNO3 in ethanol) solution to reveal the widmanstätten pattern. A New Wave Research UP-213 Nd:YAG LA-system coupled to a Thermo Scientific ELEMENT 2 sector field ICP-mass spectrometer was used for direct analysis of solid meteorites without digestion. Instrument settings of the ICP-MS and LA-units are summarized in table 2-2. Laser ablation was performed in line-scan mode with each line 1.8 mm long and 100 μm wide. A total of three lines were ablated on each sample and at least 5 lines on external standards.

		Bulk LA-ICP-MS	Mapping LA-ICP-MS	PN-ICP-MS
Element 2 ICP-MS unit				
Plasma power		850 W	850 W	1200 W
Sample introduction		LA	LA	Quartz cyclonic spray chamber and Micromist concentric nebulizer, 350 μl·min^{-1} uptake
Sampler Cone		Ni; 1.1 mm aperture diameter		
Skimmer cone		Ni; H-type; 0.8 mm aperture diameter		
Argon gas	Cool	16.00 L·min^{-1}	16.00 L·min^{-1}	16.00 L·min^{-1}
flow rates	Auxiliary	1.20 L·min^{-1}	1.20 L·min^{-1}	1.20 L·min^{-1}
	Carrier	1.573 L·min^{-1}	1.573 L·min^{-1}	0.930 L·min^{-1}
Resolution		Low, Medium (M/ΔM=300, 4000)	Low (M/ΔM=300)	Medium, High (M/ΔM=4000, 10000)
Nuclides monitored		Low resolution: ^{51}V, ^{52}Cr, ^{55}Mn, ^{59}Co, ^{60}Ni, ^{63}Cu, ^{66}Zn, ^{69}Ga, ^{74}Ge, ^{75}As, ^{90}Zr, ^{95}Mo, ^{99,101}Ru, ^{103}Rh, ^{105}Pd, ^{115}In, ^{118}Sn, ^{121}Sb, ^{178}Hf, ^{182}W, ^{185}Re, ^{190}Os, ^{193}Ir, ^{195}Pt, ^{197}Au, ^{208}Pb. Medium resolution: ^{74}Ge, ^{75}As, ^{95}Mo, ^{99}Ru, ^{101}Ru, ^{103}Rh.	Low resolution: ^{57}Fe, ^{59}Co, ^{60}Ni, ^{69}Ga, ^{74}Ge, ^{95}Mo, ^{99,101}Ru, ^{103}Rh, ^{105}Pd, ^{182}W, ^{185}Re, ^{190}Os, ^{193}Ir, ^{195}Pt, ^{197}Au.	Medium resolution: ^{51}V, ^{52}Cr, ^{55}Mn, ^{59}Co, ^{60}Ni, ^{63}Cu, ^{66}Zn, ^{69}Ga, ^{74}Ge, ^{75}As, ^{85}Rb, ^{90}Zr, ^{95}Mo, ^{99,101}Ru, ^{103}Rh, ^{105}Pd, ^{115}In, ^{128}Sn, ^{121}Sb, ^{178}Hf, ^{182}W, ^{185}Re, ^{190}Os, ^{193}Ir, ^{195}Pt, ^{197}Au, ^{208}Pb, ^{209}Bi. High resolution: ^{75}As, ^{85}Rb, ^{209}Bi.
Runs and passes		50 x 1	175 x 1 (adjusted to the time interval in which a 2800 μm line is ablated)	9 x 3
Samples per peak		10	10	20
Time per pass		2.573 (LR) +1.472 (MR) s	2.014 s	8.613 (MR) +1.307 (HR) s
New Wave Research UP-213 LA-system				
Laser wavelength		213 nm	213 nm	-
Laser pulse duration		3-5 ns	3-5 ns	-
Laser beam diameter		100 μm	40 μm	-
Laser fluence		7-8 J·cm^{-2}	7-8 J·cm^{-2}	-
Translation speed		10 μm·s^{-1}	10 μm·s^{-1}	-
Total area ablated		0.54 mm^2	7.84 mm^2	-

Table 2-2. ICP-MS and LA instrument settings used for ICP-MS analyses of iron meteorites.

Pre-ablation was always applied to avoid the effect of possible surface contamination (150 µm beam diameter, 20 µm·s-1 translation speed, 5 J·cm-2 fluence).

The well-characterized Canyon Diablo IAB iron meteorite and NBS1286 low-alloy steel CRM from NIST were used for external calibration. The data set of concentrations determined for Canyon Diablo is compiled in an appendix. The compositional homogeneity and distribution of elements within this meteorite was discussed by Wasson et al. (Wasson and Ouyang, 1990). ^{60}Ni was used as internal standard, and previously reported Ni concentrations in the iron meteorites studied were relied upon.

3.4. LA-ICP-MS element mapping. A thick section of the IIC Darinskoe iron meteorite was chosen for elemental mapping because of a complex PGE distribution and relatively high content of the elements of interest. Just before the measurement, the surface was polished with silicon carbide sandpaper (grit size P4000) and etched with 4% v/v nital solution. A New Wave Research UP-213 Nd:YAG LA-system was coupled to a Thermo Scientific ELEMENT 2 sector field ICP-mass spectrometer for elemental mapping, using the instrument settings summarized in table 2-2.

The Cheder IID iron meteorite was used as external standard for LA-ICP-MS mapping, because of its fairly high content of PGEs, similar to that in Darinskoe. The concentration values used for calibration were taken from Agafonov et al. (Agafonov et al., 2011) In total, 72 straight lines were ablated one next to the other without space in-between to form a rectangular surface area of 2800 x 2880 µm. ICP-MS signal monitoring was triggered by the LA-system and the results thus obtained were used to construct intensity and concentration maps.

3.5. Pneumatic nebulization ICP-MS. The protocol was based on that described in Folco et al. (D'Orazio and Folco, 2003) Iron meteorite fragments were cut off the bulk mass with a diamond disk saw. To avoid the effect of surface contamination, visibly altered (*i.e.* oxidized) surfaces were cleaned with silicon carbide sandpaper, subsequently etched in dilute HNO_3 in an ultrasonic bath and finally rinsed with ethanol. Fragments of about 100 mg were accurately weighed and transferred into 15 ml Savillex™ Teflon beakers and digested in 4 ml of freshly prepared aqua regia (HNO_3:HCl 1:3). For that purpose, the closed vessels were heated at 90˚C during 72 hours. The resulting digests were diluted to 50 ml with Milli-Q water, followed by an additional 500-fold dilution for Cr, Co, Ni, Cu, and a 4-fold dilution for all of the other elements in 0.4 M HCl – 0.2 M HNO_3. The final solutions were introduced into a Thermo Scientific ELEMENT 2 sector field ICP-mass spectrometer via nebulization. Instrument settings are summarized in table 2-2. Medium mass-resolution (M/ΔM=4000) was used to resolve potential spectral interferences. Arsenic (As) was measured interference-free in high mass-resolution mode (M/ΔM=10000). Quantification was performed relying on external calibration, using synthetic mixtures of single-element stock solutions diluted to concentration levels similar to those in the samples. To correct for matrix effects, instrument drift and signal instability V, Rb and Bi were used as internal standards.

3.6. ID-PN-ICP-MS determination of PGEs. Isotopically enriched Pd and Pt metal standards of approximately 5 mg were accurately weighed and dissolved in 4 ml of freshly prepared aqua regia in 15 ml Savillex™ Teflon beakers, heated at 140˚C for 72 hours. After cooling down, the beakers were opened and the solutions were evaporated to incipient dryness and the residue redissolved in 0.4 ml of concentrated HCl. This was repeated twice. Finally, the residues were re-dissolved in 10 ml of 50% HCl. The Ru and Ir metal spikes were fused with Na_2O_2/NaOH in Al_2O_3 crucibles using a Bunsen torch, and the resulting melts were dissolved in 30% HCl.

Iron meteorite fragments were cut off a bulk mass and cleaned in the same way as those prepared for PN-ICP-MS. The chips were accurately weighed into 15 ml Savillex™ Teflon beakers and appropriate amounts (0.1-0.5ml) of dilute Ru, Pd, Ir, Pt spike solutions were added gravimetrically. This was followed by digestion with 4 ml of aqua regia at 140 ^{o}C for 48 hours. The solutions were evaporated to near-dryness, re-dissolved in 2 ml of concentrated HCl and evaporated to dryness again. This procedure was repeated twice. Finally, all sample residues were re-dissolved in 10 ml of 0.5 M HCl. Air buoyancy corrections, negligible for standard ICP-MS measurements, were applied for all weighing and dilution steps prior to ID-PN-ICP-MS.

3.7. Column anion-exchange isolation of PGEs, Au and Re. 10 ml polypropylene columns (Eichrom) were packed with 1.5 ml of Eichrom AG 1X-8 anion exchange resin (mesh size 100-200). The resin was washed with 10 ml of Milli-Q water, 10 ml of 4 M HNO_3 and 10 ml of 6 M HCl and subsequently equilibrated with 10 ml of 0.5 M HCl. All 10 ml of sample was loaded onto the column and the matrix was eluted off with 10 ml of 0.5 M HCl and 10 ml of 0.8 M HNO_3. Subsequently, the PGE, Re and Au were collected using 50 ml of hot (90 ˚C) concentrated HNO_3.

Plasma power		1200 W
Sample introduction		Quartz cyclonic spray chamber and Micromist concentric nebulizer, 350 μl·min^{-1}
Sampler cone		Ni; 1.1 mm aperture diameter
Skimmer cone		Ni; H-type; 0.8 mm aperture diameter
Argon gas flow rates	Cool	15,00 L·min^{-1}
	Auxiliary	0.75 L·min^{-1}
	Nebulizer	0.924 L·min^{-1}
Resolution		Low (M/ΔM=300)
Nuclides monitored		^{99,101}Ru, ^{105,108}Pd, ^{191,193}Ir, ^{194,195}Pt
Detection mode		Triple
Scan type		E-scan
Samples per peak		30
Settling time		0.001 s
Runs and passes		15 x 15
Segment duration		0.180 s

Table 2-3. Instrument settings of the ELEMENT XR ICP-MS unit used for ID-PN-MS analysis of iron meteorites.

Solutions were evaporated to dryness, 0.4 ml of fresh aqua regia was added and the closed vessels were heated at 140˚C for 24 hours and subsequently opened and the digest evaporated to dryness. This procedure was repeated twice to destroy organic material originating from anion-exchange resin decomposition. Finally, the residues were dissolved in 0.6 M HNO_3 – 0.1 M HCl prior to the measurement.

3.8. Isotope ratio measurement for ID-PN-ICP-MS. Ru, Pd, Ir and Pt isotope ratios were measured using a Thermo Scientific ELEMENT XR ICP-mass spectrometer in the standards with a natural isotopic composition, the isotopic spike solutions and meteorite material equilibrated with the PGE isotopic spikes after chromatographic isolation. The instrument settings used for this purpose are summarized in table2-3.

For isotope dilution analysis, the Element XR ICP-MS unit was optimized for fast mass-scanning and high precision of intensity ratios. The shorter the time gap between two isotopes measured, the higher the precision of the resulting ratio. Separate methods for all 4 elements were created to avoid the use of B-scanning and reduce the time gap mentioned above. Narrow mass windows and settling times were used. Low resolution was preferred because of the flat-topped appearance of the peaks and the corresponding higher isotope ratio precision (Vanhaecke et al., 1996). The measurement time consisted of 1 min 22 s for each element. The counting detection mode is preferable in this context, because it does not introduce a detector cross-calibration error to the ratios, but in this case care must be taken to fit the intensity into the maximum range. Therefore, triple detection mode was chosen to protect the detector, but all the concentrations were adjusted to be in the range of counting detection mode ($< 3 \cdot 10^6$ counts·s^{-1}). Isotope abundance ratios ^{99}Ru/^{101}Ru, ^{105}Pd/^{108}Pd, ^{191}Ir/^{193}Ir and ^{194}Pt/^{195}Pt were used in the calculations. The concentrations of Ru, Pd, Ir and Pt in the meteorites were calculated according to the equation (Hann et al., 2001):

$$C_s = C_{tr} \cdot \frac{m_{tr}}{m_s} \cdot \frac{(R_{tr} - R_{bl})}{(R_{bl} - R_s)} \cdot \frac{f_{tr}}{f_s} \tag{2 – 2}$$

where C_s is the concentration of the element in the sample. C_{tr} is the concentration of the isotopically enriched solution, accurately determined by reverse ID-MS. These reverse ID-MS experiments relied on the use of PGE standard solutions prepared gravimetrically from high-purity metals. m_{tr} and m_s are the masses of the isotopically enriched solution and sample solution, respectively. R_{tr}, R_{bl} and R_s are the isotope ratios measured in the isotopically enriched spike solution, the sample-spike mixture and a standard with natural isotopic composition, respectively. f_{tr} and f_s are the isotopic abundances of the enriched isotope in the spike and in nature, respectively. f_{tr} values were taken from Vanhaecke et al. (Compernolle et al., 2012), where the same enriched materials were used. Extraterrestrial Ru, Pd, Ir and Pt were assumed to show a natural isotopic composition (Carlson et al., 2008), and diluted standard solutions of natural isotopic composition were used instead of non-spiked sample to save precious meteorite material. Mass bias correction was not applied as all ratios are measured under identical experimental conditions and thus, instrumental mass discrimination is automatically corrected for (G. Heumann et al., 1998).

4. Results and discussion

4.1. ns-LA-ICP-MS matrix effects. Next to sample heterogeneity, spectral interferences, lack of proper reference materials, also matrix effects are known to affect the quantitative results obtained via ns-LA-ICP-MS. The differences in physical properties of materials lead to different characteristics of laser-solid interaction and aerosol formation (Bleiner and Bogaerts, 2006; Holá et al., 2010). As a result, material transport from the solid sample to the detector of the mass spectrometer can be non-stoichiometric, resulting in a change of the relative sensitivity factors (RSFs) from one type of matrix to another (Možná et al., 2006).

A first conclusion based on the RSFs obtained (figure 2-1) is that the widely used glass CRMs are not suited as external standards in the analysis of iron materials. The absolute sensitivity observed for glass materials is almost two orders of magnitude higher than that for a metal matrix, and, even more important, the RSFs determined for glass CRMs are significantly different from those for CRMs with an iron matrix (figure 2-1 B). This means that matrix-matched calibration is a prerequisite.

Four certified reference materials with different iron matrices were analyzed using identical instrument settings; the corresponding results are shown in figure 2-1. Even among iron materials, substantial differences in ablation efficiency were observed: the differences in the absolute sensitivities (figure 2-1 A) are significantly larger than the associated analytical uncertainty. At the same time, normalization of absolute sensitivities to the sensitivity of an element with known concentration provides RSFs for different iron CRMs, which are identical within statistical error (figure 2-1 B). This implies that internal normalization is crucial in the case of analysis of iron materials with ns-LA-ICP-MS.

In the same manner, the different metal phases within an iron meteorite, distributed heterogeneously inside most meteorite fragments, also have different ablation efficiencies. Figure 2-2 shows the intensity distribution map in the thin section of the Darinskoe IIC iron meteorite. Fe and Ni are seemingly enriched in the same spots of the intensity map. As these two elements compose the matrix of the meteorite, the combined increase of both Fe and Ni can only be explained by a change of the ablation efficiency from one metal phase to another, and this effect should be corrected for by internal standard normalization.

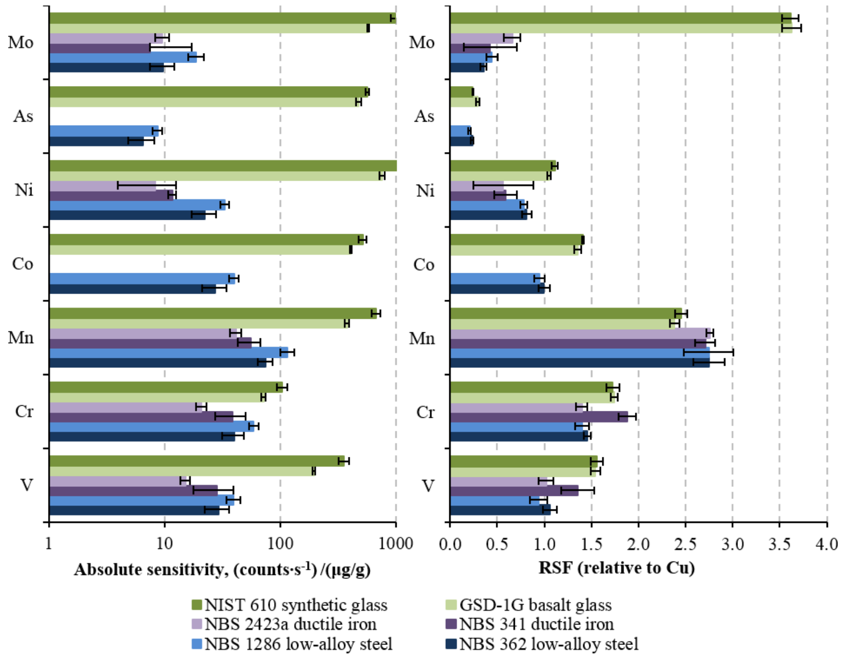

Figure 2-1. Matrix effects in LA-ICP-MS analysis of iron and glass matrix.

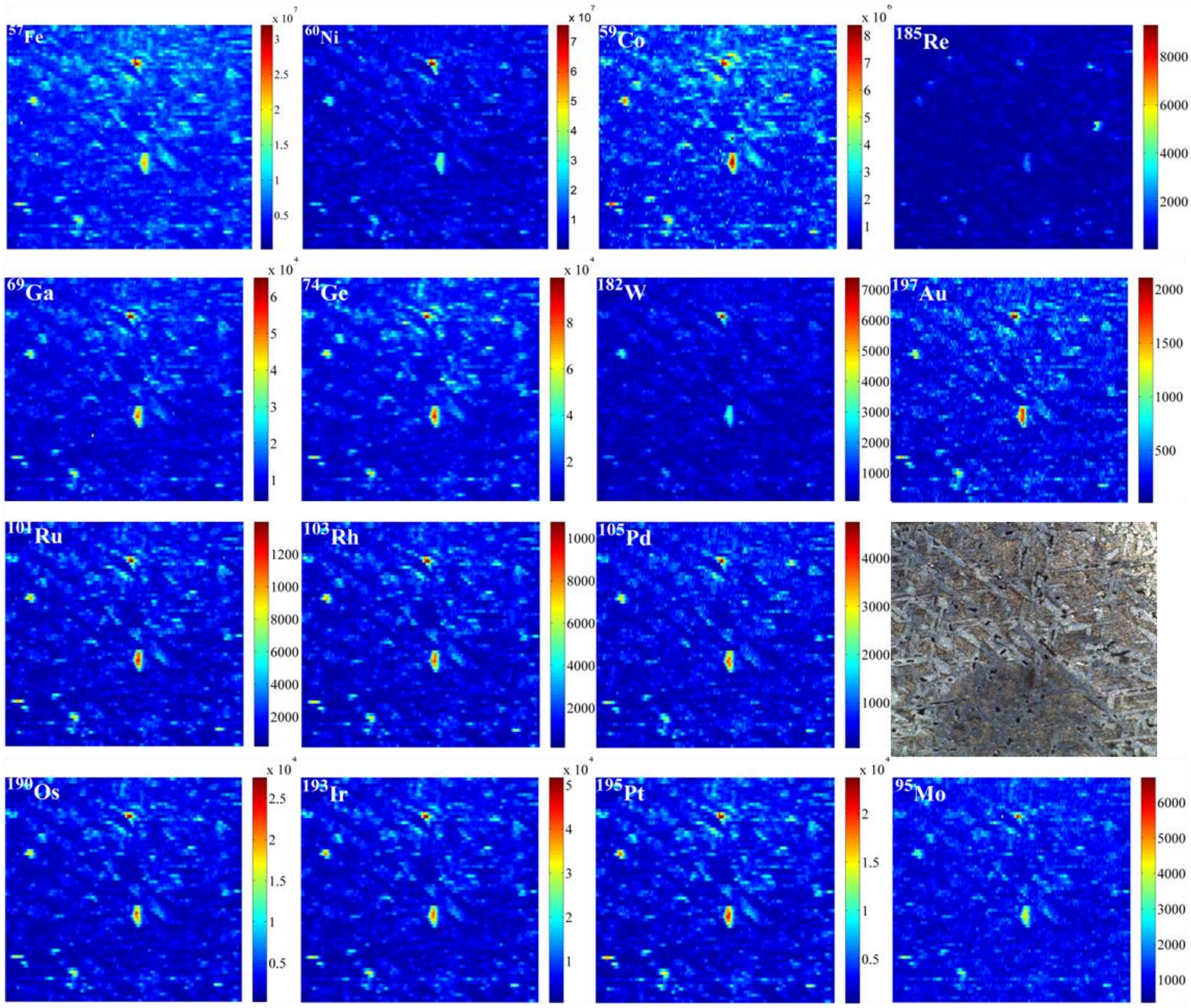

Figure 2-2. Intensity distribution maps for 15 elements in a thick section of Darinskoe IIC iron meteorite, counts per second. Each map is composed of 72 lines of 40 μm width. The width of the image is 2800 μm.

4.2. Quantification of ns-LA-ICP-MS data. For bulk LA-ICP-MS analysis, sufficiently large total areas are ablated, the Ni intensities were averaged and used as internal standard, and Ni concentration values were taken from literature. This internal standardization procedure was found sufficiently accurate and was relied upon for bulk LA-ICP-MS analysis. Alternately, one can also deploy an independent analytical method (e.g., EPMA, SEM-EDX, XRF) to determine the concentration of one of the matrix elements (Co or Ni), and apply this as internal standard (Andrew J Campbell and Humayun, 1999; Petaev and Jacobsen, 2004). The principal challenge of internal standardization for the element mapping is that none of the iron meteorites contains a homogeneously distributed element that could serve as an internal standard. Therefore, for spatially resolved LA-ICP-MS analysis, the following well-known approach (Campbell et al., 2002, 2001; Wiltsche and Günther, 2011) was used: Fe and Ni were considered to contribute 100% of the matrix and thus, the sum of their intensities was used as a virtual evenly distributed internal standard.

Unfortunately, there are no CRMs of matrix-matched composition with the elements of interest certified at a concentration level close to that of iron meteorites. Previous studies (Mullane et al., 2004) have used doped NiS beads as external standards for quantification in iron meteorite analysis, relying on the fact that NiS and FeNi matrices should have similar physical properties. Elements like Co, Ni, Mo and W can be quantified straightforwardly by application of different steel CRMs, but the only approach to quantify PGEs, Ga, Ge, etc. is to use an iron meteorite with well-known analyte concentrations. The meteorite, used as external standard is required

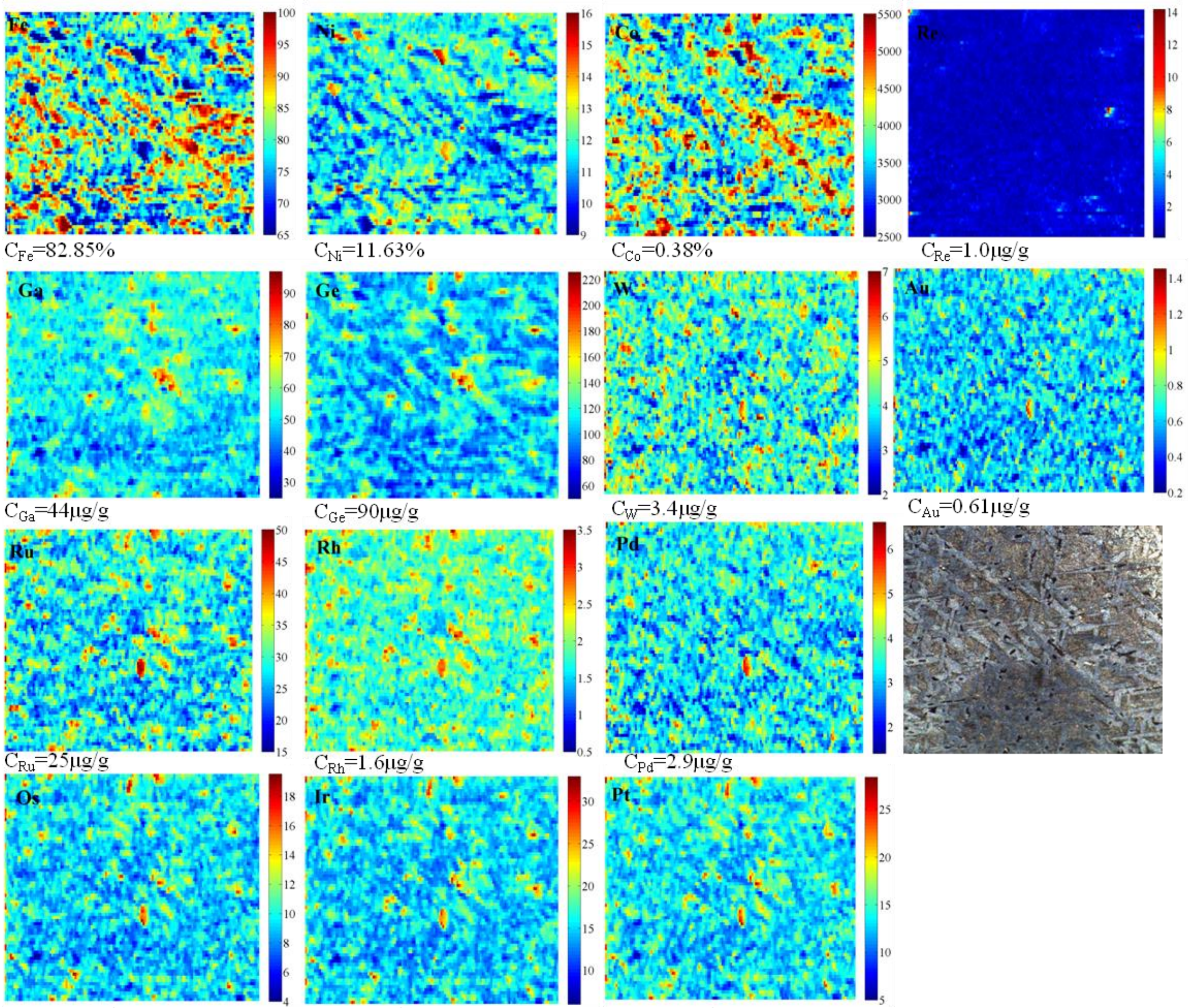

C_{Fe}=82.85% C_{Ni}=11.63% C_{Co}=0.38% C_{Re}=1.0µg/g

C_{Ga}=44µg/g C_{Ge}=90µg/g C_{W}=3.4µg/g C_{Au}=0.61µg/g

C_{Ru}=25µg/g C_{Rh}=1.6µg/g C_{Pd}=2.9µg/g

C_{Os}=9.4µg/g C_{Ir}=13µg/g C_{Pt}=14µg/g

Figure 2-3. Concentration distribution maps for 14 elements in a thick section of Darinskoe IIC iron meteorite, Fe, Ni – weight %, other elements –µg/g. The deviation from 100% stems from calculation of the concentration relative to external standard. The Mo distribution is not shown because of its low occurrence in the external standard. The width of the image is 2800 µm.

to have significant concentrations of the elements of interest, which need to be homogeneously distributed, and, even more importantly, the concentrations of these analytes need to be well-known. As such an external standard does not have certified values, an accurate survey of literature data becomes necessary. Campbell et al. (Campbell et al., 2002, 2001; A. J. Campbell and Humayun, 1999; Andrew J Campbell and Humayun, 1999) and Petaev et al. (Petaev and Jacobsen, 2004) applied IVB Hoba and IIA Filomena iron meteorites and a set of NIST steel CRMs (1158, 1263) as external standards. Hoba has a relatively high content of PGEs (4.86-42.48 µg/g), while Filomena is a hexahedrite with a homogeneous element distribution. In the present work, we have selected the IAB Canyon-Diablo iron meteorite as an external standard as it is one of the best-studied iron meteorites and is widely available.

4.3. LA-ICP-MS element mapping. The maps presenting the distribution of elements over the thick section of Darinskoe IIC iron meteorite are shown in figure 2-3. Trends of the Fe, Ni concentration coincide with the Widmanstätten pattern, visible in the reflected light image. Based on the spatially resolved quantitative data generated for the Darinskoe IIC iron meteorite, a matrix of Pearson's product-moment correlation coefficients was calculated (table 2-4). This correlation matrix provides information on the general trends that exist between the elements within space-distributed data. The closer the element-element correlation coefficient is to ±1, the higher the linear correlation between the pair of elements considered, while a value of 0 means absence of correlation. The calculated coefficients are not very high, only coefficients for Os, Ir and Pt are higher than 0.8. We treated the

	Ni	Ir	Fe	Co	Ga	Ge	Ru	Rh	Pd	Os	Pt	Au	Re	W
Ni	1													
Ir	-0.17	1												
Fe	-1.00	0.17	1											
Co	**-0.52**	0.30	**0.52**	1										
Ga	-0.28	**0.50**	0.28	0.36	1									
Ge	**-0.50**	**0.62**	**0.50**	**0.55**	**0.63**	1								
Ru	0.05	**0.65**	-0.05	0.15	0.38	0.38	1							
Rh	-0.05	**0.69**	0.05	0.20	**0.41**	**0.45**	**0.62**	1						
Pd	0.13	0.34	-0.13	-0.04	0.17	0.06	0.36	0.33	1					
Os	-0.15	**0.82**	0.15	0.27	**0.48**	**0.55**	**0.61**	**0.65**	0.37	1				
Pt	-0.16	**0.86**	0.16	0.28	**0.47**	**0.55**	**0.63**	**0.67**	0.36	**0.80**	1			
Au	-0.09	**0.42**	0.09	0.12	0.26	0.25	0.29	0.32	0.27	**0.42**	**0.44**	1		
Re	-0.09	0.35	0.09	0.12	0.17	0.24	0.23	0.28	0.15	0.34	0.34	0.16	1	
W	-0.12	**0.47**	0.12	0.14	0.29	0.29	0.32	0.38	0.24	**0.45**	**0.46**	0.30	0.22	1

Table 2-4. Matrix of Pearson's product-moment correlation coefficients calculated from the LA-ICP-MS spatially resolved quantitative data for the Darinskoe IIC iron meteorite.

coefficients higher than 0.4 or lower than -0.4 as positive or negative correlation, respectively. For example, Ni-Fe show strict negative correlation as a result of our normalization procedure, that use a "Fe+Ni = 100%" approach.

Ni correlates negatively with Co and Ge, indicating that Co and Ge became concentrated in Fe-rich kamacite lamellas during the cool-down of the Darinskoe IIC meteorite body. Interestingly, W, another refractory element, doesn't correlate neither with Ni nor with Fe, and seems to correlate positively only with the heavy PGEs (HPGEs: Ir, Os and Pt).

Five of the six PGEs (Ru, Rh, Os, Ir, Pt) show a positive correlation with each other. Among them, the HPGEs seem to show a stronger correlation to each other than to the light PGEs (LPGEs: Ru, Rh, Pd). This indicates that PGEs have the same trend of fractionation during cool-down of the meteorite parent body, while the degree of fractionation is slightly different for light and heavy PGEs. Also, analysis shows that PGEs are not found to concentrate in kamacite or taenite lamellas, but correlate positively with Ga and Ge. Interestingly, one of the LPGEs – Pd – does not show any correlation with any of the elements. It can be a demonstration of its different fractionation behavior, but it can also be caused by the fact that the levels of Pd are closer to its detection limit than for the other PGEs, and hence, the Pd data suffer more from noise.

Two refractory elements – the lithophile W and the siderophile Au – both show only weak positive correlation (0.42-0.47) to HPGEs, which means that they tend to concentrate together with them spatially inside the meteorite.

Re is dispersed over the meteorite matrix and does not correlate with any other element. An inclusion of about 50 µm that is enriched in Re (5-10 µg/g) and PGE can clearly be recognized in the middle right of the image. Such Re-containing nuggets can strongly influence the ^{187}Os/^{188}Os ratio, as ^{187}Os is produced by radioactive decay of ^{187}Re. Thus, the Re-Os chronometry results can discord with those based on the Pt-Os system (involving ^{186}Os/^{188}Os isotope ratio determination) as – in contrast to Re – Pt and Os are fairly homogeneously distributed.

Comparison of the concentration range in the element maps for Darinskoe IIC (figure 2-3) with the ranges characteristic for the IIC group meteorites demonstrate agreement (see figure 2-4). The only significant exception is Ru, the range of which seems to be too high for IIC group (Hoashi et al., 1993). Possibly, the Ru result can show bias because the reference value for the external standard Cheder IID is not very well characterized.

4.4. Comparison of mapping LA-ICP-MS with micro-XRF. Mapping of the Darinskoe meteorite section was also done with a home-built micro-XRF spectrometer over an area of 2700 x 2775 µm^2 by measuring 37 x 112 points. Each point was measured for 50 s with an estimated photon flux of 1.2·10^7 photons per second, applying 0.400 mA and 40 kV tube settings. The micro-XRF setup was based on a XOS DCC-X-Beam Mo anode source coupled with doubly curved crystal (DCC) optics providing a 150 x 50 µm^2 monochromatic x-ray beam (compare with 40 µm beam diameter in LA-ICP-MS). Quantitative elemental information was obtained from the acquired XRF spectra through Monte Carlo simulations by the iterative process of simulating the experiment (Schoonjans et al., 2013, 2012). Reference experimental parameters needed for modeling were acquired by measuring well known CRMs

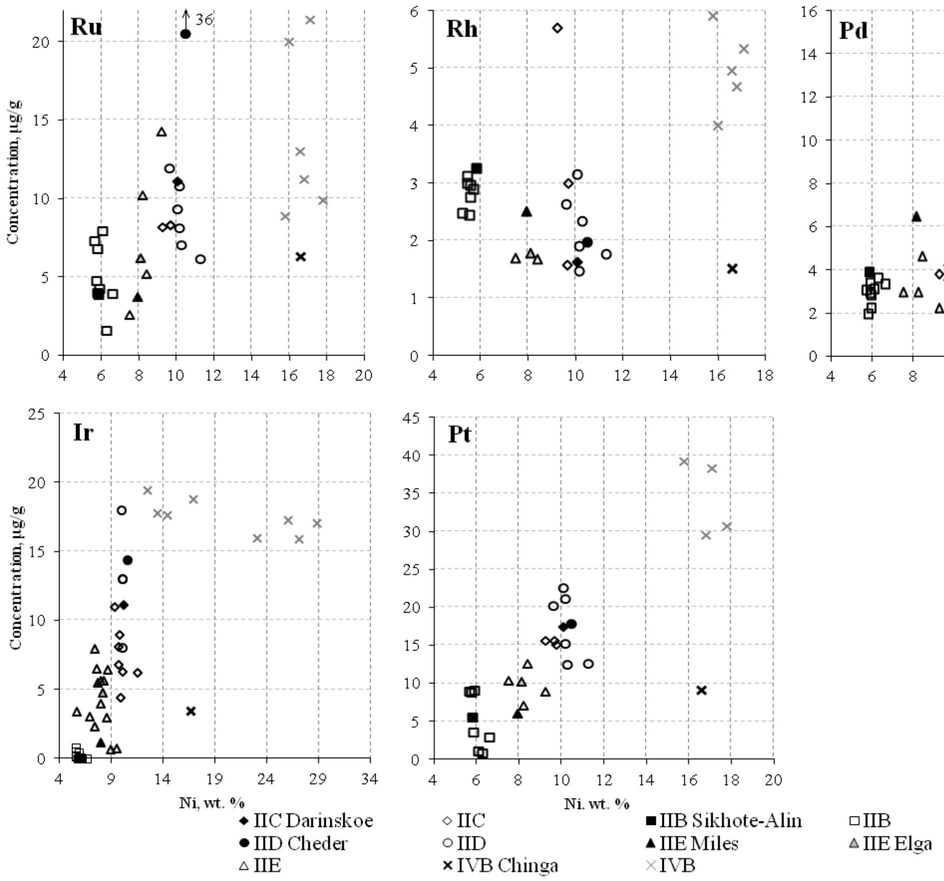

Figure 2-4. Comparison of the PGE concentrations obtained with literature data for other iron meteorites of the same group. Filled symbols – this work, open symbols – literature data.

with different matrices. The comparison of the results from both methodologies may validate the LA-ICP-MS quantification procedure.

As the map was obtained for a physically different position than the LA-ICP-MS map, it was not possible to compare them directly. Nevertheless, figure 2-5 presents the comparison of the Ni and Fe/Ni distribution of all the individual pixels. The average concentration for Fe and Ni is 83.89 % and 11.01 % respectively according to XRF. Note that the width of the distributions is substantially wider in the case of LA-ICP-MS, which can be attributed to the higher spatial resolution of the LA-ICP-MS approach, and/or to the noisier signal with LA-ICP-MS. Given the relatively small difference in terms of spatial resolution of the methods (slightly better for LA-ICP-MS in this example), the latter explanation is more probable. Indeed, for each point the signal is acquired during 50 s for the micro-XRF mapping, while the corresponding time in LA-ICP-MS is only 4s. In the case of micro-XRF, a longer acquisition time is possible owing to non-destructive nature of the technique. The total acquisition time for the mapping LA-ICP-MS of the selected area consisted about of 5 hours, while for micro-XRF the corresponding time was 57 hours.

The limits of detection (LoDs) for micro-XRF and for LA-ICP-MS in mapping mode are almost comparable. The LoDs for LA-ICP-MS in mapping mode are 0.5-20 µg/g for PGEs and other micro-elements. This level is 2-5 times higher than LoDs obtained for bulk LA-ICP-MS. In case of micro-XRF the LoDs are in the range of 20-40 µg/g for Ga and Ge for the individual spectra of the acquired XRF map while the LoDs of PGEs were not good enough for their determination.

4.5. PGE separation and ID-PN-ICP-MS. Low concentrations of PGEs ($1\cdot10^{-3}$-10^{2} µg/g) in iron meteorites and the necessity of high dilution due to the heavy iron matrix are decreasing the concentrations at which the target elements occur, to values close to the detection limits and challenge their determination by ICP-MS. Moreover, Fe, Ni and Cu, composing the matrix of iron meteorites, form argide species in the plasma which can severely interfere with

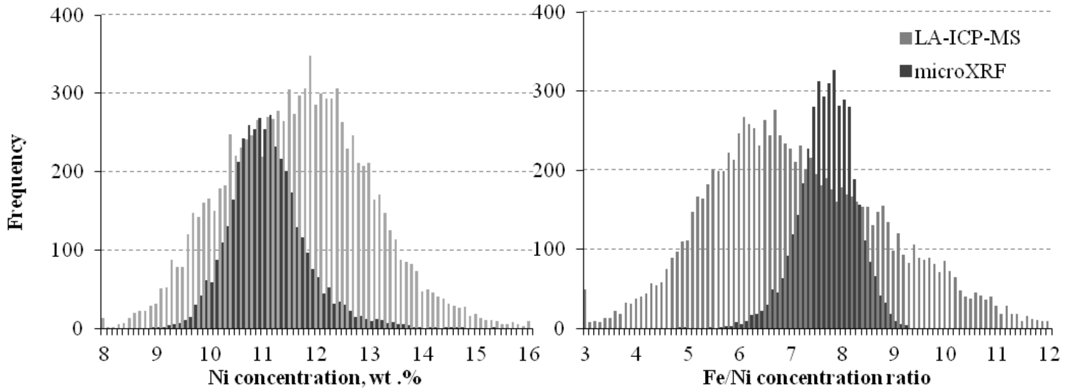

Figure 2-5. Comparison of the distribution of the Ni concentrations and Fe/Ni ratios for a polished section of Darinskoe meteorite. Average Ni concentrations are 11.63% and 11.01% for mapping LA-ICP-MS and micro-XRF respectfully. Average Fe/Ni ratios are 7.12 and 7.62.

target elements. This stresses the merits of separating and pre-concentrating PGEs prior to ICP-MS measurement. Fortuitously, the PGEs, Re and Au show high affinity to anion exchange resins in a dilute HCl medium (Matsubara et al., 2000). At the same time, this separation approach faces with problems of low recoveries due to difficulties of complete elution (Jarvis et al., 1997; Kovacheva and Djingova, 2002; Meisel et al., 2001) and strong retention dependence on the sample pretreatment (Jarvis et al., 1997; Pearson and Woodland, 2000; Yi and Masuda, 1996). Due to difficulties in reaching quantitative recoveries, the isotope dilution approach became widespread. When isotope ratios are measured instead of absolute intensities, this method is not sensitive for analyte losses, provided these occur after isotope equilibration is reached.

The anion exchange column separation of Ru, Rh, Pd, Ir, Pt, Au and Re from the iron matrix using Dowex AG 1X-8 anion exchange resin (100-200 mesh) in 0.5 M HCl medium is based on procedures described in Hann et al. (Hann et al., 2001), Hodge et al. (Hodge et al., 1986), Colodner et al. (Colodner et al., 1993) and Müller et al. (Müller and Heumann, 2000). Isolation of volatile Os, which escapes during the digestion as tetroxide, is not possible without additional measures (Pearson and Woodland, 2000), and was beyond the scope of this work. Elimination of Fe, Ni, Co, Zn, Cu, Mo and Cd was of interest in the context of PGE determination in iron meteorites. Siderophile Co, Ni, Cu and, to some extent, chalcophile Zn, are abundant in iron meteorites and can form argide ions that overlap with the signals of the light PGEs in ICP-MS analysis. Molybdenum, present in concentrations close to those of the PGEs, results in isobaric overlaps with Ru and forms oxides that interfere with the determination of Pd. Cadmium, although being very rare in meteorites, has isobars with Pd. The importance of Zr and Hf separation is widely discussed by Pearson et al. (Pearson and Woodland, 2000) but these lithophile elements have extremely low concentrations in iron meteorites and thus, are irrelevant in the context of this work.

The experimental elution curves, built relying on data obtained for a synthetic mixture of elements, are shown in figure 2-6, and the numeric figures of merit for the separation are listed in the appendix. 0.5 M HCl was used to wash off all the Fe, Co, Ni and Cu. Subsequently, 0.8 M HNO_3 was used to elute all possible Cd and Zn. A minor tail of Mo can be observed in the analyte fraction. Hot concentrated nitric acid was then used to

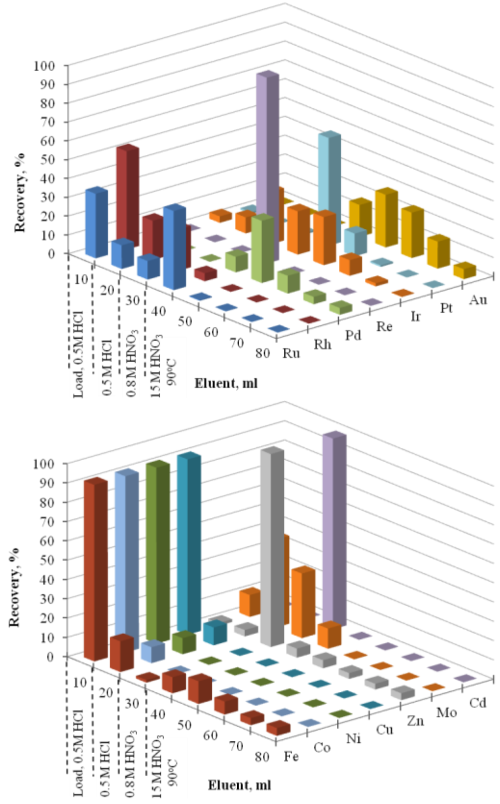

Figure 2-6. Elution profile obtained using the anion exchange procedure. Recoveries were measured in each fraction via PN-ICP-MS.

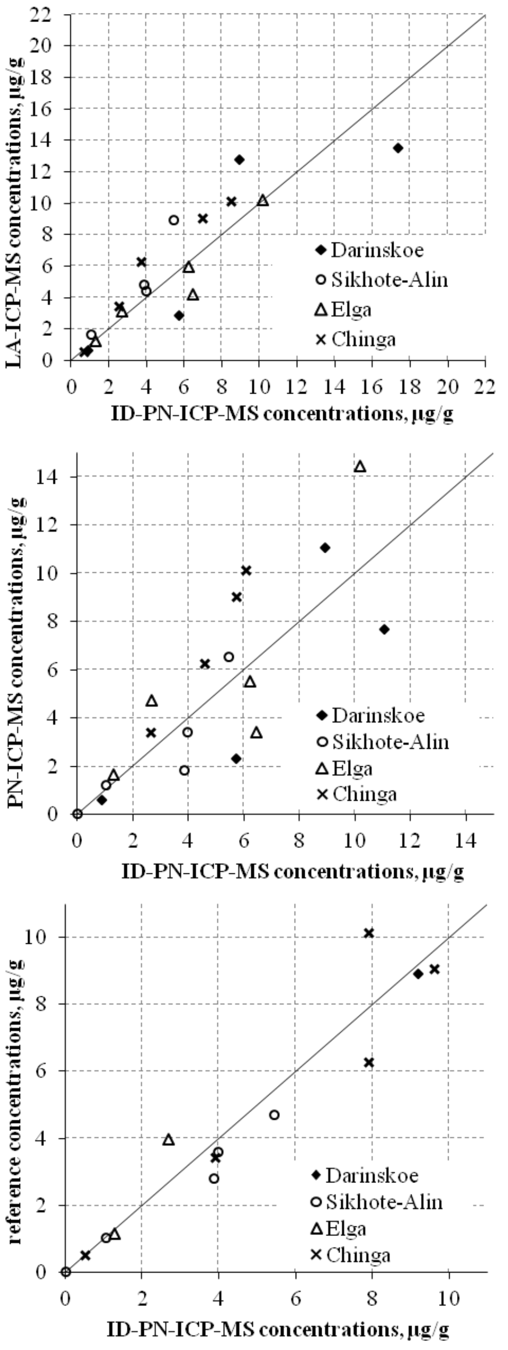

Figure 2-7. Correlation of the concentrations of the PGE, Re and Au in 4 iron meteorites determined by different methods with ID-PN-ICP-MS (this work) with A. LA-ICP-MS data, B. PN-ICP-MS data, C. reference values.

elute the analytes from the resin. Elevated levels of ubiquitous Fe and Zn originate from the lab environment and likely from the resin decomposed by HNO_3. These amounts of Fe, Zn and Mo after the separation correspond to 0.1, 0.05 and 0.03 µg respectively, corresponding to separation coefficients of about 10^3-10^4 in the case of real meteoritic element abundances. The anion exchange resin can be used only once, because it is partially digested by the hot nitric acid. Blanks of the chromatography are negligible compared to the levels of analytes processed.

As soon as isotopic equilibration is achieved during the digestion, losses of the elements of interest will not affect the results of ID-ICP-MS analysis (the recoveries are 43-70% for Ru, Pd, Ir, Pt). The mono-isotopic element Rh cannot be determined by isotope dilution, and non-quantitative recovery prevents its determination by external calibration. Rhenium and the mono-isotopic Au show relatively high recoveries in this separation and can be determined by PN-ICP-MS without isotope dilution. The performance of anion exchange column chromatography and ID-PN-ICP-MS measurements were verified by analyzing Canyon Diablo meteorite for which the concentrations of the elements of interest are well-documented. The results were found to be in a good agreement with the reference data, which proves the suitability of the method for the purpose of iron meteorite analysis. The concentrations of Ru, Pd, Ir, Pt, Au and Re in 4 iron meteorites, determined by the approach described above are shown in table 2-5**.** The results demonstrate very good agreement with the reference data, available in literature (figure 2-7, C).

4.6. Comparison of bulk LA, pneumatic nebulization, and ID-PN-ICP-MS analysis. The intensities for ^{74}Ge, ^{75}As, ^{103}Rh and ^{105}Pd were corrected for the contribution from NiO^+, $NiOH^+$ and $ArCu^+$ interferences. For this correction, their extents of formation were determined by analyzing NBS 1286 steel CRM that contains no Ge, As or PGMs. No significant differences were found between interference-corrected and non-corrected results in laser ablation mode.

The LoDs for bulk LA-ICP-MS, pneumatic nebulization ICP-MS and for anion exchange ID-PN-ICP-MS analysis of iron meteorites are shown in table 5. LoDs for LA-ICP-MS are based on 3s of the gas blank and the sensitivity, calculated using the Canyon Diablo iron meteorite. The LoDs for solution nebulization are calculated as 3s of the acid blanks, which went through all the stages of decomposition, similar to the samples. For ID-PN-ICP-MS, LoDs were calculated using a formula, developed by Yu et al. (Yu et al., 2002). According to the formula, LoDs are calculated as a function of the enrichment of the isotopic spike and the external calibration LoDs. Taking the dilution into account, the LoDs with PN-ICP-MS are 1-2 orders of magnitude lower than those for LA-ICP-MS at the spot size used. The elevated LoDs for Co, Cu, Ni, Mo and Pd in LA-ICP-MS mode can be explained by memory effects in the instrumentation applied. The LoDs for anion exchange ID-PN-ICP-MS are 1-2 orders of magnitude lower then ones for PN-ICP-MS, because high dilution is not needed since the matrix is removed chromatographically.

	LoD, 3σ			DARINSKOE				SIKHOTE-ALIN			
	I	II	III	I	II	III	IV	I	II	III	IV
Co, %	$8\cdot10^{-4}$	$1\cdot10^{-5}$	-	0.592±0.042	0.679±0.035	-	-	0.550±0.077	0.482±0.002	-	0.528
Ni, %	10^{-1}	$3\cdot10^{-4}$	-	11.4±1.3[4]	12.66±0.66	-	10.09	-	5.585±0.031	-	5.858
Cu, μg/g	10^{2}	$3\cdot10^{-1}$	-	146.9±3.4[1]	279±36	-	-	154.9±3.42	114.3±4.8	-	108
Ga, μg/g	10	$2\cdot10^{-2}$	-	44.0±9.5[4]	39.8±2.2	-	31	82.7±5.4	56.6±1.1	-	53
Ge, μg/g	10	$6\cdot10^{-1}$	-	90±19[4]	34.8±1.2	-	75	142±24	141.7±4.3	-	153
As, μg/g	6	7	-	5.6±1.9[5]	BDL<7	-	-	11.72±0.08[5]	BDL<7	-	9.0
Mo, μg/g	10	$3\cdot10^{-1}$	-	18.3±2.5[2]	8.60±0.16	-	-	10.6±4.2[2]	6.05±0.20	-	6.8
Ru, μg/g	2	$2\cdot10^{-1}$	$4\cdot10^{-3}$	25.1±2.5[4]	7.70±0.20	11.08±0.32	-	4.43±0.83	3.43±0.10	3.98±0.35	3.6
Rh, μg/g	$4\cdot10^{-1}$	$2\cdot10^{-1}$	-	1.61±0.33[4]	1.566±0.031	-	-	3.25±0.43	1.651±0.032	-	1.99
Pd, μg/g	4	$4\cdot10^{-2}$	$2\cdot10^{-3}$	2.87±0.59[4]	2.341±0.066	5.72±0.29	-	4.84±0.64[4]	1.864±0.060	3.87±0.27	2.81
W, μg/g	$2\cdot10^{-1}$	$5\cdot10^{-1}$	-	3.37±0.71[4]	0.938±0.022	-	-	1.23±0.06	0.655±0.019	-	0.76
Re, μg/g	10^{-1}	$6\cdot10^{-3}$	$3\cdot10^{-4}$	1.01±0.19[4]	1.30±0.11	1.204±0.042	-	BDL<10^{-1}	BDL<$6\cdot10^{-3}$	$3.15\pm0.26)\cdot10^{-3}$	$3\cdot10^{-3}$
Ir, μg/g	$4\cdot10^{-1}$	$9\cdot10^{-3}$	$4\cdot10^{-3}$	12.8±2.3[4]	12.1±1.2	11.103±0.073	9.2	BDL<$4\cdot10^{-1}$	$(7.3\pm1.6)\cdot10^{-2}$	$(1.790\pm0.026)\cdot10^{-2}$	$1.9\cdot10^{-2}$
Pt, μg/g	3	$2\cdot10^{-2}$	$4\cdot10^{-3}$	13.5±2.6[4]	15.0±1.2	17.4±1.1	-	8.90±0.63	6.56±0.24	5.44±0.19	4.7
Au, μg/g	$4\cdot10^{-1}$	$6\cdot10^{-1}$	$3\cdot10^{-3}$	0.61±0.15[4]	0.639±0.073	0.902±0.014	-	1.68±0.15	1.23±0.047	1.052±0.030	1.028
Pb, μg/g	10^{-1}	$6\cdot10^{-2}$	-	BDL<0.1	0.091±0.012	-	-	0.148±0.014	0.095±0.025	-	-

Table 2-5. Concentration of 16 elements in 2 iron meteorites, μg/g: I- determined by LA-ICP-MS, II – determined by pneumatic nebulization ICP-MS, III- determined after anion exchange isolation by ID-PN-ICP-MS (Ru, Pd, Ir, Pt) and PN-ICP-MS (Au, Re), IV – reference values.

	ELGA				CHINGA				MILES		CHEDER	
	I	II	III	IV	I	II	III	IV	I	IV	I	IV
Co, %	0.415±0.012	0.471±0.002	-	0.456	0.248±0.003	0.595±0.016	-	0.577	0.653±0.018	0.443	0.6781±0.003	0.550
Ni, %	-	8.226±0.030	-	8.115	-	16.22±0.14	-	16.60	-	7.960	-	10.50
Cu, µg/g	211±30	183.1±9.8	-	194	BDL<100	18.0±1.7	-	-	BDL<100	182	495±86	539
Ga, µg/g	23.6±2.8	23.71±0.74	-	23	BDL<3	BDL<2	-	0.185	29.1±0.16	26.6	136±24	131
Ge, µg/g	67±2	36.2±1.2	-	72	BDL<10	BDL<2	-	0.082	91±10	-	154±47	148
As, µg/g	9.3±3.1[5]	BDL <7	-	10.3	BDL<5[5]	BDL <7	-	1.76	10.4±4.3	9.52	19.85±0.64	16.1
Mo, µg/g	8.2±3.3[2]	8.06±0.19	-	-	5.3±1.4[2]	5.76±0.28	-	7.4	BDL<10	-	13.1±3.6[2]	15.4
Ru, µg/g	5.95±0.09	5.75±0.17	6.23±0.30	-	3.70±0.25	4.58±0.15	6.30±0.17	7.9	3.7±1.4	-	36.0±0.1	28.3
Rh, µg/g	1.775±0.072	1.466±0.051	-	-	1.54±0.52	1.47±0.15	-	2.4	2.50±0.20	-	1.96±0.27	1.7
Pd, µg/g	4.23±0.91[3]	3.42±0.10	6.47±0.63	-	8.5±2.1[3]	6.05±0.23	10.17±0.25	7.9	BDL<4	-	BDL <4	2.0
W, µg/g	0.96±0.18	0.953±0.020	-	1.19	0.616±0.018	BDL <0.5	-	0.61	0.86±0.11	0.86	4.03±0.75	-
Re, µg/g	0.41±0.14	0.376±0.017	0.327±0.014	0.390	0.95±0.12	0.927±0.058	1.143±0.014	0.96	0.11±0.06	0.10	1.30±0.76	1.5
Ir, µg/g	3.11±0.38	4.76±0.23	2.69±0.013	4.00	2.55±0.16	2.65±0.51	3.45±0.016	3.90	1.14±0.20	1.12	14.4±1.5	19.0
Pt, µg/g	10.20±0.13	14.52±0.59	10.20±0.17	-	6.98±0.43	5.74±0.92	9.09±0.31	9.6	6.0±1.7	4.6	17.8±2.4	15.0
Au, µg/g	1.25±0.12	1.711±0.080	1.298±0.031	1.18	0.670±0.043	BDL <0.6	0.544±0.010	0.510	2.18±0.06	1.13	0.86±0.43	-
Pb, µg/g	BDL<0.1	0.121±0.015	-	-	0.141±0.015	BDL <0.06	-	-	0.47±0.03	-	0.570±0.060	-

Table 2-5 (continued). Concentration of 16 elements in 4 iron meteorites, µg/g: I- determined by LA-ICP-MS, II – determined by pneumatic nebulization ICP-MS, III- determined after anion exchange by ID-PN-ICP-MS (Ru, Pd, Ir, Pt) and PN-ICP-MS (Au, Re), IV – reference values. [1] High inhomogeneity of Cu was found in Darinskoe at the level of the beam size used. Cu concentration results of 122 µg/g, 198 µg/g and 569 µg/g were found in different regions of the laser ablation line. [2] LA-ICP-MS data obtained using UP193HE ArF* LA-unit coupled to XSeries II ICP-MS instrument for Mo, because the Element2 instrument suffered from severe Mo memory effects. NBS1286 CRM was used as external standard for quantification. [3] LA-ICP-MS data obtained using UP193HE ArF* LA-unit coupled to XSeries II ICP-MS instrument for Pd, because the Element2 instrument suffered from severe Pd memory effects. [4] Value obtained via mapping LA-ICP-MS. [5] LA-ICP-MS data obtained using UP193HE ArF* LA-unit coupled to XSeries II ICP-MS instrument for As

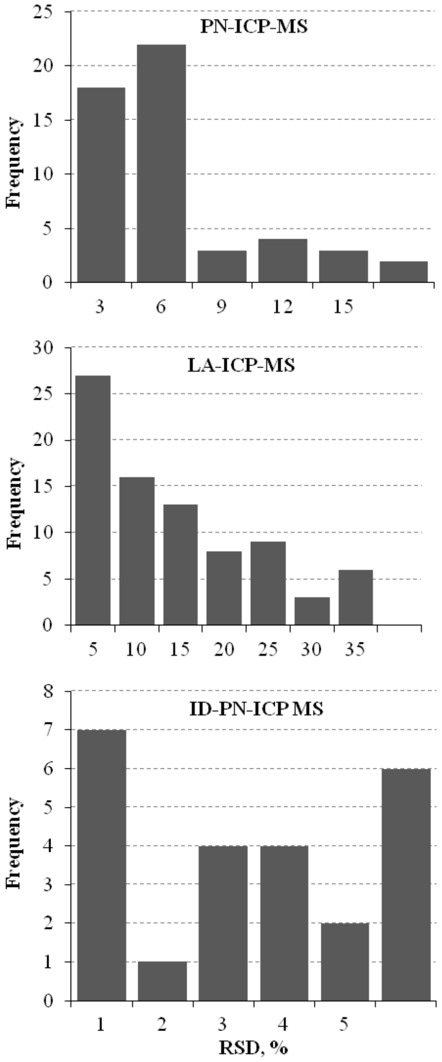

Figure 2-8. Distribution of RSDs for PN-ICP-MS, LA-ICP-MS and ID-PN-ICP-MS.

It is important to stress that in LA-ICP-MS, LoDs depend on the experimental conditions: laser frequency, beam diameter and energy fluence. The LoDs presented here are calculated for the experimental parameters shown in table 2. The LoDs for LA-ICP-MS reported here, are almost similar to those for the point analysis mode LA-ICP-MS, reported by Campbell and Humayun.[9] These authors used a similar sector field based Element ICP-MS unit and a 266 nm Nd:YAG solid state LA-system. For a similar experimental approach with line-scanning, Campbell and Humayun[9] presented 100-fold lower detection limits, levels not achievable in our study. Several ways to improve the LA-ICP-MS LoDs can be applied. Application of He as a cell-gas is a well-known method to increase the sensitivity of LA-ICP-MS with about one order of magnitude. Unfortunately, He was not available in our experimental setup. Admixture of N_2 into the ICP is also a widely-used strategy to enhance the sensitivity (Pernicka and Wasson, 1987), found to give a 5-fold improvement, but at the same time, this leads to significant increase of the level of interferences at the masses of Mo, Ge and As, and this approach was therefore not used.

The LoDs, achieved in this work for PN-ICP-MS at medium mass resolution are comparable to those for quadrupole-based ICP-MS after similar digestion and dilution procedures (see Folco et al. (D'Orazio and Folco, 2003). The LoD for As is much higher than those of other elements because of the application of the high resolution mode.

The relative standard deviation (RSD) on the LA-ICP-MS signals (below 15% in the most cases) is on average two times higher than that using PN-ICP-MS. The distributions of all the RSDs obtained in this work are shown in figure 2-8. It is important to note that many of the elements are only contained in the meteorites studied in amounts close to their LA-ICP-MS detection limits. The standard deviation for the laser ablation mode appears to depend on the proximity to the limit of detection: it increases severely at reduction of the concentration level. Dependence of the RSD on the concentration level is shown at figure 2-9. The RSD in PN-ICP-MS is within 1 to 7% for most analytes, which is comparable with the reported range (1-6%) for quadrupole-based ICP-MS after similar digestion and dilution procedures (D'Orazio and Folco, 2003). For ID-PN-ICP-MS, the RSD is below 5% in the most cases.

The results of LA-ICP-MS and PN-ICP-MS analysis of the iron meteorites are in fair to very good agreement. The concentrations of the PGEs, Au and Re, determined by different methods are plotted one versus another in figure 2-7 for comparison.

It is important to note some deviating values among the LA-ICP-MS results, which might appear due to non-homogeneous element distribution on the surface of the sampled thick section or insufficient representativeness of the area sampled. These effects of non-representativeness, being grain size-dependent, are difficult to control, because they can be less or more pronounced for different types of meteorites. As an example of the inhomogeneity effects, for the Darinskoe IIC iron meteorite, all values are discordant in bulk LA-ICP-MS (0.54 mm^2 total ablated area), but the average data from the mapping experiment with a sampled surface of 7.84 mm^2 coincide very well with the PN-ICP-MS data. For the same reason, some data were replaced by those obtained using an UP193HE ArF* LA-unit coupled to XSeries II ICP-MS instrument, because this setup allows to use a 400 μm beam size (1.52 mm^2 of total ablated area).

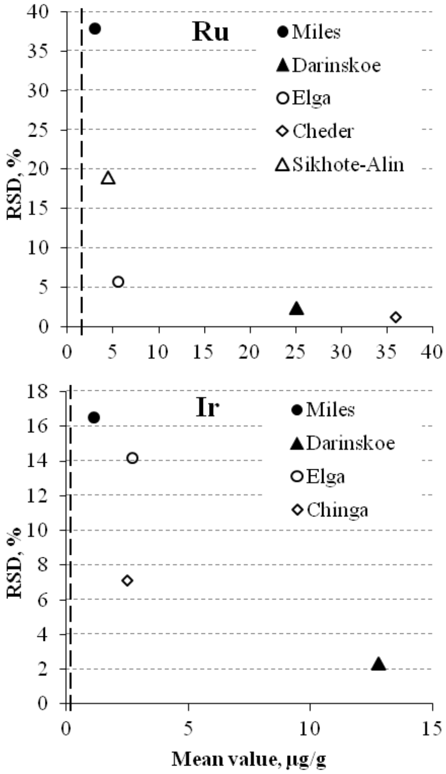

Figure 2-9. Effect of the concentration level on the relative standard deviation in LA-ICP-MS analysis. Dashed line shows 3s LOD.

The composition of the 5 iron meteorites investigated demonstrates good agreement with the literature data for other iron meteorites of the same type on PGE-Ni diagrams (figure 2-4). Literature data are taken from Pernicka and Wasson (Pernicka and Wasson, 1987), Hoashi et al. (Hoashi et al., 1993), Ryan et al. (Ryan et al., 1990), Mermelengas et al. (Mermelengas et al., 1979), Wasson et al. (Wasson et al., 2007; Wasson and Jianmin, 1986) and Rasmussen et al. (Rasmussen et al., 1984). Chinga, which is known to be an anomalous representative of IVB, shows discordant behavior. Abundances of Ir and Pt correlate nicely with other meteorites of their groups. Not only for Ir and Pd, commonly used for classification, but also for the less studied PGEs Ru, Rh and Pd, the data fit well on the PGE-Ni diagrams. The only exception is the abundance of Ru in Cheder, which seems to be too high for IID. On the other hand, the 28 μg/g Ru concentration in Cheder, reported by Agafonov et al. (Agafonov et al., 2011) is also much higher than the range of Ru known for IID (Hoashi et al., 1993; Pernicka and Wasson, 1987). Meteorites of group IIC are very rare (only 8 known members), and to the best of our knowledge, we are the first to present abundances of PGEs and other elements in Darinskoe, which fit well with previously reported data for other IIC meteorites. The concentrations of Ru, Pd and Pt are slightly higher than their known range in the IIC group.

5. Conclusions

LA-ICP-MS is a sensitive method that allows obtaining bulk and spatially resolved element information for iron meteorites. It is especially suitable for fast and quasi-nondestructive analysis of precious extraterrestrial material. LA-ICP-MS has shown to be a valuable technique for iron meteorites, not only homogeneous ataxites and hexahedrites, but also more heterogeneous ones, when considering large enough total ablated areas.

We demonstrate a significant effect of the matrix on the interaction of the nanosecond laser pulse with various phases of the metal matrix. A quantification procedure with application of a matrix-matched external standard and proper internal standardization is required to correct for these, sometimes severe, matrix effects. Careless use of intensity distribution maps without proper correction for these matrix effects can lead to incorrect interpretations.

The limits of detection for bulk LA-ICP-MS determination of trace elements in iron meteorites are in the range of 0.1-15 μg/g, which is higher than those reported in earlier works[9], but still sufficiently low for the determination of the elements of interest in almost all of the meteorites studied. The LoDs of PN-ICP-MS are 1-2 orders of magnitude lower than those of LA-ICP-MS and similar to values reported in literature. One possible way to improve the LoDs of the LA-ICP-MS analysis is to apply He as a cell gas, which was not possible in this work, because we did not have it our experimental setup. The LoDs with anion exchange ID-PN-ICP-MS ($3\cdot10^{-4}$-$2\cdot10^{-3}$ μg/g) are 1-2 orders of magnitude lower than those for PN-ICP-MS, because high dilution is not needed since the matrix is removed chromatographically. The RSD accompanying the results of LA-ICP-MS analysis of iron meteorites is below 15% in most cases, but increases when the concentration approaches the LoD. This high uncertainty can be explained by inhomogeneity in the element distribution on the surface. The RSD of PN-ICP-MS is 2-3 times lower than that typical for LA-ICP-MS (1 to 7%). For ID-PN-ICP-MS, the RSD is below 5% in the most cases.

Meteorites of IIC group are very rare (only 8 known members), and before this study, Darinskoe was the least studied member of the group. We present reliable abundances of PGEs and other elements in Darinskoe, which fit well with previously reported data for other IIC meteorites. Also, solid data are added for several meteorites that were poorly studied so far.

We have also provided information on the distribution of the analyte elements within the Darinskoe meteorite and demonstrated the application of correlation analysis in element imaging. In the context of elemental mapping using LA-ICP-MS, correlation analysis is a powerful tool that can provide valuable information on the fractionation of the elements in the parent bodies of meteorites.

The most significant improvement in LA-ICP-MS analysis of iron meteorites is expected to result from the use of femtosecond LA-systems (Možná et al., 2006; Wiltsche and Günther, 2011). In contrast to nanosecond LA, the duration of the femtosecond laser pulse is much shorter than the thermal and mechanical relaxation times in metal matrixes, which shifts the ablation processes to non-thermal mechanisms (Bleiner and Bogaerts, 2006). It results in higher aerosol formation efficiency, higher signal/background ratio, less element fractionation, less matrix effects and more stable signals. Application of sensitive fs-LA-ICP-MS systems in the future will also allow reducing the beam diameter without compromising the LoDs, which will enable precise elemental and isotopic data to be achieved for smaller inclusions.

6. Appendix

The limits of detection for both laser-ablation approaches were calculated basing on 3s of the gas blank and the sensitivity, calculated using the external standard meteorite:

$$LoD_x = \frac{C_x^{std}}{I_x^{std}} \cdot 3s_{gas\ blank} \qquad (2-3)$$

For the case of bulk LA-ICP-MS the intensities of Canyon Diablo external standard at instrument settings corresponding to that of samples were used to calculate the LoDs.

For the case of mapping LA-ICP-MS the intensities of Cheder external standard at instrument settings corresponding to that of Darinskoe analysis were used to calculate the LoDs.

It is important to stress again that sensitivity of the external standard depends on instrument settings (mainly on laser frequency, beam diameter and energy fluence), while the total level and 3s of the gas blank for most elements stays relatively constant. In this work we had relatively high LoDs for Pd and Mo in bulk LA. It is caused by contamination from samples with high content of Mo and Pd analyzed before. But the background level of these elements had decreased 10-100 times when we started mapping at another analytical session, because contamination was continuously washing out. So it is possible that even with the same instrument LoDs are different at different days.

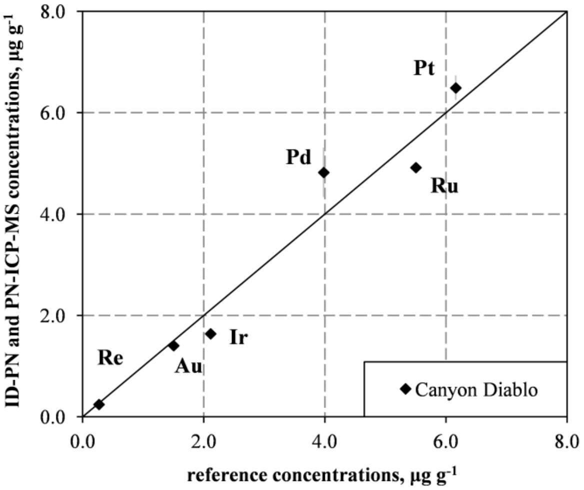

Figure 2-10. Correlation of the concentrations of the PGE, Re and Au in Canyon Diablo meteorite determined *via* ID-PN-ICP-MS (Ru, Pd, Ir, Pt) or PN-ICP-MS (Re, Au) in this work with reference values (refer to table 2-9).

CRM	Matrix	Provider
NBS 2423a	Ductile iron	NIST[1]
NBS 1286	Low-alloy steel	NIST[1]
NBS 341	Ductile iron	NIST[1]
NBS 362	Low-alloy steel	NIST[1]
NIST 610	Synthetic glass	NIST[1]
GSD-1G	Basalt glass	USGS[2]

Table 2-6. List of CRMs used. [1] - National Institute of Standards and Technology, [2] - United States Geological Survey

	Ru	Rh	Pd	Os	Ir	Pt	Au	Re
Recovery, %	43	4.3	58	1.2	58	70	89	98
Breakthrough, %	57	95	0.03	3.0	40	2.2	0.2	0.04
	Fe	Co	Ni	Cu	Zn	Mo	Cd	
Recovery, %	35	0.07	0.03	0.3	18	11	0.04	
Breakthrough, %	110	100	100	99	110	90	99	

Table 2-7. Recoveries of the elements after the anion-exchange column separation are calculated as their mass found in analyte fraction relative to the mass loaded. Breakthrough is calculated as the mass found in the wash fraction relative to the amount loaded.

X Series II ICP mass spectrometer		
Plasma power		1400 W
Sampler cone		Ni Xt cone; 1.1 mm aperture diameter
Skimmer cone		Ni Xt cone; 0.75 mm aperture diameter
Argon gas flow rates	Cool	$13.0\ \mathrm{L \cdot min^{-1}}$
	Auxiliary	$0.70\ \mathrm{L \cdot min^{-1}}$
	Nebulizer	$0.95\ \mathrm{L \cdot min^{-1}}$
Nuclides monitored		^{51}V, ^{52}Cr, ^{55}Mn, ^{59}Co, ^{60}Ni, ^{63}Cu, ^{75}As, ^{95}Mo
UP193HE ArF* excimer based laser		
He carrier gas flow rate		$0{,}182\ \mathrm{L \cdot min^{-1}}$ He
Laser wavelength		193 nm
Laser pulse duration		20 ns
Laser beam diameter		400 μm
Laser fluence		$9\text{-}10\ \mathrm{J \cdot cm^{-2}}$
Lateral scanning speed		$10\ \mathrm{\mu m \cdot s^{-1}}$
Total area ablated		$1.52\ \mathrm{mm^2}$

Table 2-8. ICP-MS and LA instrument settings used for analysis of steel and glass CRMs for determining RSFs.

Co	Ni	Cu	Ga	Ge	As	Mo	Ru	Rh	Pd	W	Re	Os	Ir	Pt	Au	Pb	Method	ref
							5.9										Gravimetry	(Hara and Sandell, 1960)
																0.224	ID-MS	(Marshall and Feitknecrt, 1964)
						7.5											ID-MS	(Wetherill, 1964)
													2.0	5.7	1.43		INAA	(Baedecker and Ehmann, 1965)
								1.5	3.6								Spectrographic	(Nichiporuk and Brown, 1965)
											0.181				1.47		INAA	(Fouché and Smales, 1966)
		125	79.7	322	12.4	7.4			3.6								INAA	(Smales et al., 1967)
			79.7	324													INAA	(Fouché and Smales, 1967)
	71900		81.8	328													INAA	(Wasson, 1967)
													1.86				INAA	(Kimberlin et al., 1968)
		138									0.252	2.07	2.02				INAA	(Herpers et al., 1969)
	69700		80	337													INAA	(Bauer and Schaudy, 1969)
													2.175		1.43		INAA	(Ehmann et al., 1970)
			80.4	324									1.97				AAS, INAA	(Wasson, 1970)
							5.2					2.1	2.0		1.47		INAA	(Crocket, 1972)
	69800				12.4					1.00			2.36		1.54		INAA	(Scott, 1977c)
									4.2								ID-TIMS	(Mermelengas et al., 1979)
	69100						5.7				0.198	2.2	2.18	5.8	1.33		INAA	(Pernicka and Wasson, 1987)
4620	69000	148			12.4					1.00	0.210		2.10		1.60		INAA	(Rasmussen et al., 1988)
	69800							1.6				2.13	2.01		1.52		INAA	(Ryan et al., 1990)
4640	69100	150	82	321	13					1.055	0.246		2.28	6.2	1.54		INAA	(Wasson and Ouyang, 1990)
4680	69200	148	83.8	322	12.7					0.99	0.228		2.17	6.3	1.57		INAA	(Wasson and Ouyang, 1990)
	69800						5.24		4.4					6.2			ETV-AAS	(Hoashi et al., 1993)
4660	70100	152	81.8	327	13.1					1.11	0.25		2.32	6.2	1.56		INAA	(Choi et al., 1995)
4630	69300	148	82.1	323	13					1.06	0.253			6.1	1.534		INAA	(Wasson and Kallemeyn, 2002)
4650	69300	150	83	330	13					1.07	0.234			6.3	1.552		INAA	(Wasson and Kallemeyn, 2002)
		142		315			5.4	1.42	4.1		0.207			6.6	1.424		PN-ICP-MS	(D’Orazio and Folco, 2003)
4647	69664	145	81.4	324.8	12.8	7.5	5.5	1.5	3.98	1.04	0.226	2.13	2.11	6.16	1.50	0.224	Average	
							4.922 ±0.020		4.82 ±0.49		0.245 ±0.012		1.643 ±0.015	6.49 ±0.24	1.406 ±0.028			This work (ID-PN-ICP-MS or PN-ICP-MS for Au and Re) ± SD

Table 2-9. Compilation of literature data (in µg/g) on the elemental composition of the Canyon Diablo meteorite, compared to the results of PGE, Au and Re determined *via* ID-PN-ICP-MS and PN-ICP-MS (this work).

7. Acknowledgments

This research has been funded by the Interuniversity Attraction Poles Program initiated by the Belgian Science Policy Office. Steven Goderis is a postdoctoral fellow of the Research Foundation – Flanders (FWO). The collection of iron meteorites from east Russia and northern Kazakhstan was kindly donated by dr. F.P. Lesnov (IGM SB RAS). Miles and Canyon Diablo were provided by the Royal Belgian Institute of Natural Sciences. The authors appreciate the generous help of Barbara Van Langenhove (OCAS NV) with LA-ICP-MS measurements at OCAS laboratory, and kindly acknowledge Maarten Moens (Umicore Precious Metals Refining) for Na_2O_2/NaOH fusion of Ru and Ir metal spikes.

8. List of references

Agafonov, L.V., Popov, V. a., Anoshin, G.N., Pospelova, L.N., Zabelin, V.I., Kudryavtsev, V.I., 2011. The Cheder iron meteorite (Tuva): mineral composition, structure, and PGE and REE contents. Russ. Geol. Geophys. 52, 620–630. doi:10.1016/j.rgg.2011.05.005

Amelin, Y., Ireland, T.R., 2013. Dating the Oldest Rocks and Minerals in the Solar System. Elements 9, 39–44. doi:10.2113/gselements.9.1.39

Baedecker, P.., Ehmann, W.., 1965. The distribution of some noble metals in meteorites and natural materials. Geochim. Cosmochim. Acta 29, 329–342. doi:10.1016/0016-7037(65)90024-4

Bauer, R., Schaudy, R., 1969. Activation analytical determination of elements in meteorites. 3. Determination of Mn, Na, Ga, Ge, Cu and Au in 21 iron meteorites and 2 mesosiderites. Chem. Geol. 6, 119–131.

Bleiner, D., Bogaerts, A., 2006. Multiplicity and contiguity of ablation mechanisms in laser-assisted analytical micro-sampling. Spectrochim. Acta Part B At. Spectrosc. 61, 421–432. doi:10.1016/j.sab.2006.02.007

Campbell, A.J., Humayun, M., 1999. Trace Element Microanalysis in Iron Meteorites by Laser Ablation ICPMS. Anal. Chem. 71, 939–46. doi:10.1021/ac9808425

Campbell, A.J., Humayun, M., 1999. Microanalysis of Platinum Group Elements in Iron Meteorites Using Laser Ablation ICP-MS, in: 30th Lunar and Planetary Science Conference. Houston, TX, p. 1974.

Campbell, A.J., Humayun, M., Meibom, A., Krot, A.N., Keil, K., 2001. Origin of zoned metal grains in the QUE94411 chondrite. Geochim. Cosmochim. Acta 65, 163–180. doi:10.1016/S0016-7037(00)00526-3

Campbell, A.J., Humayun, M., Weisberg, M.K., 2002. Siderophile element constraints on the formation of metal in the metal-rich chondrites Bencubbin, Weatherford, and Gujba. Geochim. Cosmochim. Acta 66, 647–660. doi:10.1016/S0016-7037(01)00794-3

Carlson, R.W., Shirey, S.B., Schonbachler, M., 2008. Applications of PGE Radioisotope Systems in Geo- and Cosmochemistry. Elements 4, 239–245. doi:10.2113/GSELEMENTS.4.4.239

Choi, B., Ouyang, X., Wasson, J.T., 1995. Classification and origin of IAB and IIICD iron meteorites. Geochim. Cosmochim. Acta 59, 593–612. doi:10.1016/0016-7037(94)00384-X

Colodner, D.C., Boyle, E.A., Edmond, J.M., 1993. Determination of rhenium and platinum in natural waters and sediments, and iridium in sediments by flow injection isotope dilution inductively coupled plasma mass spectrometry. Anal. Chem. 65, 1419–1425. doi:10.1021/ac00058a019

Compernolle, S., Wambeke, D., De Raedt, I., Vanhaecke, F., 2012. Evaluation of a combination of isotope dilution and single standard addition as an alternative calibration method for the determination of precious metals in lead fire assay buttons by laser ablation-inductively coupled plasma-mass spectrometry. Spectrochim. Acta Part B At. Spectrosc. 67, 50–56. doi:10.1016/j.sab.2011.12.008

Crocket, J.H., 1972. Some aspects of the geochemistry of Ru, Os, Ir and Pt in iron meteorites. Geochim. Cosmochim. Acta 36, 517–535. doi:10.1016/0016-7037(72)90073-7

D’Orazio, M., Folco, L., 2003. Chemical Analysis of Iron Meteorites by Inductively Coupled Plasma-Mass Spectrometry. Geostand. Geoanalytical Res. 27, 215–225. doi:10.1111/j.1751-908X.2003.tb00723.x

Davis, A.M., 2011. Stardust in meteorites. Proc. Natl. Acad. Sci. 108, 19142–19146. doi:10.1073/pnas.1013483108

Ehmann, W.D., Baedecker, P.A., McKown, D.M., 1970. Gold and iridium in meteorites and some selected rocks. Geochim. Cosmochim. Acta 34, 493–507. doi:10.1016/0016-7037(70)90140-7

Fouché, K., Smales, A., 1967. The distribution of trace elements in chondritic meteorites. 1. Gallium, germanium and indium. Chem. Geol. 2, 5–33. doi:10.1016/0009-2541(67)90002-2

Fouché, K.., Smales, A.., 1966. The distribution of gold and rhenium in iron meteorites. Chem. Geol. 1, 329–339. doi:10.1016/0009-2541(66)90029-5

G. Heumann, K., M. Gallus, S., Rädlinger, G., Vogl, J., 1998. Precision and accuracy in isotope ratio measurements by plasma source mass spectrometry. J. Anal. At. Spectrom. 13, 1001. doi:10.1039/a801965g

Goldstein, J.I., Scott, E.R.D., Chabot, N.L., 2009. Iron meteorites: Crystallization, thermal history, parent bodies, and origin. Chemie der Erde - Geochemistry 69, 293–325. doi:10.1016/j.chemer.2009.01.002

Hann, S., Koellensperger, G., Kanitsar, K., Stingeder, G., 2001. ICP-SFMS determination of palladium using IDMS in combination with on-line and off-line matrix separation. J. Anal. At. Spectrom. 16, 1057–1063. doi:10.1039/b102574k

Hara, T., Sandell, E., 1960. Meteoritic abundance of ruthenium. Geochim. Cosmochim. Acta 21, 145–150. doi:10.1016/S0016-7037(60)80008-7

Herpers, U., Herr, W., Wölfe, R., 1969. Evaluation of 53Mn by (n, y) Activation, 26Al and Special Trace Elements in Meteorites by γ-Coincidence Techniques, in: Millman, P.M. (Ed.), Meteorite Research, Astrophysics and Space Science Library. Springer Netherlands, Vienna, Austria, p. 387. doi:10.1007/978-94-010-3411-1

Hirata, T., Nesbitt, R.W., 1997. Distribution of platinum group elements and rhenium between metallic phases of iron meteorites. Earth Planet. Sci. Lett. 147, 11–24. doi:10.1016/S0012-821X(97)00012-5

Hoashi, M., Brooks, R.R., Reeves, R.D., 1993. Palladium, platinum and ruthenium in iron meteorites and their taxonomic significance. Chem. Geol. 106, 207–218. doi:10.1016/0009-2541(93)90027-G

Hodge, V., Stallard, M., Koide, M., Goldberg, E.D., 1986. Determination of platinum and iridium in marine waters, sediments, and organisms. Anal. Chem. 58, 616–620. doi:10.1021/ac00294a029

Holá, M., Konečná, V., Mikuška, P., Kaiser, J., Kanický, V., 2010. Influence of physical properties and chemical composition of sample on formation of aerosol particles generated by nanosecond laser ablation at 213nm. Spectrochim. Acta Part B At. Spectrosc. 65, 51–60. doi:10.1016/j.sab.2009.11.003

Horn, I., von Blanckenburg, F., Schoenberg, R., Steinhoefel, G., Markl, G., 2006. In situ iron isotope ratio determination using UV-femtosecond laser ablation with application to hydrothermal ore formation processes. Geochim. Cosmochim. Acta 70, 3677–3688. doi:10.1016/j.gca.2006.05.002

Jarvis, I., Totland, M.M., Jarvis, K.E., 1997. Assessment of Dowex 1-X8-based Anion-exchange Procedures for the Separation and Determination of Ruthenium, Rhodium, Palladium, Iridium, Platinum and Gold in Geological Samples by Inductively Coupled Plasma Mass Spectrometry. Analyst 122, 19–26. doi:10.1039/a606169i

Kimberlin, J., Charoonratana, C., Wasson, J.T., 1968. Neutron Activation Determination of Iridium in Meteorites. Radiochim. Acta 10, 69–76. doi:10.1524/ract.1968.10.12.69

Kovacheva, P., Djingova, R., 2002. Ion-exchange method for separation and concentration of platinum and palladium for analysis of environmental samples by inductively coupled plasma atomic emission spectrometry. Anal. Chim. Acta 464, 7–13. doi:10.1016/S0003-2670(02)00428-2

Lee, D., Halliday, A., 1995. Hafnium-tungsten chronometry and the timing of terrestrial core formation. Nature 378, 771–774.

MacPherson, G.J., Boss, A., 2011. Cosmochemical evidence for astrophysical processes during the formation of our solar system. Proc. Natl. Acad. Sci. U. S. A. 108, 19152–19158. doi:10.1073/pnas.1110051108

MacPherson, G.J., Thiemens, M.H., 2011. Cosmochemistry: Understanding the Solar System through analysis of extraterrestrial materials. Proc. Natl. Acad. Sci. U. S. A. 108, 19130–19134. doi:10.1073/pnas.1111493108

Marshall, R.R., Feitknecrt, J., 1964. Primitive lead from iron meteorites 28, 365–379. doi:10.1016/0016-7037(64)90110-3

Matsubara, I., Takeda, Y., Ishida, K., 2000. Improved recovery of trace amounts of gold (III), palladium (II) and platinum (IV) from large amounts of associated base metals using anion-exchange resins. Fresenius. J. Anal. Chem. 366, 213–217. doi:10.1007/s002160050042

Meisel, T., Moser, J., Fellner, N., Wegscheider, W., Schoenberg, R., 2001. Simplified method for the determination of Ru, Pd, Re, Os, Ir and Pt in chromitites and other geological materials by isotope dilution ICP-MS and acid digestion. Analyst 126, 322–328. doi:10.1039/b007575m

Mermelengas, N., De Laeter, J.., Rosman, K.J.., 1979. New data on the abundance of palladium in meteorites. Geochim. Cosmochim. Acta 43, 747–753. doi:10.1016/0016-7037(79)90258-8

Možná, V., Pisonero, J., Holá, M., Kanický, V., Günther, D., 2006. Quantitative analysis of Fe-based samples using ultraviolet nanosecond and femtosecond laser ablation-ICP-MS. J. Anal. At. Spectrom. 21, 1194–1201. doi:10.1039/B606988F

Mullane, E., Alard, O., Gounelle, M., Russell, S.., 2004. Laser ablation ICP-MS study of IIIAB irons and pallasites: constraints on the behaviour of highly siderophile elements during and after planetesimal core formation. Chem. Geol. 208, 5–28. doi:10.1016/j.chemgeo.2004.04.024

Müller, M., Heumann, K.G., 2000. Isotope dilution inductively coupled plasma quadrupole mass spectrometry in connection with a chromatographic separation for ultra trace determinations of platinum group elements (Pt, Pd, Ru, Ir) in environmental samples. Fresenius. J. Anal. Chem. 368, 109–115. doi:10.1007/s002160000494

Nichiporuk, W., Brown, H., 1965. The distribution of platinum and palladium metals in iron meteorites and in the metal phase of ordinary chondrites. J. Geophys. Res. 70, 459–470. doi:10.1029/JZ070i002p00459

Palme, H., 2008. Platinum-Group Elements in Cosmochemistry. Elements 4, 233–238. doi:10.2113/GSELEMENTS.4.4.233

Pearson, D.G.., Woodland, S.J., 2000. Solvent extraction/anion exchange separation and determination of PGEs (Os, Ir, Pt, Pd, Ru) and Reâ“Os isotopes in geological samples by isotope dilution ICP-MS. Chem. Geol. 165, 87–107. doi:10.1016/S0009-2541(99)00161-8

Pernicka, E., Wasson, J.T., 1987. Ru, Re, Os, Pt and Au in iron meteorites. Geochim. Cosmochim. Acta 51, 1717–1726. doi:10.1016/0016-7037(87)90350-4

Petaev, M.I., Jacobsen, S.B., 2004. Differentiation of metal-rich meteoritic parent bodies: I. Measurements of PGEs, Re, Mo, W, and Au in meteoritic Fe-Ni metal. Meteorit. Planet. Sci. 39, 1685–1697. doi:10.1111/j.1945-5100.2004.tb00066.x

Rasmussen, K.L., Malvin, D.J., Buchwald, V.F., Wasson, J.T., 1984. Compositional trends and cooling rates of group IVB iron meteorites. Geochim. Cosmochim. Acta 48, 805–813. doi:10.1016/0016-7037(84)90102-9

Rasmussen, K.L., Malvin, D.J., Wasson, J.T., 1988. Trace Element Partitioning between Taenite and Kamacite; Relationship to the Cooling Rates of Iron Meteorites. Meteoritics 23, 107–112. doi:10.1111/j.1945-5100.1988.tb00905.x

Ryan, D.E., Holzbecher, J., Brooks, R.R., 1990. Rhodium and osmium in iron meteorites. Chem. Geol. 85, 295–303. doi:10.1016/0009-2541(90)90006-S

Schoonjans, T., Solé, V.A., Vincze, L., Sanchez del Rio, M., Appel, K., Ferrero, C., 2013. A general Monte Carlo simulation of energy-dispersive X-ray fluorescence spectrometers — Part 6. Quantification through iterative simulations. Spectrochim. Acta Part B At. Spectrosc. 82, 36–41. doi:10.1016/j.sab.2012.12.011

Schoonjans, T., Vincze, L., Solé, V.A., Sanchez del Rio, M., Brondeel, P., Silversmit, G., Appel, K., Ferrero, C., 2012. A general Monte Carlo simulation of energy dispersive X-ray fluorescence spectrometers — Part 5. Spectrochim. Acta Part B At. Spectrosc. 70, 10–23. doi:10.1016/j.sab.2012.03.011

Scott, E.R.D., 1977. Composition, mineralogy and origin of group IC iron meteorites. Earth Planet. Sci. Lett. 37, 273–284. doi:10.1016/0012-821X(77)90173-X

Smales, A.A., Mapper, D., Fouché, K.F., 1967. The distribution of some trace elements in iron meteorites, as determined by neutron activation. Geochim. Cosmochim. Acta 31, 673–720.

Smoliar, M.I., Walker, R.J., Morgan, J.W., 1996. Re-Os Ages of Group IIA, IIIA, IVA, and IVB Iron Meteorites. Science (80-.). 271, 1099–1102. doi:10.1126/science.271.5252.1099

Ulrich, T., Kamber, B.S., Jugo, P.J., Tinkham, D.K., 2009. Imaging element-distribution patterns in minerals by laser ablation - inductively coupled plasma - mass spectrometry (LA-ICP-MS). Can. Mineral. 47, 1001–1012. doi:10.3749/canmin.47.5.1001

Vanhaecke, F., Moens, L., Dams, R., Taylor, P., 1996. Precise Measurement of Isotope Ratios with a Double-Focusing Magnetic Sector ICP Mass Spectrometer. Anal. Chem. 68, 567–569. doi:10.1021/ac9507247

Wasson, J.T., 1970. The chemical classification of iron meteorites. Icarus 12, 407–423. doi:10.1016/0019-1035(70)90009-6

Wasson, J.T., 1967. Concentrations of Ni, Ga, and Ge in a series of Canyon Diablo and Odessa meteorite specimens. J. Geophys. Res. 72, 721–730. doi:10.1029/JZ072i002p00721

Wasson, J.T., Huber, H., Malvin, D.J., 2007. Formation of IIAB iron meteorites. Geochim. Cosmochim. Acta 71, 760–781. doi:10.1016/j.gca.2006.09.032

Wasson, J.T., Jianmin, W., 1986. A nonmagmatic origin of group-IIE iron meteorites. Geochim. Cosmochim. Acta 50, 725–732. doi:10.1016/0016-7037(86)90348-0

Wasson, J.T., Kallemeyn, G., 2002. the IAB iron-meteorite complex: A group, five subgroups, numerous grouplets, closely related, mainly formed by crystal segregation in rapidly cooling melts. Geochim. Cosmochim. Acta 66, 2445–2473. doi:10.1016/S0016-7037(02)00848-7

Wasson, J.T., Ouyang, X., 1990. Compositional range in the Canyon Diablo meteoroid. Geochim. Cosmochim. Acta 54, 3175–3183. doi:10.1016/0016-7037(90)90132-5

Wetherill, G.W., 1964. Isotopic composition and concentration of molybdenum in iron meteorites. J. Geophys. Res. 69, 4403–4408. doi:10.1029/JZ069i020p04403

Wiltsche, H., Günther, D., 2011. Capabilities of femtosecond laser ablation ICP-MS for the major, minor, and trace element analysis of high alloyed steels and super alloys. Anal. Bioanal. Chem. 399, 2167–2174. doi:10.1007/s00216-010-4605-8

Woodland, S.J., Rehkämper, M., Halliday, A.N., Lee, D.-C., Hattendorf, B., Günther, D., 2005. Accurate measurement of silver isotopic compositions in geological materials including low Pd/Ag meteorites. Geochim. Cosmochim. Acta 69, 2153–2163. doi:10.1016/j.gca.2004.10.012

Yi, Y.V., Masuda, A., 1996. Simultaneous Determination of Ruthenium, Palladium, Iridium, and Platinum at Ultratrace Levels by Isotope Dilution Inductively Coupled Plasma Mass Spectrometry in Geological Samples. Anal. Chem. 68, 1444–1450. doi:10.1021/ac951121y

Yin, Q., Jacobsen, S.B., Yamashita, K., 2002. Diverse supernova sources of pre-solar material inferred from molybdenum isotopes in meteorites. Nature 415, 881–3. doi:10.1038/415881a

Young, E.D., Simon, J.I., Galy, A., Russell, S.S., Tonui, E., Lovera, O., 2005. Supra-canonical 26Al/27Al and the residence time of CAIs in the solar protoplanetary disk. Science (80-.). 308, 223–7. doi:10.1126/science.1108140

Yu, L.L., Fassett, J.D., Guthrie, W.F., 2002. Detection Limit of Isotope Dilution Mass Spectrometry. Anal. Chem. 74, 3887–3891. doi:10.1021/ac011254l

Zinner, E., 2003. Planetary science. An isotopic view of the early solar system. Science (80-.). 300, 265–267. doi:10.1126/science.1080300

Zinner, E.K., Moynier, F., Stroud, R.M., 2011. Laboratory technology and cosmochemistry. Proc. Natl. Acad. Sci. U. S. A. 108, 19135–19141. doi:10.1073/pnas.1015118108

Chapter 3

Quantitative laser ablation ICP-MS and μXRF element mapping of zoned olivines of main group pallasites

Stepan M. Chernonozhkin, Seann J. McKibbin, Stijn J. M. Van Malderen, Steven Goderis, Philippe Claeys, Frank Vanhaecke

The manuscript is prepared for publication, subject for further changes and modifications.

S.Ch. designed and carried out the experiments, processed the raw data, delivered and analysed the results, wrote the manuscript and took part in the discussion.

> *"Il semble que la perfection soit atteinte non quand il n'y a plus rien a ajouter, mais quand il n'y a plus rien a retrancher."*
>
> *"It seems to me that perfection has been achieved not when there is nothing left to add, but when there is nothing left to remove."*
>
> *Antoine de Saint-Exupery*
> *L'Avion*

1. Abstract

Pallasites are stony-iron meteorites consisting mainly of olivine and Fe-Ni metal with a formation history that remains widely debated. Despite their simple mineralogy, relatively little data are available on their geochemistry and the lateral elemental distribution in individual pallasite olivines. This work applies two microbeam techniques, i.e. laser ablation inductively coupled plasma mass spectrometry (LA-ICP-MS) and micro-X-ray fluorescence spectrometry (μXRF), for major and trace element imaging of pallasite olivines. In the LA-ICP-MS mapping approach applied, quantitative data are achieved based on oxides 100 wt% sum normalization; the results obtained are in good agreement with available literature values. Importantly, in contrast to bulk analytical methods, laterally resolved mapping techniques allow us to discriminate pixels relating to non-olivine inclusions mathematically, based on a threshold applied to the normal distribution of the selected element(s), permitting establishment of average concentration values for "pure olivine". For several elements, such as Al and Ni, this inclusion discrimination approach results in significantly lower concentrations, with important consequences for metal-olivine element distributions and stable isotope applications. The element distribution maps obtained reveal complex zoning in pallasite olivines, which can be explained as a) inherited features of olivine before the metal-olivine mixing, b) diffusion gradients formed during olivine cooling, c) crystal chemistry of element substitution due to the required charge-balancing, and d) potential misorientation in polycrystalline olivine crystals conjunct with diffusion anisotropy. Concentrations of the trace elements Cr and Al were found to be correlated both within single olivines and between olivines of different pallasites, forming a 1:1 linear trend. This is likely the result of a coupled charge-balancing mechanism in olivine, when Cr^{3+} substitution of Fe^{2+} or Mg^{2+} in octahedral sites is compensated by Al^{3+} substitution of Si^{4+} in adjacent tetrahedral sites of olivine. Additionally, principle component analysis of laterally resolved multi-element concentration data of different pallasite olivines yields slight differences in their clustering in factor score space, potentially providing an independent measure of the genetic relationships that exist between the different pallasites and their parent bodies.

Keywords: element mapping; LA-ICP-MS; pallasite; achondrite; olivine; trace element distribution; principle component analysis

2. Introduction

Pallasites are stony-iron meteorites that are composed of nearly equal parts of metal, derived from the molten metal core of a differentiated planetesimal, and a mantle-derived silicate (olivine) counterpart along with a number of accessory minerals (including chromites, sulfides, phosphates). The majority of pallasites originated from a single parent body and are classified accordingly as Main Group Pallasites (PMG). Significant differences in oxygen isotopic composition indicate that a smaller number of pallasites derive from separate parent bodies, each with only one or a few representatives; these pallasites include the Eagle Station group (Clayton and Mayeda, 1978), Milton (Jones et al., 2003), and two separate sources for pyroxene-bearing pallasites (Boesenberg et al., 2000; Bunch et al., 2005). However, the PMG exhibits a limited range of trace element compositions (Wasson and Choi, 2003) and oxygen isotope ratios closely related by mass-dependent fractionation processes (Greenwood et al., 2015, 2006). The trace element systematics of pallasite metal and preliminary chromite oxygen isotope ratio results indicate a possible link with the IIIAB iron meteorite parent body, as pallasite metals have compositions very similar to the end of the IIIAB fractional crystallization sequence (Wasson and Choi, 2003) and very similar oxygen isotopic systematics (Franchi et al., 2013). However, the cooling rates determined for pallasite metal and olivine seem to be dissociated, suggesting a complex formational history. Earlier suggestions of faster cooling of silicate at high temperature and slower cooling at lower temperatures following the metal-olivine mixing event (Tomiyama and Huss 2005; Yang et al. 2010) have recently been supported by Mn-Cr isotopic work (McKibbin et al., 2016), although the details of the pallasite formation history remain controversial. What the relationship of PMG to IIIAB iron meteorites might be (Yang et al., 2010) and how the pallasite silicates were formed (McKibbin et al., 2013) remain outstanding questions. Nevertheless, an origin related to impact mixing of molten metal and silicates, ultimately connected to core-mantle separation and interaction within differentiated planetesimals, remains a compelling possibility for the formation of pallasites.

Olivine is a magnesium-iron-silicate with an empirical formula of $[Mg_xFe_{1-x}]_2SiO_4$, forming a solid solution series between the forsterite (Mg_2SiO_4) and fayalite (Fe_2SiO_4) end-members. Ca-bearing and other solid solution members, such as $CaMgSiO_4$ and $CaFeSiO_4$, are not common in nature but form important minor contributions. The bulk contents of minor elements in the olivine phases of pallasites have been studied intensively by the application of various instrumental methods, including spark source mass spectrometry (Mason and Graham, 1970), instrumental neutron activation analysis (INAA) (Mittlefehldt, 1980; Wasson and Choi, 2003), and electron probe microanalysis (EPMA) or ion microprobe (secondary ion mass spectrometry, SIMS) (Floss, 2002; Mittlefehldt, 1980). With the continuous improvement of the lateral resolution, detection limits, and precision of in situ analytical techniques, it was revealed that pallasite olivines that were initially considered to be homogeneous (Buseck and Goldstein, 1969) actually exhibit zoning within a few hundred micrometers of the metal-olivine rim for a range of elements. Both EPMA (Miyamoto, 1997; Zhou and Steele, 1993) and SIMS (Hsu, 2003; Leitch et al., 1979; Reed et al., 1979; Tomiyama and Huss, 2006, 2005) have been used to provide laterally resolved data for minor elements. Elements, such as Ca, Cr, Ti, V, and Ni decrease from the center to the margin of olivines, Mn demonstrates almost no zoning, and major elements Fe and Mg show only faint zoning next to the olivine rim (Hsu, 2003; Miyamoto, 1997). Data on the lateral distribution of elements provide additional informative dimensions to mere bulk contents, as they provide insight into the initial igneous formation and subsequent evolution of a crystal (e.g., Ginibre et al. 2007; Turner and Costa 2007; Welsch et al. 2014). Additionally, because diffusion occurs in three spatial dimensions and anisotropy exists for diffusion coefficients in most crystal structures, including olivine (e.g., Chakraborty 1997), spatially resolved analysis in two or even three dimensions is preferable to single dimensional profiling to precisely resolve cooling rate time scales (Shea et al., 2015). For pallasites, previous in situ work was able to track such processes, but was mostly conducted in the form of one-dimensional studies, or, even more crucially, did not directly address non-divalent element relationships which involve charge-balancing, such as between Al^{3+} and Cr^{3+} (e.g., Taura et al. 1998). Thermodynamic parameters, such as temperature, pressure or oxygen fugacity all affect the valence states of substituting elements and the dimensions of the available sites in the crystal structure of olivine, possibly making some mechanisms specific to certain environments (Milman-Barris et al., 2008; Papike, 2005). Cation diffusion through crystal lattices is also sensitive to such parameters (Zhukova et al., 2014), and therefore affects any interpretation on timescales based on crystal zoning.

In the rapidly developing field of spatially resolved element analysis, LA-ICP-MS has become attractive due to a) low limits of detection (LoDs) down to sub ng g^{-1} and a wide linear dynamic range, b) mass spectra that are relatively easy to interpret and calibration procedures that allow accurate quantification to be performed, c) the multivariate character which permits a large number of elements to be monitored pseudo-simultaneously, and d) high sample throughput, which enables the experimental design to encompass many samples. Pioneering element mapping of pallasite olivines has been undertaken using LA-ICP-MS to investigate their early history (McKibbin et al., 2013), but only 2 PMGs were presented, and the research of other pallasite meteorite subgroups has not previously been undertaken.

Constantly improving laser ablation and ICP-MS instrumentation, e.g., application of low-dispersion ablation cells, femtosecond lasers and fully-simultaneous time-of-flight mass spectrometer systems can further contribute to spatial resolution, LoDs, sample throughput, and multielement capabilities of element visualization of geological samples (Gundlach-Graham et al., 2015). In this work, we demonstrate how an element visualization approach can contribute to the study of magmatic, metamorphic, and crystal-chemical processes recorded in olivines from pallasite meteorites. We provide two-dimensional maps of major elements for large PMG sections composed of various minerals using µXRF. These large-scale maps are, for selected olivine sections, combined with smaller, quantitative 2D LA-ICP-MS maps of multiple major to trace elements for regions of interest. A multivariate approach is applied to analyze and compare this spatially resolved multi-element PMG data. This helps to compare the features and patterns observed and potentially explain them by crystal- and parent body- scale processes.

3. Experimental

3.1. Samples and standard materials. Five PMG were ordered from the open market (Seymchan, Fukang, Esquel, Brahin and Springwater). Cumulus Peak 04071 was provided by the National Aeronautics and Space Administration (NASA) from the collection of Antarctic meteorites. Brenham was provided by the Research School of Earth Sciences, Australian National University. Imilac was donated by the Royal Belgian Institute of Natural Sciences. All samples were studied in the form of flat polished thick-sections, containing pallasite metal matrix and several olivine crystals. Certified reference materials (CRMs) of synthetic silicate glass of the National Institute of Standards and Technology (NIST) SRM 612 and SRM 614 together with BHVO-2G, BIR-1G, GSE-1G and GSD-1G synthetic and natural glass SRMs (standard reference materials) of the United States Geological Survey (USGS) were used for quantification.

3.2. Instrumentation. The elemental distributions of larger sections of the pallasites characterized, including Fe-Ni metal, olivine and minor minerals, were measured using a Bruker M4 Tornado X-ray fluorescence (XRF) instrument, equipped with a 30W Rh-anode X-ray source (50 kV operating voltage, operating current 150 µA) and a Be window. The X-rays are focused to a 25 µm spot (measured for Mo K_{α}) using a polycapillary lens. The instrument is equipped with two Silicon Drift Detector (SDD) spectrometers (30 mm^2, 145 eV energy resolution for Mn K_{α}), symmetrically placed relative to the sample. To improve statistics, all sections of single pallasites were scanned 5 times using a translation stage moving at 25 mm s^{-1}, resulting in acquisition times of 1 ms $pixel^{-1}$. The measurements took place under a vacuum of 20 mbar. The bulk composition of Fe and Mg in the olivine fractions of the pallasites were determined using the Fe and Mg K_{α} lines and the San Carlos olivine reference material, previously quantified via electron probe (Ito and Ganguly, 2006).

To obtain detailed major and trace element distribution maps of the pallasite olivines, a Teledyne CETAC Technologies Analyte G2 laser ablation system, based on a 193 nm ArF*excimer laser with a pulse duration <5 ns was coupled to a Thermo Scientific Element XR double-focusing sector field ICP-MS unit. The laser beam is characterized by a flat-topped energy profile and was attenuated to an energy density of 5-7 J cm^{-2} in the focus. The samples and standards were mounted in a HELEX 2 double-volume ablation cell flushed with two He flows for improved washout characteristics. The laser scanned a grid of parallel, adjacent lines using a 20x20 µm square-masked laser spot at a translation speed of 9 µm s^{-1}. The sampling grids cover 1450x600 µm rectangular areas of the sample, and were positioned in the direction from the metal-olivine margin to the olivine cores. The He carrier gas was mixed with Ar make-up gas downstream the ablation cell, and introduced into the sector field ICP-MS unit, operated in low mass resolution mode ($M/\Delta M = 300$). Semi-cold plasma conditions (800 W RF power) were used to reduce Ar-based interferences and to increase the sensitivity of the analysis. Wash-out times were typically less than 1 s. The mass scanning method was set to the speed-optimized mode, resulting in a total scan cycle time of 1.94 s. The lateral resolution achieved was approximately 20 µm. Detailed instrument settings of the LA and ICP-MS units are summarized in Appendix C.

4. LA-ICP-MS data reduction protocol

4.1. Quantification. In LA-ICP-MS, internal normalization is traditionally used to correct for point-to-point differences in the ablation efficiency, drift of the instrument parameters and some matrix effects or minor defocusing (Miliszkiewicz et al., 2015). For this purpose, the concentration of a single major element is traditionally determined using an independent analytical method, such as EPMA (Paul et al., 2014). The principal challenge with internal standardization for element imaging is that none of the naturally occurring olivines in pallasites contain a fully homogeneously distributed element with precisely known content that can serve as an internal standard. To overcome this, several elegant approaches have been proposed, including (1) sum normalization of oxides to 100 wt% (Liu et al., 2008; Selih and van Elteren, 2011), or (2) using the known stoichiometry of a target mineral, by assuming the ideal concentration of a homogeneously distributed major element as internal standard (IS). As olivine is known to have variable fayalite-forsterite contents even within a single crystal, the latter approach cannot be applied directly here.

Therefore, the following approach was applied in the LA-ICP-MS calibration process. In accordance to the empirical formula of the olivine mineral ($[Mg_xFe_{1-x}]_2SiO_4$), Mg, Si, Fe and P oxides were considered to contribute 100 wt % of the mass ablated. The raw intensities of the corresponding nuclides in each pixel of the map were first re-calculated to responses equivalent with the oxide form of these elements by multiplying the intensities with an abundance and oxide correction factor, subsequently, these virtual responses were normalized to the assumed concentration of the sum of the selected oxides, e.g., 100 % in the olivine mineral. The respective oxide sum was also known for the certified reference materials. The sensitivity of this sum of oxides was used as a virtual, evenly distributed IS (equations 3-1 and 3-2). Phosphorus was added to the equation to account for the secondary areas of inclusions, where significant amounts of P were found, thereby allowing these to be quantified (see discussion below).

$$IS = \frac{\left(\frac{I_{25Mg}}{\omega_{25Mg}} \cdot \frac{M_{MgO}}{M_{Mg}} + \frac{I_{57Fe}}{\omega_{57Fe}} \cdot \frac{M_{FeO}}{M_{Fe}} + \frac{I_{29Si}}{\omega_{29Si}} \cdot \frac{M_{SiO2}}{M_{Si}} + \frac{I_{31P}}{\omega_{31P}} \cdot \frac{M_{P2O5}}{2M_P}\right)}{\left(C_{MgO\%} + C_{FeO\%} + C_{SiO2\%} + C_{P2O5\%}\right)} \qquad (3-1)$$

In equation 3-1, ω_i stands for the isotopic abundance of the nuclide. In contrast to external calibration, normalization to ω_i is critical to account for the contributions of different oxides into the virtual internal standard. $C_{i\%}$ stands for an element oxide concentration in *wt* %. M_i stands for atomic mass of the corresponding element or oxide.

$$I_{i,norm} = \frac{I_i}{IS} \qquad (3-2)$$

The IS was calculated for each pixel of the map, as a 2D matrix, and each single element intensity was then normalized to this internal standard (equation 3-2). The intensities for the external standards were processed as a single data point, averaging data across representative surface areas of the reference glasses (3 replicates of 2 mm long line scans).

The set of synthetic glasses (NIST SRM612, NIST SRM614, USGS GSD-1G and GSE-1G) and natural basalt glasses (BHVO-2G, BIR-1G) used for external calibration provides a wide dynamic range and matrix-matched calibration, which minimizes potential matrix effects. The internally normalized data were externally quantified via linear regression. After the calibration, the averages of the sums of the 4 selected major element oxides of single pixels of the maps varied between 95-99 wt %, which supports the applicability of the internal standardization approach. The fact that the maximums of the sums distributions are not 100 wt% probably indicates minor drift of the parameters, point-to-point differences in the ablation efficiency, not completely corrected for by the internal standard, or the occurrence of minor elements (e.g., Ca is not measured, but could be present as phosphate $Ca_3(PO_4)_2$). To correct this, additional normalization was done for the concentration C_j of each elements j by fixing the sum of Mg, Fe, Si and P oxides to 100 wt% in each pixel of the map. The element concentrations, calculated according to the described procedure for several geological reference materials, used as control standards, are in moderate to good agreement with their reference values (see appendix D for the detailes).

$$k = \left(\sum_{i=P_2O_5,SiO_2,FeO,MgO} C_i\right)/100 \tag{3 – 3}$$

$$C_{norm,j} = C_j/k \tag{3 – 4}$$

4.2. Interferences. When acquiring transient signals, spectral interferences are challenging to take care of. Mathematical correction usually requires additional nuclides to be measured, increasing the duty cycle time which deteriorates the lateral resolution and limits of detection within a given experimental run time. Application of the medium ($M/\Delta M = 4000$) or high ($M/ \Delta M = 9000$) resolution modes of the ElementXR is compromised by more than 10-foldsensitivity loss. The spectral interferences potentially affecting target nuclides are listed in table 3-2 in the appendix. However, argide-based interferences are reduced by the application of cold plasma conditions (e.g., $^{36}Ar^{24}Mg^+$ and $^{40}Ar^{31}P^+$ interferences for ^{60}Ni and ^{71}Ga, respectively). Oxide-based interferences are minimized during tuning. Pairwise scatter plots for potentially interfered and interference parent nuclides of the spatially resolved data are sensitive indicators for spectral interference.

5. Results

5.1. General features of 2D multi-element maps. All pallasite thick sections contain single olivine crystals or olivine crystal aggregates in an Fe/Ni metal matrix. The areas of higher or lower relative Fe and Ni and K_α intensities for the latter elements indicate the presence of taenite and kamacite, respectively (appendix E). Schreibersite is indicated by increased Ni and P K_α intensities and typically found as thin elongate inclusions in the metal matrix (e.g., μXRF map of Imilac at figure 3-1), although schreibersite is also present over much larger areas in CMS 04071, Seymchan, and Brenham. Troilite is indicated by elevated S K_α intensities. Typically, the troilite inclusions are larger than the schreibersite ones, and are adjacent to olivine crystals or filling up the volume between olivine crystals (e.g., μXRF map of Brahin at figure 3-3). The presence of chromite is indicated by an elevated Cr K_α intensity. Phosphates are visible through elevated Ca and P K_α intensities, with only minor contributions of Fe and Ni, in contrast to schreibersite, which has no Ca and elevated Fe and Ni intensities. None of the phosphate inclusions observed have detectable Mg K_α intensities. As such, the phosphates are identified as either $Ca_3(PO_4)_2$ merrilite or $Ca_4Mg_5(PO_4)_6$ stanfieldite, but not as $Mg_3(PO_4)_2$ farringtonite. Figures 3-1, 3-2 and 3-3 represent element distribution maps of 8 PMGs that are superimposed on Fe K_α intensity μXRF maps of larger sections of the same pallasite. Only Fe K_α μXRF maps with labeled mineral phases are shown in figures 3-1, 3-2 and 3-3, as the relative Fe intensities are most suitable to distinguish between pallasite mineral phases (olivine, troilite, phosphate, chromite, schreibersite and kamacite/taenite Fe-Ni metal). Additional μXRF intensity maps for other elements (Mg, P, S, Ca, Cr, Ni) are provided in the appendix E.

In the lower parts of figures 3-1, 3-2 and 3-3, quantitative LA-ICP-MS maps of smaller olivine areas are shown, which correspond to the locations indicated on the larger μXRF maps as black rectangles. The locations for LA-ICP-MS mapping were selected close to the metal-olivine rims of large olivine crystals with the laser beam rastering from the olivine rim in the direction of the olivine core (from the left to the right side on the LA-ICP-MS maps).

All olivines were found to contain P-rich phases, usually in the form of veinlets, or in the case of CMS 04071, as a nugget. Manganese is distributed relatively homogeneously in all the olivines analyzed, while the distribution maps of the other elements demonstrate complex, often correlated, lateral distributions. Chromium exhibits concentration

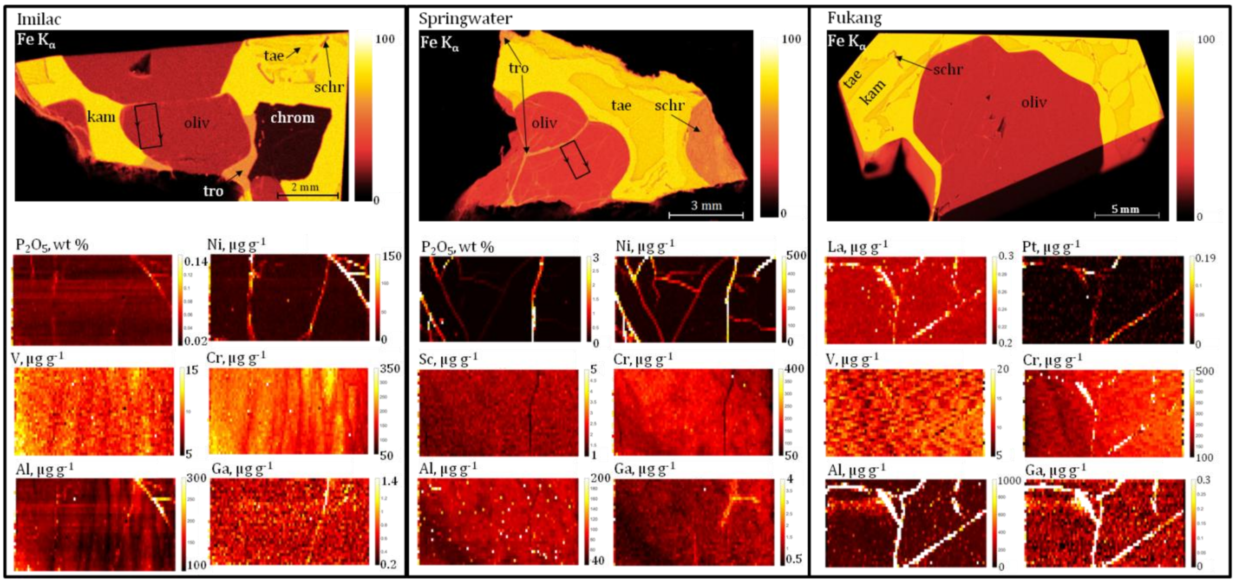

Figure 3-1. Element distribution maps for Imilac, Springwater and Fukang. In the upper row, Fe K_α intensity µXRF maps of large pallasite sections are presented, with black rectangles on the olivines indicating the smaller areas selected for quantitative LA-ICP-MS mapping. In the case of Fukang, the LA-ICP-MS map was measured at the other side of the thick section. The highlighted mineral phases are kam – kamacite, tae – taenite, oliv – olivine, schr – schreibersite, tro – troilite, and chrom – chromite. In the lower rows, quantitative LA-ICP-MS distribution maps of selected target elements in olivines are shown. Quantitative LA-ICP-MS maps of olivines are measured by scanning a grid of parallel, adjacent lines using a 20x20 µm square laser spot from the olivine-metal rim in the direction of the olivine core (left to right on the maps). Each LA-ICP-MS map is 1450 µm long and 600 µm wide

gradients in Fukang, CMS 04071, Esquel, Seymchan and Brenham to lower values near olivine margins. Similar concentration gradients in V are correlated with those of Cr in the rims of olivine adjacent to metal in Fukang and CMS 04071. Similar concentration gradients are observed for Cr, Ga, Al and Sc in Springwater olivine close to a troilite vein, although these concentration gradients are not related to or perpendicular to the olivine margin, but are inclined at an angle (figure 3-1). Imilac and Brahin olivines exhibit lamellae-like structures for Cr, Al and V (figures 3-1, 3-3). Fukang shows reduced P contents next to the olivine-metal rim. Additionally, an area with elevated concentrations of Al and Ga is present that is unrelated to the distribution of Cr (figure 3-1). A veinlet with elevated concentrations of Ga, not correlated to any other element, is present in Springwater (figure 3-1). LA-ICP-MS maps of Al, Ga and Cr in an olivine of Seymchan demonstrate a partially correlated distribution of Ga and Al (see figure 3-2). It should be noted that some distribution maps have been affected by analytical artifacts. The horizontal lines in the Al and P maps of Imilac and Brahin could represent some form of signal undersampling or memory effects, while aliasing effects degraded other distribution maps, such as V in Fukang.

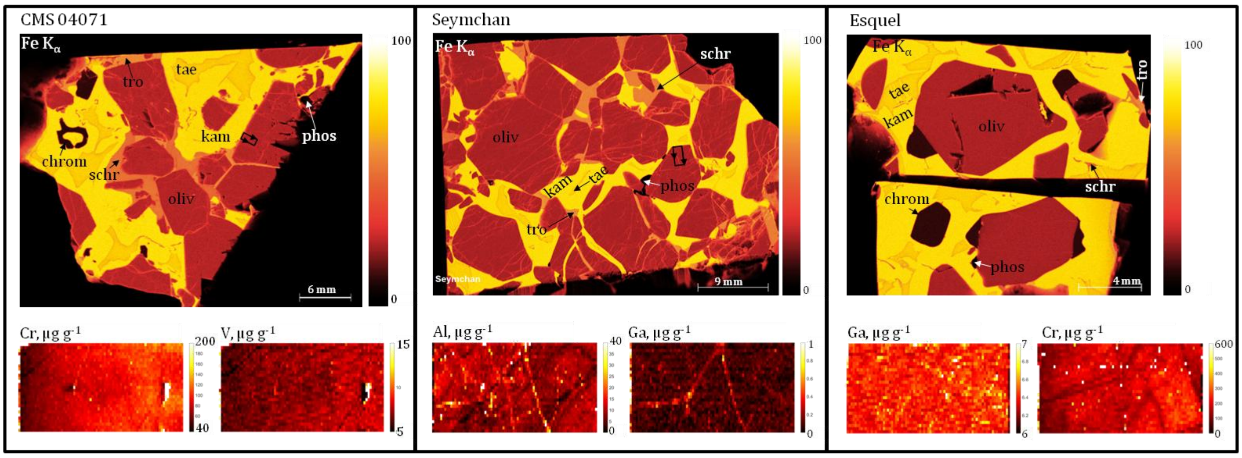

Figure 3-2. Element distribution maps for CMS 04071, Seymchan and Esquel (cf. Fig. 3-1).

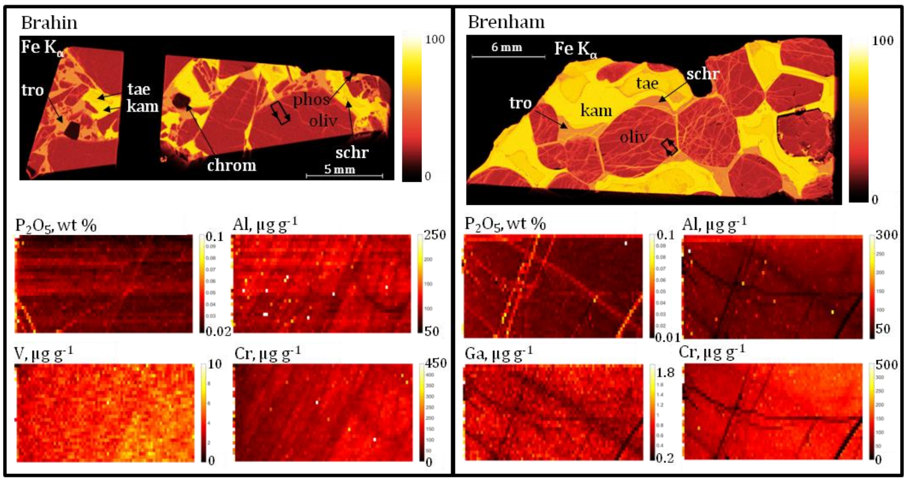

Figure 3-3. Element distribution maps for Brahin and Brenham PMGs (cf. Fig. 3-1 and 3-2).

5.2. P-rich veinlets in olivine. All olivines of PMGs contain veinlets approximately 10-20 µm in width, intersecting the olivines and visible under the optical microscope in reflected light. In the 2D element distribution maps, these veinlets are characterized by elevated P contents, and deviating concentrations for other trace elements as well (e.g., Al, Sc, V, Mn, Cr, Ni, La, Pt). Most veinlets are enriched in Al and Ni relative to the bulk olivine composition, although Brenham and Springwater veins are depleted in Al. For most elements, such as for Sc, V and Mn, these veinlets are depleted relative to the olivine bulk composition, while Ga and Cr not only vary in these veinlets but also across the PMG olivines. These P-rich veinlets probably have an origin related to shock (Desrousseaux et al., 1997) or could even represent terrestrial weathering, obscuring primary igneous and secondary metamorphic signatures. As these veinlets are all characterized by elevated P_2O_5 content, these can be filtered from the results using a simple threshold procedure. The upper limits for P_2O_5 concentrations in "pure" olivine were selected based on probability distribution histograms for each pallasite, (maximum of the best fit Gaussian line to the probability distribution histogram plus approximately 3 standard deviations), and a MATLAB script was applied to mask pixels representing veinlets in the 2D concentration matrices of all the target elements (see figure 3-4).

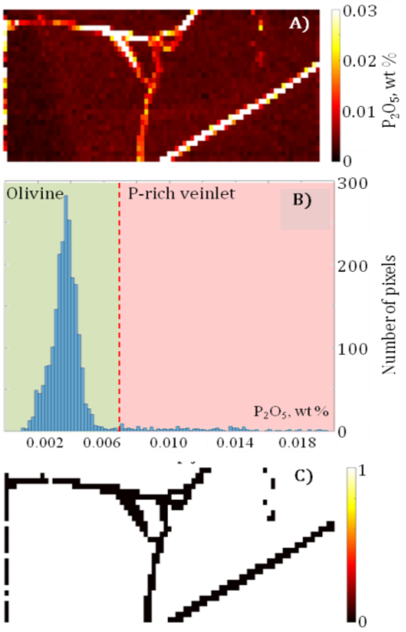

Figure 3-4. Demonstration of the mathematical procedure to filter out pixels with elevated P content from the 2D map. A) 2D quantitative P_2O_5 map of a Fukang PMG olivine. B) Probability distribution of P_2O_5 concentrations within the distribution map, with selected threshold, thus differentiating pure olivine pixels from the P_2O_5-rich inclusions. C) Binary mask constructed based on the P_2O_5 probability distribution. This mask can be applied to the other element distribution maps to cancel out the input of the P_2O_5-rich veinlets to obtain average "pure" olivine values.

5.3. Average concentrations. The limits of detection (LoDs) of the LA-ICP-MS mapping procedure based on 3s of the gas blank are presented in Table 3-1. All LoDs are higher than those typically obtained by bulk-analysis LA-ICP-MS due to the trade-off between lateral resolution and sensitivity when working in the mapping mode of laser ablation sampling. The results of the major and trace elements determination, calculated by averaging the 2D LA-ICP-MS element maps are also presented in Table 3-1. The response for pixels in the P-rich veinlets have been eliminated mathematically prior to averaging, so the reported data represent "pure olivine" element contents. Additionally, the results of the Fa# quantification (fayalite, $\mathrm{Fa\#} = \mathrm{FeO}/(\mathrm{FeO}+\mathrm{MgO}) \cdot 100$, atomic %) using µXRF with respect to the San Carlos olivine standard are given. The reported uncertainty (1s) represents both the heterogeneity of the sample and the analytical uncertainty. Moderate agreement of the LA-ICP-MS bulk data with literature is demonstrated in

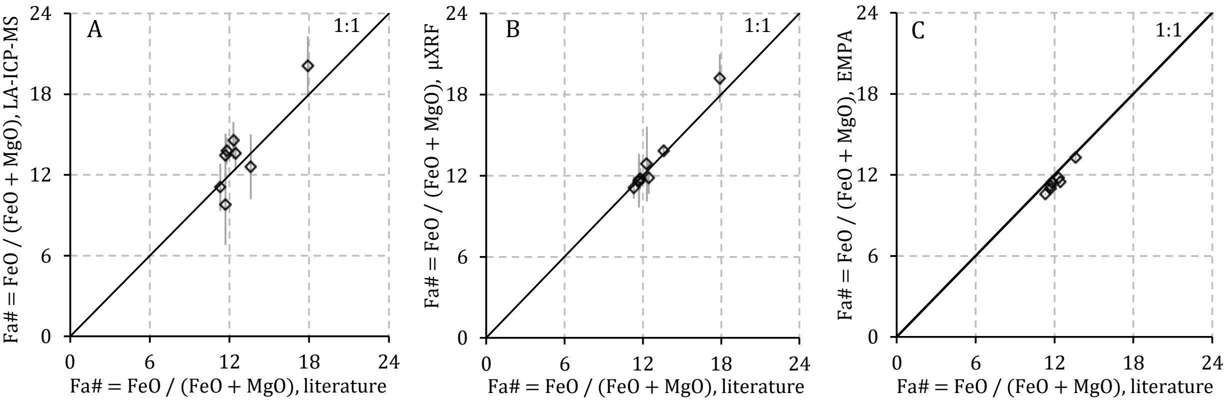

Figure 3-5. A) Correlation between the olivine Fa# in 8 PMGs determined by LA-ICP-MS in imaging mode and literature reference values. B) Correlation between the olivine Fa# in 8 PMGs determined by µXRF and literature reference values. C) Correlation between the olivine Fa# in 7 PMGs determined by EPMA and literature reference values (see chapter 7 for the datailes of EPMA measurements). Error bars represent 1 standard deviation. Fa# = [FeO / (FeO + MgO)] · 100 is calculated in atomic %. The literature data of Fa# are from (Danielson et al., 2006; Lauretta et al., 2006; van Niekerk et al., 2007; Wasson and Choi, 2003).

figure 3-5 A, which compares the measured Fa# with available literature data. For comparison µXRF bulk Fa# agree better with literature data, likely because larger areas are taken into consideration or because of relatively less stability of laser sampling comparatively to µXRF (see figure 3-5 B).

6. Discussion

6.1. Multivariate analysis. Principle component analysis (PCA) was applied on the normalized dataset of seven 2D element maps of PMG olivines (Esquel data were excluded because of the absence of Sr and Ga data). Prior to PCA, data from P-rich veinlets in the maps were filtered out, and the 2D maps were subjected to 3x3 pixel^2 median filtering to reduce negative effects of signal noise on the results of PCA, as the approach is sensitive to outliers. Lanthanum, Eu and Pt are not taken into consideration, because their concentrations are close to the corresponding LoD with the LA-ICP-MS protocol and the noisy response may thus introduce artefacts, skewing the dimension reduction. Fe, Mg and Si are taken into calculation as Fa#, because their concentrations are connected linearly via the empirical formula of olivine. The first 3 PCs explain 75.1 % of variance. Figure 3-6 A demonstrates a 3D load plot in varimax rotated component space. This plot helps general trends between the elements in olivine at the PMG parent body scale to be found. The fact that no points cluster significantly close to each other indicates that the different elements demonstrate significantly dissimilar behaviour in olivine. Elements with different valence states are shown with different marker colors: Mn and Ni are divalent, whereas Al, Ga and Sc are trivalent, Cr can exist as double- or triple-charged ion (Papike, 2005), V can be di-, tri-, tetra- or pentavalent depending on the oxygen fugacity (Mallmann and O'Neill, 2009), and P is typically pentavalent in olivine (McKibbin et al., 2013; Milman-Barris et al., 2008; Watson et al., 2015).

Figure 3-6 B represents the factor score plot for the same normalized dataset. Single pixels of the multi-element 2D maps of olivines of different PMGs are represented by different colors. PCA has successfully clustered individual PMGs. While Brenham, Brahin and CMS 04071 PMGs are shown to be closely associated, Imilac and Springwater also group closely together, suggesting a genetic relationship. As such, loading and factor score PCA of spatially resolved data highlight the effects of both planetary- and mineral-scale processes on the element composition of olivine.

Pearson's product-moment element-element correlation coefficients (R) were calculated based on the normalized spatially resolved LA-ICP-MS dataset of each individual olivine. The P-rich inclusions were excluded from the maps prior to the calculation of the correlation coefficients. Correlation coefficients for Cr versus V are calculated for all the pallasites in Table 3-1, indicating significant positive correlations for Brahin, CMS 04071, Fukang and Seymchan (R > +0.4 is assumed to be significant due to the large amount of data). Significant Pearson correlation coefficients can indicate the occurrence of structured substitution of particular elements, coupled by charge

	LoD	Imilac	Brahin	Brenham	Springwater	CMS 04071	Esquel	Seymchan	Fukang		
									Average	Olivine rim	Olivine core
Fa#, at % LA-ICP-MS^{b}		14.56±0.69	13.45±0.81	13.61±0.63	20.1±1.1	13.79±0.49	9.8±1.5	11.08±0.87	12.6±1.2	12.5±1.2	12.5±1.9
Fa#, at% μXRF^{g}		12.86±1.38	11.56±0.81	11.82±0.58	19.21±0.41	11.79±0.39	11.64±0.99	11.11±0.41	13.84±0.20		
Fa#, at% EPMA^{h}		11.78±0.12	10.98±0.30	11.47±0.15	-	11.45±0.19	11.17±0.15	10.58±0.10	13.29±0.23		
Fa#, at% literature		12.3^{c}	11.7^{c}	12.45^{c}	17.9^{c}	11.8^{f}	11.7^{c}	11.3^{e}	13.6^{d}		
Al, μg g^{-1}	10^{1}	122±20	107±22	72±20	75±28	63±52	250±380	9.6±4.6	183±480	155±120	188+520
SiO$_2$, wt%	10^{-2}	45.63±0.87	45.65±0.61	46.42±0.66	46.19±0.94	47.02±0.65	41.4±2.1	45.3±1.1	44.6±1.0	44.6±1.0	44.7+1.1
P$_2$O$_5$, wt%	10^{-3}	(3.32±0.53) 10^{-2}	(2.83±0.47) 10^{-2}	(2.38±0.60) 10^{-2}	(2.20±0.22) 10^{-2}	(2.38±0.18) 10^{-2}	(3.0±1.1) 10^{-3}	(1.18±0.47) 10^{-2}	(3.64±0.78) 10^{-3}	(2.38±0.52) 10^{-3}	(3.82±0.71) 10^{-3}
Sc, μg g^{-1}	1	3.09±0.32	3.95±0.42	2.37±0.29	1.86±0.20	1.97±0.17	-	1.60±0.27	3.46±0.44	3.67±0.42	3.49+0.50
V, μg g^{-1}	10^{-1}	9.6±1.9	4.42±0.93	7.38±0.59	11.4±1.0	7.08±0.68	16.6±2.1	4.6±1.1	11.1±1.8	11.4±1.8	11.2+2.2
Cr, μg g^{-1}	1	194±30	123±34	128±24	158±25	87±18	182±44^{a}	96±26	237±53	166±20	254+54
Mn, μg g^{-1}	1	2320±93	1702±90	1521±57	2420±130	1998±57	1820±200	1980±110	2180±150	2170±150	2170+260
Ni, μg g^{-1}	1	15±23	9.6±9.5	11±19	18±23	18±80	35±61	65±180	12±54	5.7±6.1	13+60
Ga, μg g^{-1}	10^{-1}	0.62±0.51	0.8±7.1	0.67±0.15	0.98±0.34	0.461±0.092	-	0.103±0.059	0.12±0.50	0.073±0.043	0.13+0.56
La, μg g^{-1}	10^{-2}	0.29±0. 20	0.29±0.15	< 10^{-2}	< 10^{-2}	< 10^{-2}	6.82±0.06	0.262±0.024	0.24±0.24	0.228±0.004	0.24+0.27
Eu, μg g^{-1}	10^{-2}	0.416±0.020	0.416±0.030	< 10^{-2}	< 10^{-2}	< 10^{-2}	< 10^{-2}	< 10^{-2}	< 10^{-2}	< 10^{-2}	< 10^{-2}
Pt, μg g^{-1}	10^{-2}	< 10^{-2}	0.02±0.51	0.4±8.2	< 10^{-2}	< 10^{-2}	< 10^{-2}	< 10^{-2}	< 10^{-2}	< 10^{-2}	< 10^{-2}
R_{Cr-V}		0.323	0.635	0.204	0.291	0.712	-0.036	0.524	0.435		
$R_{Fa\#-Mn}$		0.435	0.593	0.217	0.385	0.391	0.879	0.329	0.878		

Table 3-1. Average concentrations of major and trace elements in 2D element maps of PMG olivines. P-rich veinlets have been cancelled out mathematically prior to averaging. Uncertainty denotes 1 standard deviation. [a] Average is calculated after application of a 3x3 median filter to the 2D concentration maps to remove elevated noise. [b] Fa# = [FeO / (FeO + MgO)] is calculated in atomic %, as maximum of the Gaussian line fitted to the Fa# probability distribution histogram. The literature data for the Fa# are from [c] (Wasson and Choi, 2003) [d] (Lauretta et al., 2006) [e] (van Niekerk et al., 2007) [f] (Danielson et al., 2006). [g] Results obtained via μXRF using San Carlos olivine as an external standard (see appendix F). [h] See chapter 7 for the detailed description of the EPMA measurements.

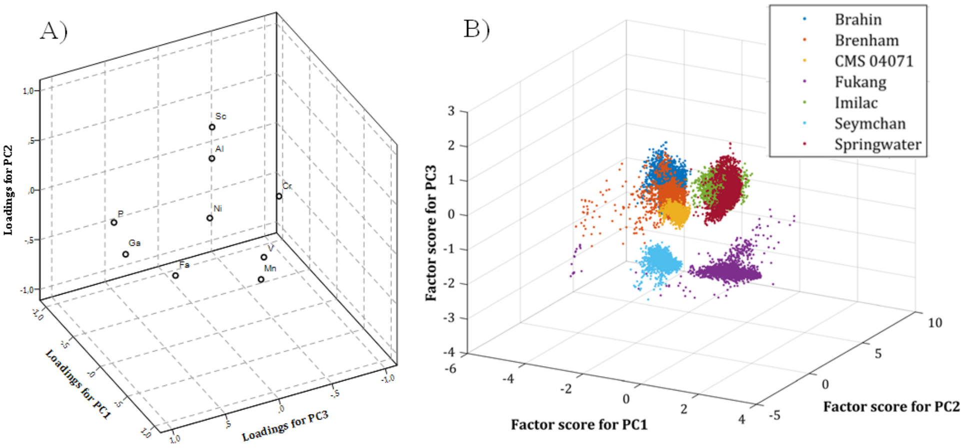

Figure 3-6. Principle component analysis scatter plots, calculated for a normalized multi-element dataset of 7 2D multi-element maps of PMG olivines, each map composed of 83x20 pixels. The P-rich inclusions are rejected from the maps and the outliers are rejected using a 3x3 median filter. A) Loading plot in varimax rotated component space. B) Factor score plot.

balancing reactions in olivine crystal lattices. At the same time, it is probably unsuitable for correlation coefficients of some elements which have tails in their distributions, and it needs to be looked at on a case-by-case basis.

A plot of the Fe/Mn versus Fe/Mg atomic ratios measured for all pallasite olivines can be used to trace processes at both the planetary scale (average values) and mineral scale (values of individual pixels within the olivine maps (figure 3-7 A). As Mn is a divalent ion and does not require charge balancing in olivine, it can substitute for Fe or Mg in octahedral positions. However, Mn^{2+} has an ion radius slightly larger than that of Fe^{2+}, and because of this, Mn^{2+} preferentially occupies M2 octahedral sites with 3 shared edges in the olivine crystal structure , similar to Fe^{2+} but to a higher extent (Papike, 2005). Due to ion radius control, Mn behaves incompatibly in olivine and serves as an indicator of igneous fractionation. Other correlation coefficients can be found in Appendix A.

6.2. P, Al and Cr lateral distribution. The crystal structure of olivine has an orthorhombic space group symmetry *Pbnm*, constructed by close-packed oxygen ions, with 1/8 of tetrahedral voids occupied by Si^{4+}, and 1/2 of octahedral spaces occupied by Fe^{2+} and Mg^{2+} ions. Octahedral positions in the olivine are distorted and not identical: octahedrons that share 6 edges are called M1, and slightly larger octahedrons that share 3 edges are called M2 (McCarty et al., 2015; Papike, 2005). Partitioning of a particular trace element into olivine depends on the elastic

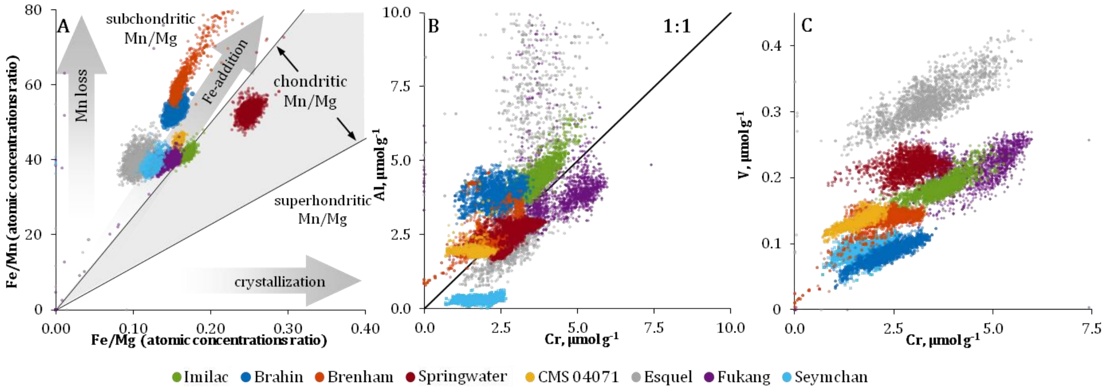

Figure 3-7. A – scatter plot of molar Fe/Mg vs. Fe/Mn in olivines of 8 PMGs. Horizontal trends in such type of plot reflect igneous fractionation processes, which change the Fe/Mg ratio, but typically do not affect the Fe/Mn ratio due to the similarities in crystal chemistry control that affect these two elements. Vertical trends reflect Mn loss/gain and, as such, Mn/Mg fractionation. Linear tends with the slopes equal to Mn/Mg ratios are recognized as an Fe loss/gain process (Goodrich and Delaney, 2000). The intra-mineral trends presented differ from those in Boesenberg *et al.* (Boesenberg et al., 2012), who reported vertical trends for single olivines. This may potentially be due to minor noise in the Fe intensity monitored via LA-ICP-MS. B – scatter plot of Al vs. Cr. C – scatter plot of V vs. Cr.

moduli of the oxygen octahedra, as well as the charges and radii of the substituting ions (Beattie, 1994; McCarty et al., 2015). In the situation of divalent ion substitution, no charge balance is needed, and occupation of the octahedral positions mostly depends on the radii of the ions. Ions of smaller radius tend to occupy M1-sites, whereas larger ions tend to occupy M2-sites. It has been demonstrated that while Ni^{2+} only occupies M1, Fe^{2+} occupies M1 and M2 randomly, and Co^{2+} occupies both M1 and M2 sites in a 3:1 ratio (McCarty et al., 2015). Non-divalent ions require charge-balancing mechanisms when substituting in the octahedral positions of olivine. The simplest mechanism is charge balance by vacancies in the surrounding crystallographic positions. For example, Cr^{3+} can form dimers balanced by one M-site vacancy ($3\ Mg^{2+}_M) \rightarrow (2\ Cr^{3+}_M\ []_M$), and pentavalent P can substitute Si^{4+} in T-sites of the olivine lattice, if charge balanced by M-site or, more rarely, T-site vacancies: ($2Si^{4+}_T\ 4Mg^{2+}_M) \rightarrow (2P^{5+}_T\ 3M^{2+}_M$) or ($5Si^{4+}_T) \rightarrow (4P^{5+}_T\ []_T$) (Milman-Barris et al., 2008). Finally, in the most complex cases, non-divalent ions can be balanced by ions of a different element, resulting in correlations between element concentrations. For example, trivalent element substitution in the M-site can be charge balanced by coupled replacement of Si^{4+} in an adjacent T-site by another trivalent ion, or by a monovalent element in the nearest site of the olivine crystal lattice (Papike, 2005). The occurrence of the latter must be quite uncommon, taking into account the low concentrations of Na in PMG olivines. Coupled element substitution, resulting in strong correlations between elements, can affect element diffusion coefficients, for example when an ordinarily fast diffusing element is charge balanced by a slower diffusing element (e.g., Cr and Al; Milman-Barris et al. 2008). Previously, P, Cr and Al have been shown to exhibit correlated zoning in olivines from a range of igneous rocks (e.g., basalts, andesites, dacites, komatiites, and martian igneous meteorites), independent of zoning in Fe-Mg. This suggests that the diffusivities under these conditions can be ordered as Fe,Mg>>Al>Cr>>P (Milman-Barris et al., 2008). It is suggested that Al^{3+} can substitute into T sites in olivine, when charge balanced with Cr^{3+} substituting into the M site with a shared corner: ($Si^{4+}_T\ Mg^{2+}_M) \rightarrow (Al^{3+}_T\ Cr^{3+}_M$). Other possible substitution types for Al are ($Si^{4+}_T\ Mg^{2+}_M) \rightarrow (Al^{3+}_T\ Al^{3+}_M$) and ($Mg^{2+}_M\ Mg^{2+}_M) \rightarrow (Na^{+}_M\ Al^{3+}_M$). It has been suggested that at different pressure conditions, one of these 3 types of Al substitution mechanisms became favourable (Taura et al., 1998). Even more complex charge-balancing mechanisms for Cr and Al have been suggested, including ($Si^{4+}_T\ 5Mg^{2+}_M) \rightarrow (P^{5+}_T\ Cr^{3+}_M\ 2Al^{3+}_M\ 2[]_M$) (Beattie, 1994; Taura et al., 1998). It is important that coupled substitution decreases the diffusion speed of the elements involved by increasing the energy barrier (E) of the diffusion coefficient (D) temperature dependence:

$$D_T = D_0 e^{-E/_{RT}} \qquad (3-5)$$

This work shows that the zoning of Cr and Al in all the pallasite olivines studied is complex, often correlated, and dominated by Cr concentration gradients (figures 3-1, 3-2, 3-3). Ratios of Cr and Al within single olivine maps of all PMGs, except Seymchan and CMS 04071, indicate weak to modest linear trends along a 1:1 line (figure 3-7 B). For 6 of the 8 pallasite olivine averages, the Cr to Al molar ratio of the map is close to 1. Taken together, these findings indicate that coupled Cr-Al substitution indeed takes place in olivines of pallasites (figure 3-7 B). This charge-balancing likely took place initially, when the olivines were formed, but might have been established later in the PMG parent body history, when the diffusion of coupled Cr and Al in the olivine crystal structure is slowed down by coupled substitution and the portion of the elements charge balanced by vacancies is lost by diffusion. The low abundance of Cr in pallasitic olivines (87-237 µg/g), comparable to the lowest level found on Earth and Mars, and significantly lower than the concentrations levels found for lunar olivines, suggests that a significant part of the Cr was present in the parent magma as Cr^{3+}, incompatible in olivine (Papike, 2005). However, Mallmann & O’Neill (2009) indicated that Cr^{2+} and Cr^{3+} are, in melts with relatively low FeO and high SiO_2, similarly compatible in olivine, even though the substitution mechanisms are different. This finding indirectly reflects differences in oxygen fugacity settings of the PMG parent body, Earth, the Moon, and Mars.

6.3. V lateral distribution. Based on an overall Cr content lower than that of terrestrial olivines, Cr is most probably present in pallasite olivines as trivalent ion (Papike, 2005). V can be tri- or tetravalent under such oxygen fugacity conditions, and it is expected that V^{3+} could behave similarly to Cr^{3+}, based on the similar ion radii, the pressure effect on the partition coefficients, and the stabilization from crystal field effects (Mallmann and O’Neill, 2009; Papike, 2005). The variations in the Cr/V ratio, or divergent behavior of Cr and V, are expected to relate to specific oxygen fugacity conditions, in which their valence states are different. The analysis of the 2D olivine maps indicates that 4 pallasites (Brahin, CMS 04071, Fukang and Seymchan) have a positive correlation between Cr and V in their olivines, while 4 other pallasites (Imilac, Brenham, Springwater and Esquel) do not demonstrate significant correlations (R <0.4) (see table 3-1). On a scatter plot of V *versus* Cr for all pallasite olivines, the data for Brahin, CMS 04071 and Imilac form well-defined linear trends along a line with a slope similar for all pallasites. The trends of Springwater, Esquel and Fukang are similar to those of the latter, but the data are more dispersed and with higher intercept for Esquel and Springwater. Seymchan and Brenham form a scatter cloud on the plot without significant correlation, probably representing multiple close trends.

6.4 Ni lateral distribution. Nickel is extremely enriched in the P-rich veinlets of the pallasite olivine. The input of P-rich veinlets can have significant effects on the overall concentrations. In the case of Seymchan "pure olivine", the rejection of veinlets from the average results in 2-fold lower Ni concentrations, while in the case of Fukang, these Ni concentrations differ by a factor of 6. Consequently, significant contents of this element are not contained in the "pure" olivine, but are rather hosted in these inclusions of unidentified mineral composition and bonding environment. As a consequence, interpreting bulk Ni olivine concentrations or isotope ratios should be done with care, for instance when studying the distribution between metal and olivine (Reed et al., 1979) or the Ni stable isotopic composition (Chernonozhkin et al., GCA, 2016, in press).

7. Implications

Although much has been written about the formational history of pallasites, it remains a topic of much debate. A better understanding of the crystal chemistry of pallasite olivine can potentially shed light on the conditions under which these meteorites formed in their parent body. The major, minor and trace element compositions of pallasite olivine are typically used to model their history of crystallization and subsequent evolution. Selected element profiles in olivine rims near the metal/olivine interface are commonly used to model and calculate cooling rates for the PMG parent body. As this requires detailed knowledge of the diffusion coefficients, and high resolution concentration profiles, this was not within our goals. The main task of this work was to extend our current knowledge on the lateral distribution of various major and trace elements in PMG olivines. First, µXRF was applied to construct large-scale major element distribution maps of pallasite thick sections, after which LA-ICP-MS was used to map major, minor and trace elements in smaller areas of olivine. The 2D LA-ICP-MS maps for the elements selected show complex relations and are often correlated, which cannot be explained as simple diffusion gradients acquired during cooling of the olivine following metal-olivine mixing. Rather, the element distributions in pallasite olivines reflect a superposition of multiple processes:

a) Primary features were inherited from the olivine formation in the parent body mantle, as is the case for the Cr-Al-V concentration oscillatory structures in Imilac and Brahin olivines. Such structures are traditionally explained by either kinetic effects at the crystal-melt interface or repeated fluctuations in the growth conditions, and can be referred to as pristine records of the magmatic conditions during the olivine formation (Ginibre et al., 2007).

b) In contrast, lamellae-like features in the olivines of Imilac and Brahin can be explained as a result of anisotropic diffusion in polycrystalline olivine.

c) Charge-balancing of substituting elements, as in the case of correlated Cr-Al distributions in all pallasite olivines studied, except for Seymchan and CMS 04071. Chromium and Al have been found to correlate strongly according to a nearly 1:1 ratio, with their atomic ratio close to unity, indicating the occurrence of a charge-balancing mechanism during their substitution into the olivine lattice.

d) Late-stage shock events and terrestrial weathering.

This study also applies multivariate analysis to the large data sets of laterally resolved trace element data obtained for multiple pallasite olivines, which highlights trends within and between the element distribution maps at the mineral and parent body scale. These relations could potentially represent genetic links between pallasites in relation to their parent body. Additionally, this work demonstrates that the results of bulk analysis of pallasite olivines should be used with care, because the ubiquitous inclusions can significantly affect the concentration values of particular elements, biasing their interpretation. Laterally resolved analysis allows discrimination of these inclusions based on a normal distribution of the selected element when calculating the element concentrations within "pure" olivine. This is the first dataset of "pure" bulk compositions for 14 elements in 7 pallasite olivines, taking into account the effects of inclusions and nuggets.

8. Appendices

Appendix A. Matrices of Pearson's correlation coefficients. A matrix of Pearson's product-moment element-element correlation coefficients for each pallasite olivine LA-ICP-MS map was calculated based on the spatially resolved quantitative multi-element data generated (figure 3-8). The P-rich veinlets were excluded from the maps prior to the calculation of the correlation coefficients, thus considering the "pure olivine" phase only. These correlation matrices provide information on the general correlations that exist between the elements within spatially resolved data. While the spatial distribution of elements in pallasite olivine is mainly explained by sub-solidus diffusion or initial overgrowth zoning, similarities in and differences between the behavior of different elements depend on the substitution mechanism and on the conditions of the processes that lead to element zoning. The limitation of the interpretation is that 2D-maps are not representative for the entire olivine crystal (e.g., due to anisotropy).

Appendix B. Fe/Mg-Fe/Mn relations. Due to the control of ion radius in substitution, Mn behaves incompatibly in olivine and serves as an indicator of igneous fractionation. Figure 3-7 A provides a Fe/Mn – Fe/Mg plot for olivines of main group pallasites. Subchondritic average Fe-Mn-Mg compositions of PMGs are in agreement with the results of (Mittlefehldt et al., 1998) who suggested that olivines of PMG are residues of partial melting in their parent body. The average compositions of Imilac, Fukang, CMS 04071, Seymchan and Esquel form a partial melting/crystallization sequence, with composition changing from nearly chondritic for Imilac to subchondritic for Esquel. The average composition of Fe-Mg-Mn in Brahin and Brenham stands out of this sequence, indicating Fe addition at constant Mg/Mn. Long trends towards 0 within all single olivines represent Fe loss/gain within single olivine minerals (probably as a result of redox processes or Fe diffusion/exchange). Compared to olivines in Earth, Moon and Mars (Papike, 2005), olivines of PMG have a smaller spread in Mn content, which indicates faster cooling.

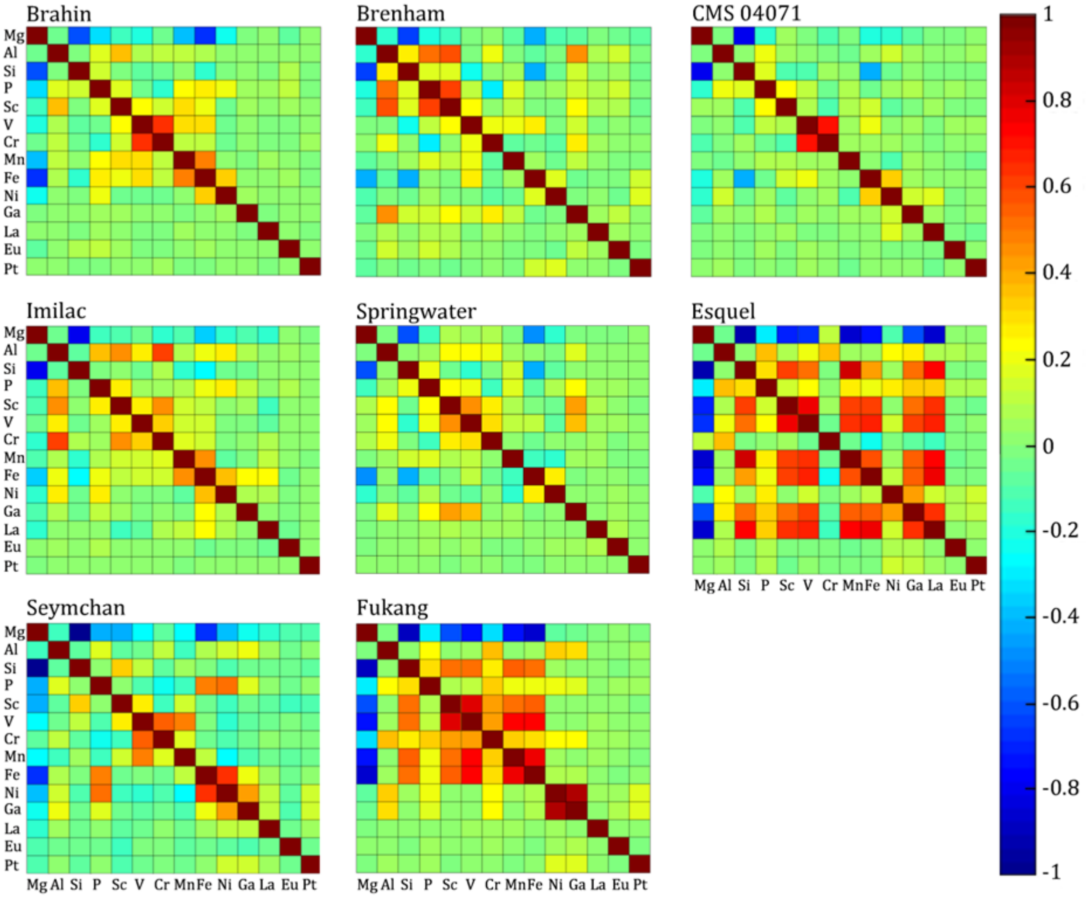

Figure 3-8. Matrices of Pearson's product–moment correlation coefficients calculated from the LA-ICP-MS spatially resolved quantitative data for the pallasite olivines. The P-rich veinlets were excluded from the maps prior to calculation of coefficients.

Appendix C. Instrument settings for ICP-MS and LA units and list of spectral interferences on the target elements

Thermo Element XR ICP-MS unit	
Sampler cone	Al; 1.1 mm aperture diameter
Skimmer cone	Al; H-type; 0.8 mm aperture diameter
RF power (cold plasma)	800 W
Resolution mode	Low (M/ÄM = 300)
Cool gas flow (Ar)	15 l min^{-1}
Auxiliary gas flow (Ar)	0.81 l min^{-1}
Sample gas flow (Ar)	0.81 – 0.99 l min^{-1}
Detection mode	Triple
Mass window	100
Samples per peak	10
Sample time	0.01 s
Runs / passes	98 / 1 (adjusted to the time interval in which a 1450 ìm line is ablated)
Duty cycle time	1.944 s
Nuclides monitored:	^{25}Mg, ^{27}Al, ^{29}Si, ^{31}P, ^{45}Sc, ^{51}V, ^{53}Cr, ^{55}Mn, ^{57}Fe, ^{60}Ni, ^{71}Ga, ^{139}La, ^{153}Eu, ^{195}Pt
Analyte G2 Laser ablation system	
Laser wavelength	193 nm
Laser pulse duration	4 ns
MFC-1 He flow rate (cell)	0.200 - 0.260 l min^{-1}
MFC-2 He flow rate (cup)	0.220 - 0.385 l min^{-1}
Energy fluence [a]	5-7 J cm^{-2}
Laser pulse frequency	20 Hz
Laser spot size	20 x 20 ìm square
Translation speed	9 ìm s^{-1}
Total area ablated	1450 x 600 ìm

Table 3-2. Instrument settings, data acquisition parameters for the Thermo Scientific Element XR ICP-MS unit and system configurations of the Analyte G2 laser ablation system used for 2D mapping of olivines.

Nuclide	Spectral interferences
^{25}Mg	$^{50}\mathrm{Ti}^{2+}$ $^{50}\mathrm{V}^{2+}$ $^{50}\mathrm{Cr}^{2+}$ $^{12}\mathrm{C}^{13}\mathrm{C}^{+}$ $^{9}\mathrm{Be}^{16}\mathrm{O}^{+}$ $^{7}\mathrm{Li}^{18}\mathrm{O}^{+}$
^{27}Al	$^{54}\mathrm{Cr}^{2+}$ $\mathbf{^{54}Fe^{2+}}$ $^{13}\mathrm{C}^{14}\mathrm{N}^{+}$ $^{11}\mathrm{B}^{16}\mathrm{O}^{+}$ $^{9}\mathrm{Be}^{18}\mathrm{O}^{+}$
^{29}Si	$^{58}\mathrm{Fe}^{2+}$ $^{13}\mathrm{C}^{16}\mathrm{O}^{+}$ $^{14}\mathrm{N}^{15}\mathrm{N}^{+}$ $^{11}\mathrm{B}^{18}\mathrm{O}^{+}$
^{31}P	$^{62}\mathrm{Ni}^{2+}$ $^{15}\mathrm{N}^{16}\mathrm{O}^{+}$ $^{13}\mathrm{C}^{18}\mathrm{O}^{+}$
^{45}Sc	$^{90}\mathrm{Zr}^{2+}$ $\mathbf{^{29}Si^{16}O^{+}}$ $^{38}\mathrm{Ar}^{7}\mathrm{Li}^{+}$
^{51}V	$^{102}\mathrm{Ru}^{2+}$ $^{35}\mathrm{Cl}^{16}\mathrm{O}^{+}$ $^{40}\mathrm{Ar}^{11}\mathrm{B}^{+}$
^{53}Cr	$^{106}\mathrm{Pd}^{2+}$ $^{37}\mathrm{Cl}^{16}\mathrm{O}^{+}$ $^{40}\mathrm{Ar}^{13}\mathrm{C}^{+}$
^{55}Mn	$^{110}\mathrm{Pd}^{2+}$ $\mathbf{^{39}K^{16}O^{+}}$ $^{40}\mathrm{Ar}^{15}\mathrm{N}^{+}$
^{57}Fe	$^{40}\mathrm{Ar}^{16}\mathrm{O}^{1}\mathrm{H}^{+}$ $^{39}\mathrm{K}^{18}\mathrm{O}^{+}$
^{60}Ni	$\mathbf{^{44}Ca^{16}O^{+}}$ $\mathbf{^{24}Mg^{36}Ar^{+}}$
^{71}Ga	$\mathbf{^{55}Mn^{16}O^{+}}$ $^{53}\mathrm{Cr}^{18}\mathrm{O}^{+}$ $\mathbf{^{31}P^{40}Ar^{+}}$
^{139}La	
^{153}Eu	$\mathbf{^{137}Ba^{16}O^{+}}$
^{195}Pt	

Table 3-3. List of spectral interferences on target isotopes. The most significant interferences are marked in bold.

Appendix D. Comparison of the measured element concentrations in GRMs with reference data

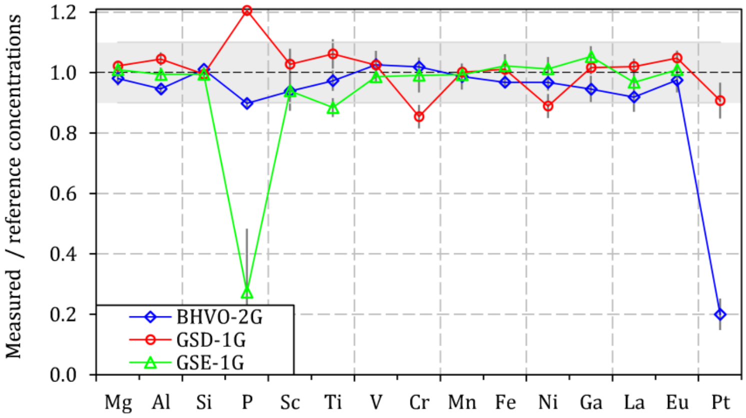

Figure 3-9. Comparison of the measured element concentrations in GRMs, used as quality control standards, with their reference data. Error bars represent standard deviation (n = 3). The grey bar represents ± 10 % deviation. The concentrations of P and Pt measured for some geological glass standards do not perfectly agree with the corresponding reference values, as 1) the concentration levels of these elements are not certified properly for these specimens and 2) because these element are not homogeneously distributed in the glass matrix.

Appendix E. large scale µXRF element distribution maps of PMG thick sections.

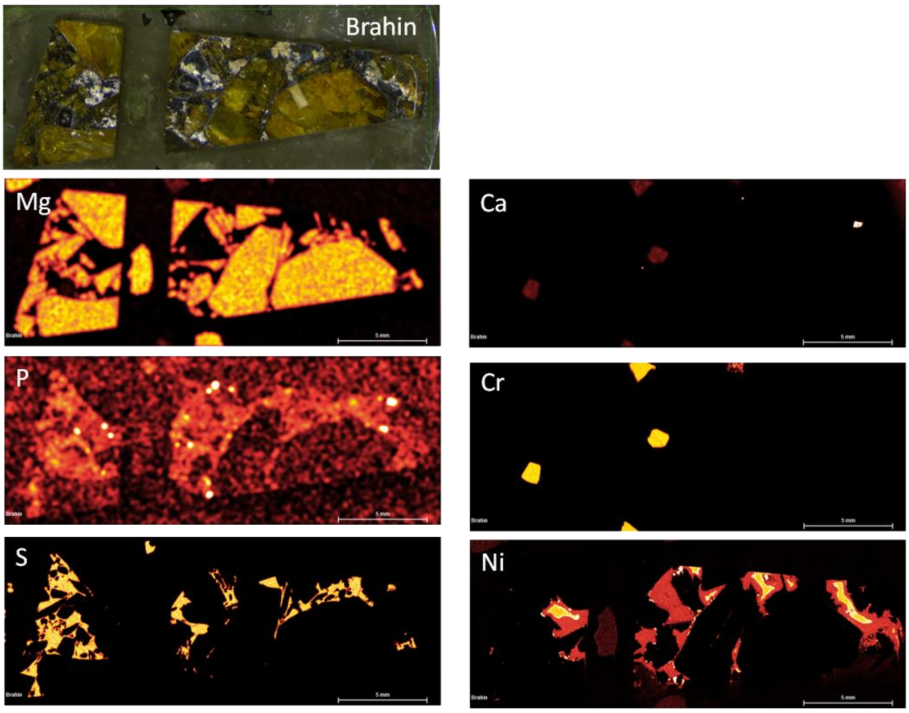

Figure 3-10. Element distribution µXRF K_{α} intencities maps of large section of Brahin PMG. In the upper row the mosaic photograph of the same section in reflected light is presented.

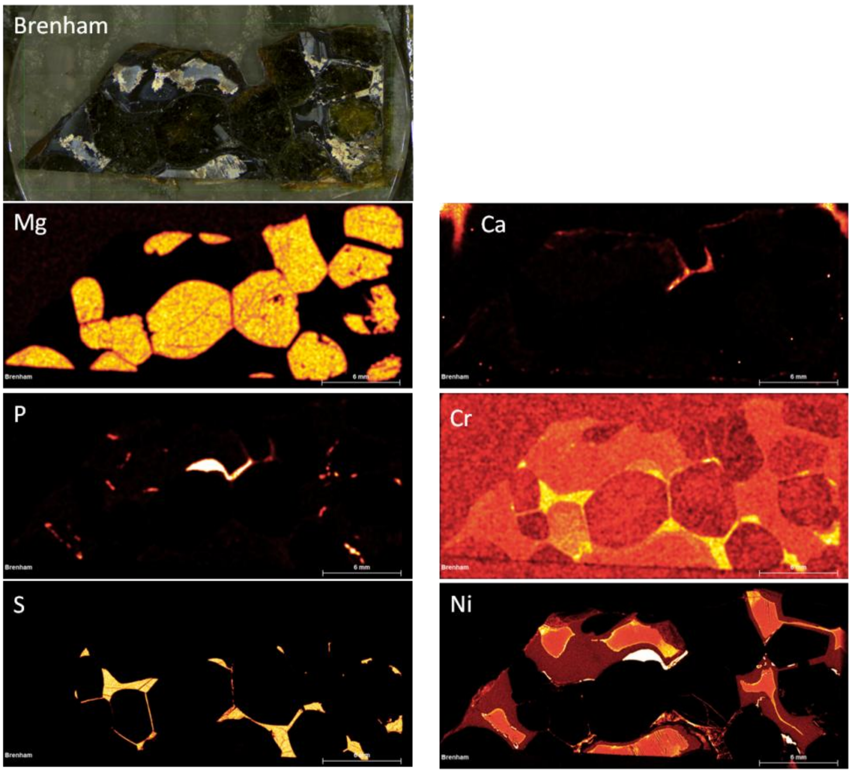

Figure 3-11. Element distribution µXRF K_α intencities maps of large section of Brenham PMG. In the upper row the mosaic photograph of the same section in reflected light is presented.

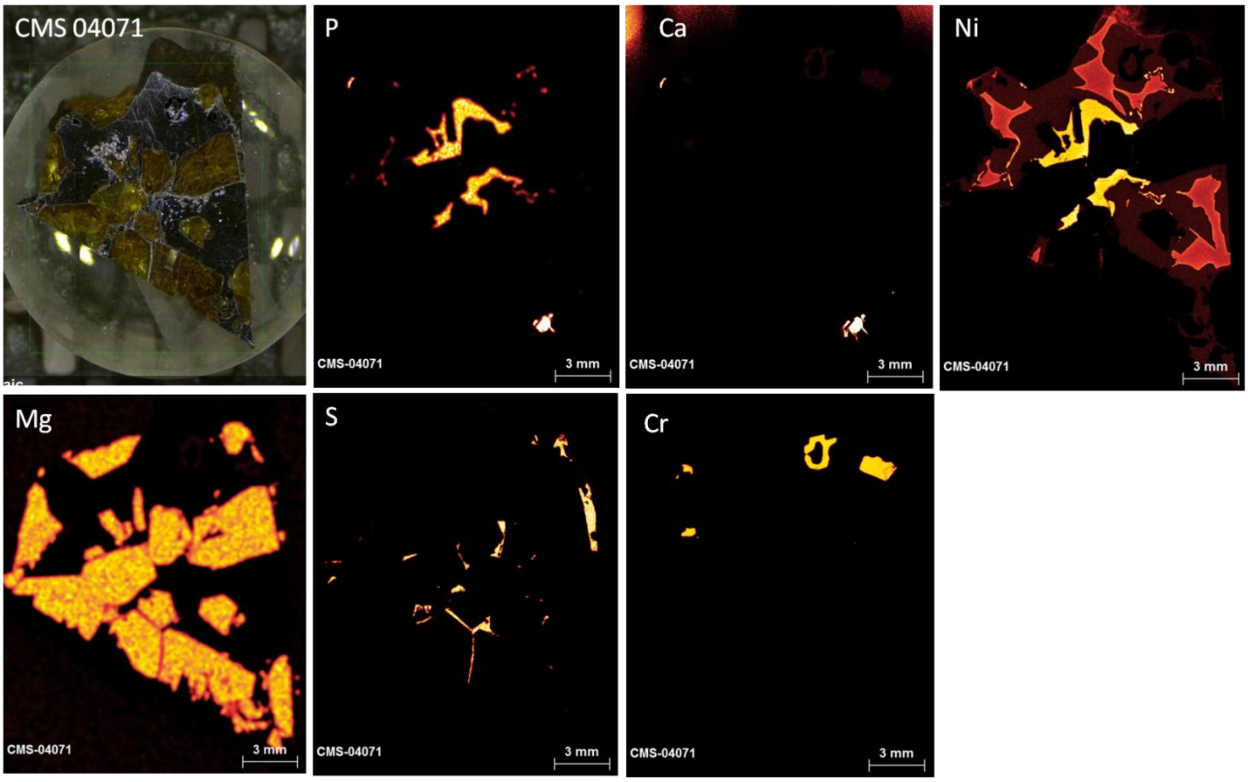

Figure 3-12. Element distribution µXRF K_α intencities maps of large section of CMS 04071 PMG. In the upper row the mosaic photograph of the same section in reflected light is presented.

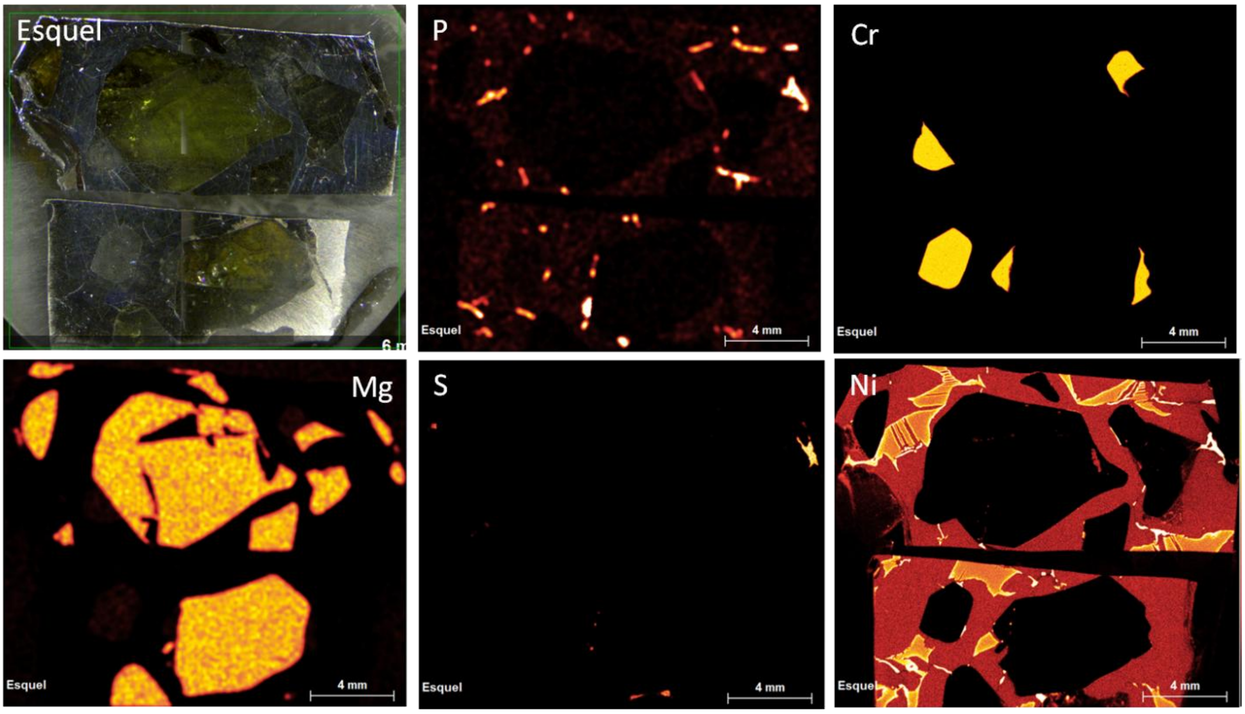

Figure 3-13. Element distribution µXRF K_{α} intencities maps of large section of Esquel PMG. In the upper row the mosaic photograph of the same section in reflected light is presented.

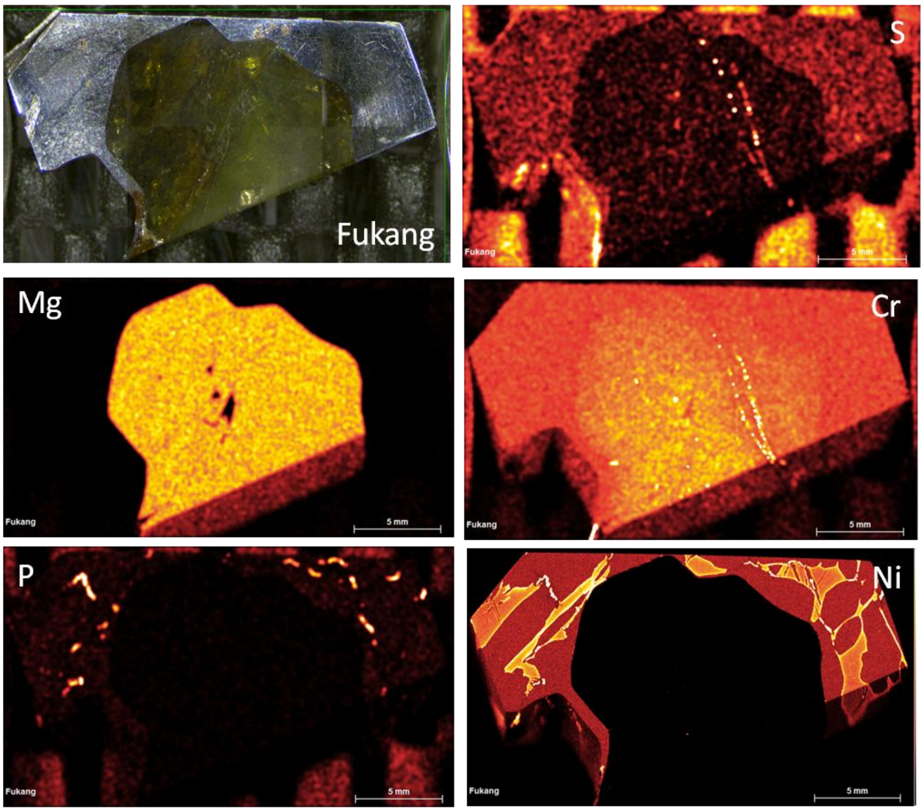

Figure 3-14. Element distribution µXRF K_{α} intencities maps of large section of Fukang PMG. In the upper row the mosaic photograph of the same section in reflected light is presented.

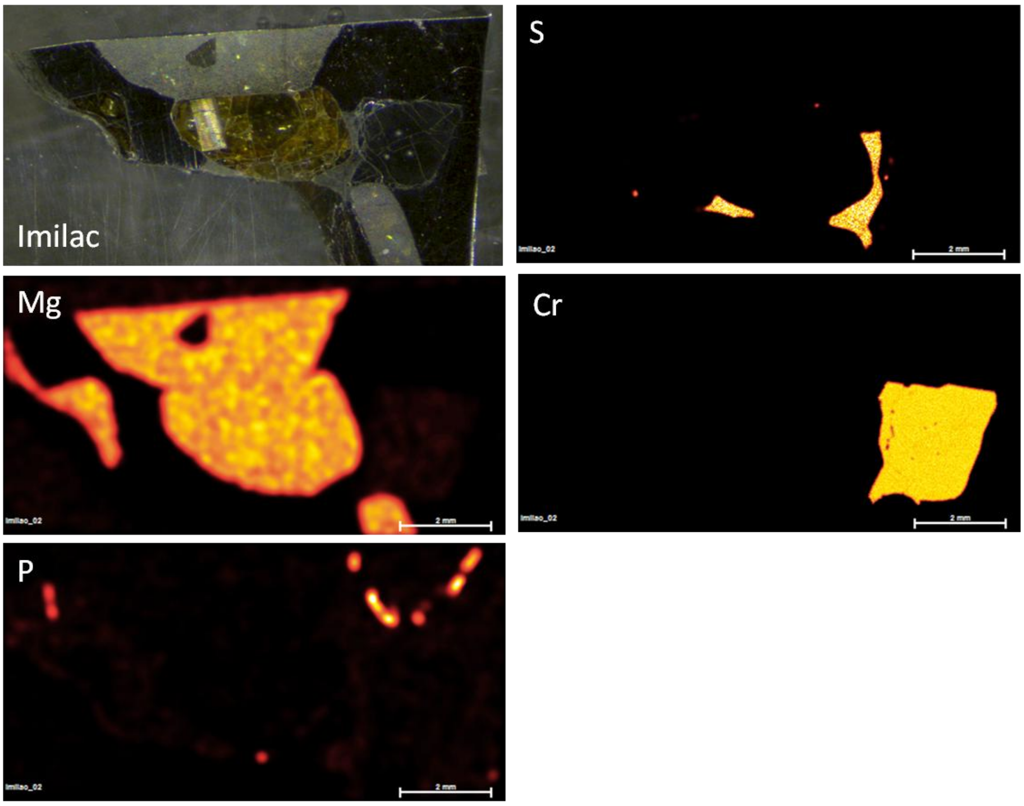

Figure 3-15. Element distribution µXRF K_{α} intencities maps of large section of Imilac PMG. In the upper row the mosaic photograph of the same section in reflected light is presented.

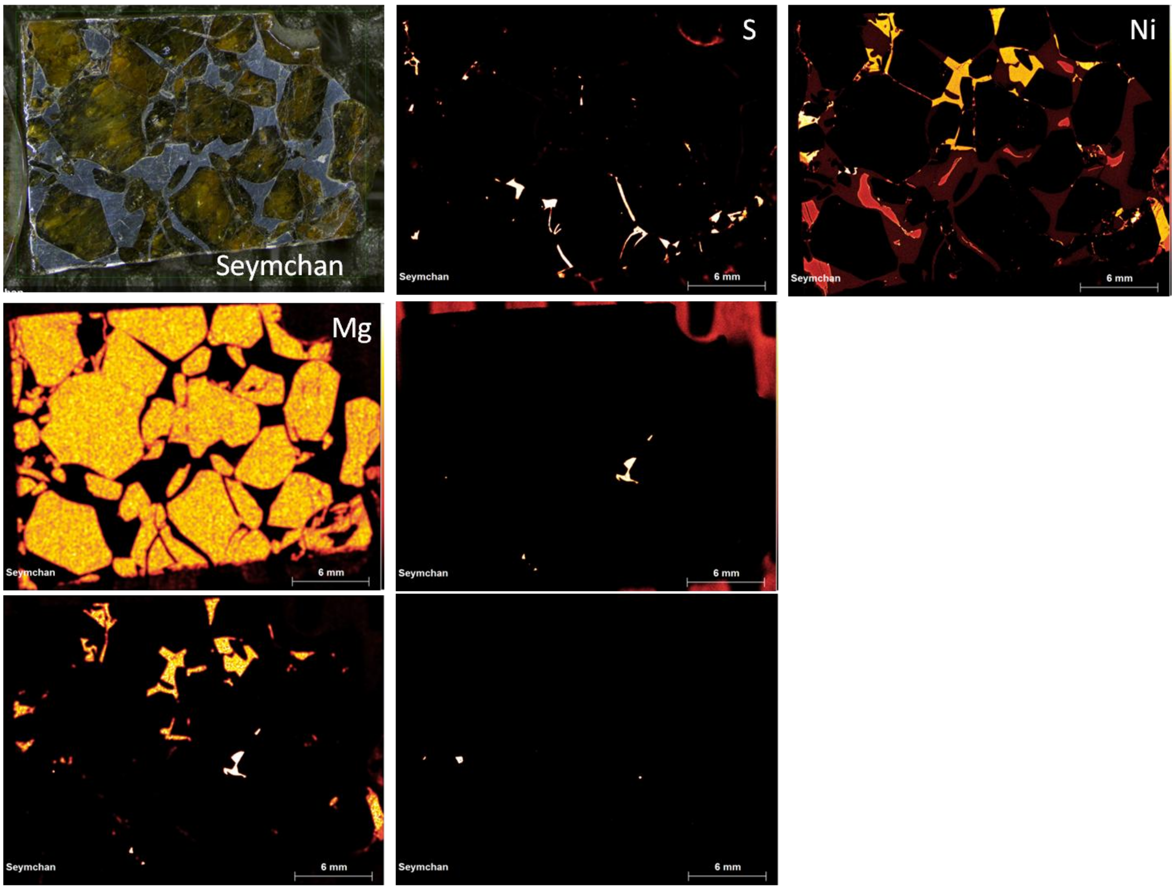

Figure 3-16. Element distribution µXRF K_{α} intencities maps of large section of Seymchan PMG. In the upper row the mosaic photograph of the same section in reflected light is presented.

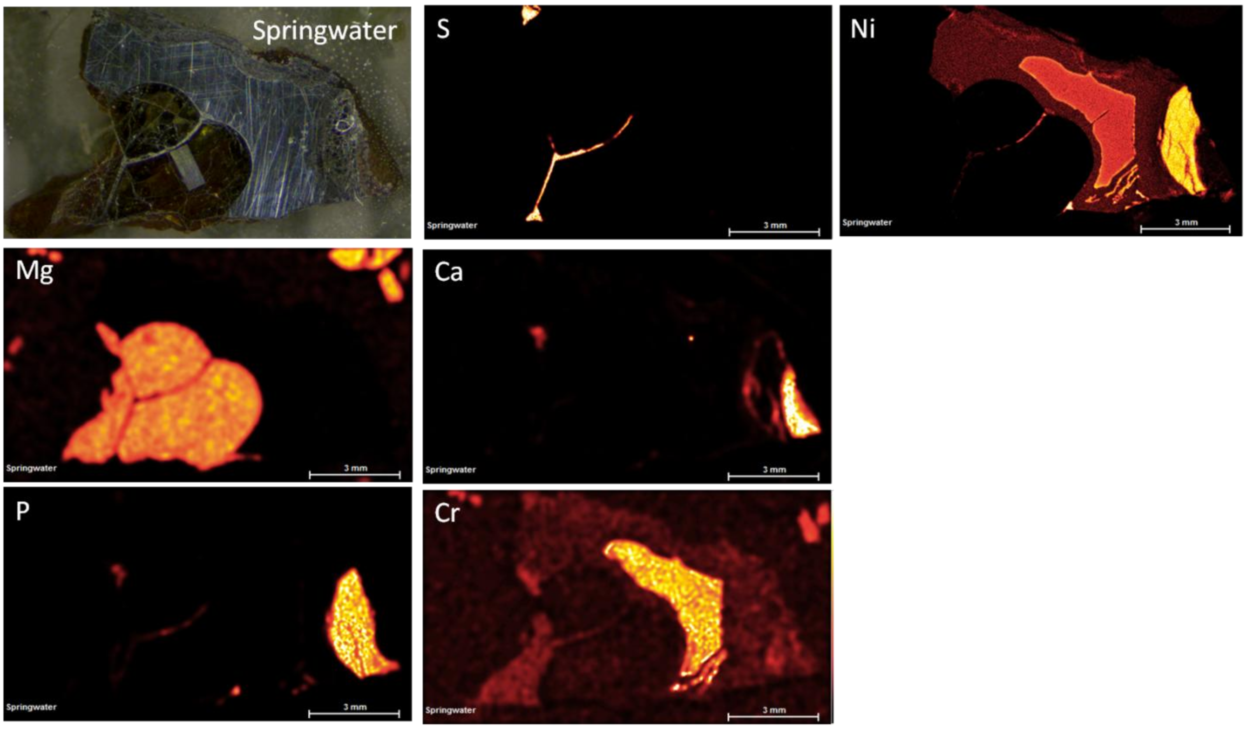

Figure 3-17. Element distribution µXRF K_α intencities maps of large section of Springwater PMG. In the upper row the mosaic photograph of the same section in reflected light is presented

Appendix F. Quantification of µXRF olivine data for Fe, Mg and Si

In XRF, the measured element intencities depend not only on the instrumental conditions and target element concentration, but are also influenced by the matrix of the sample. Matrix interactions in XRF can be described by physical models, if the fundamental parameters are well known. This allow standardless quantification to be performed, although reference materials are needed to determine the fundamental parameters. The quantification approoach used in the Bruker M4 Tornado XRF instrument software is a fundamental parameters algorithm based on the Sherman equation (the terms describing interactions of the first and the second order are shown in equations 3 – 4 and 3 – 5, respectively):

$$I_i = G \cdot \int_E \left[\frac{w_i \cdot \tau_i(E) \cdot p_i \cdot \omega_i \cdot {}^{(S_i-1)}/_{S_i}}{{}^{\mu(E)_s}/_{\sin\theta_{ein}} + {}^{\mu(E)_s}/_{\sin\theta_{aus}}} I_0\ (E) T(E)\right] dE \qquad (3-4)$$

$$S_{ij} = \frac{G}{2} \cdot \int_E \left[\frac{w_i \cdot \tau_i(E) \cdot p_i \cdot \omega_i \cdot \frac{(S_i-1)}{S_i} w_j \cdot \tau_j(E) \cdot p_j \cdot \omega_j \cdot \frac{(S_j-1)}{S_j}}{{}^{\mu(E)_s}/_{\sin\theta_{ein}} + {}^{\mu(E)_s}/_{\sin\theta_{aus}}} I_0\ (E) \times\right.$$

$$\left. \times \frac{\sin\theta_{ein}}{\mu(E)_s} \cdot \ln\left(1 + \frac{\mu(E)_s}{(\mu_j)_s \cdot \sin\theta_{ein}}\right) + \frac{\sin\theta_{aus}}{(\mu_j)_s} \cdot \ln\left(1 + \frac{(\mu_j)_s}{(\mu_j)_s \cdot \sin\theta_{aus}}\right)\right] dE \qquad (3-5)$$

Where I_i is intensity for element *i*, G is the geometry factor, τ is the linear absorbtion coefficient, *(S-1)/S* is the jump ratio, *p* is the transition probability, ω is the fluorescence yield, *w* is the weight fraction of the analyte, μ is the linear mass absorption coefficient, *E* the is energy, θ_{ein} and θ_{aus} are the incident and take off angles respectively, *T(E)* is the transmission function of the X-ray optics, C_i is the elemental correction factor and $I_0(E)$ is the excitation spectrum of the X-ray source. San Carlos olivine reference material was used to determine the elemental correction factors, which are used for quantification (the oxides of the quantified elements, FeO, MgO and SiO_2 are considered to sum up to 100 %). Although this equation cannot be solved analytically, iterative calculation is possible: the software assigns a starting composition to the sample, and Sherman’s equation to calculate the expected peak intensities for that composition. 1st and 2nd order effects (self-absorption and secondary excitation) are taken into account during the calculations. The calculated intensities are compared to those observed in the recorded spectrum, and if there are discrepancies, the composition is changed iteratively until the match is satisfactory (Haschke, 2014).

9. Acknowledgements

This research has been funded by the Planet Topers, Interuniversity Attraction Poles Program initiated by the Belgian Science Policy Office (BELSPO). Steven Goderis and Seann J. McKibbin are postdoctoral fellows of the Research Foundation – Flanders (FWO). Stijn J. M. Van Malderen is a doctoral fellow of the Research Foundation – Flanders (FWO). Frank Vanhaecke acknowledges Teledyne CETAC Technologies for financial support of his LA-ICP-MS research projects. US Antarctic meteorite samples have been recovered by the Antarctic Search for Meteorites (ANSMET) program, which has been funded by the NSF and NASA, and these sampled were characterized and curated by the Department of Mineral Sciences of the Smithsonian Institution and Astromaterials Curation Office at NASA Johnson Space Center. The Research School of Earth Sciences, Australian National University, and the Royal Belgian Institute of Natural Sciences are thanked for providing additional pallasite samples.

10. List of references

Beattie, P., 1994. Systematics and energetics of trace-element partitioning between olivine and silicate melts: Implications for the nature of mineral/melt partitioning. Chem. Geol. 117, 57–71. doi:10.1016/0009-2541(94)90121-X

Boesenberg, J.S., Davis, A.M., Prinz, M., Weisberg, M.K., Clayton, R.N., Mayeda, T.K., 2000. The pyroxene pallasites, Vermillion and Yamato 8451: Not quite a couple. Meteorit. Planet. Sci. 35, 757–769. doi:10.1111/j.1945-5100.2000.tb01460.x

Boesenberg, J.S., Delaney, J.S., and Hewins, R.H. (2012) A petrological and chemical reexamination of Main Group pallasite formation. Geochimica et Cosmochimica Acta, 89, 134–158.

Bunch, T.E., Rumble, D., I., Wittke, J.H., Irving, A.J., 2005. Pyroxene-rich Pallasites Zinder and NWA 1911: Not Like the Others, in: 68th Annual Meeting of the Meteoritical Society. Gatlinburg, Tennessee, p. 5219.

Buseck, P.R., Goldstein, J.I., 1969. Olivine compositions and cooling rates of pallasitic meteorites. Geol. Soc. Am. Bull. 80, 2141–2158. doi:10.1130/0016-7606(1969)80[2141:OCACRO]2.0.CO;2

Chakraborty, S., 1997. Rates and mechanisms of Fe-Mg interdiffusion in olivine at 980°–1300°C. J. Geophys. Res. 102, 12,317–12,331. doi:10.1029/97JB00208

Clayton, R.N., Mayeda, T.K., 1978. Genetic relations between iron and stony meteorites. Earth Planet. Sci. Lett. 40, 168–174. doi:10.1016/0012-821X(78)90087-0

Danielson, L.R., Humayun, M., Righter, K., 2006. Highly Siderophile Elements in Pallasites and Diogenites, Including the New Pallasite, CMS 04071, in: 37th Annual Lunar and Planetary Science Conference. League City, Texas, p. 2304.

Desrousseaux, A., Doukhan, J.C., Leroux, H., Van Duysen, J.C., 1997. An analytical electron microscope investigation of some pallasites. Phys. Earth Planet. Inter. 103, 101–115. doi:10.1016/S0031-9201(97)00025-3

Floss, C., 2002. Queen Alexandra Range 93148: A new type of pyroxene pallasite? Meteorit. Planet. Sci. 37, 1129–1139. doi:10.1111/j.1945-5100.2002.tb00882.x

Franchi, I.A., Greenwood, R.C., Scott, E.R.D., 2013. The IIIAB-pallasite relationship revisited the oxigen isotope perspective, in: 76th Annual Meteoritical Society Meeting. p. 5326.

Ginibre, C., Worner, G., Kronz, A., 2007. Crystal Zoning as an Archive for Magma Evolution. Elements 3, 261–266. doi:10.2113/gselements.3.4.261

Goodrich, C.A., and Delaney, J.S. (2000) Fe/Mg-Fe/Mn relations of meteorites and primary heterogeneity of primitive achondrite parent bodies. Geochimica et Cosmochimica Acta, 64, 149–160.

Greenwood, R.C., Barrat, J.-A., Scott, E.R.D., Haack, H., Buchanan, P.C., Franchi, I.A., Yamaguchi, A., Johnson, D., Bevan, A.W.R., Burbine, T.H., 2015. Geochemistry and oxygen isotope composition of main-group pallasites and olivine-rich clasts in mesosiderites: Implications for the "Great Dunite Shortage" and HED-mesosiderite connection. Geochim. Cosmochim. Acta 169, 115–136. doi:10.1016/j.gca.2015.07.023

Greenwood, R.C., Franchi, I.A., Jambon, A., Barrat, J.A., Burbine, T.H., 2006. Oxygen isotope variation in stony-iron meteorites. Science 313, 1763–1765. doi:10.1126/science.1128865

Hashike, M., 2014. Laboratory micro-X-ray fluorescence spectroscopy, Springer International Publishing, Cham, 2014. doi:10.1007/978-3-319-04864-2.

Hsu, W., 2003. Minor element zoning and trace element geochemistry of pallasites. Meteorit. Planet. Sci. 38, 1217–1241. doi:10.1111/j.1945-5100.2003.tb00309.x

Ito, M., Ganguly, J., 2006. Diffusion kinetics of Cr in olivine and 53Mn–53Cr thermochronology of early solar system objects. Geochim. Cosmochim. Acta 70, 799–809. doi:10.1016/j.gca.2005.09.020

Jones, R.H., Wasson, J.T., Larson, T., Sharp, Z.D., 2003. Milton: A New, Unique Pallasite, in: 34th Annual Lunar and Planetary Science Conference. League City, Texas, p. 1683.

Lauretta, D.S., Hill, D.H., Della-Giustina, D.N., Killgore, M., 2006. The Fukang pallasite: evidence for non-equilibrium shock processing, in: 37th Annual Lunar and Planetary Science Conference. League City, Texas, p. 2250.

Leitch, C.A., Steele, I.M., Hutcheon, I.D., Smith, J. V., 1979. Minor Elements in Pallasites: Zoning in Springwater Olivine, in: 10th Lunar and Planetary Science Conference. pp. 716–718.

Liu, Y., Hu, Z., Gao, S., Gunther, D., Xu, J., Gao, C., Chen, H., 2008. In situ analysis of major and trace elements of anhydrous minerals by LA-ICP-MS without applying an internal standard. Chem. Geol. 257, 34–43. doi:10.1016/j.chemgeo.2008.08.004

Mallmann, G., O'Neill, H.S.C., 2009. The crystal/melt partitioning of V during mantle melting as a function of oxygen fugacity compared with some other elements (Al, P, Ca, Sc, Ti, Cr, Fe, Ga, Y, Zr and Nb). J. Petrol. 50, 1765–1794. doi:10.1093/petrology/egp053

Mason, B., Graham, A.L., 1970. Minor and trace elements in meteoritic minerals. Smithson. Contrib. to Earth Sci. 3, 1–17.

McCarty, R.J., Palke, A.C., Stebbins, J.F., Hartman, J.S., 2015. Transition metal cation site preferences in forsterite (Mg2SiO4) determined from paramagnetically shifted NMR resonances. Am. Mineral. 100, 1265–1276. doi:10.2138/am-2015-5150

McKibbin, S.J., Ireland, T.R., Holden, P., O'Neill, H.S.C., Mallmann, G., 2016. Rapid cooling of planetesimal core-mantle reaction zones from Mn-Cr isotopes in pallasites. Geochemical Perspect. 2, 68–77. doi:10.7185/geochemlet.1607

McKibbin, S.J., O'Neill, H.S.C., Mallmann, G., Halfpenny, A., 2013. LA-ICP-MS mapping of olivine from the Brahin and Brenham meteorites: Complex elemental distributions in the pallasite olivine precursor. Geochim. Cosmochim. Acta 119, 1–17. doi:10.1016/j.gca.2013.05.031

Miliszkiewicz, N., Walas, S., Tobiasz, A., 2015. Current approaches to calibration of LA-ICP-MS analysis. J. Anal. At. Spectrom. 30, 327–338. doi:10.1039/C4JA00325J

Milman-Barris, M.S., Beckett, J.R., Baker, M.B., Hofmann, A.E., Morgan, Z., Crowley, M.R., Vielzeuf, D., Stolper, E., 2008. Zoning of phosphorus in igneous olivine. Contrib. to Mineral. Petrol. 155, 739–765. doi:10.1007/s00410-007-0268-7

Mittlefehdt, D.W., 1980. The composition of mesosiderite olivine clasts and implications for the origin of pallasites. Earth Planet. Sci. Lett. 51, 29–40. doi:10.1016/0012-821X(80)90254-X

Mittlefehldt, D.W., McCoy, T.J., Goodrich, C.A., Kracher, A., 1998. Non-chondritic meteorites from asteroidal bodies, in: Papike, J.J. (Ed.), Reviews in Mineralogy. Vol 36: Planetary Materials. Mineralogical Society of America, pp. 4–01–4–195.

Miyamoto, M., 1997. Chemical zoning of olivine in several pallasites. J. Geophys. Res. 102, 21,613–21,618. doi:10.1029/97JE01852

Papike, J.J., 2005. Comparative planetary mineralogy: Valence state partitioning of Cr, Fe, Ti, and V among crystallographic sites in olivine, pyroxene, and spinel from planetary basalts. Am. Mineral. 90, 277–290. doi:10.2138/am.2005.1779

Paul, B., Woodhead, J.D., Paton, C., Hergt, J.M., Hellstrom, J., Norris, C.A., 2014. Towards a Method for Quantitative LA-ICP-MS Imaging of Multi-Phase Assemblages: Mineral Identification and Analysis Correction Procedures. Geostand. Geoanalytical Res. 38, 253–263. doi:10.1111/j.1751-908X.2014.00270.x

Reed, S.J.B., Scott, E.R.D., Long, J.V.P., 1979. Ion microprobe analysis of olivine in pallasite meteorites for nickel. Earth Planet. Sci. Lett. 43, 5–12. doi:10.1016/0012-821X(79)90150-X

Selih, V.S., van Elteren, J.T., 2011. Quantitative multi-element mapping of ancient glass using a simple and robust LA-ICP-MS rastering procedure in combination with image analysis. Anal. Bioanal. Chem. 401, 745–55. doi:10.1007/s00216-011-5119-8

Shea, T., Costa, F., Krimer, D., Hammer, J.E., 2015. Accuracy of timescales retrieved from diffusion modeling in olivine: A 3D perspective. Am. Mineral. 100, 2026–2042. doi:10.2138/am-2015-5163

Taura, H., Yurimoto, H., Kurita, K., Sueno, S., 1998. Pressure dependence on partition coefficients for trace elements between olivine and the coexisting melts. Phys. Chem. Miner. 25, 469–484. doi:10.1007/s002690050138

Tomiyama, T., Huss, G.R., 2006. Minor and Trace Element Zoning in Pallasite Olivine: Modeling Pallasite Thermal History, in: 37th Annual Lunar and Planetary Science Conference. pp. 1–2.

Tomiyama, T., Huss, G.R., 2005. Minor element behavior of pallasite olivine: understandidng pallasite thermal history and chronology, in: 36th Lunar and Planetary Science Conference. p. 2071.

Turner, S., Costa, F., 2007. Measuring Timescales of Magmatic Evolution. Elements 3, 267–272. doi:10.2113/gselements.3.4.267

van Niekerk, D., Greenwood, R.C., Franchi, I.A., Scott, E.R.D., Keil, K., 2007. Seymchan: a main group pallasite - not an iron meteorite, in: 70th Annual Meteoritical Society Meeting. p. 5196.

Wasson, J.T., Choi, B.-G., 2003. Main-group pallasites: Chemical composition, relationship to IIIAB irons, and origin. Geochim. Cosmochim. Acta 67, 3079–3096. doi:10.1016/S0016-7037(03)00306-5

Watson, E.B., Cherniak, D.J., Holycross, M.E., 2015. Diffusion of phosphorus in olivine and molten basalt. Am. Mineral. 100, 2053–2065. doi:10.2138/am-2015-5416

Welsch, B., Hammer, J., Hellebrand, E., 2014. Phosphorus zoning reveals dendritic architecture of olivine. Geology 42, 867–870. doi:10.1130/G35691.1

Yang, J., Goldstein, J.I., Scott, E.R.D., 2010. Main-group pallasites: Thermal history, relationship to IIIAB irons, and origin. Geochim. Cosmochim. Acta 74, 4471–4492. doi:10.1016/j.gca.2010.04.016

Zhou, Y., Steele, I.M., 1993. Chemical zoning and diffusion of Ca, Al, Mn, and Cr in olivine of Springwater pallasite, in: 24th Lunar and Planetary Science Conference. pp. 1573–1574.

Zhukova, I., StC O'Neill, H., Cambell, I.H., Kilburn, M.R., 2014. The effect of silica activity on the diffusion of Ni and Co in olivine. Contrib. to Mineral. Petrol. 168, 1029. doi:10.1007/s00410-014-1029-z

Chapter 4

Development of an isolation procedure and MC-ICP-MS measurement protocol for the study of stable isotope ratio variations of nickel

based on publication by
Stepan M. Chernonozhkin, Steven Goderis, Lara Lobo, Philippe Claeys and Frank Vanhaecke. 2015, Journal of Analytical Atomic Spectroscopy, Volume 30, Issue 7, P. 1518-1530.

S.Ch. designed and carried out the experiments, processed the raw data, delivered and analysed the results, wrote the manuscript and took part in the discussion.

1. Abstract

Variations in the isotopic composition of Ni resulting from natural mass-dependent processes in terrestrial or extraterrestrial conditions, inhomogeneous distribution of nucleosynthetic components and/or ingrowth from radioactive parent nuclides, help us to further understand the early formation history of Solar System materials and the nature of the processes these materials subsequently experienced. In studies of Ni isotope systematics, mass-dependent variations in the isotopic composition of Ni are often bypassed because of the challenges associated with the sample preparation. At the level of natural variation studied, Ni isotope ratio measurements are extremely sensitive to spectral interference, artificial on-column isotope fractionation and possibly even to the mass bias correction model applied. To adequately address these complications, an isolation procedure and measurement protocol relying on multi-collector ICP-mass spectrometry (MC-ICP-MS) have been designed and validated in this work. The overall reproducibility obtained based on repeated measurement of a Sigma-Aldrich high-purity Ni standard is 0.036 ‰, 0.049 ‰, 0.078 ‰ and 0.53 ‰ for $\delta^{60/58}$Ni, $\delta^{61/58}$Ni, $\delta^{62/58}$Ni and $\delta^{64/58}$Ni, respectively (n = 14; 2 SD). Nickel isotope ratio variations have been studied in a set of iron meteorites and geological reference materials, and the results obtained, except for those suffering from an elevated ^{64}Zn background, show good agreement with the available literature data. By using the flexible generalized power law with a variable discrimination exponent and the three-isotope method, the processes underlying natural mass fractionation of Ni for terrestrial reference materials were found to have a mixed equilibrium/kinetic nature. Mass-dependent Ni fractionation was observed between sample fractions of the Canyon Diablo iron meteorite, and the extracted fractionation factor β corresponds to isotope partitioning following the power law.

2. Introduction

In the process of the formation and evolution of meteorite parent bodies, the isotopic composition of various transition metals (e.g., Fe, Cr, Ni, Cu, Zn) has been established to result from multiple superimposed processes, including nucleosynthesis in different stellar environments, (incomplete) mixing of the presolar carriers of these nucleosynthetic components in the crescent solar nebula, isotope fractionation during differentiation processes, ingrowth through radiogenic decay, and perturbation of the isotopic composition due to spallation by cosmic rays (Lauretta, 2011; Rumble et al., 2011).

In this context, isotopic analysis of Ni shows great potential for geo- and planetary applications. As an abundant element in the Solar System, Ni is present in sufficiently high concentrations in most meteorites. Ni, mostly partitioned into the metal-silicate-troilite system, experiences mass-dependent fractionation of its isotopes during evaporation/condensation, core formation, and magmatic processes. Other transition metals that have recently been studied in this context include Fe (Weyer et al., 2005), Cr (Sanborn et al., 2014), Mo (Wieser and De Laeter, 2009), Zn (Moynier et al., 2007) and W (Breton and Quitté, 2014). In contrast to other elements, Ni only occurs in a single stable oxidation state and surrounding coordination only, apart from its neutral metal state. Hence, redox-controlled mass-dependent fractionation processes do not affect the isotopic composition of Ni, restricting the mechanism underlying mass-dependent fractionation to isotopic exchange between phases (Gueguen et al., 2013; Lazar et al., 2012; Richter et al., 2009; Young et al., 2015). A comparative study of the effect of mass-dependent isotope fractionation observed for Ni in genetically related meteorite fractions could not only show a correlation with the concentration of particular major elements (*e.g.*, P, S), but also with the cooling rate of the meteorite and/or the isotopic composition of other fractionated elements (*e.g.*, O, Cr).

When applied to terrestrial igneous rocks, information on the mass-dependent isotope fractionation for Ni constitutes a useful marker of high-temperature processes and crystallization effects in magmatic systems (Richter et al., 2009; Young et al., 2015). Ni isotope fractionation processes appear to be systematic, with positive and negative fractionations, characteristic of low- and high-temperature processes, respectively (Gueguen et al., 2013).

Ni isotopes were recently also used to track the process of continental weathering (Estrade et al., 2015; Ratié et al., 2015). In addition, Ni isotope ratios can be used to highlight ancient ocean chemistry changes (*e.g.*, the decline of marine methanogens or the onset of the Great Oxidation Event) (Konhauser et al., 2009) via investigation of fractionation effects taking place during marine sedimentation (Porter et al., 2014; Wasylenki et al., 2015), in the water cycle (Cameron and Vance, 2014), or during interaction with biological systems (Cameron et al., 2009; Deng et al., 2014; Estrade et al., 2015).

At the same time, mass-dependent fractionation of Ni isotopes occurring during the evolution of meteorite parent bodies can be quantified and cancelled out using mass-fractionation laws (Baxter et al., 2012b) and one pair of Ni isotopes that are not prone to non mass-dependent effects as internal standard. Different to some other elements (e.g., W (Markowski et al., 2006; Scherstén et al., 2006), the neutron capture cross-sections are small for all Ni isotopes, making any resolvable cosmogenic spallation effects on Ni isotopes unlikely (Quitté et al., 2006; Steele et al., 2011), and thus, the pristine initial isotopic composition of Ni can be determined. As Ni has five isotopes, the remaining non mass-dependent Ni isotopic compositions of extraterrestrial material (including pre-solar grains) – *i.e.* after removing the mass-dependent component – can refine our knowledge of the contributions of the different stellar nucleosynthetic sources to the solar nebula (Marhas et al., 2008), or permit insight into the homogeneity/heterogeneity of the distribution of Ni in the protosolar nebula to be obtained (Regelous et al., 2008). Information on the non mass-dependent Ni isotopic composition can be used to evaluate possible mass-independent fractionation (Steele et al., 2011) (as Ni has both odd and even isotopes (Epov et al., 2011; Malinovsky and Vanhaecke, 2011) during the evolution of meteorite parent bodies. In addition, ^{60}Ni is a part of a short-life isotopic decay system ($^{60}\text{Fe} \rightarrow {}^{60}\text{Ni} + \beta^{-} + \bar{\nu}$; $T_{1/2}$=2.62 My (Rugel et al., 2009) that serves as a chronometer providing information on the time-scales of planetesimal melting and planetary differentiation, ultimately leading to core formation (Quitté et al., 2006). Because ^{60}Fe is produced in stars only, its initial abundance can be calculated to provide a constraint on the stellar contribution of radionuclides to the early Solar System and on the nature of this stellar source (Tachibana et al., 2006).

Insight into the non mass-dependent contribution to the isotope fractionation observed for Ni in conjunction with other isotopic systems, such as those of O, Cr, Ti, can provide supporting evidence for petrogenic relationships between different meteorites and their groups (Sanborn et al., 2014). As the non mass-dependent Ni isotopic composition is interpreted to result from mixing of presolar sources, Ni isotope ratios provide knowledge on the genetic ancestry of particular meteorite groups.

MC-ICP-MS is a state-of-the-art analytical technique for isotopic analysis, but it requires target element isolation to reduce matrix effects and spectral interferences. At the same time, chromatographic isolation is known to introduce artificial isotope fractionation, which, together with the limited scale of Ni isotope ratio variations caused by natural fractionation, challenges Ni isotopic analysis. To avoid this undesirable bias during sample preparation, 100 % recovery of Ni should be realized. After isolation, Ni mass-dependent isotope fractionation can be studied using MC-ICP-MS relying on an admixed internal standard (e.g., Cu) for correction of instrumental mass discrimination or, alternatively, using the double-spike technique. The latter was often preferred in previous studies of Ni mass-dependent fractionation, as it is less sensitive to the isolation procedure. However, double-spiking is much more laborious and can typically provide information on a single Ni isotope ratio only (Gall et al., 2012; Gueguen et al., 2013).

Although several studies of non mass-dependent isotope fractionation have focused on Ni, the robustness of the figures of merit achieved remains debatable. At the reported levels of precision, it remains unclear whether Ni isotope ratio data can be applied to study the problems discussed above, as the relevant levels of Ni fractionation are at the limit of the capabilities of the MC-ICP-MS technique (sub part per ten thousand units).

For the applications in which isotope ratios involving all of the Ni isotopes are required, clean lab conditions become crucial to produce reliable data for ratios involving ^{64}Ni. This is the least abundant Ni isotope, very sensitive to spectral interferences, especially as the result of isobaric overlap due to Zn contamination. As a result, adequate separation factors should be aimed at in the design of the isolation procedures. Also, the low isotopic abundance of ^{64}Ni (0.9255 % (Berglund and Wieser, 2011) deteriorates the precision of its measurement, and questions the utility of isotope ratios involving ^{64}Ni for the issues discussed above.

To overcome the challenges mentioned and understand which applications of Ni isotopic studies can be addressed by the current state-of-the-art analytical techniques, Ni isolation procedures, MC-ICP-MS measurement protocols and mass bias correction methods have to be evaluated and optimized.

3. Experimental

3.1. Reagents and samples. Only high-purity reagents and acids were used throughout the experiments. Pro analysis grade nitric acid (65 %, Chem-Lab, Belgium) was further purified through sub-boiling in a PFA apparatus. Optima-grade hydrochloric (37 %, Seastar Chemicals Inc, Canada) and trace-metal grade hydrofluoric (47-51 %, Seastar Chemicals Inc, Canada) acids were used as such. Water was purified (resistivity ≥18.2 MΩ cm) in a Milli-Q Element water purification system (Millipore, France). Purissima grade acetone, ultrapure 9.8 M H_2O_2 and dymethylglyoxime (DMG) were purchased from Sigma Aldrich (Belgium). All the Teflon® recipients, disposable plastic tubes and pipette tips used for the sample preparation were additionally cleaned by soaking in 10 % pro-analysis HCl under class-10 clean lab conditions for 48 h. 1000 mg ml^{-1} single-element stock solutions were acquired from Merck (Darmstadt, Germany), PlasmaCAL (Quebec, Canada), Inorganic ventures (Christiansburg,Virginia, USA) and Alfa Aesar GmbH (Karlsruhe, Germany).

Four iron meteorite specimens (IVB-an Chinga, IIB Sikhote-Alin, IIE Elga and IIC Darinskoe) were obtained from the Central Siberian Geological Museum, V.S. Sobolev Institute of Geology and Mineralogy, Russia, while IAB-MG Canyon Diablo was obtained from a commercial meteorite dealer. For three of these materials (Sikhote-Alin, Chinga and Canyon Diablo), information on their Ni isotopic composition were published in previous studies, allowing cross-validation of the results obtained in this work. Terrestrial mafic rock reference materials were used to expand the validation of the isolation procedure. These geological reference materials (GRMs) include the basalts BHVO-1, BHVO-2 and BIR-1, peridotite PCC-1, diabase DNC-1 and dunite DTS-1 from the United States Geological Survey (USGS, USA), ultramafic rock OKUM from Geosciences Laboratories (Sudbury, Ontario, Canada), basalt JB-1b and peridotite JP-1 from the Geological Survey of Japan (GSJ) and basalt BE-N and iron

Column 1 (2.5 ml Dowex 50W-X4 200-400 mesh)		
Sample load	10 ml	0.6 M HCl – 90 % acetone
Matrix wash off	35 ml	0.6 M HCl – 90 % acetone
	10 ml	0.6 M HCl – 95 % acetone
Ni collection	6 ml	0.6 M HCl – 95 % acetone – 0.1 M DMG
Column 2 (1 ml Eichrom 1X8 100-200 mesh)		
Sample load, Ni collection	5 ml	0.5 M HF – 1 M HCl
Ni collection	4 ml	0.5 M HF – 1 M HCl
Column 3 (1 ml Eichrom 1X8 100-200 mesh)		
Sample load, Ni collection	1 ml	6 M HCl + 0.01 % H_2O_2
Ni collection	4 ml	6 M HCl + 0.01 % H_2O_2

Table 4-1. Summary of the Ni ion-exchange isolation procedure

formation IF-G from the Centre de Recherches Pétrographiques et Géochimiques (CRPG, France). Reference materials of iron (NBS 365, NBS 461) and alloyed steel (NBS 19g, NBS 125b, NBS 362, NBS 1286) from the National Institute of Standards and Technology (NIST, USA) with a Ni content varying from 0.04 to 2.8 wt% were used to emulate the behavior of the matrix of iron meteorites in the ion exchange separation experiments.

3.2. Digestion. Iron meteorite fragments were cut from the bulk mass with a diamond disk saw. To avoid surface contamination effects, visibly altered (*i.e.* oxidized) surfaces were cleaned with silicon carbide sandpaper, subsequently etched with dilute HNO_3 in an ultrasonic bath and finally rinsed with ethanol and dried. Fragments of about 100 mg were weighed and transferred into 15 ml Savillex Teflon® beakers and digested in 4 ml of freshly prepared *aqua regia* (1:3 HNO_3:HCl). For that purpose, the closed vessels were heated at 90 ^oC during 72 hours. Digestion of silicate samples was performed using a two-step microwave-assisted acid digestion in an MLS-1200 MEGA Microwave digestion system (Milestone, Italy). Each step consists of 30 minutes of heating in a Teflon® vessel at the maximum power of 650 W. First, a mixture of HF : HNO_3 (2.5 ml : 5 ml) was used to dissolve a weighed amount of geological reference material (GRM) powder of about 150 mg. After evaporation to incipient dryness (90 °C), the digestion was continued using the same program with 6 ml of *aqua regia*. After cooling down, the vessels were opened and the solutions were evaporated to incipient dryness at 90 °C. The residues were redissolved in 0.4 ml of concentrated HCl and evaporated to incipient dryness again. The last step was repeated twice. Finally, the residues were redissolved in the corresponding medium for chromatographic isolation of Ni.

3.3. Isolation. Ni isolation was carried out in a 3-step ion exchange chromatographic procedure. In a first step, Ni is separated from the main part of the matrix. Two additional steps are subsequently applied to separate Ni from Ti, Fe and Zn. A summary of the Ni ion-exchange isolation procedure is provided in table 4-1.

Step 1: For the first step of the chromatographic isolation procedure, 2.5 ml of Dowex 50WX4 resin (200-400 mesh) were loaded into a 2 ml polypropylene column with an inner diameter of 8 mm (Eichrom Technologies, France). The resin was washed with 10 ml of H_2O, 10 ml of 6 M HCl and conditioned using 10 ml of 0.6 M HCl - 90 % acetone (a mixture of 0.5 ml of 12 M HCl, 0.5 ml of MQ-water and 9 ml of acetone). The sample was loaded onto the column in 10 ml of 0.6 M HCl - 90 % acetone. The column was then washed with 35 ml of 0.6 M HCl - 90 % acetone and 10 ml of 0.6 M HCl - 95 % acetone. Ni was eluted with 6 ml of 0.6 M HCl - 95 % acetone - 0.1 M DMG and collected into a 15 ml Savillex Teflon® beaker. The target fraction was evaporated to dryness. The organic residue in the resulting fraction was destroyed via repeated oxidation by concentrated acids. First, 0.3 ml of 14 M HNO_3 and 0.1 ml of H_2O_2 were added and the closed beaker was heated at 140 ^oC for 3 h, and the resulting digest was evaporated to dryness. This step was repeated twice and alternated with 15 min of ultrasonification. The decomposition of organic material was completed with 0.4 ml of *aqua regia* at 140 ^oC for 3 hours, and the digest was evaporated to dryness. The residue was redissolved in 0.1 ml of 12 M HCl and again evaporated to dryness in order to eliminate possible nitride ions in the second ion exchange step of the Ni isolation procedure. All the evaporations were done at 90 ^oC, apart from evaporation of the acetone fractions, performed at 80 ^oC.

Step 2: 1 ml of Eichrom 1x8 anion-exchange resin (100-200 mesh) was loaded into a 2 ml polypropylene column with an inner diameter of 0.8 cm (Eichrom Technologies, France). The resin was washed with 10 ml of H_2O, 5 ml of 1 M HNO_3 and 5 ml of 6 M HCl before conditioning using 5 ml 0.5 M HF – 1 M HCl. The sample was loaded onto the column in 5 ml of 0.5 M HF - 1 M HCl medium. Ni starts to elute immediately and was quantitatively washed off with an additional 4 ml of 0.5 M HF - 1 M HCl and collected in a Savillex Teflon® beaker. The Ni fraction was evaporated, the residue redissolved in 0.1 ml of 12 M HCl and evaporated to dryness again to eliminate fluorides.

Step 3: A similar Eichrom columns was loaded with 1 ml of Eichrom 1x8 anion exchange resin (100-200 mesh). The resin was washed with 10 ml of H_2O, 5 ml of 1 M HNO_3, and conditioned using 5 ml of 6 M HCl. The sample was loaded onto the column in 1 ml of 6 M HCl medium. With an additional 5 ml of 6 M HCl, Ni was eluted quantitatively in a Savillex Teflon® beaker and evaporated to dryness. The residue was dissolved in 0.1 ml of 14 M HNO_3 and evaporated to dryness again. The latter was repeated twice to eliminate the clorides. Finally, the residue was dissolved in 3 % HNO_3 for ICP-MS measurements.

An aliquot from the final fraction was taken for elemental analysis, while the main fraction was used for Ni isotopic analysis. The last two stages of the Ni isolation procedure were carried out under class-10 clean lab conditions to prevent airbourne contamination.

3.4. Instrumentation. To record the elution profiles of the single Ni isolation steps, GRMs and synthetic mixtures of mono-element standard solutions were processed following the procedures described above. Element concentrations in the individually collected fractions were determined using a Thermo Scientific Element XR sector field ICP-MS instrument via external calibration. Rh was relied on as an internal standard. Medium ($m/\Delta m = 4000$) and high ($m/\Delta m = 10,000$) mass resolution settings were used to resolve interferences.

All target (Ni), and the corresponding leading and tailing chromatographic fractions of the samples selected for Ni isotope characterization were first analyzed for their element composition to ensure full Ni recovery and adequate separation from interfering elements. For this purpose, a Thermo Scientific XSeries II quadrupole-based ICP-MS instrument was used. External calibration was used for this purpose with Rh as an internal standard.

Isotope ratios were measured using a Thermo Scientific Neptune multi-collector ICP-MS unit in medium resolution mode (see table 4-2). Samples and standards were presented in 3 % HNO_3 solution with a Ni concentration of

Instrument settings		
RF power[a], W		1250
Gas flow rates[a], l min^{-1}	Cool	15
	Auxiliary	0.8
	Nebulizer	0.98
Sampler cone		Ni: 1.1 mm aperture diameter
Skimmer cone		Ni, H-type: 0.8 mm aperture diameter
Sample uptake		Pumped via peristaltic pump, 0.1 ml min^{-1}
Nebulizer		Concentric, 100 µl min^{-1}
Spray chamber		Double, cyclonic and Scott-type sub-units
Resolution mode		Medium[b]
Data acquisition		
Mode		Dynamic (^{56}Fe and ^{66}Zn are measured non-simultaneously for mathematical correction[b])
Idle time, s		3
Integration time, s		4.194
Number of integrations		3
Number of blocks		4
Number of cycles per block		3

Cup configuration[c]							
Cup	L_4	L_2	L_1	C	H_1	H_2	H_3
Amplifier	$10^{11}\Omega$	$10^{11}\Omega$	$10^{11}\Omega$	$10^{12}\Omega$	$10^{11}\Omega$	$10^{12}\Omega$	$10^{11}\Omega$
1st line	^{58}Ni, ^{58}Fe	^{60}Ni	^{61}Ni	^{62}Ni	^{63}Cu	^{64}Ni, ^{64}Zn	^{65}Cu
2nd line				^{56}Fe			
3rd line				^{66}Zn			

Table 4-2. Instrument settings, data acquisition parameters and multi-collector detector configuration for the Thermo Scientific Neptune MC-ICP-MS instrument used for Ni isotopic analysis. [a] Parameters optimised on a daily basis for highest sensitivity and stability. [b] Δm for pseudo-high resolution in MC-ICP-MS is defined as the mass diference between $m_{5\%}$ and $m_{95\%}$, corresponding to 5 % and 95 % of the signal intensity level on the plateau, respectively. A resolving power of 7400 was measured using the ^{238}U signal in MR mode. Such a definition of resolving power exceeds that based on atomic mass difference by more than a factor of two (Vanhaecke and Moens, 2004). [c] See 'Results and discussion' section for further information.

1000 µg l^{-1}. The instrumental background originating from the Ni cones was insignificant compared to the signal of samples (< 10^{-2} V and 15 V respectively). Each sample was measured 2-3 times during a daily sequence to improve the precision. Ni isotope ratios are expressed relatively to the NIST SRM 986 Ni isotopic standard (NIST, USA). 10^{12} Ω amplifiers are used for the least intense signals to improve counting statistics.

3.5. Correction for instrumental mass discrimination was performed via internal correction, relying on (a) the $^{63}Cu/^{65}Cu$ isotope ratio of an admixed in-house Cu isotopic standard, or (b) the $^{62}Ni/^{58}Ni$ isotope ratio of the sample itself. These corrected ratios are indicated hereafter as $(^{x}Ni/^{58}Ni)_{Cu\,corr}$ and $(^{x}Ni/^{58}Ni)_{Ni\,corr}$, respectively. The latter approach not only corrects for instrumental mass discrimination, but also cancels out any natural or artificial mass-dependent Ni isotope fractionation experienced by the sample during its evolution or sample preparation (Baxter et al., 2012b; Steele et al., 2011). The Russell (kinetic) law (Russell et al., 1978) was found suitable for the correction of mass bias, with the version revised by Baxter found most successful (Baxter et al., 2006). For the details on the evaluation of the different correction laws, the reader is referred to the appendix. Finally, sample-standard bracketing was applied to correct for minor drift of instrumental parameters. Isotope ratios internally corrected with Cu are reported as the relative differences of the Ni isotope ratio ($\delta^{x/58}Ni$) relative to that in the NIST SRM 986 Ni isotopic reference material, measured within the same sample-standard bracketing sequence:

$$\delta^{x/58}Ni = \left[\frac{(^{x}Ni/^{58}Ni)_{Cu\,corr,smp}}{(^{x}Ni/^{58}Ni)_{Cu\,corr,NIST986}} - 1\right] \cdot 1000 \qquad (4-1)$$

Hereafter, these mass-dependent variations are reported in permil (‰) and the corresponding results are called mass-dependent. When reporting isotope ratios, internally corrected by $^{62}Ni/^{58}Ni$, to cancel out all natural mass-dependent fractionation effects, the $\varepsilon^{x/58}Ni$ notation is used to distinguish these results from those normalized by Cu correction. As these deviations with respect to the isotopic reference material are generally smaller, they are reported in pptt (part per ten thousand) and the corresponding results are called non mass-dependent:

$$\varepsilon^{x/58}Ni = \left[\frac{(^{x}Ni/^{58}Ni)_{Ni\,corr,smp}}{(^{x}Ni/^{58}Ni)_{Ni\,corr,NIST986}} - 1\right] \cdot 10000 \qquad (4-2)$$

4. Results and discussion

4.1. Mathematical corrections of isobaric interferences. The Thermo Neptune multi-collector ICP mass spectrometer used is equipped with 9 Faraday cups, which is theoretically sufficient to monitor all Ni isotopes simultaneously, the Cu isotopes for the internal correction, as well as ^{56}Fe and ^{66}Zn for mathematical correction of isobaric interferences. However, due to instrument limitations, the mass range of interest, ranging from 56 to 66 amu cannot be covered simultaneously. As a result, a dynamic mode of acquisition was applied, and the relevant isotopes of Fe and Zn were not monitored simultaneously. The intensity of the ^{56}Fe signal was always found to be very low compared to that of the Ni isotopes. The ^{56}Fe signals of samples and bracketing standards were found to be similar (about 10^{-2} V). For comparison, intensities for ^{58}Ni were typically around of 15 V. Typically, the ^{66}Zn signals for the samples were similar to those obtained for the bracketing standards (<10^{-3} V), but occassionally reached intensities 2-5-fold higher. Mathematical corrections for isobaric interferences affecting ^{58}Ni and ^{64}Ni were based on non-simultaneous measurement of ^{56}Fe and ^{66}Zn, the Russell exponential law, and a mass bias correction factor calculated using the Cu internal standard. For this purpose, standards with natural Fe, Cu and Zn isotopic composition were measured to calculate the linear correlation parameters of the fractionation coefficients $f_{Fe} - f_{Cu}$ and $f_{Zn} - f_{Cu}$ (Woodhead, 2002). These parameters were then used to calculate the mass-biased $^{66}Zn/^{64}Zn$ and $^{58}Fe/^{56}Fe$ ratios for the samples, and finally, these ratios were used to correct the ^{58}Ni and ^{64}Ni intensities for isobaric overlap resulting from the trace levels of Fe and Zn, respectively. The effect of the mathematical correction on ^{58}Ni was always insignificant, as this is the most abundant isotope of Ni, interfered by the least abundant isotope of Fe. On the other hand, the effect of ^{64}Zn on ^{64}Ni is substantial. Figure 4-1 (A) shows the data for NIST SRM 986, suffering from a background Zn contamination (originating from the different autosampler vials) before and after the mathematical correction. As ^{64}Ni was found to be very sensitive to background Zn interference, the levels of Zn which could be corrected for mathematically were determined experimentally. Figure 4-1 (B) shows the ^{64}Zn-corrected results for the NIST SRM 986 Ni isotopic standard (1 µg g^{-1}), when doped with different concentrations of Zn. These plots show that Zn background levels of up to 10 ng g^{-1} can be corrected for without significant

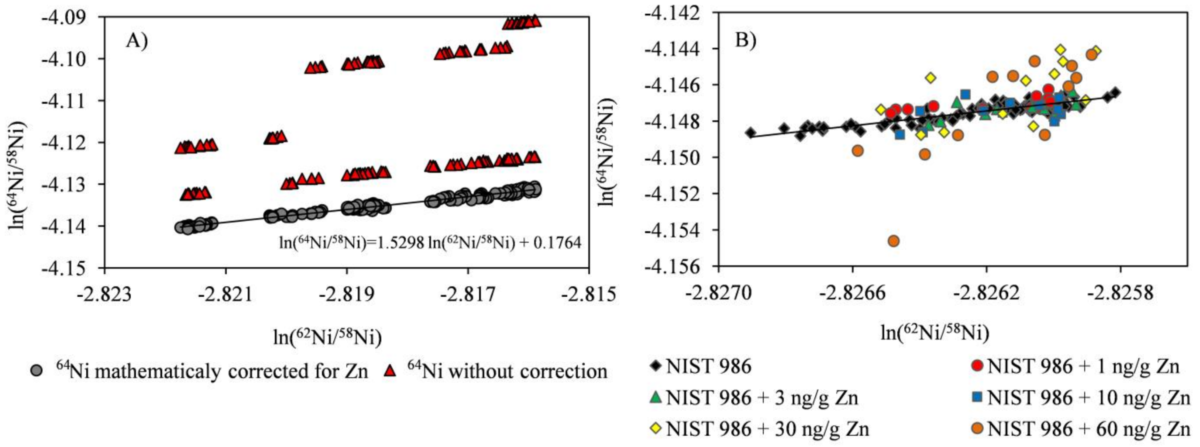

Figure 4-1. A – The effect of a mathematical correction on the ^{64}Zn/^{64}Ni isobaric interference. Red triangles represent uncorrected data suffering from a background Zn contamination measured in different autosampler vials. B – The effect of Zn on the ^{64}Ni/^{58}Ni isotope ratio after the mathematical correction. Different amounts of Zn are added to the NIST 986 and the data mathematically corrected for ^{64}Zn are plotted on the 3-isotope plot.

deterioration in the precision of the ^{64}Ni/^{58}Ni ratio. At Zn levels higher than 10 ng g^{-1}, the spread in the ^{64}Ni/^{58}Ni ratios increases with more pronounced deviations from the NIST SRM 986 reference line.

The concentration level of Zn at which mathematical correction can be applied is also limited by the non-simultaneous character of the ^{64}Ni and ^{64}Zn monitoring. Based on our experiments, the number of lines in a dynamic mode does not affect the precision of the Ni isotope ratio measurements themselves, as all of the Ni isotopes are measured simultaneously (1st line). The precision deteriorates only when both a) the non-simultaneously measured ^{66}Zn intensity is included in the calculations, and b) the Zn background concentration is higher than the limit determined.

4.2. Other interferences. At the level of natural variation of Ni isotope ratios studied, many elements, present in the natural matrices, can give rise to spectral interferences that affect the results of Ni isotope ratio measurements. The medium resolution mode ($m/\Delta m = 7400$) of the Thermo Neptune was used to resolve most of these species. Among all the elements evaluated, only the effect of Ti was found to be significant, even when its concentration is below that of the target analyte Ni. For a more detailed description of the effect of spectral interferences, the reader is referred to the appendix.

Thus, Ti and Zn are the most critical interfering elements and these need to be reduced to background levels during sample preparation. The presence of other interfering elements in amounts lower than that of Ni will not affect the measurement of Ni isotope ratios.

4.3. Development of the ion-exchange chromatographic isolation of Ni. The earliest reports on Ni isotopic analysis relied on the extraction of Ni using a dimethylglyoxime (DMG) solution – a highly selective compound that binds Ni into a chelate complex (Morand and Allegre, 1983; Quitté and Oberli, 2006). Despite the high efficiency of such a separation, sufficiently low blank levels cannot be ensured.

Later works on Ni isolation procedures were based on a combination of cation and anion exchange chromatographic separation steps (Moynier et al., 2007; Quitté et al., 2006). This approach relies on the fact that Ni, in contrast to many other elements, does not form chloro-complex anions. As a result, Ni can be separated from chloro-complex-forming elements by binding to a cation exchanger. Similarly, anion exchange chromatography can be used with a reversed elution order. Attractive by its simplicity, the potential of this approach to separate Ni from alkali and alkaline earth metals is compromised by the limited differences in the distribution coefficients (K_d) and the corresponding necessity of a highly efficient column with a high number of theoretical plates (Strelow, 1960). Complete separation of Ni from abundant elements that possess chemical properties very similar to those of Ni, such as Co, and some transition elements that can be present in a diversity of chemical forms in the solution (*e.g.*, Cr, V, Ti) is hard to achieve. Nevertheless, this separation approach can be used efficiently when these limitations are properly addressed (*e.g.*, for the analysis of iron meteorites).

Application of organic solvents as a separation medium increases the peak resolution of the cation exchange column and thus, improves the separation factors (Korkisch and Ahluwalia, 1967). A general trend is that Ni distribution coefficients in a weak HCl – strong cation exchange system increase when the concentration of organic solvent is increased, while those for Fe, Co and Zn decrease. According to the K_d values published, separation of Ni from Al, Ca, Co, and K is feasible when using 0.5 M HCl in 90 % acetone (Strelow et al., 1971). But, this approach does not solve the problem of Ni separation from Cr, Mg, Na and Ti, elements which are abundantly present in meteorite matrices. Therefore, separation in HCl – acetone medium on a cation exchange resin was combined with additional anion exchange columns to isolate Ni from iron meteorites and chondrites and determine its isotopic composition (Chen et al., 2009; Cook et al., 2006; Tang and Dauphas, 2012).

A solution to the insufficient selectivity described above lies in the simultaneous use of DMG and ion exchange chromatography. This can be achieved by using the commercially available Ni-specific Eichrom resin, containing DMG fixed in its pores (Cameron et al., 2009; Gueguen et al., 2013; Quitté and Oberli, 2006; Yamakawa et al., 2009), or the conventional 50W-X4 strong cation exchanger in a weak HCl - acetone - DMG medium (Gall et al., 2012; Regelous et al., 2008; Steele et al., 2011). The latter method was first described by Wahlgren *et al.*(Wahlgren et al., 1970) and later by Victor (Victor, 1986). At the first stage of this separation, elements that form chloro-complex anions and do not show affinity to the cation exchanger in HCl – acetone medium are eluted with 0.6 M HCl – 90 % acetone. At the same time, other elements (e.g., Al, Ca, Na, K, Mg, see Strelow et al. (Strelow et al., 1971) for K_d) are retained on the resin, together with Ni. A solution of DMG in acetone is then used for a selective elution of the retained Ni. K_d of Ni decreases from 250 down to 4 when adding 0.1 M DMG to 0.6 M HCl – 95 % acetone (Victor, 1986). The presence of Ti in the final elution of this separation is described in literature, and for its removal, an additional column is needed to further purify the Ni fraction (Gall et al., 2012; Regelous et al., 2008; Steele et al., 2011). Also, blank levels of organic solvents cannot be as low as those achieved in aqueous solutions. Finally, it needs to be considered that working with acetone brings about additional technical challenges – evaporation of the solvent, the low viscosity, acetone polymerization in acid, and the formation of air bubbles in the column. Another drawback is the presence of organic material in the final elution. This can affect Ni isotope measurements in a non-spectral way or lead to complexation of Ni cations, which could corrupt subsequent ion exchange separation steps. Therefore, this organic material has to be decomposed effectively before the next separation step or MC-ICP-MS isotopic analysis take place.

An improvement of the abovementioned method for Ni purification was described by Gall *et al.* (Gall et al., 2012; Strelow et al., 1972). This approach minimizes the amounts of acetone and DMG used with the aim of keeping the post-purification treatment of the sample as limited as possible. For this purpose, elements such as Al, Cr, Fe, and Ti are first eluted off as oxalic complexes with an oxalic acid-HCl solution, followed by the application of HCl-acetone to wash off Cd, Cu, Mn, Sn, and Zn. In a final step, Ni is collected in an HCl-acetone-DMG medium.

Another approach for additional Ni fraction purification, based on the original separation of Strelow (Strelow, 1990), was proposed by Gall *et al.* (Gall et al., 2012). Ni is loaded in a dilute solution of di-ammonium citrate and NH_4OH on a cationic exchanger, and the excess of ammonia complexes Ni and some other electronegative divalent ions and binds these to the cation exchanger. At the same time, alkali and alkaline earth elements and other cations abundant in geological materials tend to form citrate complexes, which show no affinity towards the resin. As a result, Ni can be separated from the geochemically abundant elements - Al, Ca, Cr, Fe, Ti, Mg, and V.

Based on the literature available, cation and anion exchange chromatographic steps were combined in this work (see table 1 for a summary) in order to ensure isolation of Ni from the matrix and interfering elements and guarantee that on-column isotope fractionation does not affect the final result. The first step comprises cation exchange separation in 0.6 M HCl – 95 % acetone – 0.1 M DMG to separate Ni from most of the matrix elements and to reduce the concentration of potentially interfering elements to background levels. An elution profile is shown in figure 2 (the final fractions were eluted with 6 M HCl to calculate the recoveries of elements bound to the resin). Application of the 50W-X4 cation exchange resin (4 % cross-linkage) was found advantageous compared to similar resins with higher cross-linkage. Strong tailing of the Ni peak was observed when using 50W-X8 (8 % cross-linkage). 16 ml of 0.6 M HCl – 95 % acetone – 0.1 M DMG were needed to obtain quantitative Ni recovery with the latter resin, compared to 6 ml in the case of 50W-X4 with similar mesh size. The elution profiles of synthetic mixtures of single-element standards, GRMs and iron meteorites all show similar peak positions. This demonstrates the absence of matrix effects on the elution behaviour.

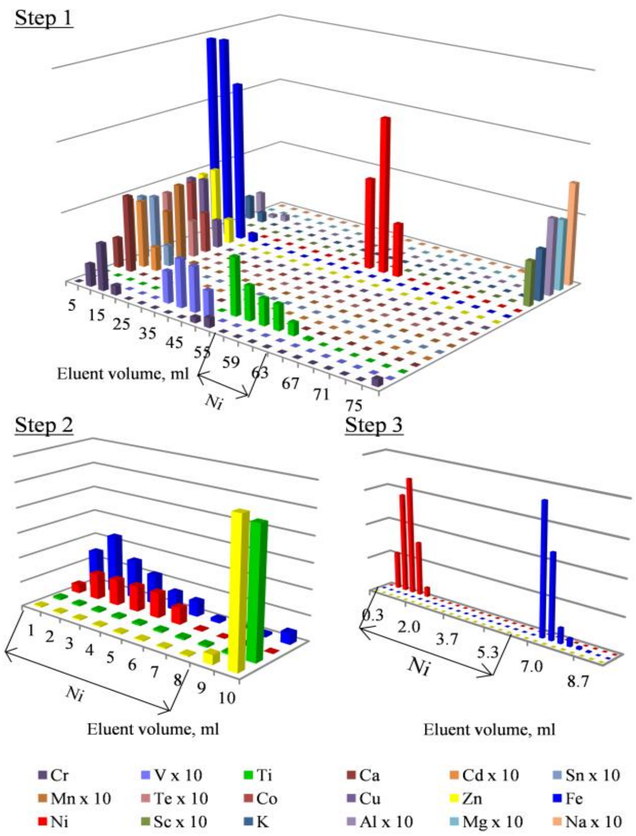

Figure 4-2. Elution profiles for Ni ion-exchange isolation

After this first separation step, the level of most interfering elements decreases below the limits appropriate for Ni isotope ratio determination (below a 1:1 ratio relative to Ni, as documented in the previous section). Only the chromatographic peaks of Ti, Cr and minor peaks of V and Al overlap with the peak of Ni in the elution profiles. As Ti was found to be one of the elements significantly affecting Ni isotopic analysis, the use of a second column for cleaning the Ni fraction is crucial.

Crushing and removing the organic residue remaining after the first elution was found critical for further isolation. This can be achieved via repeated digestion by concentrated inorganic acids and H_2O_2 at high temperature. Such treatment converted the brown residue into a tiny green-blue dot.

The second column is based on anion exchange chromatography in a HCl – HF mixture medium and aimed at Ni separation from Ti. HF strongly complexes Ti and Zn, such that these elements are strongly adsorbed onto the anion exchanger (Nelson et al., 1960). As a result, these elements can be separated from Ni that does not form fluoro-complex anions and hence, does not show significant adsorbance. With increasing HCl concentration, the adsorption of Ti becomes negligible. At the same time, Fe is only adsorbed in HCl – HF medium at higher HCl concentrations, and thus, Ni cannot be separated from Fe during separation of Ni from Ti and Zn. The elution profile obtained under the optimized conditions is shown at figure 4-2.

A third chromatographic column (see table 4-1) is needed to achieve sufficiently low background levels of Fe and Zn. Although these elements are efficiently separated from Ni in the first column step, sufficiently low blanks cannot be obtained because of the use of organic solvents and DMG. The separation presented here is based on the use of anion exchange chromatography (see figure 4-2 for elution profiles) (Kraus et al., 1954). Fe and Zn form anionic chloro-complexes that are strongly bound to the exchanger, while Ni is eluted. Small amounts of H_2O_2 are added to prevent Fe from being reduced from Fe(III) to Fe(II), which cannot form chloro-complex anions. Ni recoveries were quantitative for the second and third columns.

Element-to-Ni mass ratios were measured after isolation of Ni from geological, iron and low-alloyed steel reference materials, which approximate the matrix of iron meteorites. The abundances of the interfering elements after isolation were found to be much lower than the experimentally determined tolerance limits. The characteristics of the complete isolation method are summarized in the appendix. If trace levels of Ti (Ti:Ni ratio higher than 10^{-3}) were found present after Ni isolation from GRMs, Ni isotope ratios measurements were performed using high mass-resolution mode at the cost of deteriorated precision on $^{64}Ni/^{58}Ni$ isotope ratio.

The recoveries for Ni, calculated for the complete isolation procedure, including the three ion exchange columns and all of the intermediate sample treatment procedures are 81 – 87 % and 82 - 106 % for iron and geological matrices, respectively. The minimum recovery calculated for the total procedure is equivalent to 93 % recovery for each of the three ion exchange separation steps.

The application of anion exchange separation after the first column has the important advantage that the chemical forms of Ni present have almost no affinity to the resin. It not only makes these separations faster, improves recovery, but also prevents losses of Ni, leading to fractionation. Thus, in the case of incomplete DMG decomposition, neutral Ni complexes will be eluted from the 2nd and 3rd columns together with Ni^{2+}. Another advantage of anion exchange is that on-column mass-dependent fractionation is self-evidently absent as this can only occur for an element showing affinity towards the resin.

4.4. Studies of on-column fractionation of Ni. To evaluate the effect of on-column isotope fractionation, a digest of isotopic reference material NIST SRM 986 was loaded on the first column and the band of Ni was collected in aliquots of 0.5 ml in Savillex Teflon® beakers. The isotopic composition of Ni in these separate fractions was then measured relative to NIST SRM 986. $\delta^{x/58}$Ni values along the elution profile of the first column are shown in figure 4-3.

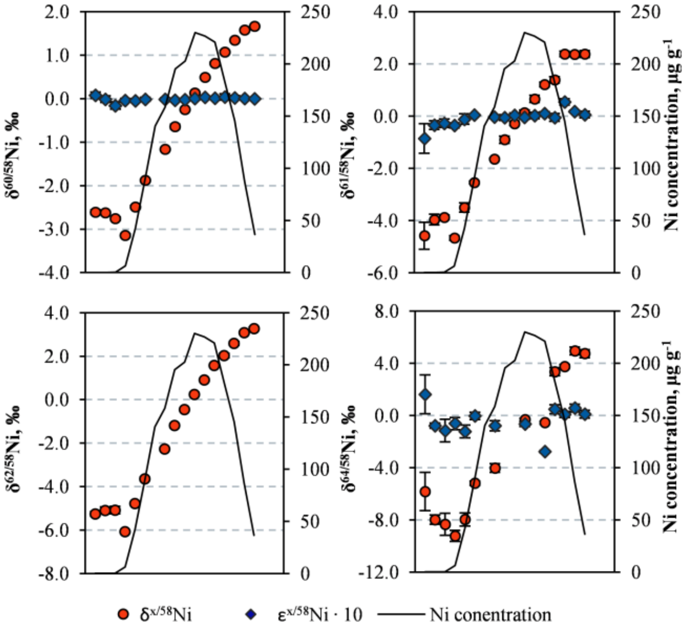

Figure 4-3. Profiles of $\delta^{x/58}$Ni and $\varepsilon^{x/58}$Ni along the Ni elution band from the first column of the chromatographic isolation protocol.

It can be seen that the leading fractions of the Ni elution band are isotopically lighter, while the tailing fractions are heavier. This on-column isotopic fractionation can be corrected for when using a pair of Ni isotopes. Isotopic fractionation on the first column is purely mass-dependent and fits a first order mass-dependent fractionation law for isotope partitioning at equilibrium, according to the method described by Young *et al*. (cf. figure 4-4) (Wombacher and Rehkamper, 2003; Young et al., 2002b). The β fractionation exponent was extracted from the experimental data for on-column Ni isotope fractionation and compared to the theoretically expected β parameters for equilibrium and kinetic mass-dependent fractionation processes. β is a fractionation exponent coupling isotopic fractionation factors $\alpha_{x/58}$ as:

$$\alpha_{62/58} = \alpha_{60/58}^{\beta} \qquad (4-3)$$

Following Wombacher and Rehkamper (Wombacher and Rehkamper, 2003), the theoretical equilibrium and kinetic β factors are calculated as:

$$\beta_{eq} = \frac{\left({}^{1}/_{m_{58}} - {}^{1}/_{m_{62}}\right)}{\left({}^{1}/_{m_{58}} - {}^{1}/_{m_{60}}\right)} \qquad (4-4)$$

$$\beta_{kin} = \frac{ln\left({}^{m_{58}}/_{m_{62}}\right)}{ln\left({}^{m_{58}}/_{m_{60}}\right)} \qquad (4-5)$$

$$\beta_{pow} = \frac{(m_{58}-m_{62})}{(m_{58}-m_{60})} \qquad (4-6)$$

The maximum spread of on-column isotopic enrichment found for the first column mounted up to ± 4 ‰ for $\delta^{60/58}$Ni, implying the need for recoveries close to 100 % to avoid on-column bias when natural mass-dependent isotope fractionation needs to be studied. Hence, a higher volume of eluent than strictly necessary was always used to wash Ni from the first column. A Ni standard was processed together with each batch of samples studied, and the results obtained were compared to a non-processed standard to detect any isotope fractionation occurring during sample preparation.

Similar experiments were carried out for the 2nd and 3rd anion exchange columns, but no on-column fractionation effects were detected. This can be explained by the simple fact that Ni shows no significant affinity to the anion exchanger, and thus, there is no chemical interaction that can fractionate the Ni isotopes.

4.5. Precision. The precision attainable with the method for Ni isotopic analysis used defines the applications within reach. Chronological applications require the highest precision, as the uncertainty on the isotope ratio measurement is translated via error propagation into millions years of uncertainty on the final radioisotopic date (Schoene et al., 2013).

The reproducibility of the relative isotope ratio differences attained was calculated via repeated measurement of digested Sigma Aldrich high-purity Ni metal during all of the measurement sessions throughout this work. The overall reproducibility achieved (2 SD, n = 14) is 0.033 ‰, 0.045 ‰, 0.071 ‰ and 0.51 ‰ for $\delta^{60/58}$Ni, $\delta^{61/58}$Ni, $\delta^{62/58}$Ni and $\delta^{64/58}$Ni, respectively. Another estimation of the overall reproducibility was done by repeated measurement of a real sample, since small deviations can potentially be introduced during the chemical isolation of Ni. In this work, reproducibilities of 0.048 ‰, 0.14 ‰, 0.065 ‰ and 0.39 ‰ were found for $\delta^{60/58}$Ni, $\delta^{61/58}$Ni, $\delta^{62/58}$Ni and $\delta^{64/58}$Ni, respectively, for repeated measurements of the PCC-1 peridotite GRM (2 SD, n = 8). Previous works (Cameron et al., 2009; Gall et al., 2012; Gueguen et al., 2013; Moynier et al., 2007) have reported reproducibilities between 0.034 and 0.08 ‰ for $\delta^{60/58}$Ni. These figures of merit need to be compared with the natural isotopic variation for Ni. The spread of $\delta^{60/58}$Ni within 150 meteorites of different groups reported by Moynier *et al.* (Moynier et al., 2007) is on the order of 0.20 ‰ (2 SD). Within groups of meteorites, even smaller deviations of 0.06 ‰ have been reported (Cameron et al., 2009). As such, the reproducibility obtained in this work should at least be enough to resolve different groups of meteorites.

When correcting Ni isotope ratio data internally by ^{62}Ni/^{58}Ni to filter out the non mass-dependent data, the reproducibility attained is 0.53 pptt, 1.1 pptt, and 6.8 pptt for $\varepsilon^{60/58}$Ni, $\varepsilon^{61/58}$Ni and $\varepsilon^{64/58}$Ni, respectively (2 SD via repeated measurement of a digested Sigma Aldrich high purity Ni metal, n = 14). These results are slightly higher than those reported by Quitté *et al.* (Quitté et al., 2006) (0.3 pptt and 0.6 pptt for $\varepsilon^{60/58}$Ni and $\varepsilon^{61/58}$Ni, respectively). For repeated measurements of PCC-1 peridotite, reproducibilities of 0.25 pptt, 1.1 pptt and 1.3 pptt were found for $\varepsilon^{60/58}$Ni, $\varepsilon^{61/58}$Ni and $\varepsilon^{64/58}$Ni, respectively (2 SD, n = 8). These figures are similar to the spread in the natural variation of $\varepsilon^{60/58}$Ni found by Quitté *et al.* (0.53 pptt) (Quitté et al., 2006) and Cook *et al.* (0.3 pptt) (Cook et al., 2006) in a diversity of iron

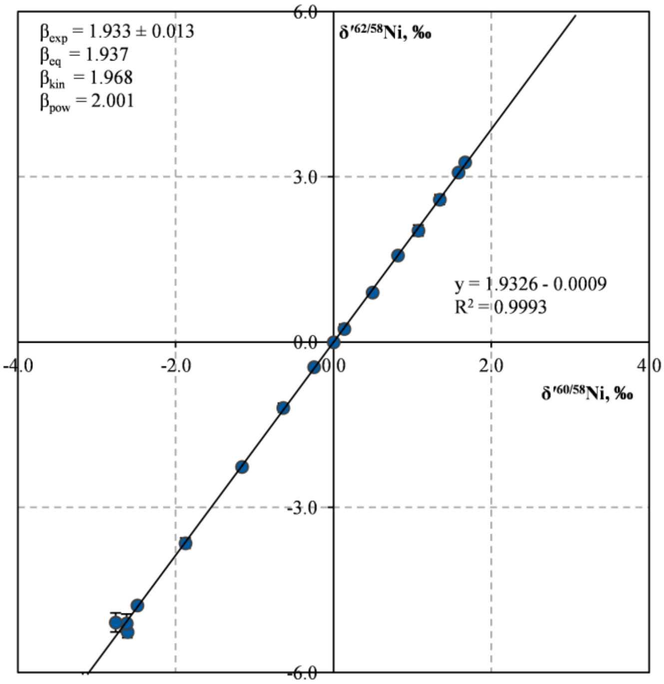

Figure 4-4. Three-isotope plots constructed using the approach described by Young *et al.* (Wombacher and Rehkamper, 2003; Young et al., 2002b) and the experimental Ni isotope ratio data for the Ni elution profile of the first column. The slope of the regression line is equal to the fractionation exponent β between the isotope ratios. By definition

$$\delta'^{x/58Ni} = ln\left[\left({}^{x}Ni/{}^{58}Ni\right)_{smp}/\left({}^{x}Ni/{}^{58}Ni\right)_{std}\right]\cdot 1000.$$

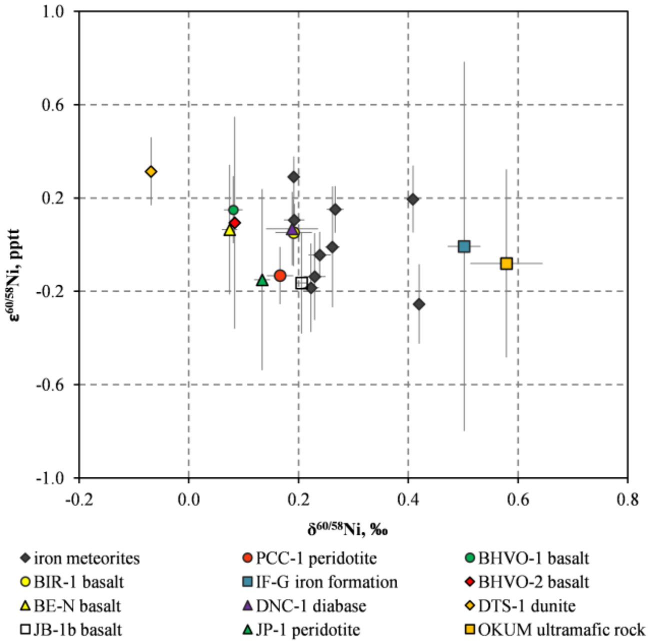

Figure 4-5. Plot of mass-dependent $\delta^{60/58}$Ni vs. non mass-dependent $\varepsilon^{60/58}$Ni. All the data couples reported are from the same measurement and the two values are obtained after different correction for mass bias, relying on admixed Cu and one Ni isotope ratio, respectively.

meteorites. Because the differences studied are small, the investigation of non mass-dependent effects affecting Ni isotope ratios remains highly challenging.

5.5. Results. The non mass-dependent Ni isotopic data obtained in this work are presented in table 4-3. To obtain these results, all natural mass-dependent contributions to the fractionation are canceled out by an assumed fractionation “law”. Taking the associated analytical uncertainties into consideration, none of the results obtained indicates a significant difference with respect to NIST SRM 986. Also when comparing the results to one another, no significant effects can be seen (see table 4-3). The precision of $\varepsilon^{64/58}$Ni is compromised particularly by considering the effect of the Zn background in the calculation of the uncertainty budget. This input has a random nature and can be smaller or higher in particular case (e.g. BHVO-2 and BIR-1 in table 4-3). As such, the applicability of Ni isotope data of iron meteorites for chronological purposes or to assess specific nucleosynthesic contributions remains debatable. Here, it needs to be stressed that available literature data on the non mass- dependent Ni isotope compositions of iron meteorites are also not resolvable from NIST SRM 986 within the obtainable level of analytical resolution. To validate the mass bias correction model used, non mass-dependent $\varepsilon^{60/58}$Ni are plotted versus mass-dependent $\delta^{60/58}$Ni in figure 4-5. For the iron meteorites and terrestrial GRMs studied, no significant correlation exists between the mass-dependent and non mass-dependent data, suggesting that natural and instrumental mass-dependent isotope fractionation effects are entirely cancelled out after the correction and no artefacts due to overcorrection are present.

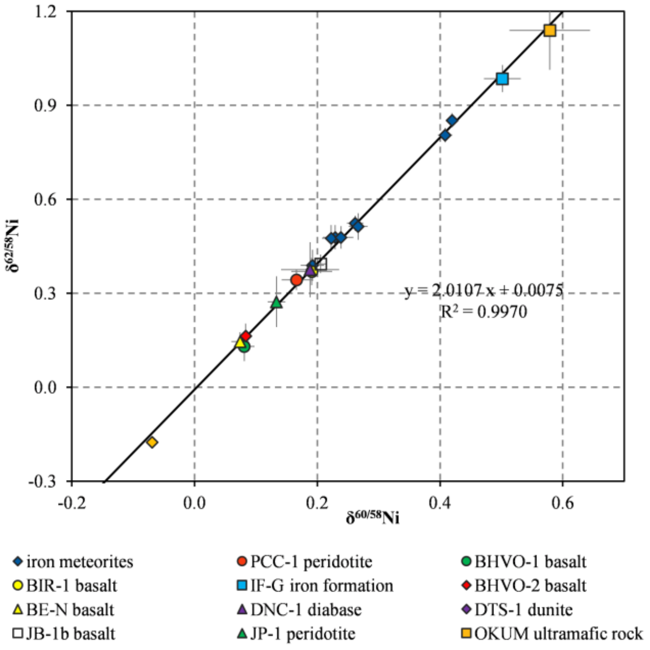

Figure 4-6. Three-isotope plot of the mass-dependent Ni isotopic compositions for 6 iron meteorites and 11 GRMs.

Mass-dependent data are presented in table 4-3. $\delta^{60/58}$Ni values vary between -0.069 ‰ and 0.58 ‰ for the terrestrial GRMs studied, and between 0.191 ‰ and 0.408 ‰ for the iron meteorites studied. In general, the results obtained in this work for the GRMs are in good agreement with those previously obtained using a double spike approach (Gueguen et al., 2013; Steele et al., 2011) (t-test, $t_{exp} < t_{crit}$, $p < 0.05$). The $\delta^{60/58}$Ni result for PCC-1 peredotite is slightly higher than that reported by Gueguen *et al.* (Gueguen et al., 2013). The Ni isotopic composition of iron meteorites and terrestrial silicate GRMs indicates the influence of a mass-dependent isotope fractionation process, as the measured $\delta^{x/58}$Ni values follow a linear correlation in three-isotope space (figure 4-6). As the Ni isotopic compositions of meteorites fall within experimental uncertainty onto the terrestrial fractionation line, this suggests a common nature of the Ni source and a similar control by isotope fractionation processes.

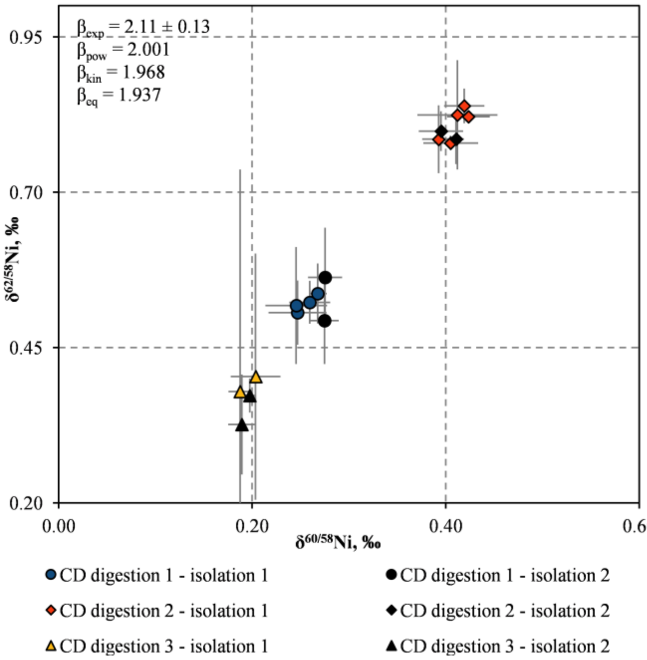

Figure 4-7. Three-isotope plot of the mass-dependent Ni isotopic compositions for 3 different digestions of the Canyon Diablo IAB-MG iron meteorite.

Figure 7 presents the Ni isotopic compositions of 3 separate digestions of the Canyon Diablo IAB-MG iron meteorite. As each digestion was

	$\varepsilon^{60/58}$Ni, pptt	$\varepsilon^{61/58}$Ni, pptt	$\varepsilon^{64/58}$Ni, pptt	$\delta^{60/58}$Ni, ‰	$\delta^{61/58}$Ni, ‰	$\delta^{62/58}$Ni, ‰	$\delta^{64/58}$Ni, ‰	$\varepsilon^{60/58}$Ni, pptt, Ref	$\varepsilon^{61/58}$Ni, pptt, Ref	$\varepsilon^{64/58}$Ni, pptt, Ref	$\delta^{60/58}$Ni, ‰, Ref
Canyon Diablo	-0.01±0.51	0.21±0.24	-1.7±5.8	0.262±0.026	0.407±0.022	0.523±0.048	0.67±0.44	-0.19±0.23[a]; 0.06±0.07[b]	-0.59±0.79[a]; 0.14±0.58 [b]	0.19±0.8[b]	
Canyon Diablo[*]	0.20±0.28	0.2±2.2	-1.7±5.6	0.408±0.024	0.63±0.22	0.805±0.046	1.36±0.88				
Canyon Diablo[**]	0.29±0.17	0.33±0.78	0.5±1.5	0.191±0.020	0.30±0.10	0.370±0.064	0.590±0.050				
Sikhote-Alin	0.11±1.4	-0.07±0.88	-1.7±1.6	0.192±0.038	0.29±0.13	0.389±0.099	0.51±1.1	0.33±0.25[a]	0.27±0.27[a]		
Sikhote-Alin[*]	0.15±0.20	0.7±1.7	-1.0±3.8	0.267±0.031	0.46±0.18	0.513±0.085	0.68±0.44				
Darinskoe (*n*=2)	-0.14±0.37	-0.4±1.5	-1.4±2.9	0.229±0.040	0.31±0.14	0.478±0.078	0.57±0.41				
Chinga (*n*=2)	-0.19±0.38	-0.2±1.4	-1.4±4.1	0.222±0.029	0.33±0.13	0.476±0.083	0.77±0.77	0.12±0.17[a]	0.67±1.23[a]		
Elga (*n*=2)	-0.04±0.20	-0.2±1.1	-1.8±3.0	0.238±0.041	0.334±0.085	0.478±0.072	0.62±1.3				
DNC-1 (*n*=5)	0.07±0.32	0.4±1.4	-2.2+5.4	0.188±0.095	0.312±0.070	0.38±0.18	0.16±0.32				0.132±0.056[c]
PCC-1 (*n*=8)	-0.13±0.25	0.1±1.1	-0.6±1.3	0.166±0.048	0.25±0.14	0.342±0.065	0.62±0.39				0.11[d]; 0.119±0.045[c]
BHVO-2 (*n*=5)	0.09±0.91	0.0±1.0	-1.9±0.3	0.083±0.019	0.109±0.076	0.164±0.079	-2.2±3.9				0.060±0.050[d]; 0.006±0.041[c]; 0.13±0.03[e]; 0.01±0.02[f]
BHVO-1 (*n*=2)	0.15±0.29	0.9±2.2	-0.34±0.96	0.081±0.034	0.19±0.20	0.130±0.093	0.14±0.1				
BE-N (*n*=1)	0.06±0.56	-0.68±0.27	-0.83±0.86	0.074±0.029	0.043±0.072	0.146±0.059	0.139±0.004				
BIR-1(*n*=2)	-0.01±0.37	0.5±2.6	-2.1±5.6	0.191±0.066	0.33±0.31	0.369±0.088	0.29±0.42				0.120±0.035[c]
DTS-1 (*n*=2)	0.31±0.29	0.49±0.70	0.6±2.1	-0.069±0.006	-0.136±0.052	-0.176±0.015	-0.35±0.10				-0.071±0.053[c]
JB-1b (*n*=1)	-0.16±0.44	-0.1±3.1	-	0.205±0.017	0.30±0.30	0.394±0.059	-1.4±1.8				
JP-1 (*n*=1)	-0.15±0.78	-0.9±3.1	-	0.134±0.029	0.217±0.077	0.27±0.16	0.54±0.53				0.100±0.08[g]
OKUM (*n*=1)	-0.08±0.81	-1.5±4.0	-	0.58±0.13	0.68±0.13	1.13±0.25	-0.45±0.49				
IF-G (*n*=2)	-0.0±1.6	-0.0±0.13	0.6±2.8	0.502±0.060	0.753±0.076	0.985±0.087	1.46±0.11				0.455±0.032[c]

Table 4-3. Non mass-dependent (presented in pptt) and mass-dependent (presented in ‰) Ni isotopic data for 5 iron meteorites, 11 GRMs and some literature data for reference, uncertainty denotes 2 SD. *n* denotes number of separate digestions. [*] Denotes separate digestions. [a] - (Quitté et al., 2006); [b] - (Cook et al., 2006); [c] - (Gueguen et al., 2013); [d] - (Gall et al., 2012); [e] - (Cameron et al., 2009); [f] - (Ratié et al., 2015); [g] - (Steele et al., 2011).

processed through the isolation method and measurement protocol twice, the mass-dependent fractionation observed can not result from on-column fractionation or instrumental bias. According to Wasson *et al.* (Wasson and Kallemeyn, 2002), the IAB meteorite group has a non-magmatic origin and was formed from a chondritic parent body after the rapid cooling of impact-generated melt early in the Solar System evolution. As this type of meteorite has a heterogeneous internal structure, characterized by different Ni contents (*e.g.*, Ni-rich/poor lamellae, silicate inclusions), the slope of the mass-dependent line on the three-isotope plot likely represents Ni isotope fractionation between petrologic phases of Canyon Diablo. Although the exact spatial connection of the sampled fractions is unclear, these fragments most probably represent kamatite and taenite (Fe/Ni alloys with < 10 wt% and 22-77 wt% of Ni, respectively (McSween and Huss, 2010) in different proportions, as non-metal inclusions were avoided during sample preparation for the meteorites. The experimental β_{exp} extracted from the space-resolved data corresponds to Ni isotope partitioning following the power law. This β_{exp} for Ni in Canyon Diablo meteorite cannot result from artificial on-column fractionation, as isotopic fractionation on the first column fits a first order mass-dependent fractionation law for isotope partitioning at equilibrium (see figure 4-4), and second and third columns do not introduce any on-column fractionation.

5. Conclusions

The chemical properties of Ni challenge its isolation from geological matrices, so that target element concentration, isotope ratio measurement precision attainable, separation factors from interfering elements and artificial on-column fractionation have to be carefully considered. A method for high-precision analysis of mass-dependent natural variations of Ni isotopes, suitable for applications in the planetary sciences, has been developed and evaluated. The optimized isolation method involves three chromatographic separation steps and was tested for a variety of silicate and iron matrices, and the columns were calibrated to avoid the effect of artificial on-column fractionation on the final results. The separation factors attained were sufficient to avoid spectral interference to a large extent, while the blanks were negligible compared to the amount of Ni processed. Mathematical correction for the remaining isobaric interferences was found to be one of several critical aspects. The overall precision for mass-dependent results is equivalent to or better than that of other methods reported, including double-spiking techniques, and sufficient to distinguish between the stable isotopic signatures of various geological materials. Because the non mass-dependent effects on the isotopic composition of Ni in iron meteorites are so small (< 0.3 pptt (Cook et al., 2006), the current level of analytical resolution does not allow to fully quantify such effects. The method developed was applied to terrestrial and extraterrestrial samples and the results of mass-dependent Ni isotope fractionation for several reference materials are in good agreement with previously reported data. Some perspectives for the use of Ni isotope ratios to trace geo- and cosmochemical processes are presented.

6. Appendices

6.1. Evaluation of the instrumental mass-discrimination correction model. At the level of natural variation studied, Ni isotope ratio measurements can even be sensitive to the mass bias correction model applied. When the mathematical model assumed for the correction does not fully correspond to the nature of the underlying processes of instrumental mass discrimination and natural isotope fractionation (kinetic/equilibrium), this can result in small under/overcorrections. To examine these undesired artifacts, the application of the flexible generalized power law (GPL) was evaluated. This law is characterized by a variable discrimination exponent *n* (Wombacher and Rehkamper, 2003). With the application of different values for *n*, the law can take on a mathematical form for equilibrium, kinetic or power law fractionation, or show a mixed character.

$$({}^{x}Ni/{}^{58}Ni)_{corr} = ({}^{x}Ni/{}^{58}Ni)_{meas} \cdot f_{GPL}^{(m_x^n - m_{58}^n)} \tag{4 – 7}$$

In this equation, $({}^{x}Ni/{}^{58}Ni)_{meas}$ is the measured isotope ratio, m_x and m_{58} are the masses of the Ni isotopes considered, and f_{GPL} represents a fractionation coefficient. The same equation can be written for the isotope ratio of the internal standard. Optimum model discrimination exponents *n* for the GPL can be found for each target element isotope ratio following the method described by Baxter *et al.* (Baxter et al., 2012b; Wombacher and Rehkamper, 2003). Calculation of the optimum discrimination exponent *n* for different isotope ratios of a target element results in dissimilar *n* (and different corresponding isotope fractionation models) for different isotope ratios.

To correct for the time-dependent variation of instrumental mass discrimination, fractionation coefficients f_{GPL} were calculated for isotope ratios of the target element and the internal standard of all bracketing standards measured in a daily sequence. Fractionation coefficients for the target element and the internal standard were plotted versus each other and a regression line was fitted through the data using the least squares method and the intersection (*a*) and slope (*b*) of the line were calculated. In comparison to the mathematically more correct "York regression" (York, 1966), the least square method was found to yield similar Ni isotope ratio results within the associated uncertainty. The calculated linear regression parameters were applied to the measured ratios of the internal standard and used to produce $({}^{x}Ni/{}^{58}Ni)_{corr}$. Finally, sample-standard bracketing was applied to correct for minor drift of instrumental parameters.

The results of the application of the GPL-based model for the geological peridotite reference material PCC-1 with varying discrimination exponent between -1 to +1 are shown in figure 4-8. This diagram allows a direct comparison of results for a spectrum of different models used for mass bias correction. Varying the optimal discrimination exponent *n* generally results in small overall differences in the final isotope ratio. The optimal discrimination exponents (red diamonds in figure 4-8) describe the nature of the actual processes underlying natural isotope fractionation of Ni, as mixed between equilibrium (n = -1) and kinetic (n→0). This can be a result of (a) the mixing of different Ni sources; (b) the involvement of multiple natural processes of different nature that fractionate Ni isotopes; (c) the association with kinetic processes that fractionate Ni isotopes when Ni is bound to another element involved.

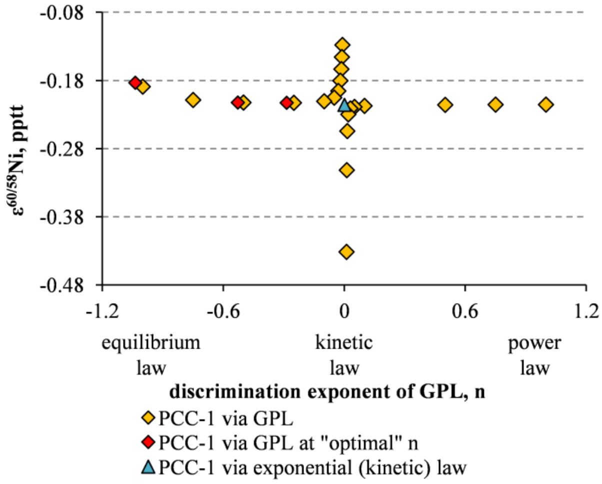

Figure 4-8. The results of application of the GPL for the geological reference material peridotite PCC-1 for a varying discrimination exponent *n*. The correction is made using the $^{62/58}$Ni ratio as internal reference. Red diamonds represent the discrimination exponent results with n optimized for three isotope ratios of Ni (see text).

Because differences between isotope ratios calculated via the GPL with optimized n and kinetic law (n→0) are less than 3 ppm and not resolvable using MC-ICP-MS (see figure 4-8), the exponential (kinetic) law (Russell et al., 1978) was found suitable for the correction of mass bias, with the version revised by Baxter found most successful (Baxter et al., 2006).

***6.2. Spectral interferences*.** The medium resolution mode (m/Δm = 7400) of the Thermo Neptune was used to resolve interfering ion species originating from noble gas atoms in the ICP (ArO^+, $ArNe^+$, Xe^{2+}). It needs to be stressed that the quotation of resolving power used for the pseudo-high resolution of the MC-ICP-MS unit exceeds that calculated according to the 10 % valley definition by about a factor of two (Vanhaecke and Moens, 2004). As such, pairs of ions with m/Δm ratios higher than 4500 (were m and Δm denotes ion mass and mass difference respectively, *e.g.* hydrides) cannot be resolved even with the high resolution mode of the instrument. Table 4-4 lists spectral interferences that can potentially affect the Ni isotope ratios. At the medium resolution mode, minor hydride contributions must be removed by sample-standard bracketing, since the samples and standards should be affected equally. Gas-based interferences cannot be reduced by ion exchange chromatography, but can be corrected for by application of medium instrument resolution mode and sample-standard bracketing. Because of differences in resolving power notations and obscurity of real formation rates of potentially interfering species, the effect of potentially interfering elements listed in table 4-4 needs to be evaluated. For this purpose, the NIST SRM 986 Ni isotopic standard was doped with single-element solutions in relative abundances ranging between 0.1 and 1 and measured using the instrument settings described.

Some of the results are presented in figure 4-9 in the form of linearized three-isotope plots. In the concentration range studied, only Ti appears to affect the $^{60}Ni/^{58}Ni$, $^{61}Ni/^{58}Ni$ and $^{64}Ni/^{58}Ni$ ratios. The most significant effects are observed for ratios involving the least abundant ^{64}Ni isotope. The theoretical mass resolution, calculated based on atomic masses, needed to resolve Ti species from ^{64}Ni is about of 3200. This mass resolution is not achieved in medium resolution, but can be achieved in the high mass-resolution mode of the instrument (see figure 4-9). The peak profiles of a 1 µg g^{-1} Ni solution doped with 10 µg g^{-1} Ti in medium and high mass-resolution modes are shown in figure 4-9.

	^{58}Ni (68.3%)		^{60}Ni (26.1%)		^{61}Ni (1.13%)		^{62}Ni (3.59%)		^{64}Ni (0.91%)	
	Interference	m/Δm	Interference	m/Δm	Interference	m/Δm	Interference	m/Δm	Interference	m/Δm
Isobars	^{58}Fe (0.28%)	28 060							^{64}Zn (48.6%)	54 314
Hydride ions	$^{57}Fe^{1}H^{+}$	7 364	$^{59}Co^{1}H^{+}$	5 856	$^{60}Ni^{1}H^{+}$	8 065	$^{61}Ni^{1}H^{+}$	5 878	$^{63}Cu^{1}H^{+}$	6 761
Polyatomic ions	$^{42}Ca^{16}O^{+}$	3 189	$^{44}Ca^{16}O^{+}$	3 056	$^{45}Sc^{16}O^{+}$	3 082	$^{46}Ca^{16}O^{+}$	3 056	$^{48}Ti^{16}O^{+}$	4 292
	$^{41}K^{17}O^{+}$	2 264	$^{43}Ca^{17}O^{+}$	2 210	$^{44}Ca^{17}O^{+}$	2 586	$^{46}Ti^{16}O^{+}$	3 225	$^{48}Ca^{16}O^{+}$	3 281
	$^{40}K^{18}O^{+}$	2 085	$^{42}Ca^{18}O^{+}$	2 220	$^{43}Ca^{18}O^{+}$	2 267	$^{45}Sc^{17}O^{+}$	2 320	$^{46}Ti^{18}O^{+}$	2 683
	$^{40}Ca^{18}O^{+}$	2 196	$^{46}Ca^{14}N^{+}$	2 307	$^{47}Ti^{14}N^{+}$	2 562	$^{44}Ca^{18}O^{+}$	2 355	$^{46}Ca^{18}O^{+}$	2 569
	$^{44}Ca^{14}N^{+}$	2 499	$^{46}Ti^{14}N^{+}$	2 405	$^{46}Ti^{15}N^{+}$	2 810	$^{48}Ca^{14}N^{+}$	2 272	$^{47}Ti^{17}O^{+}$	2 788
	$^{43}Ca^{15}N^{+}$	2 465	$^{45}Sc^{15}N^{+}$	2 375	$^{38}Ar\,^{23}Na^{+}$	2 841	$^{48}Ti^{14}N^{+}$	2 731	$^{50}Ti^{14}N^{+}$	3 213
	$^{27}Al^{31}P^{+}$	2 906	$^{36}Ar^{24}Mg^{+}$	2 749	$^{36}Ar\,^{25}Mg^{+}$	2 729	$^{47}Ti^{15}N^{+}$	2 632	$^{49}Ti^{15}N^{+}$	3 194
	$^{26}Mg^{32}S^{+}$	3 002	$^{29}Si^{31}P^{+}$	3 078	$^{30}Si^{31}P^{+}$	3 698	$^{38}Ar\,^{24}Mg^{+}$	3 187	$^{50}V^{14}N^{+}$	2 871
	$^{25}Mg^{33}S^{+}$	2 642	$^{28}Si^{32}S^{+}$	3 291	$^{29}Si^{32}S^{+}$	3 480	$^{36}Ar\,^{26}Mg^{+}$	2 842	$^{50}Cr^{14}N^{+}$	3 022
	$^{24}Mg^{34}S^{+}$	3 302	$^{27}Al^{33}S^{+}$	2 698	$^{28}Si^{33}S^{+}$	3 516	$^{27}Al^{35}Cl^{+}$	2 809	$^{40}Ar^{24}Mg^{+}$	3 285
			$^{26}Mg^{34}S^{+}$	3 046	$^{27}Al^{34}S^{+}$	3 321	$^{31}P_2^{+}$	3 229	$^{38}Ar^{26}Mg^{+}$	3 683
							$^{30}Si^{32}S^{+}$	3 540	$^{36}Ar^{28}Si^{+}$	3 873
							$^{29}Si^{33}S^{+}$	3 158	$^{27}Al^{37}Cl^{+}$	3 282
							$^{28}Si^{34}S^{+}$	3 765	$^{30}Si^{34}S^{+}$	4 673
									$^{31}P^{33}S^{+}$	3 705
									$^{32}S_2^{+}$	3 952
									$^{32}S^{16}O_2^{+}$	1 884
Doubly charged ions	$^{116}Cd^{2+}$	3 405	$^{120}Sn^{2+}$	2 951	$^{122}Sn^{2+}$	2 949	$^{124}Te^{2+}$	2 685	$^{124}Te^{2+}$	2 635
	$^{116}Sn^{2+}$	3 735	$^{120}Te^{2+}$	2 824	$^{122}Te^{2+}$	2 977				
Gas-based interferences	$^{40}Ar^{18}O^{+}$	2 214	$^{40}Ar\,^{20}Ne^{+}$	2 493	$^{40}Ar\,^{21}Ne^{+}$	2 420	$^{40}Ar\,^{22}Ne^{+}$	2 436	$^{124}Xe^{2+}$	2 686
	$^{36}Ar^{22}Ne^{+}$	2 459	$^{38}Ar^{22}Ne^{+}$	2 569			$^{124}Xe^{2+}$	2 517		
	$^{38}Ar^{20}Ne^{+}$	2 925								

Table 4-4. The list of spectral interferences potentially affecting the measurement of Ni isotopes. Resolution is calculated as $m_{Ni}/\Delta m$, were Δm is calculated based on nuclide masses, taken from Audi *et al.* (Audi et al., 2003) The quotation of resolving power used for pseudo high resolution mode of MC-ICP-MS exceeds that calculated based on atomic masses by about of a factor of two (Vanhaecke and Moens, 2004).

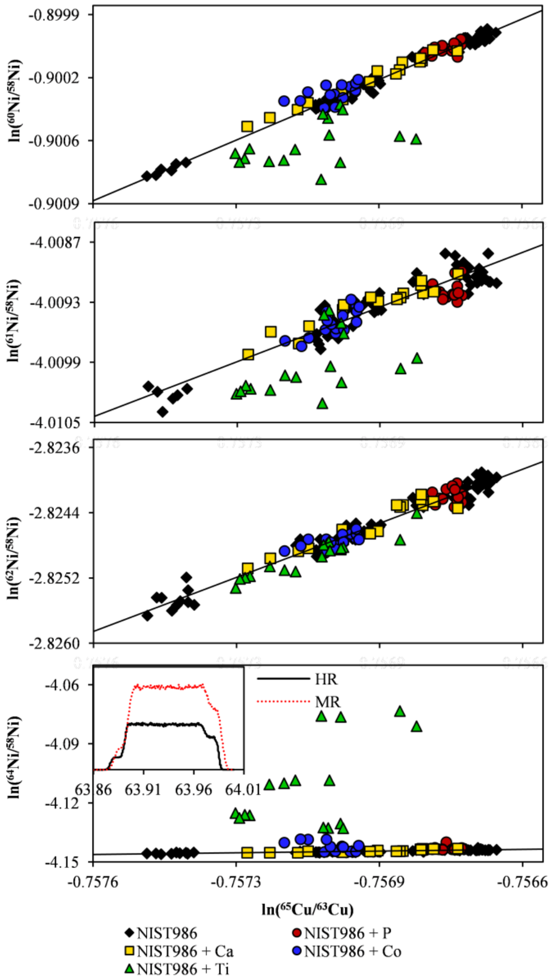

Figure 4-9. The effect of particular elements admixed to NIST SRM 986 in relative abundances ranging between 0.1 and 1 on the determined Ni isotope ratios. The ^{64}Ni spectral peak profile shows 1 µg g^{-1} Ni doped with 10 µg g^{-1} Ti at medium and high resolution modes.

6.3. Evaluation of the Ni isolation procedure. Table 4-5 presents the element to Ni mass ratios in steel and geological reference materials after the complete Ni isolation procedure.

		Iron and steel reference materials	Geological reference materials
Isobars	Fe	10^{-6} – 10^{-4}	10^{-4} – 10^{-3}
	Zn	10^{-6} – 10^{-4}	10^{-5} – 10^{-4}
Hydride-forming elements	Co	10^{-5}	10^{-5}
	Cu	10^{-7} – 10^{-5}	10^{-6} – 10^{-5}
Elements forming polyatomic ions	Na	10^{-5} – 10^{-3}	10^{-5} – 10^{-3}
	Mg	10^{-5} – 10^{-3}	10^{-4} – 10^{-3}
	Al	10^{-5} – 10^{-3}	10^{-6} – 10^{-4}
	K	10^{-5} – 10^{-3}	10^{-5} – 10^{-4}
	Ca	10^{-5} – 10^{-3}	10^{-4} – 10^{-3}
	Sc	10^{-8} – 10^{-6}	10^{-5}
	V	10^{-5} – 10^{-3}	10^{-5} – 10^{-3}
	Ti	10^{-5} – 10^{-3}	10^{-6} – 10^{-2}
	Cr	10^{-4} – 10^{-1}	10^{-6} – 10^{-1}
	Mn	10^{-6} – 10^{-4}	10^{-4}
Elements forming doubly charged ions	Cd	10^{-9} – 10^{-6}	10^{-8}
	Sn	10^{-8} – 10^{-6}	10^{-7}
Ni recovery		81 – 87 %	82 – 106 %

Table 4-5. Element-to-Ni mass ratios after the complete Ni isolation procedure

7. Acknowledgments

This research has been funded by the Interuniversity Attraction Poles Program initiated by the Belgian Science Policy Office. Steven Goderis is a postdoctoral fellow of the Research Foundation – Flanders (FWO). The collection of iron meteorites from east Russia and northern Kazakhstan was kindly donated by Dr F. P. Lesnov (IGM SB RAS).

8. List of references

Audi, G., Wapstra, A.H., Thibault, C., 2003. The Ame2003 atomic mass evaluation. Nucl. Phys. A 729, 337–676. doi:10.1016/j.nuclphysa.2003.11.003

Baxter, D.C., Rodushkin, I., Engström, E., 2012. Isotope abundance ratio measurements by inductively coupled plasma-sector field mass spectrometry. J. Anal. At. Spectrom. 27, 1355–1381. doi:10.1039/c2ja30153a

Baxter, D.C., Rodushkin, I., Engström, E., Malinovsky, D., 2006. Revised exponential model for mass bias correction using an internal standard for isotope abundance ratio measurements by multi-collector inductively coupled plasma mass spectrometry. J. Anal. At. Spectrom. 21, 427–430. doi:10.1039/b517457k

Berglund, M., Wieser, M.E., 2011. Isotopic compositions of the elements 2009 (IUPAC Technical Report). Pure Appl. Chem. 83, 397–410. doi:10.1351/PAC-REP-10-06-02

Breton, T., Quitté, G., 2014. High-precision measurements of tungsten stable isotopes and application to earth sciences. J. Anal. At. Spectrom. 29, 2284–2293. doi:10.1039/C4JA00184B

Cameron, V., Vance, D., 2014. Heavy nickel isotope compositions in rivers and the oceans. Geochim. Cosmochim. Acta 128, 195–211. doi:10.1016/j.gca.2013.12.007

Cameron, V., Vance, D., Archer, C., House, C.H., 2009. A biomarker based on the stable isotopes of nickel. Proc. Natl. Acad. Sci. U. S. A. 106, 10944–10948. doi:10.1073/pnas.0900726106

Chen, J.H., Papanastassiou, D.A., Wasserburg, G.J., 2009. A search for nickel isotopic anomalies in iron meteorites and chondrites. Geochim. Cosmochim. Acta 73, 1461–1471. doi:10.1016/j.gca.2008.11.040

Cook, D.L., Wadhwa, M., Janney, P.E., Dauphas, N., Clayton, R.N., Davis, A.M., 2006. High precision measurements of non-mass-dependent effects in nickel isotopes in meteoritic metal via multicollector ICPMS. Anal. Chem. 78, 8477–8484. doi:10.1021/ac061285m

Deng, T.-H.-B., Cloquet, C., Tang, Y.-T., Sterckeman, T., Echevarria, G., Estrade, N., Morel, J.-L., Qiu, R.-L., 2014. Nickel and zinc isotope fractionation in hyperaccumulating and nonaccumulating plants. Environ. Sci. Technol. 48, 11926–11933. doi:10.1021/es5020955

Epov, V.N., Malinovskiy, D., Vanhaecke, F., Bégué, D., Donard, O.F.X., 2011. Modern mass spectrometry for studying mass-independent fractionation of heavy stable isotopes in environmental and biological sciences. J. Anal. At. Spectrom. 26, 1142–1156. doi:10.1039/c0ja00231c

Estrade, N., Cloquet, C., Echevarria, G., Sterckeman, T., Deng, T., Tang, Y., Morel, J.-L., 2015. Weathering and vegetation controls on nickel isotope fractionation in surface ultramafic environments (Albania). Earth Planet. Sci. Lett. 423, 24–35. doi:10.1016/j.epsl.2015.04.018

Gall, L., Williams, H., Siebert, C., Halliday, A., 2012. Determination of mass-dependent variations in nickel isotope compositions using double spiking and MC-ICPMS. J. Anal. At. Spectrom. 27, 137–145. doi:10.1039/c1ja10209e

Gueguen, B., Rouxel, O., Ponzevera, E., Bekker, A., Fouquet, Y., 2013. Nickel Isotope Variations in Terrestrial Silicate Rocks and Geological Reference Materials Measured by MC-ICP-MS. Geostand. Geoanalytical Res. 37, 297–317. doi:10.1111/j.1751-908X.2013.00209.x

Konhauser, K.O., Pecoits, E., Lalonde, S. V, Papineau, D., Nisbet, E.G., Barley, M.E., Arndt, N.T., Zahnle, K., Kamber, B.S., 2009. Oceanic nickel depletion and a methanogen famine before the Great Oxidation Event. Nature 458, 750–753. doi:10.1038/nature07858

Korkisch, J., Ahluwalia, S.S., 1967. Cation-exchange behaviour of several elements in hydrochloric acid—organic solvent media. Talanta 14, 155–170. doi:10.1016/0039-9140(67)80175-9

Kraus, K.A., Nelson, F., Smith, G.W., 1954. Anion Exchange Studies. IX. Adsorbability of a Number of Metals in Hydrochloric Acid Solutions. J. Phys. Chem. 58, 11–17. doi:10.1021/j150511a003

Lauretta, D.S., 2011. A Cosmochemical View of the Solar System. Elements 7, 11–16. doi:10.2113/gselements.7.1.11

Lazar, C., Young, E.D., Manning, C.E., 2012. Experimental determination of equilibrium nickel isotope fractionation between metal and silicate from 500°C to 950°C. Geochim. Cosmochim. Acta 86, 276–295. doi:10.1016/j.gca.2012.02.024

Malinovsky, D., Vanhaecke, F., 2011. Mass-independent isotope fractionation of heavy elements measured by MC-ICPMS: a unique probe in environmental sciences. Anal. Bioanal. Chem. 400, 1619–1624. doi:10.1007/s00216-011-4856-z

Marhas, K.K., Amari, S., Gyngard, F., Zinner, E., Gallino, R., 2008. Iron and Nickel Isotopic Ratios in Presolar SiC Grains. Astrophys. J. 689, 622–645. doi:10.1086/592599

Markowski, A., Quitté, G., Halliday, A., Kleine, T., 2006. Tungsten isotopic compositions of iron meteorites: Chronological constraints vs. cosmogenic effects. Earth Planet. Sci. Lett. 242, 1–15. doi:10.1016/j.epsl.2005.11.048

McSween, H.Y.J., Huss, G.R., 2010. Cosmochemistry. Cambridge University press, Cambridge.

Morand, P., Allegre, C.J., 1983. Nickel isotopic studies in meteorites. Earth Planet. Sci. Lett. 63, 167–176. doi:10.1016/0012-821X(83)90034-1

Moynier, F., Blichert-Toft, J., Telouk, P., Luck, J.-M., Albarède, F., 2007. Comparative stable isotope geochemistry of Ni, Cu, Zn, and Fe in chondrites and iron meteorites. Geochim. Cosmochim. Acta 71, 4365–4379. doi:10.1016/j.gca.2007.06.049

Nelson, F., Rush, R.M., Kraus, K.A., 1960. Anion-exchange Studies. XXVII. Adsorbability of a Number of Elements in HCl-HF Solutions 1,2. J. Am. Chem. Soc. 82, 339–348. doi:10.1021/ja01487a021

Porter, S.J., Selby, D., Cameron, V., 2014. Characterising the nickel isotopic composition of organic-rich marine sediments. Chem. Geol. 387, 12–21. doi:10.1016/j.chemgeo.2014.07.017

Quitté, G., Meier, M., Latkoczy, C., Halliday, A., Gunther, D., 2006. Nickel isotopes in iron meteorites–nucleosynthetic anomalies in sulphides with no effects in metals and no trace of 60Fe. Earth Planet. Sci. Lett. 242, 16–25. doi:10.1016/j.epsl.2005.11.053

Quitté, G., Oberli, F., 2006. Quantitative extraction and high precision isotope measurements of nickel by MC-ICPMS. J. Anal. At. Spectrom. 21, 1249–1255. doi:10.1039/b607569j

Ratié, G., Jouvin, D., Garnier, J., Rouxel, O., Miska, S., Guimarães, E., Cruz Vieira, L., Sivry, Y., Zelano, I., Montarges-Pelletier, E., Thil, F., Quantin, C., 2015. Nickel isotope fractionation during tropical weathering of ultramafic rocks. Chem. Geol. 402, 68–76. doi:10.1016/j.chemgeo.2015.02.039

Regelous, M., Elliott, T., Coath, C.D., 2008. Nickel isotope heterogeneity in the early Solar System. Earth Planet. Sci. Lett. 272, 330–338. doi:10.1016/j.epsl.2008.05.001

Richter, F., Dauphas, N., Teng, F., 2009. Non-traditional fractionation of non-traditional isotopes: Evaporation, chemical diffusion and Soret diffusion. Chem. Geol. 258, 92–103. doi:10.1016/j.chemgeo.2008.06.011

Rugel, G., Faestermann, T., Knie, K., Korschinek, G., Poutivtsev, M., Schumann, D., Kivel, N., Günther-Leopold, I., Weinreich, R., Wohlmuther, M., 2009. New Measurement of the Fe60 Half-Life. Phys. Rev. Lett. 103, 072502. doi:10.1103/PhysRevLett.103.072502

Rumble, D., Young, E.D., Shahar, A., Guo, W., 2011. Stable Isotope Cosmochemistry and the Evolution of Planetary Systems. Elements 7, 23–28. doi:10.2113/gselements.7.1.23

Russell, W.A., Papanastassiou, D.A., Tombrello, T.A., 1978. Ca isotope fractionation on the Earth and other solar system materials. Geochim. Cosmochim. Acta 42, 1075–1090. doi:10.1016/0016-7037(78)90105-9

Sanborn, M.E., Yin, Q.-Z., Irving, A.J., 2014. Isotope Forensics Utilizing Δ17O-ε54Cr Systematics Provide Supporting Evidence for Differentiated Parent Bodies Overlain by Chondritic Veneers: A Case for the CR Parent Body, in: Lunar and Planetary Science Conference. p. 2032.

Scherstén, A., Elliott, T., Hawkesworth, C., Russell, S., Masarik, J., 2006. Hf–W evidence for rapid differentiation of iron meteorite parent bodies. Earth Planet. Sci. Lett. 241, 530–542. doi:10.1016/j.epsl.2005.11.025

Schoene, B., Condon, D.J., Morgan, L., McLean, N., 2013. Precision and Accuracy in Geochronology. Elements 9, 19–24. doi:10.2113/gselements.9.1.19

Steele, R.C.J., Elliott, T., Coath, C.D., Regelous, M., 2011. Confirmation of mass-independent Ni isotopic variability in iron meteorites. Geochim. Cosmochim. Acta 75, 7906–7925. doi:10.1016/j.gca.2011.08.030

Strelow, F.W.E., 1990. Distribution coefficients and cation-exchange behaviour of some ammines and aquo complexes of metallic elements in ammonium nitrate solution. Anal. Chim. Acta 233, 129–134. doi:10.1016/S0003-2670(00)83468-6

Strelow, F.W.E., 1960. An Ion Exchange Selectivity Scale of Cations Based on Equilibrium Distribution Coefficients. Anal. Chem. 32, 1185–1188. doi:10.1021/ac60165a042

Strelow, F.W.E., Victor, A.H., Van Zyl, C.R., Eloff, C., 1971. Distribution coefficients and cation exchange behavior of elements in hydrochloric acid-acetone. Anal. Chem. 43, 870–876. doi:10.1021/ac60302a015

Strelow, F.W.E., Weinert, C.H.S.W., Eloff, C., 1972. Distribution coefficients and anion exchange behavior of elements in oxalic acid-hydrochloric acid mixtures. Anal. Chem. 44, 2352–2356. doi:10.1021/ac60322a001

Tachibana, S., Huss, G.R., Kita, N.T., Shimoda, G., Morishita, Y., 2006. 60 Fe in Chondrites: Debris from a Nearby Supernova in the Early Solar System? Astrophys. J. 639, L87–L90. doi:10.1086/503201

Tang, H., Dauphas, N., 2012. Abundance, distribution, and origin of 60Fe in the solar protoplanetary disk. Earth Planet. Sci. Lett. 359-360, 248–263. doi:10.1016/j.epsl.2012.10.011

Vanhaecke, F., Moens, L., 2004. Overcoming spectral overlap in isotopic analysis via single- and multi-collector ICP-mass spectrometry. Anal. Bioanal. Chem. 378, 232–240. doi:10.1007/s00216-003-2175-8

Victor, A., 1986. Separation of nickel from other elements by cation-exchange chromatography in dimethylglyoxime/hydrochloric acid/acetone media. Anal. Chim. Acta 183, 155–161. doi:10.1016/0003-2670(86)80083-6

Wahlgren, M., Orlandini, K., Korkisch, J., 1970. Specific cation-exchange separation of nickel. Anal. Chim. Acta 52, 551–553.

Wasson, J.T., Kallemeyn, G., 2002. the IAB iron-meteorite complex: A group, five subgroups, numerous grouplets, closely related, mainly formed by crystal segregation in rapidly cooling melts. Geochim. Cosmochim. Acta 66, 2445–2473. doi:10.1016/S0016-7037(02)00848-7

Wasylenki, L.E., Howe, H.D., Spivak-Birndorf, L.J., Bish, D.L., 2015. Ni isotope fractionation during sorption to ferrihydrite: Implications for Ni in banded iron formations. Chem. Geol. 400, 56–64. doi:10.1016/j.chemgeo.2015.02.007

Weyer, S., Anbar, A.D., Brey, G.P., Munker, C., Mezger, K., Woodland, A.B., Münker, C., Mezger, K., Woodland, A.B., 2005. Iron isotope fractionation during planetary differentiation. Earth Planet. Sci. Lett. 240, 251–264. doi:10.1016/j.epsl.2005.09.023

Wieser, M.E., De Laeter, J.R., 2009. Molybdenum isotope mass fractionation in iron meteorites. Int. J. Mass Spectrom. 286, 98–103. doi:10.1016/j.ijms.2009.07.006

Wombacher, F., Rehkamper, M., 2003. Investigation of the mass discrimination of multiple collector ICP-MS using neodymium isotopes and the generalised power law. J. Anal. At. Spectrom. 18, 1371–1375. doi:10.1039/b308403e

Woodhead, J., 2002. A simple method for obtaining highly accurate Pb isotope data by MC-ICP-MS. J. Anal. At. Spectrom. 17, 1381–1385. doi:10.1039/b205045e

Yamakawa, A., Yamashita, K., Makishima, A., Nakamura, E., 2009. Chemical separation and mass spectrometry of Cr, Fe, Ni, Zn, and Cu in terrestrial and extraterrestrial materials using thermal ionization mass spectrometry. Anal. Chem. 81, 9787–9794. doi:10.1021/ac901762a

York, D., 1966. Least-sqares fitting of a straight line. Can. J. Phys. 44, 1079–1086. doi:10.1139/p66-090

Young, E.D., Galy, A., Nagahara, H., 2002. Kinetic and equilibrium mass-dependent isotope fractionation laws in nature and their geochemical and cosmochemical significance. Geochim. Cosmochim. Acta 66, 1095–1104. doi:10.1016/S0016-7037(01)00832-8

Young, E.D., Manning, C.E., Schauble, E.A., Shahar, A., Macris, C.A., Lazar, C., Jordan, M., 2015. High-temperature equilibrium isotope fractionation of non-traditional stable isotopes: Experiments, theory, and applications. Chem. Geol. 395, 176–195. doi:10.1016/j.chemgeo.2014.12.013

Chapter 5

Evaluation of the use of cold plasma conditions for Fe isotopic analysis via MC-ICP-MS: effect on spectral interferences and instrumental mass discrimination

Stepan M. Chernonozhkin, Marta Costas-Rodríguez, Philippe Claeys and Frank Vanhaecke
The manuscript is prepared for publication and thus subject to further changes and modifications

S.Ch. designed and carried out the experiments, processed the raw data, delivered and analysed the results, wrote the manuscript and took part in the discussion.

> *"Nature can always be more complicated than we imagine."*
>
> *Harold Urey*

1. Abstract

The advantages and disadvantages associated with the use of cold plasma conditions in combination with both the standard and the high-transmission ('jet') plasma interface and in dry and wet plasma conditions in the context of high-precision isotopic analysis of Fe by multi-collector inductively coupled plasma-mass spectrometry (MC-ICP-MS) were evaluated. When using the standard interface and a wet plasma, cold plasma condtions suppressed the occurrence of the polyatomic ions $^{40}Ar^{14}N^+$ and $^{40}Ar^{16}O^+$, but not that of $^{40}Ar^{16}O^1H^+$. Dry plasma conditions efficiently removed the oxide ions, but at the cost of a dramatic increase in the prevalence of nitride ions. Thus, interference-free $^{56}Fe/^{57}Fe$ measurement can be performed at low mass resolution using cold plasma conditions and the standard plasma interface. Hence, the possibility to work at low mass resolution compensates for the loss in sensitivity at low RF power. No alleviation of the spectral interferences due to Ar-based ions were obtained with the 'jet' interface in cold plasma conditions. With cold plasma conditions, the instrumental mass discrimination affecting the Fe isotope ratios was mitigated compared to that obtained with a hot plasma when the standard interface was used, which is probably due to reduced amount of Ar^+ ions sampled from ICP. This mitigation in instrumental mass discrimination in cold plasma conditions was not observed when the high-transmission interface was used.

2. Introduction

In inductively coupled plasma mass-spectrometry (ICP-MS), cold plasma conditions can be used to suppress the occurrence of Ar-based ions, thus alleviating the corresponding spectral interferences (Tanner, 1995). Very often these cold plasma conditions were relied on to avoid or at least strongly suppress the interference due to overlap of the signals of $^{40}Ar^{16}O^+$ on ^{56}Fe. However, as a result of the widespread application of sector-field instruments capable of working at higher mass resolution and quadrupole-based instruments equipped with a collision/reaction cell, cold plasma conditions became nearly forgotten. Also the drawbacks accompanying the use of cold plasma conditions contributed to this waning success: deterioration of the sensitivity for elements characterized by a high first ionization energy, more pronounced matrix effects and an increased formation of oxide ions. Although successfully used for isotope ratios measurements of Fe (Kehm et al., 2003), Li (Bryant et al., 2003) and Cr (Schiller et al., 2014) via multicollector-ICP-MS (MC-ICP-MS), high mass resolution (Malinovsky et al., 2003) is the typical approach used to avoid spectral overlap in MC-ICP-MS nowadays, although occasionally, also collision cell technology has been used (Dauphas et al., 2004). Recently, high-transmission plasma interfaces were introduced in ICP-MS (also termed the 'jet' interface), which provide a much higher ion extraction efficiency from the plasma (Lloyd et al., 2013). In combination with dry plasma conditions, achieved via sample aerosol desolvation (either via membrane desolvation or solvent evaporation techniques (Minnich and Houk, 1998), precise measurement of isotope ratios at element concentrations down to 0.5 ng g^{-1} is enabled (Bazzano et al., 2015). In this work we re-evaluate the capabilities and limitations of cold plasma conditions in combination with the high-transmission 'jet' interface and membrane aerosol desolvation for high-precision Fe MC-ICP-MS isotope measurements. The effect on the occurrence of interfering ions and the extent of instrumental mass discrimination was paid specific attention to.

3. Experimental

3.1. Materials. IRMM-014 (Institute for Reference Measurements and Materials, Belgium) and NIST SRM 986 (National Institute for Science and Technology, USA) isotopic certified reference materials of Fe and Ni, respectively, were used throughout this study. Conventional mono-element standard solution of Fe with isotope ratios known from 5 years of in-house measurements was used as Fe isotopic reference material. NIST SRM 997, NIST SRM 981, NIST SRM 987, IRMM-16 and NIST SRM 951 certified isotopic reference materials of Tl, Pb, Sr, Li and B, respectively, were used to study the instrumental mass discrimination under different plasma conditions.

3.2. Instrumentation. The isotope ratios of Fe were measured using a Thermo Scientific (Germany) Neptune multi-collector ICP-MS unit, equipped with a large dry interface pump (100 m^3 h^{-1} pumping speed). Fe isotope ratios were measured using 8 different instrument setups, realized via a combination of: cold or hot plasma conditions, dry or wet plasma conditions and standard or 'jet' interface. Cold plasma conditions were obtained by gradual decrease of the plasma RF power, optimization of the ICP torch position, and corresponding reduction of sample gas flow rate . The latter is needed to optimize the position of the normal analytical zone of the ICP – or the zone with the highest analyte ion density - to that of the sampler cone of the interface as to achieve maximum sensitivity for the Fe isotopes (Vanhaecke et al., 1993).Either high-transmission 'jet' Ni interface cones (jet-type sampling cone and X-type skimmer cone) or 'standard' Ni interface cones (standard sampling cone with an orifice diameter of 1.1 mm and standard skimmer cone with an orifice diameter of 0.8 mm) were used to test the effect of an enhanced interface transmission efficiency on spectral interferences and the extent of instrumental mass discrimination. A 100 µl min^{-1} concentric nebulizer with a Scott-type double-pass spray chamber a or an Aridus II desolvating nebulizer system (Teledyne CETAC Technologies Inc., USA) were used to study the effect of wet and dry plasma conditions. Detailed instrument settings are shown in table 5-1.

3.3. MC-ICP-MS measurements and signal correction protocol. The sample solutions had a 3% HNO_3 matrix. Depending on the instrument configuration, the Fe solutions were diluted to 50-1000 ng ml^{-1} concentrations in order to obtain similar intensities in the different configurations. Ni isotopic reference material NIST SRM 986 was added to all samples and standards in a concentration equal to that of Fe to serve as an internal standard relied on for internal mass discrimination correction. Concentrations of samples and bracketing standards were fitted within ±3 %. The measurements of Fe isotope ratios were carried out in a sample-standard bracketing (SSB) sequence with IRMM-014 Fe isotopic reference material as external standard. Correction for instrumental mass discrimination was performed according to the exponential model revised by Baxter *et al.* (Baxter et al., 2006), which corrects for both

Instrument settings			
		Hot plasma conditions	Cold plasma conditions
Resolution mode		Medium	Medium, Low
RF power, W		1260^{a}	600
Gas flow rates^{a}, l min^{-1}	Cool	15	15
	Auxiliary	0.8	0.8
	Nebulizer	0.997	0.570
Dry plasma (Teledyne Cetac Technologies Aridus II)			
Gas flow rates^{a}, l min^{-1}	Nebulizer	0.680	0.580
	Sweep Ar	4.85	4.85
	N_2	0.008	0
Spray chamber temperature, °C		110	110
Membrane desolvator temperature, °C		160	160
Wet plasma (pneumatic nebulization)			
Sample uptake		Pumped via peristaltic pump, 0.1 ml min^{-1}	
Nebulizer		Concentric, 100 µl min^{-1}	
Spray chamber		Double, cyclonic and Scott-type sub-units	
Interface			
		'Standard' interface	'Jet' interface
Interface pump		High-efficiency dry interface pump (100 m^{3} h^{-1} pumping speed)	
Sampler cone		Standard Ni sampler (1.1 mm aperture)	Jet type Ni sampler
Skimmer cone		H-type Ni skimmer (0.8 mm apperture)	X-type Ni skimmer
Data acquisition			
Mode		Static; multi-collection	
Idle time, s		3	
Integration time, s		4.194	
Number of integrations		1	
Number of blocks		9	
Number of cycles per block		5	

Cup configuration for Fe isotope ratio measurements						
Cup	L_4	L_2	L_1	C	H_1	H_3
Amplifier	10^{11} Ω	10^{11} Ω	10^{11} Ω	10^{11} Ω	10^{11} Ω	10^{11} Ω
Nuclide	^{54}Fe	^{56}Fe	^{57}Fe	^{58}Fe, ^{58}Ni	^{60}Ni	^{62}Ni

Table 5-1. Instrument settings, data acquisition parameters and multi-collector detector configuration for the Thermo Scientific Neptune MC-ICP-MS instrument used for Fe isotopic analysis at different instrument settings.
^{a} Parameters optimized on a daily basis for highest sensitivity and stability

the mass- and time-dependent contributions to the instrumental mass discrimination. After internal correction, the Fe isotope ratios are reported in delta notations, relative to the bracketing isotopic reference material IRMM-014s:

$$\delta^{x/54}Fe = \left[\frac{({}^{x}Fe/{}^{54}Fe)_{Ni\,corr,smp}}{({}^{x}Fe/{}^{54}Fe)_{Ni\,corr,IRMM014}} - 1\right]\cdot 1000 \tag{5 – 1}$$

4. Results

4.1. Wet plasma conditions. Figure 5-1 (A, B) presents peak profiles at m/z ratios of 54, 56 and 57 measured in medium mass resolution mode (MR, m/Δm = 4500 using 5 -95 % on plateau notation, see Vanhaecke and Moens 2004) with standard interface cones and in hot (A) and cold (B) plasma conditions, respectively. Under hot plasma conditions and at low mass resolution, the ^{54,56,57}Fe peaks are overlapped by those of the Ar-based polyatomic ions $^{40}Ar^{14}N^{+}$, $^{40}Ar^{16}O^{+}$ and $^{40}Ar^{16}O^{1}H^{+}$, respectively. High mass resolution allows to separate the Fe^{+} signals (separate plateau), enabling interference-free Fe isotope ratio measurements (A). A reduction of the plasma RF power from 1260 W down to 600 W efficiently suppresses the signals of $^{40}Ar^{14}N^{+}$ and $^{40}Ar^{16}O^{+}$ with this setup. Complete absence of these interferences in cold plasma conditions is confirmed by accurate ^{56}Fe/^{54}Fe isotope ratio measurement in low mass resolution (LR, m/Δm ≈ 300) mode. The ^{56}Fe/^{54}Fe isotope ratios measured for our in-house isotope standard in cold plasma conditions in LR and MR are in agreement with the corresponding 5-year average. However, $^{40}Ar^{16}O^{1}H^{+}$ ions cannot be fully removed, not even by reducing the RF power to values lower than 600 W. As a result, the ^{56}Fe/^{54}Fe ratio can only be measured in MR. Transition to the cold plasma conditions is associated with a 2-fold loss in sensitivity, after re-optimization of the Ar gas flow rates and torch position. At the same time, when using LR and cold plasma conditions, even a small gain in Fe sensitivity is achieved as compared

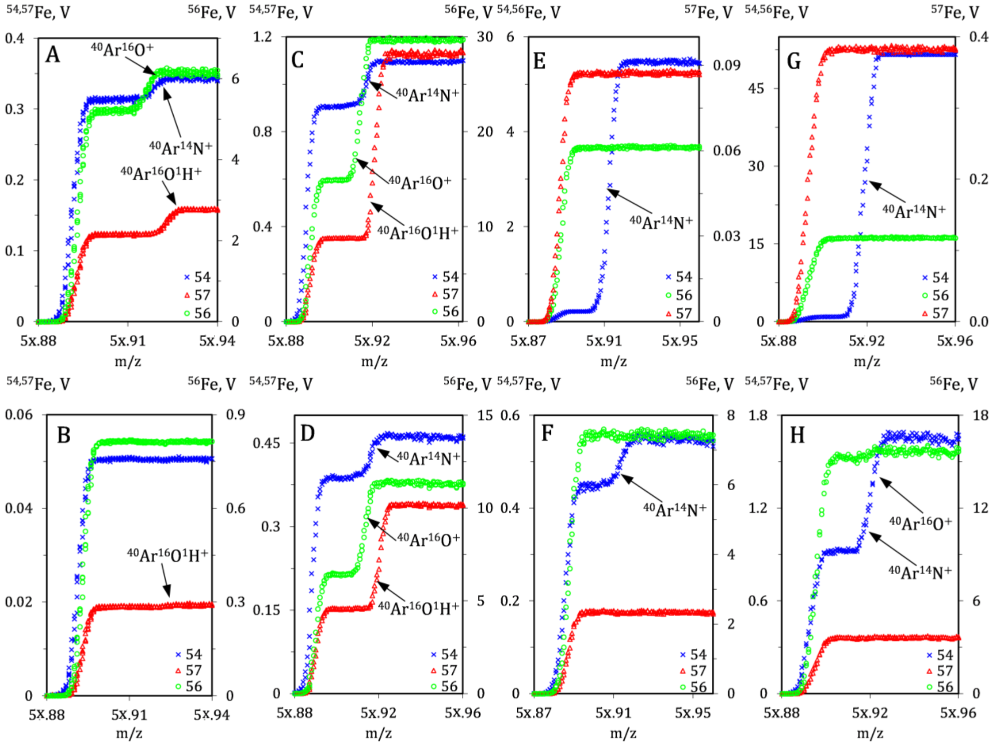

Figure 5-1. Peak profiles at m/z = 54, 56, 57 in medium resolution mode (m/Δm = 4500) and in different instrument configurations. The peak at m/z=54 is typically a combination of signals from $^{54}Fe^+$ overlapped with that from $^{40}Ar^{14}N^+$; the peak at m/z=56 consists of the $^{56}Fe^+$ signal overlapping with that from $^{40}Ar^{16}O^+$; the peak at m/z=57 consists of the $^{57}Fe^+$ signal overlapped with that from $^{40}Ar^{14}O^1H^+$. A – hot plasma conditions (1260 W), pneumatic nebulization and standard interface; B – cold plasma conditions (600 W), pneumatic nebulization and standard interface; C – hot plasma, pneumatic nebulization and ‘jet’ interface; D – cold plasma, pneumatic nebulization and ‘jet’ interface; E – hot plasma, membrane desolvation nebulization and standard interface; F – cold plasma, membrane desolvation nebulization and standard interface; G - hot plasma, membrane desolvation nebulization and ‘jet’ interface; H - cold plasma, membrane desolvation nebulization and ‘jet’ cones.

to MR at hot plasma conditions.

Critically, after transition to cold plasma conditions, also the voltages of the focus lenses array need to be tuned significantly to achieve maximum and stable sensitivity. This might be because the extracted ion beam is defocused after reduction of RF power. Although we cannot directly observe amount of Ar^+ ions, extracted into the mass-spectrometer from the ICP, the necessary change in lens voltages can possibly be an indirect indication that the amount of extracted Ar^+ in cold plasma is significantly smaller than in hot plasma conditions. This would lead to necessity to re-optimize the focusing lens voltages.

Figure 5-1 (C, D) presents the peak profiles at m/z ratios of 54, 56 and 57 measured with high-transmission ‘jet’ interface cones and in hot and cold plasma conditions, respectively. In comparison with standard interface cones, the sensitivity achieved with the jet interface is 2-foldhigher. At the same time, the higher ion transmission efficiency is associated with a significantly higher level of Ar-based spectral interference, as can be seen in figure 5-1 (C). With the jet interface, the Ar-based interferences are not suppressed by cold plasma conditions, such that Fe isotope measurements absolutely require a higher mass resolution under these conditions; see figure 5-1 (D). At the same time, conversion to cold plasma conditions is associated with a 2.85-fold decrease in Fe sensitivity, which renders application of cold plasma conditions futile with high-transmission ‘jet’ interface cones.

4.2. Dry plasma conditions. Dry plasma conditions were achieved using a Teledyne Cetac Technologies Aridus II membrane desolvating nebulizer. This device utilizes a PFA C-type nebulizer (100 µl min^{-1}) and heated spray chamber, combined with a PTFE membrane desolvator unit, see figure 5-2. This combination provides an increase in sensitivity due to a more efficient analyte transfer into plasma and a reduction in solvent-based interferences (*e.g.*, oxide, hydride and hydroxide ions). The desolvation unit was operated with a 4.85 l min^{-1} Ar sweep gas flow. The N_2 gas flow needs to be tuned finely. It was found that in hot plasma conditions an N_2 flow rate of about 10 ml min^{-1}

	Hot plasma	Cold plasma
	Pneumatic nebulization (wet plasma)	
Standard interface		a. 2-fold loss in sensitivity compared to hot plasma conditions (in MR) b. Application of low mass resolution is possible for ^{56}Fe/^{54}Fe - $^{40}Ar^{16}O^+$ and $^{40}Ar^{14}N^+$ are removed and the $^{56}Fe^+$ and $^{54}Fe^+$ signals are interference-free - $^{40}Ar^{16}O^1H^+$ is still interfereing with the meadurement of $^{57}Fe^+$ c. The extent of instrumental mass discrimination is significantly smaller than in hot plasma d. Lens array voltages have to be retuned compared to hot plasma conditions
'Jet' interface	a. 2-fold improvement in sensitivity compared to standard interface b. increased levels of $^{40}Ar^{16}O^+$, $^{40}Ar^{14}N^+$ and $^{40}Ar^{16}O^1H^+$ compared to standard interface c. ≈20% improvement of isotope ratio precision compared to standard interface	a. 2.85-fold loss in sensitivity compared to hot plasma conditions b. Application of low mass resolution mode is impossible, $^{40}Ar^{16}O^+$, $^{40}Ar^{14}N^+$ and $^{40}Ar^{16}O^1H^+$ are not suppressed by cold plasma conditions c. The extent of instrumental mass discrimination is similar to that in hot plasma conditions
	Membrane desolvation nebulization (dry plasma)	
Standard interface	a. 7-fold improvement in sensitivity compared to pneumatic nebulization b. $^{40}Ar^{16}O^+$ and $^{40}Ar^{16}O^1H^+$ are removed by membrane desolvation unit c. $^{40}Ar^{14}N^+$ is much higher than in the case of pneumatic nebulization	a. 1.5-fold loss in sensitivity compared to hot plasma conditions b. Application of low mass resolution is not possible: - $^{40}Ar^{14}N^+$ is not suppressed fully by cold plasma conditions c. The extent of instrumental mass discrimination is smaller than in hot plasma conditions
'Jet' interface	a. 2-fold improvement in sensitivity compared to standard interface b. $^{40}Ar^{16}O^+$ and $^{40}Ar^{16}O^1H^+$ are removed by the membrane desolvation unit c. Application of MR is not sufficient any longer because of enhanced levels of $^{40}Ar^{14}N^+$ compared to standard interface	a. Fe^+- intensity is 10-foldlower than in hot plasma conditions b. Application of low mass resolution is not possible: - $^{40}Ar^{16}O^+$ is present (if N_2 gas flow is switched off) - $^{40}Ar^{14}N^+$ is decreased but not fully removed by cold plasma conditions c. The isotope ratio precision is deteriorated in comparison to hot plasma conditions

Table 5-2. Summary of effects observed under cold and hot plasma conditions in different instrument configurations: wet/dry plasma and standard/'jet' interface cones.

provides the highest Fe sensitivity, while in cold plasma the highest sensitivity was achieved at a near-to-zero N_2flow rate. Aerosol desolvation provided a 7-fold improvement in Fe sensitivity in hot plasma conditions in comparison to pneumatic nebulization. Figure 5-1 (E, F) presents peak profiles at m/z ratios of 54, 56 and 57 in hot and cold plasma conditions, respectively, when using standard interface cones and dry plasma. The $^{40}Ar^{16}O^+$ and $^{40}Ar^{16}O^1H^+$ ions were successfully removed, rendering the ^{56,57}Fe isotopes interference-free, but the signal from $^{54}Fe^+$, typically used as the reference isotope, suffers from significant overlap with the $^{40}Ar^{14}N^+$ signal. It makes application of low resolution impossible. This argon nitride peak most probably originates from air surrounding inside the nebulizer and spray chambler of the Teledyne Cetac Aridus II, because it is present even when the N_2 gas flow is switched off.

Conversion to cold plasma conditions is associated with a 1.5-fold loss in sensitivity compared to hot plasma conditions. In contrast to wet plasma conditions, the $^{40}Ar^{14}N^+$ interference peak is not fully removed by conversion to cold plasma conditions, although it is reduced significantly. This ArN^+ interference makes it impossible to measure at low mass resolution in cold plasma / dry plasma / standard interface configuration. Among all the configurations studied, the combination of membrane desolvation (dry plasma) and the high-transmission "jet" interface in hot plasma conditions provides the highest sensitivity for iron isotopes. Similarly to the situation with standard interface cones, ArO^+ and $ArOH^+$ ions are fully removed by membrane desolvation. However, this configuration results in an even higher level of $^{40}Ar^{14}N^+$, which saturates the faraday cup detector with a 10^{11} Ω amplifier, rendering measurements at low mass resolution mode impossible. Although this interfering peak is resolved in medium resolution mode, we did not manage to achieve correct ^{5x}Fe/^{54}Fe isotope ratios. This is likely the result of an insufficient abundance sensitivity of the instrument to avoid the influence of the tail of the huge $^{40}Ar^{14}N^+$

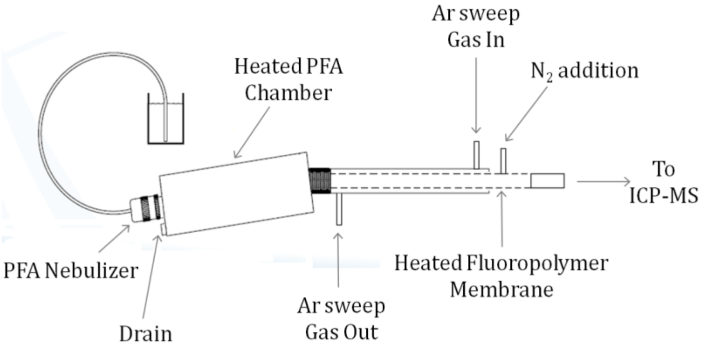

Figure 5-2. Schematic design of the Teledyne Cetac Technologies Aridus II membrane desolvating nebulizer.

peak onto the plateau of the $^{54}Fe^+$ signal. At the same time, $^{57}Fe/^{56}Fe$ ratios measured in medium mass resolution mode were within the range expected for the in-house standard.

Conversion to cold plasma conditions when using the high-transmission 'jet' interface and dry plasma conditions, leads to 10-fold drop in the sensitivity compared to that in hot plasma conditions. Although the occurrence of $^{40}Ar^{14}N^{+\ +}$ is not fully avoided by cold plasma conditions, it is suppressed enough to allow $^{54}Fe^+$ to be measured in medium mass resolution mode. When the N_2 gas flow rate in the membrane desolvator is decreased in order to provide the highest sensitivity, a small $^{40}Ar^{16}O^+$ interference starts affecting the $^{56}Fe^+$ peak. This small interference can be removed fully when the N_2 flow rate is optimized, but in latter case, the overall Fe sensitivity is compromised.

Table 5-2 provides an overview of the results obtained in 8 different instrument configurations: cold/hot plasma conditions, wet/dry plasma and standard/'jet' interface cones.

4.3. Instrumental mass discrimination. Instrumental mass discrimination is an inherent drawback of MC-ICP-MS and it refers to a non-stoichiometric transmission of the target element isotopes (Albarède et al., 2015; Rehkämper et al., 2001) from the ICP ion source to the detector. Typically, the heavier of two isotopes is transmitted more efficiently, with stronger effect for light elements. Coulomb repulsion (space-charge effects) and scattering effects within the ion beam were previously suggested to be the main contributors to the instrumental mass discrimination (Kivel et al., 2012), although also other effects were described (Andren et al., 2004; Taylor and Farnsworth, 2012). Various strategies to correct for instrumental mass discrimination are efficiently used (Al-Ammar and Barnes, 2001; Baxter et al., 2006; Yang, 2009), but reducing the extent of discrimination would possibly allow achieving even higher precisions for isotope ratio measurements. Ar is the major component of the ICP discharge and its ions and excited atoms serve for RF energy transfer to the analyte via charge transfer and penning ionization mechanisms. As a result, after charge separation, the Ar^+ ions dominate the ion beam in the ion optics after the interface. The presence of large amounts of Ar^+ ions in the plasma and the ion beam cannot only result in molecular spectral interferences, but also affect the instrumental mass discrimination due to the aforementioned Coulomb repulsion. Figure 5-3 presents isotope plots for several isotopic CRMs measured under cold and hot plasma conditions. It was found that in cold plasma conditions (600 W), when the number of Ar^+ ions in the beam is lower, the magnitude of instrumental mass discrimination observed for Fe and Ni is smaller than in the case of hot plasma conditions (figure 5-3 A). This observation is in agreement with the observed effect of U on Pb isotope ratios (Santos et al., 2007). However, with the high-transmission 'jet' interface and wet plasma conditions, the magnitudes of instrumental mass discrimination in cold and hot plasma conditions are similar. This unexpected behavior with the 'jet' interface might be a result of the extraction of a much larger number of Ar^+ ions from the plasma by the high-transmission interface, thus rendering the effect of changing over to cold plasma less significant. After 1 year of experience with the 'jet' interface, we have also observed that its regular application leads to an at least 2-fold faster degradation of the resolution slits compared to the standard interface, even though target analyte intensities are kept the same. We associate this observation to the enhanced amount of Ar^+ extracted from plasma by the 'jet' interface. An indirect confirmation of our assumption concerning the Ar^+ effect on the extent of instrumental mass discrimination observed for Fe is that when the strongest effect of switching over to cold plasma conditions on instrumental mass discrimination is observed (with standard interface cones and in wet plasma conditions), the voltages of focusing

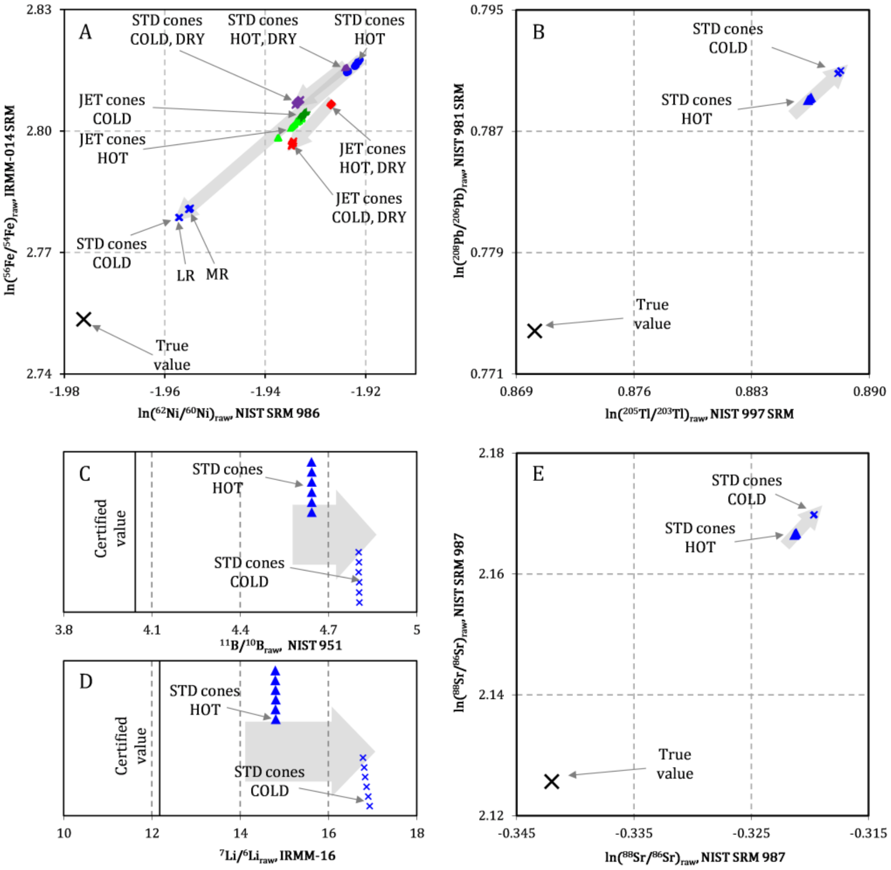

Figure 5-3. Isotope plots measured using the Neptune MC-ICP-MS unit under 8 different instrument settings: hot/cold and dry/wet plasma conditions and standard/'jet' interface cones. Measured raw isotope ratios are presented in ln-scale for A) Fe and Ni isotope ratios measured in IRMM-14 and NIST SRM 986, B) Pb and Tl isotope ratios measured in NIST SRM 981 and NIST SRM 997 C) B isotope ratios measured in NIST SRM 951, D) Li isotope ratios measured in IRMM SRM 16 and E) Sr isotope ratios measured in NIST SRM 987. All the ratios presented are not corrected for instrument instrumental mass discrimination (raw). The arrows indicate the direction of the change in instrumental mass discrimination when the plasma power is decreased. The Sr isotope ratios presented were corrected iteratively for Rb and Kr isobaric interferences according to natural isotopic abundances and the exponential fractionation law. For the details of the instrument configuration for Pb, B, Li and Sr isotope ratio measurements, please see (Bazzano et al., 2015; Devulder et al., 2013; Rich et al., 2012; Van Hoecke et al., 2015).

lens array had to be re-tuned more significantly in order to achieve the highest intensity for Fe^+.

Differently to Fe and Ni, both heavier elements Sr, Pb and Tl (figure 5-3 B, E) as and the lightest ones Li and B (figure 5-3 C, D) were found to suffer a larger extent of instrumental mass discrimination in cold plasma conditions than in hot plasma ones. This observation indicates that the prevailing mechanisms of mass discrimination are potentially different for Fe and the other elements evaluated. This confirms that the mechanisms behind instrumental mass discrimination have not been fully unraveled yet.

5. Summary

In the standard configuration (standard interface cones and sample introduction via pneumatic nebulization), cold plasma conditions can efficiently suppress/remove $^{40}Ar^{16}O^+$ and $^{40}Ar^{14}N^+$ ions, but not $^{40}Ar^{16}O^{1}H^+$. Once interference from $^{40}Ar^{16}O^+$ and $^{40}Ar^{14}N^+$ are fully removed by cold plasma conditions, accurate $^{56}Fe/^{54}Fe$ measurement can be done at low mass resolution, providing a gain in intensity, at the cost of the possibility to monitor the ^{57}Fe isotope.

Application of a membrane desolvation nebulizer efficiently removes oxide-based interferences, but leads to a substantial increase in the $^{40}Ar^{14}N^+$ signal intensity. This peak of $^{40}Ar^{14}N^+$ can be suppressed in cold plasma conditions to some extent, but not fully removed.

Application of the high-efficiency ‘jet’ interface provides a higher sensitivity owing to a higher ion transmission efficiency, but it also significantly enhances the level of spectral interferences and decreases the tolerance of isotopic analysis to matrix elements. None of the relevant interferences can be fully removed by application of cold plasma conditions under these conditions. This high amounts of Ar-based ions, being introduced continuously into the massspectrometer for a long time rapidly deteriorates the resolution slits.

Overall, conversion from hot to cold plasma conditions is associated with a lower extent of instrumental mass discrimination for Fe, except with the ‘jet’ interface, for which the mass discrimination is nearly equal for hot and cold plasma conditions. Although it was not proven experimentally, we assume that the reduction in the extent of mass discrimination is a result of introducing fewer Ar-based ions (mainly Ar^+) into the mass spectrometer, which alleviates space-charge effects to some extent. An indirect confirmation of our assumption is that the voltages of the lenses have to be re-optimized after switching from hot to the cold plasma conditions.

6. List of references

Al-Ammar, A., Barnes, R., 2001. Improving isotope ratio precision in inductively coupled plasma quadrupole mass spectrometry by common analyte internal standardization. J. Anal. At. Spectrom. 16, 327–332. doi:10.1039/b100973g

Albarède, F., Albalat, E., Télouk, P., 2015. Instrumental isotope fractionation in multiple-collector ICP-MS. J. Anal. At. Spectrom. 30, 1736–1742. doi:10.1039/C5JA00188A

Andren, H., Rodushkin, I., Stenberg, A., Malinovsky, D., Baxter, D.C., 2004. Sources of mass bias and isotope ratio variation in multi-collector ICP-MS: optimization of instrumental parameters based on experimental observations. J. Anal. At. Spectrom. 19, 1217–1224. doi:10.1039/b403938f

Baxter, D.C., Rodushkin, I., Engström, E., Malinovsky, D., 2006. Revised exponential model for mass bias correction using an internal standard for isotope abundance ratio measurements by multi-collector inductively coupled plasma mass spectrometry. J. Anal. At. Spectrom. 21, 427–430. doi:10.1039/b517457k

Bazzano, A., Latruwe, K., Grotti, M., Vanhaecke, F., 2015. Lead isotopic analysis of Antarctic snow using multi-collector ICP-mass spectrometry. J. Anal. At. Spectrom. 30, 1322–1328. doi:10.1039/C4JA00484A

Bryant, C.J., McCulloch, M.T., Bennett, V.C., 2003. Impact of matrix effects on the accurate measurement of Li isotope ratios by inductively coupled plasma mass spectrometry (MC-ICP-MS) under ”cold“ plasma conditions. J. Anal. At. Spectrom. 18, 734. doi:10.1039/b212083f

Dauphas, N., Janney, P.E., Mendybaev, R.A., Wadhwa, M., Richter, F.M., Davis, A.M., van Zuilen, M., Hines, R., Foley, C.N., 2004. Chromatographic separation and multicollection-ICPMS analysis of iron. Investigating mass-dependent and -independent isotope effects. Anal. Chem. 76, 5855–63. doi:10.1021/ac0497095

Devulder, V., Degryse, P., Vanhaecke, F., 2013. Development of a Novel Method for Unraveling the Origin of Natron Flux Used in Roman Glass Production Based on B Isotopic Analysis via Multicollector Inductively Coupled Plasma Mass Spectrometry. Anal. Chem. 85, 12077–12084. doi:10.1021/ac403176c

Kehm, K., Hauri, E.., Alexander, C.M.O., Carlson, R.., 2003. High precision iron isotope measurements of meteoritic material by cold plasma ICP-MS. Geochim. Cosmochim. Acta 67, 2879–2891. doi:10.1016/S0016-7037(03)00080-2

Kivel, N., Günther-Leopold, I., Vanhaecke, F., Günther, D., 2012. Isotope fractionation during ion beam formation in multi-collector inductively coupled plasma mass spectrometry. Spectrochim. Acta Part B At. Spectrosc. 76, 126–132. doi:10.1016/j.sab.2012.06.045

Lloyd, N.S., Trinquier, A., Bouman, C., 2013. Improvements in Isotope Ratio Accuracy and Precision using “Jet” Sample Cone for ICP-MS, in: American Geophysical Union, Fall Meeting. p. #V53B–2776.

Malinovsky, D., Stenberg, A., Rodushkin, I., Andren, H., Ingri, J., Ohlander, B., Baxter, D.C., 2003. Performance of high resolution MC-ICP-MS for Fe isotope ratio measurements in sedimentary geological materials. J. Anal. At. Spectrom. 18, 687. doi:10.1039/b302312e

Minnich, M.G., Houk, R.S., 1998. Comparison of cryogenic and membrane desolvation for attenuation of oxide, hydride and hydroxide ions and ions containing chlorine in inductively coupled plasma mass spectrometry. J. Anal. At. Spectrom. 13, 167–174. doi:10.1039/a704274d

Rehkämper, M., Schönbächler, M., Stirling, C.H., 2001. Multiple Collector ICP-MS: Introduction to Instrumentation, Measurement Techniques and Analytical Capabilities. Geostand. Geoanalytical Res. 25, 23–40. doi:10.1111/j.1751-908X.2001.tb00785.x

Rich, S., Manning, S.W., Degryse, P., Vanhaecke, F., Van Lerberghe, K., 2012. Strontium isotopic and tree-ring signatures of Cedrus brevifolia in Cyprus. J. Anal. At. Spectrom. 27, 796. doi:10.1039/c2ja10345a

Santos, R., Canto Machado, M.J., Ruiz, I., Sato, K., Vasconcelos, M.T.S.D., 2007. Space charge and mass discrimination effects on lead isotope ratio measurements by ICP-QMS in environmental samples with high uranium content. J. Anal. At. Spectrom. 22, 783. doi:10.1039/b618783h

Schiller, M., Van Kooten, E., Holst, J.C., Olsen, M.B., Bizzarro, M., 2014. Precise measurement of chromium isotopes by MC-ICPMS. J. Anal. At. Spectrom. 29, 1406–1416. doi:10.1039/C4JA00018H

Tanner, S.D., 1995. Characterization of ionization and matrix suppression in inductively coupled “cold” plasma mass spectrometry. J. Anal. At. Spectrom. 10, 905–921. doi:10.1039/ja9951000905

Taylor, N., Farnsworth, P.B., 2012. Experimental characterization of the effect of skimmer cone design on shock formation and ion transmission efficiency in the vacuum interface of an inductively coupled plasma mass spectrometer. Spectrochim. Acta Part B At. Spectrosc. 69, 2–8. doi:10.1016/j.sab.2012.02.003

Van Hoecke, K., Belza, J., Croymans, T., Misra, S., Claeys, P., Vanhaecke, F., 2015. Single-step chromatographic isolation of lithium from whole-rock carbonate and clay for isotopic analysis with multi-collector ICP-mass spectrometry. J. Anal. At. Spectrom. 30, 2533–2540. doi:10.1039/C5JA00165J

Vanhaecke, F., Dams, R., Vandecasteele, C., 1993. “Zone model” as an explanation for signal behaviour and non-spectral interferences in inductively coupled plasma mass spectrometry. J. Anal. At. Spectrom. 8, 433–438. doi:10.1039/JA9930800433

Vanhaecke, F., Moens, L., 2004. Overcoming spectral overlap in isotopic analysis via single- and multi-collector ICP-mass spectrometry. Anal. Bioanal. Chem. 378, 232–240. doi:10.1007/s00216-003-2175-8

Yang, L., 2009. Accurate and precise determination of isotopic ratios by MC-ICP-MS: a review. Mass Spectrom. Rev. 28, 990–1011. doi:10.1002/mas

Chapter 6

Effect of parent body evolution on equilibrium and kinetic isotope fractionation: a combined Ni and Fe isotope study of iron and stony-iron meteorites

based on publication by
Stepan M. Chernonozhkin, Steven Goderis, Marta Costas-Rodríguez, Philippe Claeys and Frank Vanhaecke, 2016, Geochimica Cosmochimica Acta, 2016, Volume 186, P. 168-188.

S.Ch. designed and carried out the experiments, processed the raw data, delivered and analysed the results, wrote the manuscript and took part in the discussion.

1. Abstract

Various iron and stony-iron meteorites have been characterized for their Ni and Fe isotopic compositions using multi-collector inductively coupled plasma-mass spectrometry (MC-ICP-MS) after sample digestion and chromatographic separation of the target elements in an attempt to further constrain the planetary differentiation processes that shifted these isotope ratios and to shed light on the formational history and evolution of selected achondrite parent body asteroids. Emphasis was placed on spatially resolved isotopic analysis of iron meteorites, known to be inhomogeneous at the µm to mm scale, and on the isotopic characterization of adjacent metal and silicate phases in main group pallasites (PMG), mesosiderites, and the IIE and IAB complex silicate-bearing iron meteorites. In a 3-isotope plot of $^{60/58}$Ni versus $^{62/58}$Ni, the slope of the best-fitting straight line through the laterally resolved Ni isotope ratio data for iron meteorites reveals kinetically controlled isotope fractionation (β_{exper} = 1.981 ± 0.039, 1 SD), predominantly resulting from sub-solidus diffusion (with the fractionation exponent β connecting the isotope fractionation factors, as $\alpha_{62/58} = \alpha_{60/58}{}^{\beta}$). The observed relation between $\delta^{56/54}$Fe and Ir concentration in the metal fractions of PMGs and in IIIAB iron meteorites indicates a dependence of the bulk Fe isotopic composition on the fractional crystallization of an asteroidal metal core. No such fractional crystallization trends were found for the corresponding Ni isotope ratios or for other iron meteorite groups, such as the IIABs. In the case of the IIE and IAB silicate-bearing iron meteorites, the Fe and Ni isotopic signatures potentially reflect the influence of impact processes, as the degree of diffusion-controlled Ni isotope fractionation is closer to that of Fe compared to what is observed for magmatic iron meteorite types. Between the metal and olivine counterparts of pallasites, the Fe and Ni isotopic compositions show clearly resolvable differences, similar in magnitude but opposite in sign ($\Delta^{56/54}\mathrm{Fe}_{met\text{-}oliv}$ of +0.178 ± 0.092 ‰ and $\Delta^{60/58}\mathrm{Ni}_{met\text{-}oliv}$ of -0.212 ± 0.082 ‰, 2SD). As such, the heavier Fe isotope ratios for the metal ($\delta^{56/54}$Fe = +0.023 to +0.247 ‰) and lighter values for the corresponding

olivines ($\delta^{56/54}$Fe = -0.155 to -0.075 ‰) are interpreted to reflect later-stage Fe isotopic re-equilibration between these phases, rather than a pristine record of mantle-core differentiation. In the case of mesosiderites, the similarly lighter Ni and Fe isotopic signatures found for the silicate phase (-0.149 to +0.023 ‰ for $\delta^{60/58}$Ni, -0.214 to -0.149 ‰ for $\delta^{56/54}$Fe) compared to the metal phase (+0.168 to +0.191 ‰ for $\delta^{60/58}$Ni, +0.018 to +0.120 ‰ for $\delta^{56/54}$Fe) likely result from Fe and Ni diffusion. Overall, the Fe and Ni isotopic compositions of iron-rich meteorites reflect multiple, often superimposed, processes of equilibrium or kinetic nature, illustrating convoluted parent body histories and late-stage interaction between early-formed planetesimal reservoirs.

Keywords: Fe and Ni isotopic composition; pallasites; mesosiderites; iron meteorites; mass-dependent isotope fractionation; core formation

2. Introduction

At present, natural stable isotope fractionation has been shown to affect elements with ≥2 isotopes. Generally, differences of the order of ~1‰ are observed for the isotope ratios on the bulk meteorite scale, with usually even larger effects for lighter elements. The overwhelming part of these isotope fractionations exhibit a mass-dependent character, indicating that the extent of the observed isotope fractionation, caused by chemical reaction or phase change, depends on the masses of the isotopes. Based on the underlying natural process, the distinction is made between equilibrium and kinetic mass-dependent fractionation. Equilibrium mass-dependent isotope fractionation occurs during exchange between compounds (or between phases) as a result of differences in the equilibrium reaction constants for different isotopes, which arise from slightly different vibrational energy levels for the molecules that contain these different isotopes. As such, equilibrium isotope fractionation largely depends on the bonding environment of the atom and the temperature of the governing process. In contrast, kinetic mass-dependent isotope fractionation arises without achieving equilibrium in the system, as a result of the different rates at which the isotopes with different masses are involved in a process (either physical rates, as in the case of diffusion, or chemical reaction rates). A classical example of kinetic isotope fractionation is the irreversible evaporation to the vacuum of an element, where the rate constants depend on the isotopic masses (Alexander and Wang, 2001; Dauphas *et al.*, 2004; F. Richter *et al.*, 2009). For ordinary chondrites, isotopic variations of Ni, Cu and Zn have been suggested to result from vapor-solid reactions, followed by mineral sorting during accretion (Moynier *et al*, 2007). Similarly, the isotope ratios of the elements taking part in chemical or thermal diffusion can be affected, due to the fact that isotopes tend to diffuse at dissimilar rates as a result of differences in their masses (F. M. Richter *et al.*, 2009). Equilibration of the isotope ratios between two adjacent phases is achieved via diffusive isotopic exchange, which, in its turn, is associated with kinetic isotope effects. During slow cooling of mineral assemblages, diffusion will effectively stop at a particular temperature. In some cases, when equilibrium cannot be achieved, some degree of the kinetic control on the isotope ratios will be preserved, dependent on, for instance, the cooling rate, the target element and the mineral assemblage studied (*e.g.* Mueller *et al.* 2010). In practice, the distinction between kinetic and equilibrium mass-dependent isotope effects can be made by calculating the theoretical fractionation exponents β for equilibrium and kinetic isotope control, and by comparing these to the experimental slope obtained from the corresponding 3-isotope plot (Young *et al.* 2002):

$$\beta_{eq} = \frac{\left({}^{1}/_{m_{58}} - {}^{1}/_{m_{62}}\right)}{\left({}^{1}/_{m_{58}} - {}^{1}/_{m_{60}}\right)} \tag{6 – 1}$$

$$\beta_{kin} = \frac{ln\left({}^{m_{58}}/_{m_{62}}\right)}{ln\left({}^{m_{58}}/_{m_{60}}\right)} \tag{6 – 2}$$

In the Early Solar System, the intense heating of initially undifferentiated planetesimals as a result of short-lived β^- isotope decay of ^{26}Al led to the differentiation of these bodies with the formation of silicate-dominated mantles and iron-rich cores, from which iron-rich achondritic meteorites derive (Grimm and Mcsween, 1993). These planetary fractionation processes not only affected the elemental composition, but also the isotopic composition of the meteorite parent bodies (Moynier *et al.*, 2007). In the case of iron-rich meteorites, Fe and Ni can experience resolvable equilibrium isotope fractionation in the processes associated with the melting of undifferentiated precursors and subsequent segregation of metal from silicate. The degree of equilibrium isotope fractionation between the co-existing phases depends on the temperature at which these processes occurred. Under the temperature and pressure conditions in asteroid-size parent bodies, heavier Fe isotopic compositions for the metal core and lighter isotope ratios for silicate phases relative to the initial isotopic composition of the precursor material are expected (Polyakov, 2009). Trace element concentration trends within most iron meteorite groups reflect fractional crystallization (Scott, 1972; Goldstein *et al.*, 2009), which confirms the formation of ~2 to 100 km sized metallic cores within differentiated meteorite parent bodies (Chabot and Haack, 2006). However, another class of iron meteorites, known as the IAB complex and IIE silicate-bearing groups (previously designated "non-magmatic"), shows no compositional trends indicative of fractional crystallization. Instead, these meteorites contain enclosed silicates and are interpreted to have formed as a result of planetesimal collision. For instance, the IAB meteorite complex is thought to result from impact on a partially differentiated asteroid that experienced less peak heating and in part preserved a chondritic composition (Goldstein *et al.*, 2009; Ruzicka, 2014). If this presumed model is correct, the expected Fe-Ni isotopic variations in silicate-bearing iron meteorites arising due to impact processing should be different from those resulting from magmatic processing and core formation in the purely magmatic iron meteorites groups. Impact processing potentially includes preferential evaporation of light isotopes in a process similar to the modeled evaporation to vacuum, with an associated shift to heavier isotopic compositions. In contrast to magmatic processes, for which Fe and Ni isotope ratios depend on crystal chemistry constraints and on the corresponding fractions that went into the silicate and metal fractions, the relative isotope ratio shifts for Fe and Ni in the case of impact should be of similar magnitude, given the comparable element volatilities. CB chondrites are thought to have some components that formed by condensation in impact plume (Tang and Dauphas, 2012; Richter *et al.*, 2014; Weyrauch *et al.*, 2015).

However, later-stage processes leading to Fe and Ni isotope fractionation in iron meteorite parent bodies, such as sub-solidus diffusion during the Widmanstätten pattern growth, also need to be considered. This diffusion results from the growth of Ni-poor kamacite (bcc α-iron) from taenite (fcc γ-iron) during the slow (a few to thousands ˚C Myr^{-1}; (Goldstein *et al.*, 2014) cooling of iron meteorite parent bodies and the dissimilar diffusivities for the different isotopes. During cooling, initially stable taenite decomposes to form intergrown kamacite and taenite lamellae *via* solid state diffusion of Ni and Fe atoms, a process that is accompanied by kinetic isotope fractionation. The fractionation of Fe and Ni isotopes during the growth of kamacite out of taenite during the formation of the Widmanstätten pattern has been modeled for a set of cooling rates ranging from 25 to 500 ˚C Myr^{-1} (Dauphas, 2007). As equilibrium fractionation of Fe and Ni isotopes due to the redistribution between α and γ phases following crystal chemistry constraints is also possible, the contributions of kinetic and equilibrium isotope fractionation need to be evaluated. The cooling histories of the iron meteorite parent bodies are reflected in the metallographic cooling rates determined for the iron meteorite group members. For instance, IVA iron meteorites are characterized by a wide range of cooling rates between 100 and 6600 ˚C Myr^{-1} (1500 ˚C Myr^{-1} for Gibeon) (Goldstein *et al.* 2014). These cooling rates depend on the size of the parent body, the depth within the core and prevalence and thickness of any covering mantle.

Stony-iron meteorites, consisting of pallasites and mesosiderites, are closely related to iron meteorites. Both meteorite groups are composed of nearly equal parts of metal, derived from the metal core of a differentiated asteroid, and a silicate counterpart. This silicate is made up of mantle-derived olivine crystals in the case of pallasites or brecciated remains of basaltic minerals of predominantly crustal origin in the case of mesosiderites. Besides the observation that the parent bodies of both meteorite groups show extensive evidence for processes related to impact and collision, there is no data to support a common origin from the same parent body (Greenwood *et al.*, 2006). For instance, the Δ^{17}O oxygen isotopic compositions of olivines in pallasites and mesosiderites differ by ~0.06 ‰ (Greenwood *et al.*, 2015). An alternative hypothesis for mesosiderite formation envisions mixing of brecciated basaltic/pyroxenic silicates (Ruzicka *et al.*, 1994) derived from igneous differentiated asteroid crust/regolith with asteroidal core fragments upon impact (Wasson and Rubin, 1985; Hassanzadeh *et al.*, 1990). Although the exact formational mechanism of pallasites is still heavily debated, a model involving collision with a substantially molten parent body, which separated a partially solidified core and mantle containing olivine and silicate melt, remains a compelling possibility (Ruzicka, 2014). In a "hit and run" impact scenario, molten metal and silicate mantle material from the core-mantle boundary would be mixed and re-accreted (Yang et al., 2010). Poitrasson *et al.* (Poitrasson *et al.*, 2005) reported heavy Fe isotopic compositions for the metal part of pallasites ($\delta^{57/54}$Fe of -0.020 to +0.237 ‰) and light Fe isotopic compositions for the corresponding olivine fractions ($\delta^{57/54}$Fe of -0.090 to +0.021 ‰). If the conditions for Fe isotopic equilibration between the adjacent olivine and metal phases are fulfilled, the resulting Fe isotope ratio signatures can be used as an isotope geothermometer, relying on the temperature dependence of the distribution of Fe isotopes between the phases (Polyakov 2009, Dauphas *et al.* 2012). However, it remains unclear whether the olivine-metal Fe isotope equilibration and the corresponding temperatures were fully achieved in the process of initial metal-silicate segregation of the parent body, or if such equilibrium was altered during later re-equilibrating thermal events.

In this work, new stable Fe and Ni isotope ratio data are provided for 4 pallasites and 4 magmatic iron meteorites, permitting one to study the isotope fractionation of these elements between adjacent silicate-metal and metal-metal phases and to provide insight into the formation history and evolution of their parent bodies. Stable isotope fractionation of Fe and Ni was also studied in 3 mesosiderites and 5 silicate-bearing iron meteorites, including IAB-ung Udei Station. Although the stable Fe and Ni isotope signatures of these meteorites are not related to core formation processes, they could potentially reveal links with the cooling histories of these meteorite parent bodies, or late-stage collision events. Different to previous work, the current study focuses on the isotopic analysis of both Ni and the relatively well-understood Fe, of the same meteorite sub-samples digestions. This strategy provides additional constraints on the processes that lead to Fe-peak element stable isotope fractionation. The previously studied occurrence of nucleosynthetic anomalies or the radiogenic ingrowth of Ni isotopes are not addressed in this work (Dauphas *et al.*, 2008; Regelous *et al.*, 2008; Steele *et al.*, 2011; Tang and Dauphas, 2014).

3. Experimental

3.1. Samples. In total, 4 iron meteorite specimens (Henbury IIIAB, Campo del Cielo IAB-MG, Gibeon IVA and Canyon Diablo IAB-MG) as well as 3 main group pallasites (Seymchan, Fukang and Esquel) were purchased from commercial meteorite vendors. Four iron meteorites (Chinga IVB-an, Sikhote-Alin IIB, Elga IIE and Darinskoe IIC) were obtained from the Central Siberian Geological Museum, V. S. Sobolev Institute of Geology and Mineralogy, Russia. A selection of these iron meteorites were characterized for major and trace element concentrations in a previous work (Chernonozhkin *et al*., 2014). Three mesosiderites, EET 87500, RKPA 79015 and QUE 93001 and main group pallasite CMS 04071 were provided from the Antarctic meteorite collection by the National Aeronautics and Space Administration (NASA). Three ordinary chondrites A 10224 (L3), A 09135 (LL3) and A 09436 (H3) were provided by the Royal Belgian Institute of Natural Sciences (RBINS) from their Antarctic meteorite collection. OKUM is a certified reference material of an ultramafic komatiite (Geosciences Laboratories, Sudbury, Ontario, Canada). PCC-1 and BHVO-1 are certified reference materials of peridotite and basalt (United States Geological Survey, Denver, Colorado, USA).

3.2. Reagents and labware. Only high-purity reagents and acids were used throughout the experiments. Pro analysis grade nitric acid (65%, Chem-Lab, Belgium) was further purified through sub-boiling in PFA equipment. Optima-grade hydrochloric (37%, Seastar Chemicals Inc., Canada) and trace-metal grade hydrofluoric (47–51%, Seastar Chemicals Inc., Canada) acids were used as such. Ultrapure water (resistivity ≥18.2 MΩ cm) was obtained from a Milli-Q Element water purification system (Millipore, France). Purissima grade acetone, ultrapure 9.8 M H_2O_2 and dimethylglyoxime (DMG) were purchased from Sigma Aldrich (Belgium). Savillex™ Teflon® beakers were pre-cleaned by alternating 24 h soaking steps in pro-analysis 6 M HCl and 7 M HNO_3 at 110°C (4 times). All the Teflon® recipients, disposable plastic tubes and pipette tips used for the sample preparation were additionally cleaned by soaking in 10% pro-analysis HCl for 48 h at 110°C. The chromatographic isolation of the target elements, hot-plate evaporation and labware cleaning procedures were performed under class-10 clean lab conditions to reduce airborne contamination.

3.3. Sub-sampling and sample preparation. The allocated mesosiderite chips were first broken into smaller pieces and manually ground in an agate mortar that was pre-cleaned by grinding pro-analysis quartz grains to powder 3 times, rinsing with ultrapure water, and drying. The ground mesosiderites were separated into non-magnetic (150-200 mg) and magnetic (350-600 mg) fractions using a hand magnet. These fractions are called silicate and metal fractions, respectively, hereafter, although this magnetic fraction might contain magnetic species other than metal, such as oxides. A diamond disk saw was used to cut 100-200 mg fragments from the bulk mass of the pallasite metal. Visibly oxidized surfaces were removed by cleaning with silicon carbide sandpaper, etching with dilute HNO_3 in an ultrasonic bath, and finally rinsing with ethanol to avoid contamination of the surface. The olivine crystals (200-300 mg) closely attached to the sampled metal parts were split from the pallasites using stainless steel

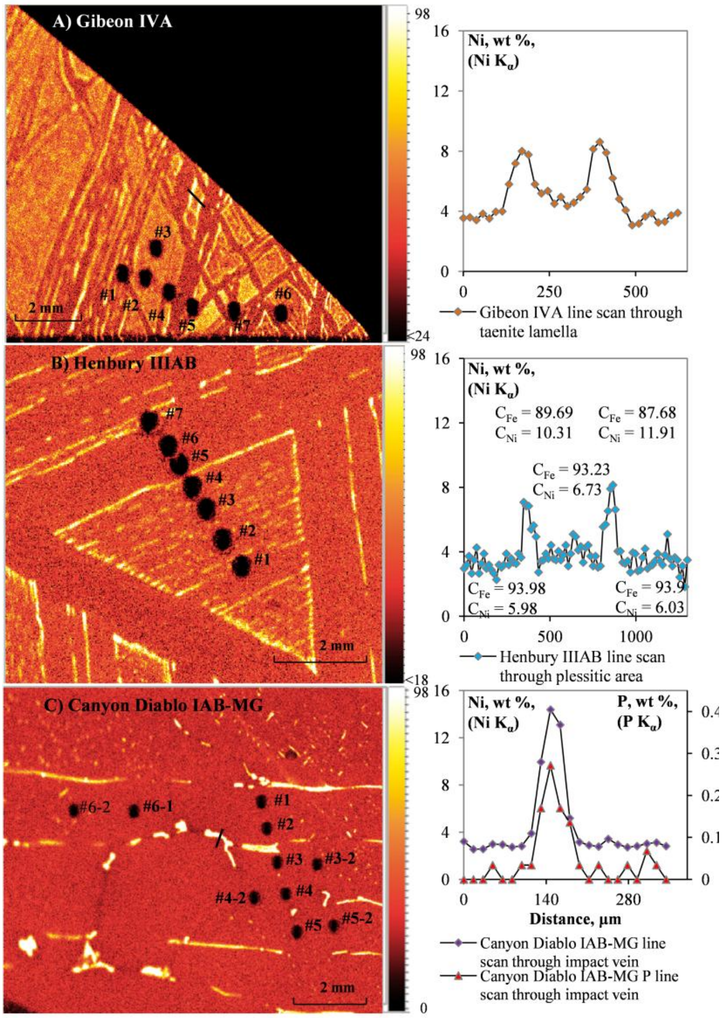

Figure 6-1. 2D Ni K_α intensity distribution maps of 3 thick sections of iron meteorites as obtained using µXRF, black round spots represent micro-drilling sampling positions (see table 6-1). The color code is given in relative intensities. Gibeon IVA (A) and Henbury IIIAB (B) iron meteorites demonstrate clear Widmanstätten patterns, while Canyon Diablo does not (C). Typical Ni concentration profiles for 3 iron meteorites are shown (marked by black bar in fig. 6-1 A and C). Higher Ni concentrations are predicted in taenite in contact with kamacite according to the phase diagram, so the concentrations shown here result from insufficient spatial resolution (Yang *et al.* 1996).

tweezers. The olivine crystals were collected into an agate mortar and manually ground with an agate pestle. Any remaining minor metal was removed using a hand magnet.

Five iron meteorites (Gibeon, Henbury, Canyon Diablo, Campo del Cielo and Chinga) were further sub-sampled *via* computer-assisted micro-drilling under an optical microscope. Sampling positions for 3 of these meteorites are shown in the two-dimensional (2D) distribution maps of the Ni K_α intensity obtained by micro X-ray fluorescence spectrometry (µXRF) (Figure 1A, B and C). The uniform distribution maps obtained for Campo del Cielo and Chinga are not shown. Sampling pure taenite phases was difficult because the drill bit diameter is larger than the taenite lamellae. In addition, drilling can mix phases vertically. As a result, drilling resulted in phase mixtures characterized by different taenite/kamacite ratios. In the case of Canyon Diablo, bright Ni-rich veinlets were not attributed to taenite, as they also contain elevated contents of P. These veinlets were avoided during sampling.

Approximately 400 µm deep pits were drilled in a polished thick section of the iron meteorites at 1750 rpm in the presence of a 10 µl droplet of ultrapure water. The wet sample powder was collected with a pipet into a Savillex™ Teflon® beaker. The surface of the sample was cleaned with ethanol under a microscope after each spot drilling to avoid cross-contamination. The potential contamination from the material of the drill bit (tungsten carbide, WC) was controlled by monitoring the W content in the digested samples using sector field ICP-MS (SF-ICP-MS). The presence of W, predominantly present in the WC drill bit, and relatively depleted in iron meteorite material, was either below the detection limit, or negligible compared to the contents of Fe and Ni. As such, any contamination of meteorite material with Fe and Ni from the drill bit is considered to be insignificant. In addition, to evaluate potential isotope fractionation resulting from melting that may occur during the drilling, several micro-drillings of the Chinga IVB homogeneous ataxite were sampled and the resulting Fe and Ni isotope ratios were compared to bulk sample measurements. As the results were indistinguishable within analytical uncertainty, isotope fractionation during micro-drilling was considered to be insignificant. The ordinary chondrite material (50-100 mg) was sampled by drilling multiple 1-2 mm deep holes from the inside of the samples provided using a 1 mm diameter WC drill bit at low rotation speeds. The fusion crusts of the same samples were collected separately (10-20 mg), by drilling shallow (0.5-1 mm) spots at the exterior of these meteorites.

The metal fractions of pallasites and mesosiderites were digested using 6 ml of freshly prepared *aqua regia* (1.5 ml HNO_3 and 4.5 ml HCl) in closed Savillex™ Teflon® beakers at 90°C for 96 h. Micro-drilled sub-samples of iron meteorites were digested in a similar way using 1 ml of *aqua regia* only. As the metal fractions of mesosiderites were not digested completely (silicate particles might have been captured during magnetic separation), centrifugation was used to separate off the residue. The chondrites and the silicate counterparts of stony-iron meteorites were first digested in 3 ml of 14 M HNO_3 at 90°C for 24 h in closed Savillex™ Teflon® beakers. Subsequently, the mixtures thus obtained were transferred into microwave Teflon vials and further digested *via* a two-step microwave-assisted acid digestion. In a first step, a combination of HF and HNO_3 is used to break down the silicates, while, following evaporation to dryness at 90°C, the digestion is completed in *aqua regia* to dissolve insoluble fluorides (Chernonozhkin *et al.*, 2015). Finally, all solutions were evaporated to incipient dryness in open vessels at 90°C, 0.1 ml of 12 M HCl was added to all the digests, and the solutions were evaporated again to dryness at 90°C. This last step was repeated 3 times to convert all nitrates to chlorides before the isolation procedure. The meteorite digests were divided in 3 parts to perform *i)* element analysis, *ii)* isotopic analysis of Ni, and *iii)* isotopic analysis of Fe. The bulk digestions of iron meteorites, previously used for Ni isotopic analysis (Chernonozhkin *et al.*, 2015), were used in this study to determine Fe isotope ratios. Small aliquots of the digested meteorites were taken and diluted in 3% HNO_3 for the quantitative determination of the target elements using SF-ICP-MS.

The Ni isolation from the iron and silicate matrices was carried out using a 3-step ion exchange chromatographic procedure, previously described in detail (Chernonozhkin *et al.*, 2015). In a first step, Ni is separated from the main part of the matrix using Dowex 50WX4 cation exchange resin in a medium of HCl-acetone-dimethylglyoxime. A second step utilizes a column packed with AG1X8 anion exchange resin in HCl-HF medium to separate Ni from Ti, while a third anion exchange isolation step is used for final clean-up of the Ni fraction from traces of Fe and Zn in 6 M HCl. The Fe isolation from the iron meteorites and silicate matrices relies on anion exchange column chromatography using AG MP-1 strong anion exchange resin in HCl medium. An adaptation of the chromatographic isolation method first described for geological samples was utilized (Maréchal *et al.*, 1999; Van Heghe *et al.*, 2012). The Ni and Fe concentrations were also determined in the isolated fractions to verify quantitative recoveries and the purity of the fractions.

3.4. Instrumentation and measurement protocols. The 2D element distribution maps of the thick iron meteorite sections were obtained using a Bruker M4 Tornado XRF instrument at the Vrije Universiteit Brussel, equipped with a 30W Rh-anode X-ray source (50 kV operating voltage, operating current 150 μA) and a Be side-window. The X-rays are focused to a 25 μm spot (measured for Mo Kα) using a polycapillary lens. The instrument is equipped with two Silicon Drift Detector (SDD) spectrometers (30 mm^2, 145 eV energy resolution for Mn Ka), symmetrically placed relative to the sample. Measurements were performed under a vacuum of 20 mbar. To acquire the 2D elemental distribution maps, a motorized sample stage moves at a speed of 25 mm s^{-1} (1 ms per pixel), scanning the surface for 8 cycles.

The 2D element distribution maps of pallasite olivines were obtained using a 193 nm Teledyne Cetac Technologies Photon Machines Analyte G2 ArF* excimer-based laser ablation (LA) system with a double-volume ablation cell coupled to a SF-ICP-MS unit (see below) at Ghent University. The maps were acquired at 9 μm s^{-1} translation speed, 20 μm spot diameter, 3.54 J cm^{-2} energy fluence, and covered a square area of 1450x600 μm from the metal-olivine margin in the direction of the olivine cores. The He carrier gas was mixed with the Ar sample gas downstream of the ablation cell, and introduced into the ICP-MS unit, operated at low mass resolution and cold plasma conditions. Wash-out times were typically less than 1 s. The signal was acquired in the "speed mode" of the instrument, at 1.94 s per scan total scanning speed. The spatial resolution achieved was approximately 20x20 μm. Quantification relied on a combination of external calibration (versus the synthetic glasses NIST SRM 612, NIST SRM 614 and artificial and natural CRM glasses from the USGS GSD-1G, GSE-1G, BHVO-2G and BIR-1G) and internal sum normalization using the intensities of Mg, Fe and Si and relying on the empirical formula of the olivine mineral.

A solid sampling system Merchantek MicroMill equipped with a drill mounted on a video microscope assembly and a set of motorized stages was used for the micro-drilling and milling of the samples at the Vrije Universiteit Brussel. A 300 μm diameter WC drill bit (Komet dental) was used.

For the acid digestion of the samples, a MLS-1200 MEGA Microwave digestion system (Milestone, Italy) was used at Ghent University.

Element concentrations were determined using a Thermo Scientific Element XR SF-ICP-MS unit operated in low and medium resolution modes, using In as an internal standard, at Ghent University.

The isotopic analysis of Ni and Fe was performed in separate measurement sessions using a Thermo Scientific Neptune multi-collector ICP-MS (MC-ICP-MS) unit equipped with a jet interface and dual spray chamber, consisting of a cyclonic and a Scott-type sub-unit, with a 100 µl min^{-1} concentric nebulizer in medium resolution mode. For the detailed description of the instrument settings, the reader is referred to the electronic supplementary information (ESI). Measurement of Ni and Fe isotope ratios was performed in a sample-standard bracketing (SSB) sequence relative to the NIST SRM 986 and IRMM-014 isotopic reference materials, respectively. The concentrations of Fe and Ni were adjusted to 400 ng g^{-1} using 3% HNO_3 and doped with Cu and Ni internal standards, respectively. Mass bias correction relied on the internal isotopic standard, according to the Russell equation revised by Baxter *et al.* 2006, which corrects for both the mass- and time-dependent functional parts of the instrumental mass discrimination. After the internal mass bias correction, the isotope ratios are reported as delta values, relative to the bracketing isotopic reference material to correct for minor drift of the instrumental parameters:

$$\delta^{x/58}Ni = \left[\frac{({}^{x}Ni/{}^{58}Ni)_{Cu\,corr,smp}}{({}^{x}Ni/{}^{58}Ni)_{Cu\,corr,NISTSRM986}} - 1\right]\cdot 1000 \tag{6 – 3}$$

$$\delta^{x/54}Fe = \left[\frac{({}^{x}Fe/{}^{54}Fe)_{Ni\,corr,smp}}{({}^{x}Fe/{}^{54}Fe)_{Ni\,corr,IRMM014}} - 1\right]\cdot 1000 \tag{6 – 4}$$

where *x* is 60, 61, 62 or 64 for Ni and 56 or 57 for Fe, and the subscripts denote that the ratios were first corrected by an exponential model. For further details, the reader is referred to previous publications of our group (Van Heghe *et al.*, 2012; Chernonozhkin *et al.*, 2015).

4. Results

The Ni concentration of and 2D distribution in various meteorites (Gibeon, Henbury, Canyon Diablo, Campo del Cielo and Chinga) were characterized using µXRF. Among these meteorites, Gibeon shows the widest taenite lamellae, less than 0.5 mm in width, with distinctive M-shaped Ni concentration profiles reaching a maximum of 11.06 – 12.22 wt % Ni (figure 6-1), with 6.09–6.35 wt% Ni in the neighboring kamacite. Even higher Ni concentrations are predicted in the taenite that is in direct contact with kamacite according to the phase diagram, so the concentrations shown here are affected by insufficient spatial resolution (Yang *et al.* 1996). Henbury shows wide kamacite bands (5.76–6.23 wt% Ni) surrounded by subordinate, thin (< 100 µm) taenite lamellae (10.17–11.70 wt% Ni), with large triangular or trapezoidal plessitic areas (6.73–6.92 wt % Ni on average). A Ni concentration profile through kamacite-taenite-plessite-taenite-kamacite is shown in figure 6-1B. Canyon Diablo exhibits a homogeneous Ni distribution in its metal. Campo del Cielo and Chinga demonstrate uniform Ni distribution maps, indicating that these are fully homogeneous in terms of Ni. The range of Ni concentrations in the micro-drilled iron meteorite sub-samples varies from 0.04 wt% (Chinga) to 0.8 wt% (Henbury), consistent with the values reported in the literature for bulk samples.

The results of the Fe and Ni isotope ratio determination are summarized in table 6-1. The $\delta^{56/54}$Fe values for the 3 ordinary chondrites analyzed vary from -0.008 to +0.015 ‰, which is in good agreement with the range reported in literature (see a compilation by Barrat *et al.*, 2015). Unfortunately, the amount of Ni stable isotope data published in literature for chondrites is limited. For 46 ordinary chondrites, Moynier *et al*., reported a $\delta^{60/58}$Ni range of 0.49 ‰, while for 6 carbonaceous chondrites and 6 enstatite chondrites, these authors found a range of 0.27‰ and 0.26‰, respectively (Moynier *et al.*, 2007). It should be noted that the values in that paper are reported relative to an in-house Ni standard, as NIST SRM 986 was not commercially available at that time. The recalculated $\delta^{60/58}$Ni values for 6 chondrites reported by Cook *et al.* vary from +0.05 to +0.44 ‰ (Cook *et al*., 2007). In the study referred to, all these $\delta^{60/58}$Ni values are not reported directly due to the possibility of non-mass dependent isotope effects on ^{60}Ni. As such, these values were recalculated from the $\delta^{62/58}$Ni values assuming the equilibrium fractionation law. Because the largest absolute non-mass dependent isotope effects reported for $\delta^{60/58}$Ni in iron meteorites are on the order of 0.02 ‰ (Cook *et al*., 2006), comparable to the precision attained in this work, these effects were assumed to be negligible. The results of $\delta^{60/58}$Ni for 3 ordinary chondrites, presented in this work vary from +0.149 to +0.242 ‰. This demonstrates the non-chondritic isotopic composition of the NIST SRM 986 Ni isotopic standard, which appears to have shifted during Ni purification by the Mond process (Tanimizu and Hirata, 2006; Steele *et al.*, 2011). The isotopic composition of both Fe and Ni in the fusion crusts of the chondrites characterized coincides with their

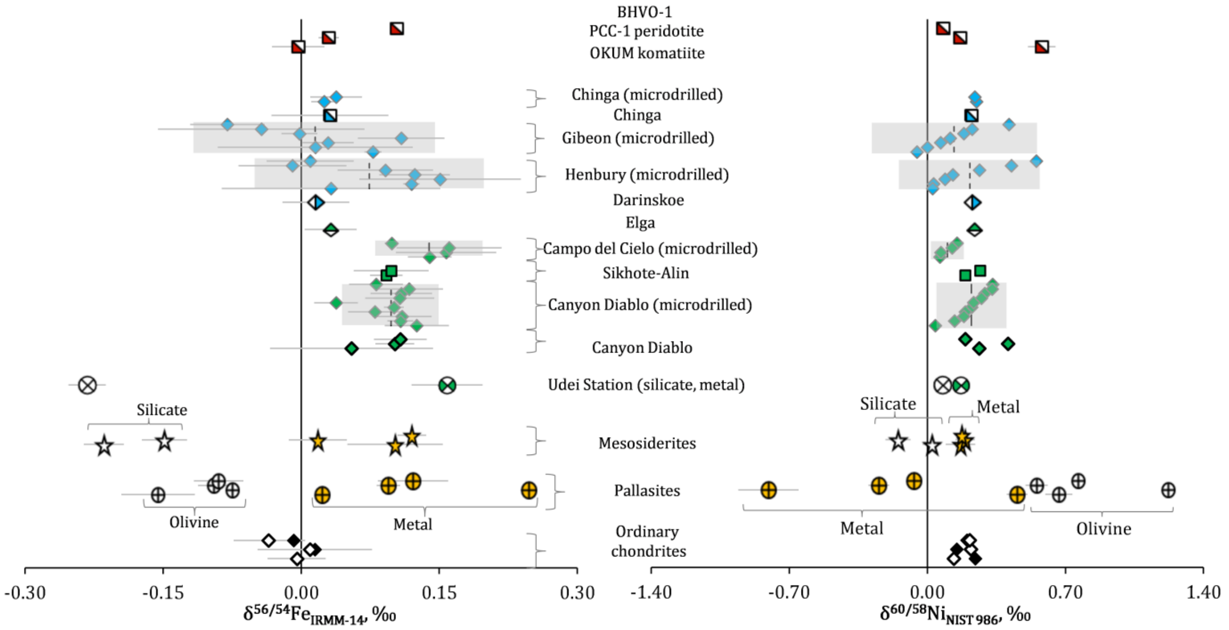

Figure 6-2. Isotope plots for $\delta^{56/54}$Fe and $\delta^{60/58}$Ni. Open diamonds represent fusion crusts of the corresponding ordinary chondrites. The values for GRMs BHVO-1, OKUM and PCC-1 are taken from literature (Dauphas *et al*., 2009; Chernonozhkin *et al*., 2015). The data of $\delta^{56/54}$Fe in OKUM are from this work.

measured bulk compositions within analytical uncertainty, different from the work of Hezel *et al.* 2015, who observed that the fusion crusts of ordinary chondrites are enriched in heavy Fe isotopes. This could either result from our sampling technique, by mixing bulk meteorite material, unaffected by atmospheric entry, with sample from the fusion crust, or could alternatively represent the effect of terrestrial weathering on fusion crusts. Hezel *et al.* (2015) selected the samples based on their size and the presence of visibly unaltered crusts to avoid Fe isotope exchange with the terrestrial environment. In this work, only Antarctic chondrites were analyzed and the fusion crusts of the selected samples appeared relatively fresh.

$\delta^{56/54}$Fe values of iron meteorites range from -0.080 to +0.161 ‰, while $\delta^{60/58}$Ni shows a wider variability, between -0.054 to +0.551 ‰. The average $\delta^{56/54}$Fe value for individual iron meteorites (bulk digestions and averaged sub-samples) varies from +0.015 to +0.139 ‰, which is similar to or higher than the chondrite values reported in literature ($\delta^{56/54}$Fe of -0.05 to +0.1‰ for the majority of chondrites, *e.g.* $\delta^{56/54}$Fe of +0.018 ‰ for Allende CV3; Barrat *et al*., 2015). Average $\delta^{60/58}$Ni values for individual iron meteorites (bulk digestions and averaged sub-samples) vary from +0.102 to +0.420 ‰, within the reported range of 0.05–0.44 ‰ for bulk metal of ordinary, carbonaceous and enstatite chondrites with an average $\delta^{60/58}$Ni of +0.26 ‰, as recalculated from $\delta^{62/58}$Ni data for 6 chondrites (Cook *et al*., 2007). The average $\delta^{60/58}$Ni results reported in the present work for Gibeon (+0.14 ‰), Henbury (+0.22 ‰), and Canyon Diablo (+0.22 ‰ for micro-drilled sub-samples and +0.29 ‰ for bulk analysis) correspond well with the recalculated results of Cook *et al.* (2007) (+0.19 ‰ for Gibeon, +0.19 to +0.22 ‰ for Henbury, and +0.26 ‰ for Canyon Diablo).

In the metal part of pallasites, Fe is always isotopically heavier than in the corresponding olivine fraction. In contrast, Ni in pallasite metal is always isotopically lighter than in the corresponding olivine (table 6-1). For 3 pallasites, Fukang, Esquel and CMS 04071, $\delta^{60/58}$Ni is negative, below the range observed for iron meteorites (table 6-1). This is in agreement with the observed light Ni isotopic compositions of the metal parts of pallasites in previous work ($\delta^{60/58}$Ni between -0.18 and +0.07 ‰, recalculated based on $\delta^{62/58}$Ni assuming equilibrium-controlled isotope fractionation and neglecting possible non-mass dependent input from ^{60}Fe decay; Cook *et al*., 2007).

For the mesosiderites analyzed in this study, the metal fractions are characterized by relatively heavier Fe isotopic compositions ($\delta^{56/54}$Fe of +0.018 to +0.120 ‰; table 6-1), while the corresponding silicate parts exhibit relatively light Fe isotopic compositions ($\delta^{56/54}$Fe of -0.214 to -0.149 ‰). Similar to Fe, Ni is isotopically heavier in the metal fractions of mesosiderites ($\delta^{60/58}$Ni between +0.168 and +0.191 ‰) in comparison to the silicate fractions, which have relatively lighter Ni isotopic signatures ($\delta^{60/58}$Ni between -0.149 and +0.023 ‰; table 6-1).

	$\delta^{56/54}$Fe ± SD, ‰	$\delta^{57/54}$Fe ± SD, ‰	$\delta^{60/58}$Ni ± SD, ‰	$\delta^{61/58}$Ni ± SD, ‰	$\delta^{62/58}$Ni ± SD, ‰	$\delta^{64/58}$Ni ± SD, ‰	Ni, wt %
Ordinary chondrites							
A-10224 (L3), bulk	-0.005±0.032	-0.017±0.053	+0.242±0.007	+0.411±0.072	+0.487±0.016	-	
A 10224 (L3), fusion crust	-0.004±0.022	+0.052±0.153	+0.133±0.009	+0.242±0.031	+0.266±0.015	-	
A 09135 (LL3), bulk	+0.015±0.062	-0.011±0.089	+0.149±0.012	+0.291±0.027	+0.305±0.016	-	
A 09135 (LL3), fusion crust	+0.010±0.045	+0.031±0.052	+0.220±0.016	+0.367±0.031	+0.436±0.032	-	
A 09436 (H3), bulk	-0.008±0.013	-0.001±0.091	+0.200±0.018	+0.313±0.020	+0.373±0.025	-	
A 09436 (H3), fusion crust	-0.035±0.038	-0.054±0.014	+0.214±0.016	+0.321±0.020	+0.396±0.050	-	
Pallasites							
Seymchan PMG, olivine	-0.155±0.040	-0.192±0.028	+0.667±0.069	+0.98±0.15	+1.25±0.14	+1.69±0.60	
Seymchan PMG, metal	+0.0229±0.0063	-0.008±0.040	+0.455±0.053	+0.60±0.10	+0.82±0.11	+1.01±0.55	
Fukang PMG, olivine	-0.0746±0.0074	-0.129±0.026	+1.221±0.029	+1.836±0.047	+2.381±0.019	+4.11±0.18	
Fukang PMG, metal	+0.2474±0.0091	+0.332±0.032	-0.81±0.15	-1.21±0.37	-1.55±0.41	-	
Esquel PMG, olivine	-0.095±0.017	-0.127±0.023	+0.554±0.056	+0.80±0.17	+1.06±0.17	+0.917±0.023	
Esquel PMG, metal	+0.095±0.013	+0.175±0.037	-0.246±0.052	-0.35±0.12	-0.531±0.077	-1.07±0.80	
CMS-04071 PMG, olivine	-0.090±0.027	-0.126±0.046	+0.764±0.024	+1.182±0.060	+1.515±0.070	+1.96±0.15	
CMS-04071 PMG, metal	+0.121±0.038	+0.188±0.016	-0.069±0.010	-0.094±0.050	-0.127±0.016	-0.046±0.082	
Mesosiderites							
EET 87500 mesosiderite, silicate	-0.214±0.022	-0.318±0.045	+0.023±0.047	-0.086±0.083	-0.01±0.12	-0.58±0.31	
EET 87500 mesosiderite, metal	+0.102±0.052	+0.071±0.040	+0.168±0.075	+0.24±0.22	+0.32±0.16	+0.12±0.51	
QUE 93001 mesosiderite, silicate	-0.149±0.025	-0.233±0.025	-0.149±0.064	-0.25±0.17	-0.28±0.17	-1.28±0.45	
QUE 93001 mesosiderite, metal	+0.018±0.031	-0.021±0.036	+0.191±0.049	+0.32±0.19	+0.40±0.25	-	
RKPA 79015 mesosiderite, metal	+0.120±0.016	+0.241±0.026	+0.175±0.019	+0.276±0.023	+0.344±0.020	+0.666±0.014	
Silicate-bearing iron meteorites							
Udei Station IAB-ung, silicate	-0.232±0.020	-0.365±0.020	+0.077±0.011	+0.107±0.046	+0.163±0.035	-	
Udei Station IAB-ung, metal	+0.158±0.039	+0.238±0.039	+0.167±0.014	+0.240±0.062	+0.343±0.047	-	
Canyon Diablo (bulk digestion 1)	+0.055±0.089	+0.104±0.083	+0.262±0.013	+0.407±0.011	+0.523±0.024	+0.67±0.22	
Canyon Diablo (bulk digestion 2)	+0.102±0.021	+0.157±0.057	+0.408±0.012	+0.63±0.11	+0.805±0.023	+1.36±0.44	
Canyon Diablo (bulk digestion 3)	+0.108±0.029	+0.145±0.059	+0.191±0.010	+0.301±0.056	+0.370±0.032	+0.590±0.025	
Canyon Diablo IAB-MG bulk digestions average	+0.088±0.029	+0.136±0.028	+0.29±0.11	+0.45±0.17	+0.57±0.22	+0.87±0.42	
Canyon Diablo (microdrilled #1)	+0.101±0.011	+0.1886±0.0046	+0.2242±0.0017	+0.372±0.041	+0.438±0.034	+1.0102±0.0085	6.771±0.061
Canyon Diablo (microdrilled #2)	+0.080±0.029	+0.133±0.054	+0.191±0.011	+0.359±0.028	+0.369±0.042	+1.103±0.029	6.83±0.14
Canyon Diablo (microdrilled #3)	+0.081±0.029	+0.146±0.060	+0.330±0.012	+0.509±0.043	+0.624±0.013	+1.22±0.40	6.973±0.092
Canyon Diablo (microdrilled #3-2)	+0.109±0.033	+0.166±0.070	+0.2909±0.0070	+0.457±0.048	+0.543±0.033	+1.056±0.030	6.761±0.092
Canyon Diablo (microdrilled #4)	+0.038±0.024	+0.065±0.062	+0.2340±0.0068	+0.376±0.025	+0.462±0.020	+1.011±0.072	6.635±0.056
Canyon Diablo (microdrilled #4-2)	+0.110±0.032	+0.147±0.073	+0.1838±0.0047	+0.277±0.036	+0.354±0.030	+1.059±0.017	6.50±0.10
Canyon Diablo (microdrilled #5)	+0.107±0.038	+0.160±0.079	+0.274±0.013	+0.425±0.040	+0.590±0.079	+1.007±0.030	6.749±0.078
Canyon Diablo (microdrilled #5-2)	+0.117±0.037	+0.181±0.026	+0.327±0.012	+0.491±0.032	+0.589±0.037	+1.08±0.16	6.665±0.158
Canyon Diablo (microdrilled #6-1)	+0.108±0.014	+0.182±0.041	+0.137±0.017	+0.201±0.032	+0.267±0.036	+0.88±0.31	6.719±0.10
Canyon Diablo (microdrilled #6-2)	+0.126±0.035	+0.221±0.038	+0.039±0.010	+0.061±0.031	+0.089±0.034	+0.57±0.48	6.838±0.099

	$\delta^{56/54}$Fe ± SD, ‰	$\delta^{57/54}$Fe ± SD, ‰	$\delta^{60/58}$Ni ± SD, ‰	$\delta^{61/58}$Ni ± SD, ‰	$\delta^{62/58}$Ni ± SD, ‰	$\delta^{64/58}$Ni ± SD, ‰	Ni, wt %
Canyon Diablo IAB-MG average of microdrilled samples	+0.098±0.025	+0.159±0.042	+0.223±0.090	+0.35±0.14	+0.43±0.17	+1.00±0.17	6.98[a]
Campo del Cielo (microdrilled #1)	+0.0983±0.0076	+0.188±0.023	+0.150±0.015	+0.226±0.048	+0.262±0.040	+0.462±0.053	6.536
Campo del Cielo (microdrilled #2)	+0.140±0.024	+0.216±0.026	+0.0630±0.0080	+0.115±0.045	+0.076±0.030	+0.27±0.12	6.564
Campo del Cielo (microdrilled #3)	+0.157±0.055	+0.231±0.054	+0.0680±0.0001	+0.129±0.091	+0.165±0.051	+0.16±0.24	6.324
Campo del Cielo (microdrilled #4)	+0.161±0.057	+0.241±0.056	+0.1250±0.0090	+0.231±0.057	+0.211±0.042	+0.294±0.065	6.289
Campo del Cielo IAB-MG average of microdrilled samples	+0.139±0.029	+0.219±0.023	0.102±0.043	0.175±0.062	+0.179±0.079	+0.30±0.12	6.62[b]
Elga IIE (bulk digestion)	+0.032±0.028	+0.071±0.022	+0.238±0.020	+0.334±0.043	+0.478±0.036	+0.66±0.64	
Magmatic iron meteorites							
Darinskoe IIC (bulk digestion)	+0.016±0.036	+0.047±0.056	+0.229±0.020	+0.311±0.070	+0.478±0.039	+0.57±0.21	
Sikhote Alin (bulk digestion 1)	+0.093±+0.018	+0.164±+0.024	+0.192±0.019	+0.289±0.063	+0.389±0.050	+0.51±0.56	
Sikhote Alin (bulk digestion 2)	+0.098±0.041	+0.177±0.076	+0.267±0.015	+0.459±0.092	+0.513±0.043	+0.68±0.22	
Sikhote Alin IIAB average	+0.0952±0.0038	+0.1706±0.0089	+0.230±0.053	+0.37±0.12	+0.451±0.088	+0.60±0.12	
Henbury (microdrilled #1)	+0.091±0.052	+0.11±0.150	+0.263±0.011	+0.413±0.046	+0.487±0.032	+0.83±0.12	7.115
Henbury (microdrilled #2)	+0.123±0.038	+0.211±0.162	+0.128±0.014	+0.200±0.038	+0.224±0.021	+0.46±0.22	7.273
Henbury (microdrilled #3)	+0.120±0.10	+0.195±0.095	+0.0310±0.0050	+0.035±0.053	+0.038±0.028	-0.015±0.049	7.255
Henbury (microdrilled #4)	+0.151±0.088	+0.210±0.135	+0.089±0.011	+0.138±0.048	+0.126±0.015	+0.256±0.056	7.261
Henbury (microdrilled #5)	-0.009±0.059	+0.04±0.11	+0.4250±0.0090	+0.650±0.037	+0.817±0.024	+1.189±0.082	6.889
Henbury (microdrilled #6)	+0.010±0.047	-0.054±0.062	+0.551±0.014	+0.849±0.043	+1.098±0.022	+1.53±0.17	7.056
Henbury (microdrilled #7)	+0.03±0.12	-0.07±0.22	+0.026±0.011	+0.030±0.025	+0.055±0.031	-0.007±0.084	7.774
Henbury IIIAB average of microdrilled samples	+0.074±0.062	+0.09±0.12	+0.22±0.19	+0.33±0.29	+0.41±0.38	+0.61±0.53	7.47[c]
Gibeon (microdrilled #1)	-0.080±0.040	-0.146±0.010	+0.4130±0.0090	+0.595±0.037	+0.810±0.021	+1.14±0.18	7.651
Gibeon (microdrilled #2)	+0.029±0.028	+0.0903±0.0010	+0.0670±0.0040	+0.105±0.058	+0.1120±0.0050	+0.02±0.12	7.753
Gibeon (microdrilled #3)	+0.109±0.047	+0.196±0.055	+0.1150±0.0070	+0.175±0.033	+0.221±0.014	+0.273±0.074	7.686
Gibeon (microdrilled #4)	-0.002±0.019	-0.028±0.025	+0.1840±0.0030	+0.311±0.061	+0.348±0.040	+0.415±0.038	7.723
Gibeon (microdrilled #5)	+0.078±0.010	+0.157±0.023	-0.0540±0.0080	-0.074±0.050	-0.104±0.014	-0.16±0.10	7.880
Gibeon (microdrilled #6)	-0.04±0.11	-0.064±0.043	+0.2260±0.0030	+0.350±0.033	+0.485±0.028	+0.61±0.14	7.793
Gibeon (microdrilled #7)	+0.02±0.11	-0.00±0.17	-0.0005±0.0080	+0.0390±0.0060	+0.012±0.030	-0.049±0.045	7.809
Gibeon IV average of microdrilled samples	+0.015±0.065	+0.03±0.12	+0.14±0.14	+0.21±0.21	+0.27±0.28	+0.32±0.42	7.93[d]
Chinga (bulk digestion)	+0.031±0.063	+0.045±0.041	+0.222±0.015	+0.329±0.064	+0.476±0.042	+0.77±0.38	
Chinga (microdrilled #1)	+0.025±0.014	+0.061±0.044	+0.248±0.015	+0.385±0.028	+0.513±0.037	+1.04±0.13	16.48±0.22
Chinga (microdrilled #2)	+0.038±0.028	+0.080±0.017	+0.239±0.013	+0.393±0.010	+0.527±0.025	+0.950±0.042	16.52±0.10
Chinga IVB-an average	+0.0314±0.0065	+0.062±0.018	+0.236±0.013	+0.369±0.035	+0.505±0.026	+0.92±0.14	16.5[e]
Other materials							
OKUM komatiite CRM	-0.003±0.029	+0.040±0.054	+0.580±0.070	+0.680±0.070	+1.13±0.13	-	
BHVO-1 basalt CRM	+0.138±0.013	+0.207±0.041	+0.081±0.034	+0.19±0.20	+0.130±0.093	+0.14±0.10	
PCC-1 peridotite CRM	+0.048±0.060	+0.111±0.096	+0.166±0.048	+0.25±0.14	+0.342±0.065	+0.62±0.39	

Table 6-1. Ni and Fe isotopic compositions of chondrites, stony-iron, magmatic iron, silicate-bearing iron meteorites and reference materials. Every sample was measured 3 to 5 times during at least 2 different measurement sessions. The results are presented in per mille deviations versus the corresponding reference material (NIST SRM 986 for Ni and IRMM-014 for Fe). The Ni isotopic compositions in geological reference materials and in bulk digests of iron meteorites have been reported previously (Chernonozhkin et al., 2015), while the Fe isotopic composition was determined using the same solutions of these digested meteorites. The Ni concentration data has been taken from the following references: a) (Scott, 1977a) b) (Wasson, 1970b) c) (Pernicka and Wasson, 1987) d) (Rasmussen et al., 1988) and e) (Rasmussen et al., 1984)

Our results for the Fe isotope ratios in BHVO-1 and PCC-1 are in full agreement with values reported previously in literature (Telus *et al.*, 2012, Dauphas *et al.*, 2009). OKUM is a new reference material of powdered ultramafic komatiite that has been certified for major and trace element abundances only. As $\delta^{56/54}$Fe values of komatiites have previously been found to be near-chondritic (+0.044 ‰ on average), indicating minor fractionation during komatiite magma genesis (Dauphas *et al.*, 2010), the -0.003 ‰ result obtained for OKUM is in agreement with the conclusions of Dauphas *et al.* (for more information the reader is referred to figure 6-11 in the appendix)

5. Discussion

5.1. Equilibrium isotope fractionation of Fe in pallasites. Resolvable enrichment of the metal fractions of pallasites in heavy Fe isotopes and corresponding depletion in olivines has previously been attributed to equilibrium fractionation during core-mantle differentiation (Poitrasson *et al.*, 2005). Figure 6-2 shows the Fe isotope fractionation between native metal and silicate phases in the 4 pallasites and 3 mesosiderite meteorites analyzed in this work (for the three-isotope plots of stony-iron meteorites, the reader is referred to figure 6-7, provided in the appendix). The literature data available for Esquel ($\delta^{57/54}\mathrm{Fe}_{metal}$ = +0.237 ± 0.055 ‰, $\delta^{57/54}\mathrm{Fe}_{olivine}$ = -0.084 ± -0.051 ‰) (Poitrasson *et al.*, 2005) validates the results obtained here (see the discussion below). Both the petrography and the distribution of trace elements suggest that the olivine and metal phases are in equilibrium (Boesenberg *et al.* 2012). As such, the fractionation factors α can be related to the equilibrium constant *K* for the isotopic exchange between the olivine and metal:

$$^{57}Fe_{oliv} + {}^{54}Fe_{met} \rightleftharpoons {}^{54}Fe_{oliv} + {}^{57}Fe_{met};\ K = \frac{^{57/54}Fe_{met}}{^{57/54}Fe_{oliv}} = \alpha = \exp(-\,\Delta G/kT) \tag{6 – 5}$$

Here, subscripts denote the phases between which Fe isotopes are exchanged, *G* represents the free energy, *k* is the Boltzmann constant and *T* is temperature. In turn, the difference in free energy is associated with a difference in the vibrational motions of the crystal lattice due to the difference in isotope masses. More details on the theoretical background of this equation can be found in the literature (O'Neil, 1986; Hoefs, 2009; Young *et al.*, 2015). Hence, the distribution of isotopes between phases depends on the crystal chemistry constraints, leading to an enrichment of the heavier isotopes in the phase where the chemical bonds are stiffer and the coordination number is low (Young *et al.*, 2015). Importantly, the distribution of isotopes also depends on the equilibration temperature, which makes Fe isotope ratios in equilibrated phases useful as an isotopic geothermometer. Figure 6-3 compares the measured Fe

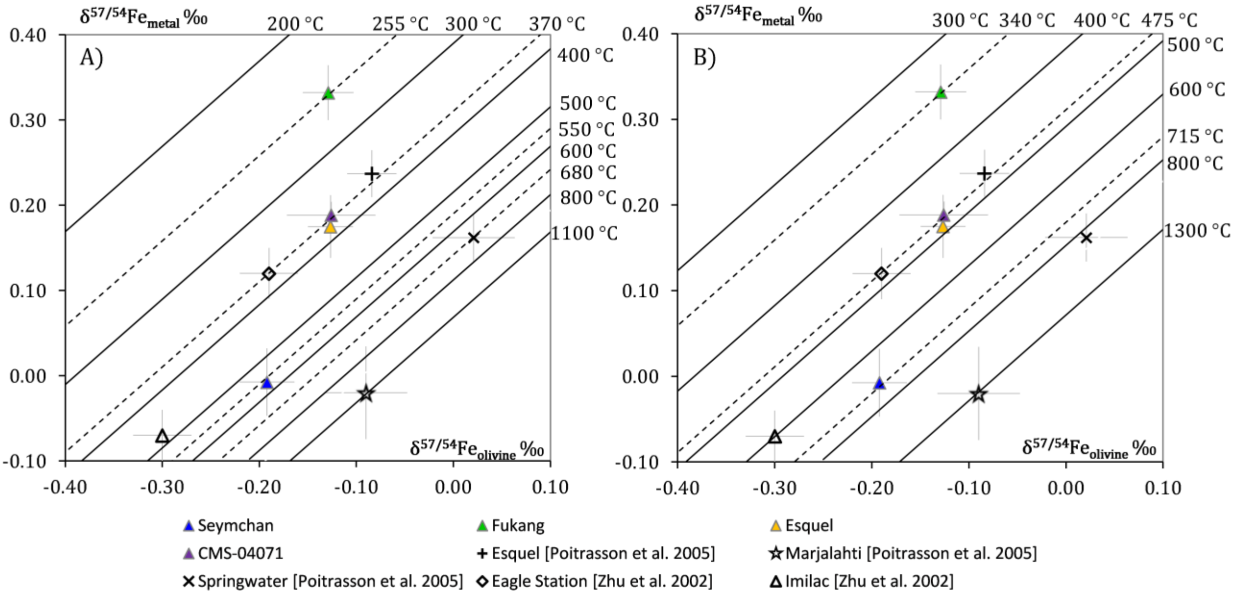

Figure 6-3. $\delta^{57/54}\mathrm{Fe}_{metal}$ *vs* $\delta^{57/54}\mathrm{Fe}_{olivine}$ plot for pallasites. Geothermometric isotherms for metal-olivine equilibration at different temperatures are calculated A) using parameters of Mössbauer spectroscopy for olivine and native iron (Polyakov and Mineev, 2000) and B) using parameters of NRIXS for olivine and γ-Fe (fcc) (Dauphas *et al.* 2012, Dauphas *et al.* 2014). The reference values for pallasites are taken from (Zhu *et al.*, 2002; Poitrasson *et al.*, 2005).

isotope ratio data for pallasites to the isotherms calculated for the Fe isotope partitioning between metal and olivine, based on the temperature dependence of the fractionation factors α, as determined using Mössbauer spectroscopy (Polyakov and Mineev, 2000) and nuclear resonance inelastic X-ray scattering (NRIXS) (Dauphas *et al.*, 2012; Dauphas *et al.*, 2014). Previous applications of Mössbauer spectroscopy for isotope geothermometry were criticized as the results obtained are sensitive to a number of complications inherent to this method (*e.g.*, second-order Doppler shift or hyperfine field parameters caused by changes in chemical or magnetic nature), and NRIXS is preferred as a more robust method. Comparison between the Mössbauer and NRIXS calibration (fig. 6-3) indicates that the latter systematically yields equilibration temperatures approximately 100 ˚C higher for the low-temperature region (200-400 ˚C) and 200 ˚C higher for the high-temperature region. As the difference between the Mössbauer (Polyakov and Mineev, 2000) and NRIXS (Dauphas *et al.*, 2012; Dauphas *et al.*, 2014) calibrations of metal-olivine only slightly exceeds the analytical uncertainty of isotope ratio measurements, the following conclusions are independent of the calibration method applied. It should also be noted that the model used here to calculate the metal-olivine Fe isotope isotherms is simplified, because it is not accounting for a range of minor parameters that can potentially affect the measured equilibrium temperatures, such as pressure, oxygen fugacity and the effect of minor solute elements (P, S, C, Ni) on the crystallographic constraints (Shahar *et al.*, 2008; Polyakov, 2009).

Although the absolute Fe isotopic composition data for the Esquel pallasite reported by Poitrasson *et al.* do not coincide with the data obtained in this work within the associated analytical uncertainty, both results fall on the same isotherm for an equilibration temperature of 475 ˚C (or 370 ˚C in the case of Mössbauer isotope thermometry calibration), demonstrating similar isotope ratio differences between the olivine and metal and initial Fe isotopic heterogeneity within this meteorite. The Fukang pallasite equilibrated at approximately 340 ˚C (or 255 ˚C for Mössbauer), while the final metal-silicate isotopic equilibration in Seymchan took place at 715 ˚C (550 ˚C for Mössbauer). Similarly, the reported variation of $\delta^{57/54}Fe_{metal}$ versus $\delta^{57/54}Fe_{olivine}$ indicates that Marjalahti, Springwater and Imilac last equilibrated at 1300 ˚C (1100 ˚C for Mössbauer), 800 ˚C (680 ˚C for Mössbauer) and 600 ˚C (500 ˚C for Mössbauer) respectively, while CMS 04071, Eagle Station and Esquel fall on a similar trend line that represents a final metal-silicate isotopic equilibration at 475 ˚C (370 ˚C for Mössbauer) (data from Zhu *et al.*, 2002; Poitrasson *et al.*, 2005).

Although the minor parameters that are not accounted for in this thermometric model, such as oxygen fugacity, and the effect of solutes on the crystal chemistry and the strength of the chemical bonds, can potentially affect the absolute temperature values produced in this model, these effects are expected to be nearly similar for all PMGs as a result of their formation at the relatively thin core-mantle boundary layer of the PMG parent body and their nearly similar compositions. As such, the broad range of the olivine-metal equilibration temperatures (340 to 1300 ˚C or 255 to 1100 ˚C depending on the thermometric calibration applied) is difficult to explain in terms of a formation model, in which pallasites form at a quiescent core-mantle boundary following parent body metal-silicate segregation (Boesenberg *et al.*, 2012). On the other hand, the equilibration temperature of 1100-1300 ˚C obtained for Marjalahti (Poitrasson *et al.* 2005) appears realistic, close to the schreibersite and Fe-FeS eutectic temperatures (Boesenberg *et al.*, 2012; McKibbin *et al.*, 2016). As such, the equilibrium isotope fractionation observed here and in previous works could be attributed to a later-stage, presently unidentified (possibly incomplete) re-equilibration event, different from the core-mantle segregation. This process clearly disturbed the Fe isotopic composition of the initially equilibrated metal and olivine. Possibly, a collisional event and large scale melting was followed by the removal of the solidified core, after which the pallasites (incompletely) equilibrated at various temperatures, buried at different depths in a secondary-accreted parent body (Yang *et al.*, 2010, Ruzicka 2014). Alternatively, aqueous alteration may be a process that re-distributed Fe isotopes between olivine and accessory minerals in small cracks and veinlets (Telus *et al.*, 2016).

Alternatively, a potential explanation for the low equilibration temperature measured for Fukang could be the sensitivity of the thermometric method to sampling, as the measured isotopic composition of the metal fraction might not be fully representative of its bulk-metal isotopic composition (*e.g.*, by sampling a larger fraction of isotopically heavier taenite, which shifts the equilibration temperature obtained to the colder side of the plot). But even if the lowest temperature determined for Fukang is disqualified as unrealistically low and is considered to result from oversampling of isotopically heavy taenite, unrepresentative sampling cannot account for another “cold” PMG – Esquel, for which the Fe isotope temperature coincides with that reported in previous publications (Poitrasson *et al.* 2005) and is confirmed by the analysis of other pallasites (CMS 04071, Eagle Station).

The equilibration temperatures of 475 ˚C have previously been noted to be unrealistically low for pallasites (Poitrasson *et al.* 2005), because it is unlikely that cm-sized olivine crystals reached full equilibration with their surrounding metal in terms of Fe isotopes. Based on the diffusion data of Jaoul *et al.*, 1995, the full equilibration at such temperatures has been estimated to take an unrealistic amount of time, on the order of several Gyr. Such low temperatures for some pallasites were explained by incomplete equilibration and disturbance by diffusion effects. However, more refined studies of diffusion demonstrate that diffusion coefficients highly depend on multiple parameters, such as crystallographic orientation, making estimations of equilibration time highly imprecise (Dohmen *et al.*, 2007; Dohmen and Chakraborty, 2007). Additionally, previously measured electron probe (EPMA) concentration profiles have shown that olivines in the Esquel pallasite are compositionally uniform, with only slight < 0.5 mol% zoning of fayalite (Fa = Fe/(Mg+Fe); Miyamoto, 1997). Whether this abundance gradient is correlated with isotopic zoning is a task for more detailed *in situ* work, but it seems unrealistic that such limited concentration profile is accompanied by a shift in the $\delta^{57/54}$Fe value of olivine by approximately 0.2 ‰, needed to obtain more realistic equilibration temperatures (*e.g.* see Oeser *et al.*, 2015 or Sio *et al.*, 2013). Besides faster cooling, the higher abundance of olivine to metal in Imilac, Eagle Station and Esquel compared to Marjalahti and Springwater has been suggested to be another factor limiting isotopic re-equilibration, because of the larger average distance the Fe atoms have to diffuse into olivine to equilibrate with the adjacent metal (Zhu *et al*., 2002; Poitrasson *et al*., 2005).

5.2. Isotope fractionation of Fe in IIIAB and PMG meteorites as a result of fractional crystallization of asteroidal cores. IIIAB iron meteorites are known to form a fractional crystallization sequence, with decreasing concentrations of Ir (and particular other elements) as the crystallization proceeds, and the compositions of PMG (*e.g.,* Au-As trends) are broadly compatible with late-stage crystallization of a core with IIIAB-like composition, suggesting a possible genetic relationship (although additional explanations are needed to explain Ga and Ge trends) (Scott, 1977b; Scott, 1977c; Wasson and Choi, 2003). There are currently several arguments pro and contra- a shared origin of these meteorites. Potential evidence for a common origin of IIIAB and pallasite metal is based on similar oxygen three-isotope compositions for pallasites and chromite inclusions in particular IIIAB irons, although this is not the case for Cape York IIIAB, having significantly distinct oxigen isotope signatures (Franchi *et al*., 2013). Similarly, the Mo isotopic signatures for the metal phases (Dauphas et al., 2002) and the Hf-W short-lived isotopic decay system (Quitté *et al*., 2005) suggest a common origin for IIIAB and PMG meteorites. On the other hand, the Re-Os isotope chronometer has produced a whole-rock pallasite isochron distinct from those of iron meteorites, indicating that iron meteorites underwent fractional crystallization processes ~60 Myr later than pallasite metals (Chen *et al.*, 2002). Metallographic studies of metal phases imply that below 975 K, IIIAB irons experienced faster cooling rates

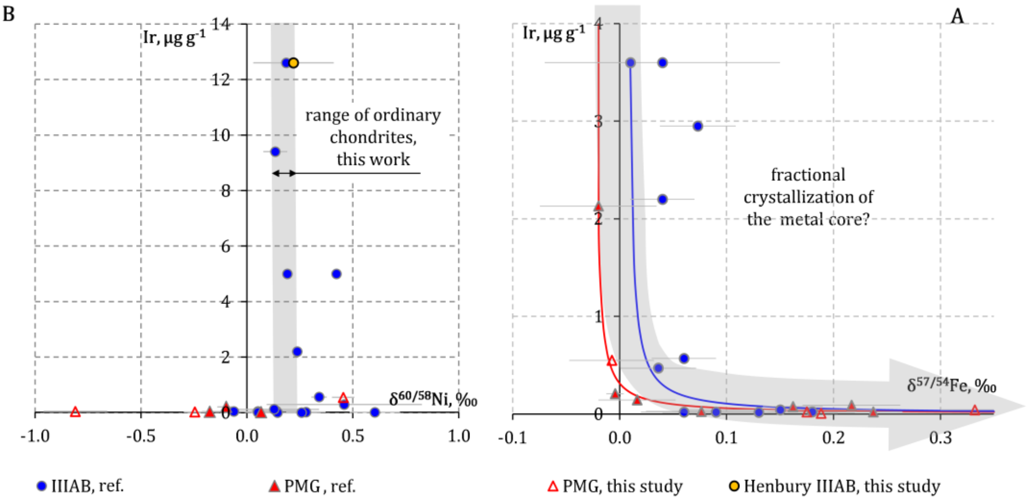

Figure 6-4. A. $\delta^{60/58}$Ni and $\delta^{57/54}$Fe *vs* Ir concentration in metal fractions of pallasites and IIIAB irons, suggested they share a genetic link. The detailed explanation of the trend line shown is provided in the ESI. B. The fractional crystallization trend for Ni isotopes is elusive, demonstrating the low impact of fractional crystallization on Ni isotopes. Additional literature data for Fe and Ni isotopic composition of meteorites are from (Zhu *et al*., 2001; Poitrasson *et al*., 2005; Weyer *et al*., 2005; Williams *et al*., 2006; Schoenberg and Blanckenburg, 2006; Cook *et al*., 2007). The data for bulk Ir content in meteorites are from (Scott *et al*., 1973; Wasson, 1999; Wasson and Choi, 2003; Danielson *et al*., 2009).

than pallasites and that different pallasites cooled at disparate rates, probably because this cooling took place at a different depth in the parent body (Yang *et al.*, 2010; Goldstein *et al.*, 2014). Although the range of non-mass-dependent W isotopic signatures within the IIIAB iron group is narrower than for whole iron meteorites (Markowski *et al*., 2006), which makes the genetic link between pallasites and IIIAB iron meteorites elusive, mass-dependent W isotopic compositions of IIIAB and pallasites fall on the same mass-dependent isotope fractionation line (Fukami *et al*., 2010). Negative correlation of W isotope fractionation to Ir suggests that W stable isotopes in IIIAB and pallasites fractionated during fractional crystallization of liquid metal (Fukami *et al*., 2010).

Figure 6-4 plots the Ni and Fe isotope compositions for PMG and IIIAB against their Ir concentrations. Figure 6-4B indicates a trend between the Fe isotope ratio and the Ir content, as a result of fractional crystallization of the parent body core(s). The trends for PMG and IIIAB iron meteorites are similar, with heavier Fe isotope ratios as the Ir concentration decreases. As $\delta^{57/54}$Fe in PMG and IIIAB group meteorites display a nearly identical trend *versus* Ir, this might indicate similar crystallization processes in their parent bodies, and could confirm a shared parent body for PMGs and IIIAB iron meteorites. In contrast to IIIAB and metal fractions of PMGs, no trend was found for IIAB iron meteorites in a plot of $\delta^{57/54}$Fe versus Ir content (appendix, figure 6-9). The fact that IIAB irons do not show a similar trend is indeed enigmatic, and we have to invoke possible effects of initial concentrations of minor elements or the size of the parent bodies and corresponding cooling rates or later disturbances of the Fe isotope signatures. ESI contains more detailed modeling of Fe isotope fractionation during metal differentiation.

5.3. Isotope fractionation of Ni in pallasites: equilibrium or kinetic in nature? The Ni isotopic composition of stony-iron meteorites is presented in figure 6-2. Different to Fe, the light Ni isotopic composition of pallasite metals in comparison to iron meteorites argues against a derivation of pallasites from the IIIAB iron meteorite parent body that are reported to have heavier Ni stable isotope signatures (this study, Cook *et al*., 2007). This is in contrast to the trend observed for Ir concentrations versus Fe isotope ratios.

Fractional crystallization of a molten metal core in the PMG-IIIAB parent body cannot explain the light Ni isotopic signatures measured. Any trends in a plot of ^{60}Ni/^{58}Ni ratios *versus* Ir concentrations remain elusive, which demonstrates the limited preservation of fractional crystallization effects on the Ni isotopic compositions of the PMG metal fraction (figure 6-4). Also, scenarios admixing Ni from external sources during PMG formation appear unlikely, as Ni is a major element and unrealistically high amounts are needed to account for a shift in the metal Ni isotopic signatures to lighter values. The light isotopic composition in the metal phase of the PMG can also not be explained by condensation from a vapor phase in a Rayleigh-like process, for instance as a result of planetary collision, because in that case, a matched enrichment in light isotopes of Fe would be found, which is not the case.

Several possible scenarios can be invoked to explain the light isotopic composition of Ni in the metal fractions of pallasites compared to a heavier Ni isotopic signature in the adjacent olivine:

(i) The sampling of metal might not be representative for the bulk Ni isotopic composition. Light Ni isotopic compositions can be caused by oversampling of particular metal phases, e.g., taenite or swathing kamacite, which is not reflected in the Fe isotopes due to the higher overall abundance of Fe and smaller isotopic differences between kamacite and taenite. However, the light stable isotopic signatures of Ni measured in metals are in full agreement with those previously reported for the metal fractions of 3 other pallasites (Cook *et al*., 2007).

(ii) The heavy Ni stable isotopic composition of olivine and the comparatively lower values for the corresponding metal could result from equilibrium isotope fractionation during core-mantle segregation. In this case, the reversed character of metal-olivine fractionation factors for Ni and Fe is striking, while these 2 elements possess nearly similar physical properties, such as volatilities and ionic radii. One characteristic, which differentiates Ni from Fe, is its inability to take on a 3+ oxidation state. As such, a redox mechanism that reverses the fractionation factor of Fe with respect to that of Ni might hypothetically be involved, for instance if charge-balancing is needed for Fe substitution of trivalent ions in olivine. Different to Fe, the theoretical silicate-metal fractionation factors for Ni are scarcely studied, but experimental work did indicate an enrichment of heavy Ni isotopes in metal relative to talc at temperatures of 500°C to 950°C and pressures of 0.8-1.3 GPa (Lazar *et al*., 2012). To clarify the equilibrium fractionation constraints, the crystal chemistry of Ni in olivine should be studied in more detail, because the bonding environment is a factor affecting the isotope fractionation strongly. Different to Fe, Ni is a trace element in olivine, and can either substitute Fe in the crystal lattice of olivine, be compensated for by vacancies, or be concentrated in inclusions. Figure 6-5 presents a 2D LA-ICP-MS distribution image of Ni in olivine of Seymchan, representative for

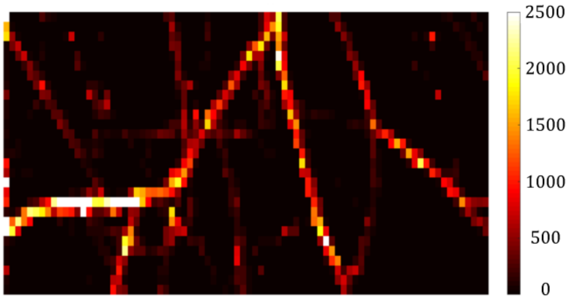

Figure 6-5. 2D element distribution map of Ni in olivine of Seymchan PMG. The map was produced in the direction from the metal-olivine margin (left side) to the core of the olivine (right side). The image dimension is 1460x600 µm, and each pixel represents 20x20 µm. The color bar shows the Ni concentration in µg g^{-1}.

all PMGs evaluated in this study. The veins with elevated concentrations of P and Ni probably have a shock origin (Desrousseaux *et al.*, 1997). The concentration of Ni in bulk olivine is of the order of 10 µg g^{-1}, while Ni concentrations of up to several thousands µg g^{-1} are found in the veinlets. This indicates that a significant part of the Ni is contained in the veins of the bulk silicate. If the process that formed these features also led to Ni exchange between metal, olivine and veins, after the initial olivine/metal Ni isotopic equilibration, this could have led to a significant shift in the Ni isotopic composition of the bulk silicate (olivine + vein).

(iii) Light Ni stable isotopic signatures of metal and heavy signatures of adjacent olivine could result from disequilibration of the initial isotopic signatures. The initial isotopic composition of metal and olivine can be affected by a later thermal event, such as impact or internal heating, and disturbed by kinetic isotope fractionation during solid-state diffusion of Ni between metal/olivine/veins. However, the fact that Ni in silicate is consistently isotopically heavier than that in the adjacent metal indicates the direction of possible Ni diffusion from olivine into the metal as light isotopes diffuse faster, which is opposite to the concentration gradient. However, taking into account that Ni is a siderophile element, the chemical potential gradient can easily be opposite to the concentration gradient in the case of the metal-olivine boundary, which would allow for self-diffusion of Ni isotopes. Previous work has presented concentration gradients of doubly charged ions in pallasitic olivines due to solid-state diffusion (Tomiyama and Huss, 2006; McKibbin *et al.*, 2013). These profiles are suggested to reflect re-equilibration of olivine and metal, mixed as a result of an impact, that is followed by fast cooling. However, taking mass-balance considerations into account, it is unlikely that diffusion of Ni isotopes from olivine into the metal could explain light Ni isotope signatures of the metal phase, because of its several orders of magnitude lower content in olivine compared to metal.

As the mechanism of the Ni distribution between metal and olivine remains unclear, more spatially resolved *in situ* isotopic analyses of closely associated metal, olivine and possibly Ni contained in veins, are needed to shed light onto the Ni isotope fractionation mechanism.

5.4. Origin of metal and silicate in mesosiderites. Mesosiderites have enigmatic formation histories, with most models suggesting that they formed by mixing of material from two different parent bodies. Silicate clasts of mesosiderites indicate their origin from the evolved crust of a differentiated asteroid (Stewart et al., 1994, Greenwood et al., 2015, Haack et al., 2003), potentially linking it to the crust of asteroid 4 Vesta (McSween et al., 2011). Mesosiderites have a restricted range of metal compositions, suggesting that the metal did not undergo fractional crystallization and that the metal was molten when mixed with the colder silicates (Hassanzadeh *et al.*, 1990). The compositional range of the metallic portions of mesosiderites suggests that mesosiderite metal may have crystallized from a core with an original melt composition similar to IIIAB and H-group chondrite metal (Wasson et al., 1974). Differences between slow metallographic cooling rates at 500 ˚C (Goldstein et al., 2014) and fast cooling of pyroxene clasts at peak metamorphic temperatures above 800 ˚C (Ruzicka *et al.*, 1994; Schwandt *et al.*, 1998), probably due to equilibration of mixed hot and cold fragments, suggest a change of cooling regime when mesosiderites were buried deep in a re-accreted parent body (Bogard and Garrison, 1998).

The $^{56/54}$Fe isotopic compositions of the metal fractions of 3 Antarctic mesosiderites vary between +0.018 and +0.120 ‰ (figure 6-2, table 6-1), which is close to the values for chondritic (this study; Barrat *et al.*, 2015) and iron meteorites (this study; Poitrasson *et al.*, 2005; Williams *et al.*, 2006) (figure 6-2, table 6-1). The Ni isotopic composition of the metal fractions is comparable to or slightly lighter than that of chondrites and iron meteorites (fig. 6-2). The Fe and Ni stable isotope signatures in the metal fractions of mesosiderites are within the range of chondrites or iron meteorites, which is in agreement with the trace element compositions, suggesting that the metal in mesosiderites shares an origin with chondrites or asteroidal metal cores (Wasson *et al.*, 1974).

The isotopic signatures of both Fe and Ni in the silicate portions of mesosiderites are relatively light (figure 6-2, table 6-1). These signatures can either be derived from the basaltic regolith of the differentiated asteroid, from which the silicate fraction of mesosiderites originates, or be acquired during the evolution of the mesosiderites. As stable Ni isotope data for asteroidal crusts in literature are rare, this is hard to evaluate in the case of Ni. However, the negative Fe isotopic signatures in the silicate portions of mesosiderites may indicate that these result from late-stage evolution and isotope fractionation, because all the terrestrial and extraterrestrial crust silicates reported to date have either chondritic or heavy Fe isotopic compositions (*e.g.*, Barrat *et al.*, 2015). Therefore, the light Fe and associated light Ni isotopic signatures of mesosiderites are more likely to result from diffusion of light Fe and Ni isotopes out of hot metal into silicates that initially showed chondritic or heavier isotope ratios following the formational mixing event. The Fe and Ni isotopic signatures of the metal phases might not have been affected significantly by this diffusion because of the higher overall concentrations of Fe and Ni, and thus remained unchanged.

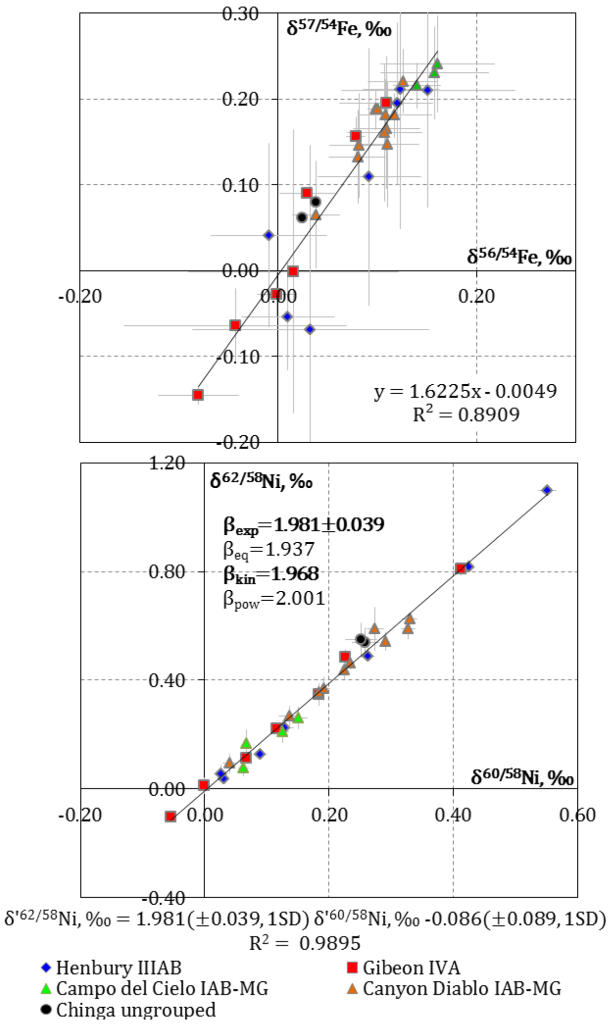

Figure 6-6. Three-isotope plots based on data from the laterally resolved isotopic analyses of Fe and Ni in magmatic and silicate-bearing iron meteorites (microdrilled sub-samples). The experimental fractionation exponent βexp was extracted from the laterally resolved data of all single microdrilled iron meteorites using the approach described by Young et al. (Young et al., 2002). The slope of the regression line in δ′- δ′ three-isotope plot is equal to the fractionation exponent β between the corresponding isotope ratios. By definition $\delta'^{x/58}\mathrm{Ni} = \ln[({}^{x}\mathrm{Ni}/{}^{58}\mathrm{Ni})_{smp}/({}^{x}\mathrm{Ni}/{}^{58}\mathrm{Ni})_{std}] \cdot 1000$.

5.5. Kinetic isotope fractionation of Fe and Ni in iron meteorites due to sub-solidus diffusion. The Toluca IAB iron meteorite was extensively studied for Fe-Ni isotope fractionation as a result of Widmanstätten pattern growth (Poitrasson *et al.*, 2005; Dauphas, 2007; Cook *et al.*, 2007). Due to slow cooling of meteorite parent bodies, taenite changes into this structure of kamacite/taenite. If kamacite and taenite are in full equilibrium, isotope fractionation is controlled by the crystal chemistry constraints and temperature in a manner similar to that described for pallasites. At the same time, kamacite grows via sub-solidus diffusion of Fe and Ni atoms, and as light isotopes tend to diffuse faster than heavy ones, a factor of kinetic control is added to the isotope fractionation mechanism. For a detailed description of the isotope fractionation mechanism during disequilibrium crystal-growth phenomena, also for the particular case of Widmanstätten pattern growth, the reader is referred to earlier publications (Dauphas, 2007; Watson and Müller, 2009; Mueller *et al.*, 2014).

However, Toluca belongs to the IAB complex silicate-bearing iron meteorite group, which has experienced impact processing during its formation history (Goldstein *et al.*, 2009; Ruzicka, 2014). To expand the pool of data available, two magmatic iron meteorites of different groups (Henbury IIIAB and Gibeon IVA) with distinct cooling histories were also studied in this work. Four to 10 drillings on each etched sample surface were performed to represent the spread of isotope ratios contained in the inhomogeneous iron meteorite body. Because the drilling is done with a finite spot size (300 µm diameter) and because the phase composition cannot be controlled with the depth of the drilling (400 µm), all of the micro-drilled samples represent mixtures of kamacite and taenite in different proportions (including the plessitic fine mixture of both minerals). The highest and the lowest isotope ratios measured in this way can be assumed to approximate the lowest and highest estimates of isotopic compositions in the center of the kamacite and taenite phases, respectively. However, given the large number of local measurements, a fractionation line can be constructed with higher precision. Figure 6-6 provides three-isotope plots based on data from spatially resolved analyses of iron meteorites for their Fe and Ni isotopic compositions. The theoretical equilibrium (β_{eq}) and kinetic (β_{kin}) fractionation factors can be calculated (Wombacher and Rehkamper, 2003; Young et al. 2002). The experimental fractionation factor, extracted from $\delta^{62/58}$Ni - $\delta^{60/58}$Ni data (β_{exp}=1.981±0.039) corresponds best to kinetically controlled isotope fractionation. This confirms that the contribution of sub-solidus diffusion prevails over equilibrium isotope fractionation control (Dauphas, 2007). The fractionation factors β_{exp} for Fe and the other Ni isotopes show less precision as a result of the limited amount of Fe isotope fractionation or the lower abundance of the corresponding Ni isotopes, preventing their use in this context. It is interesting to note that the average of the data obtained for 7 spatially resolved analyses of the Henbury IIIAB iron meteorite measured in this study ($\delta^{60/58}$Ni = +0.22 ‰) corresponds well to previously reported bulk analyses data, varying between +0.22 ‰ and +0.19 ‰ (Cook *et al.*, 2007).

Magmatic iron meteorite groups exhibit element trends compatible with fractional crystallization, initiated by the cooling of molten asteroid cores. The silicate-bearing groups (IIE group and the IAB complex, which includes the former IIICD) are believed to have formed through impact of melted bodies and as such, experienced a different crystallization and cooling history (Ruzicka, 2014). The range of stable isotope signatures of Ni is wider than that of Fe in laterally resolved samples due to the effect of sub-solidus diffusion and its lower concentration relative to Fe. However, for the silicate-bearing IAB-MG iron meteorite Canyon Diablo, and especially for Campo del Cielo, this effect is less pronounced. This could result from impact processing, when the isotope ratios of both Fe and Ni in silicate-bearing irons were first shifted to heavier values as a result of evaporation following impact (the 50% condensation temperatures in a Solar System composition gas are 1353 and 1334 K for Ni and Fe, respectively; Lodders, 2003). Subsequently, the Fe and Ni isotopes were fractionated between kamacite/taenite as a result of sub-solidus diffusion, although to a lesser degree than experienced by the magmatic groups, as a result of faster cooling rates (Goldstein *et al.*, 2014). The cooling rate will affect the degree of kinetic fractionation because of its effect on diffusive closure and because it will control the growth rate of the exsolution features. However, it is impossible to determine the timing of the impact from the Fe-Ni isotopic signatures. The effect of impact processing on the isotopic composition of Ge has previously been described for silicate-bearing iron meteorites, which show lower and more variable Ge isotopic compositions than do magmatic irons (Luais, 2007).

The Udei Station meteorite consists of a mixture of metal and silicates. However, it is classified as IAB-ungrouped according to the Meteoritical Bulletin, based on the composition of its metal fraction (Wasson, 1970a), the petrographic characteristics of the silicates (Mason, 1967), and the higher metallographic cooling rates compared to mesosiderites (Powell, 1969). The Fe and Ni isotopic signatures in the metal phase of Udei Station are close to those of other iron meteorites, but negative in the silicate fraction. These negative signatures are unlikely to derive from the initial parent material of the silicates, as there is strong evidence for a chondritic origin (Choi *et al.*, 1995; Wasson and Kallemeyn, 2002). Consequently, the isotopic signatures of the Udei Station silicate might result from Fe and Ni diffusion out of the metal phase of this meteorite, similar to what has been observed for mesosiderites. On the other hand, recent work suggests that the silicates in Udei Station experienced low degrees (3-10 %) of partial melting, which could potentially have fractionated the Fe and Ni isotopes (Ruzicka and Hutson, 2010).

6. Summary

This study contributes high-precision Fe and Ni isotope ratio data for bulk magmatic and silicate-bearing iron, pallasite, and mesosiderite meteorites obtained *via* MC-ICP-MS to the existing literature. Importantly, co-occurring silicate and metal portions for various stony iron meteorites were compared in terms of their Fe and Ni isotopic compositions. For this purpose, relatively large sample aliquots (generally > 100 mg) guaranteed representative sampling considering the isotopic heterogeneity at the micrometer to millimeter scale that generally reflects sub-solidus diffusion. In the case of magmatic and silicate-bearing iron meteorites, micro-drilling using a 300 µm diameter drill bit also allowed laterally resolved isotopic analysis of Fe and Ni. Unlike chondrites, for which the Fe and Ni isotope signatures result from nebular processes and the isotopic range is limited to ~0.2 ‰ (Moynier *et al*, 2007; Craddock and Dauphas 2011), metal-rich achondritic materials such as iron and stony-iron meteorites typically exhibit much wider ranges of up to 0.6 ‰ for $\delta^{56/54}$Fe and ~2 ‰ for $\delta^{60/58}$Ni between the metal and silicate phase in stony irons. By comparing the magnitude and sign of the Fe and Ni isotope stable isotope shifts between meteorite groups and fractions, it becomes clear that the stable isotope signatures of these achondrites result from unique combinations of distinct planetary processes, such as metal segregation and fractional crystallization during core formation, primary equilibration between planetary reservoirs of pristine parent bodies, evaporation during collisional disruption, diffusive re-equilibration during re-accretion on secondary parent bodies, and subsequent diffusion during prolonged cooling histories. As such, stable isotope signatures can also be used to highlight possible genetic relations (*e.g.*, between pallasite metal and IIIAB irons).

The stable isotope fractionation of Fe and Ni related to sub-solidus diffusion exhibits a narrower range for silicate-bearing than for magmatic iron meteorites. This is interpreted to reflect the slower cooling rates experienced by the latter. Additionally, impact volatilization may also have played a role in the Ni and Fe isotopic signatures of silicate-bearing iron meteorites. In contrast, Fe isotopes of the PMG and in the IIIAB parent bodies' metal core(s) fractionated in the process of fractional crystallization, as revealed by the Ir concentration - $\delta^{56/54}$Fe trend. No such Fe fractional crystallization trend is found for the IIAB iron meteorite group, the only other iron meteorite group for which enough high-precision Fe isotope data exists. Unlike Fe, Ni isotopes do not indicate fractionation coupled to the fractional crystallization of the parent body core.

In the case of mesosiderites, light Ni and Fe isotopic signatures were observed in the silicate portions analyzed relative to the heavier, near-chondritic signatures of the corresponding metal phases. These compositions likely result from diffusion of Ni and Fe from the metal into the silicate portion of these meteorites, following the mixing between an impactor and the original parent body.

The metal and olivine portions of pallasites show resolvable Fe isotope fractionation. However, if the Fe isotopes did originally achieve equilibrium, the extension of the wide range of derived equilibration temperatures (255-340˚C to 1100-1300˚C) for different groups of pallasites suggests that Fe isotope fractionation is not the result of a core-mantle segregation event, but rather represents later re-equilibration at different depths in a secondary parent body. Nickel shows an isotope fractionation factor between metal and olivine in pallasites that is reversed compared to that of Fe, with lighter isotopic compositions for metal ($\delta^{60/58}$Ni from -0.81 to +0.455 ‰) and heavier compositions for the corresponding olivine ($\delta^{60/58}$Ni from +0.554 to +1.221 ‰). This result is unlikely to derive from equilibrium isotope fractionation during core-mantle segregation, as Fe and Ni generally exhibit similar chemical properties. Similarly, a control by kinetic isotope fractionation linked to Ni diffusion out of the olivine into the metal phase would not explain the light Ni isotopic signatures in pallasite metal. Because the crystal chemistry constraints on Ni remain unclear and large portions of silicate Ni were found to reside in inclusions, additional *in situ* analyses are needed to shed light on the actual mechanism of Ni isotope fractionation.

7. Appendices

7.1. Appendix A

7.2. Appendix B. Fractionation of Fe isotopes due to fractional crystallization of a metal core. Although the observed trend of $\delta^{57/54}$Fe versus Ir has strong curvature, difficult to describe quantitatively, figure 6-7 A presents the fitting of empirical hyperbolic lines to the (filtered) PMG (red) and IIIAB meteorites (blue) data sets. The shift between the vertical asymptotes for IIIAB and PMG, if significant, probably indicates differences in the initial bulk isotopic compositions of the crystallizing Fe. The calculated empirical parameters of the Ir-$\delta^{57/54}$Fe dependence were used to estimate the Fe isotopic compositions of IIIAB and PMG meteorites using the available Ir concentration data (see figure 6-8), and predict the initial isotopic composition of the molten parent body core. While 48 PMGs yield an average $\delta^{57/54}$Fe of +0.079 ‰ and a median $\delta^{57/54}$Fe of +0.065 ‰, 150 IIIAB iron meteorites yield an average $\delta^{57/54}$Fe of +0.15 ‰ and a median $\delta^{57/54}$Fe of +0.01 ‰.

The classical equation, formulated by Scott (Scott, 1972), is used to describe fractional crystallization patterns of elements in iron meteorites (equation 6-6). Although it is known that additional detailed elaborations to the model are needed in order to explain the element data observed, such as dependence of the distribution coefficients on changing molar fractions of minor elements (P, S, C), this simplified model can intuitively demonstrate the possible effect of fractional crystallization on the isotopic composition. It is known that the distribution coefficients, in particular that of Ir, depend on the concentrations of substitutional alloying elements (Shahar et al., 2008; Wasson, 1999a), and also those of P and S. The latter tend to concentrate in the remaining liquid while crystallization proceeds, changing the distribution coefficients of Ir (and other elements). However, it is not accounted for in the following discussion, as the bottleneck of any modeling in this case is the precision of the isotope ratio

Instrument settings			
		Ni	Fe
RF power^a, W		1250	1300
Gas flow rates^a, l min^{-1}	Cool	15	15
	Auxiliary	0.8	0.7
	Nebulizer	0.98	0.99
Sampler cone		Ni jet type sampler cone: 1.1 mm aperture diameter	Ni, jet type sampler cone: 1.1 mm aperture diameter
Skimmer cone		Ni skimmer cone: 0.8 mm aperture diameter	Ni skimmer cone: 0.8 mm aperture diameter
Sample uptake		Pumped via peristaltic pump, 0.1 ml min^{-1}	Pumped via peristaltic pump, 0.1 ml min^{-1}
Nebulizer		Concentric, 100 μl min^{-1}	Concentric, 100 μl min^{-1}
Spray chamber		Double, cyclonic and Scott-type sub-units	Double, cyclonic and Scott-type sub-units
Resolution mode		Medium^b	Medium^b

Data acquisition		
Mode	Dynamic (^{56}Fe and ^{66}Zn are measured non-simultaneously for mathematical correction^b)	Static; multi-collection
Idle time, s	3	3
Integration time, s	4.194	4.194
Number of integrations	3	1
Number of blocks	4	9
Number of cycles per block	3	5

Cup configuration for Ni isotope ratio measurements (dynamic acquisition)							
Cup	L_4	L_2	L_1	C	H_1	H_2	H_3
Amplifier	$10^{11}\Omega$	$10^{11}\Omega$	$10^{11}\Omega$	$10^{12}\Omega$	$10^{11}\Omega$	$10^{12}\Omega$	$10^{11}\Omega$
1st line	^{58}Ni, ^{58}Fe	^{60}Ni	^{61}Ni	^{62}Ni	^{63}Cu	^{64}Ni, ^{64}Zn	^{65}Cu
2nd line				^{56}Fe			
3rd line				^{66}Zn			

Cup configuration for Fe isotope ratio measurements						
Cup	L_4	L_2	L_1	C	H_1	H_3
Amplifier	$10^{11}\Omega$	$10^{11}\Omega$	$10^{11}\Omega$	$10^{11}\Omega$	$10^{11}\Omega$	$10^{11}\Omega$
Nuclide	^{54}Fe	^{56}Fe	^{57}Fe	^{58}Fe, ^{58}Ni	^{60}Ni	^{62}Ni

Table 6-2. Instrument settings, data acquisition parameters and multi-collector detector configuration for the Thermo Scientific Neptune MC-ICP-MS instrument used for Ni and Fe isotopic analysis.^{a} Parameters optimised on a daily basis for highest sensitivity and stability. $^b\Delta$m for pseudo-high resolution in MC-ICP-MS is defined as the mass difference between $m_{5\%}$ and $m_{95\%}$, corresponding to 5 % and 95 % of the signal intensity level on the plateau, respectively. A resolving power of 7400 was measured using the ^{238}U signal in MR mode. Such a definition of resolving power exceeds that based on atomic mass difference by more than a factor of two (Vanhaecke and Moens, 2004).

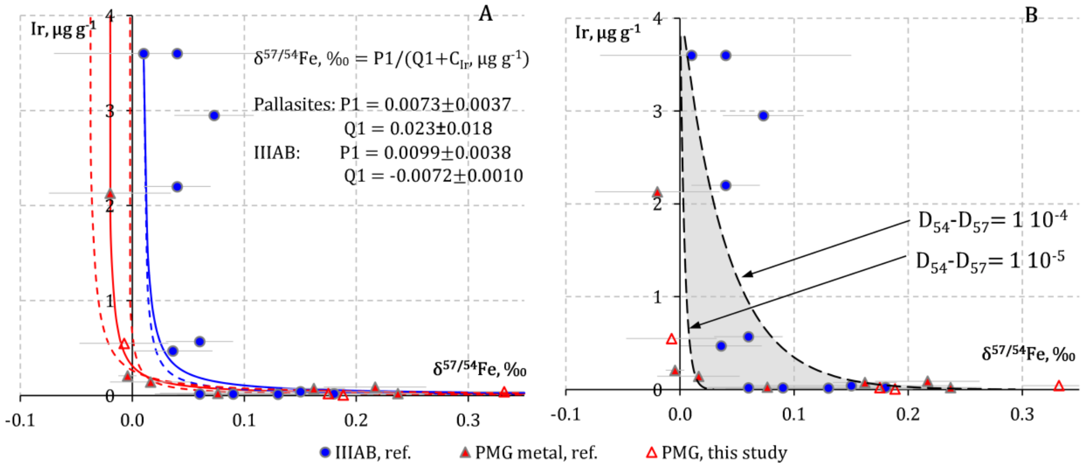

Figure 6-7. $\delta^{60/58}$Ni and $\delta^{57/54}$Fe vs Ir concentration in metal fractions of pallasites and IIIAB irons. Literature data for the Fe isotopic compositions of these meteorites are from (Zhu *et al.*, 2001; Poitrasson *et al.*, 2005; Weyer *et al.*, 2005; Williams *et al.*, 2006; Schoenberg and Blanckenburg, 2006; Cook *et al.*, 2007). The bulk Ir content data are from (Scott *et al.*, 1973; Wasson, 1999; Wasson and Choi, 2003; Danielson *et al.*, 2009). A) Continuous lines represent the result of empirical fitting of hyperbolic lines to the PMG (red) and IIIAB meteorites (blue) data sets. The 95% confidence intervals of the coefficients are also shown graphically using dashed lines. B) Dashed lines represent modeling of the Fe isotope fractionation in IIIAB meteorites due to fractional crystallization with different solid-liquid distribution coefficients for the Fe isotopes (see equation 6-9).

measurements, disturbance of bulk Fe isotope data by kamacite/taenite sampling and the strong curvature of the trend.

$$C(Ir) = D_{Ir} C_{0(Ir)} (1-g)^{D_{Ir}-1} \qquad (6-6)$$

Here, *C(Ir)* is the Ir concentration in the crystallizing metal and $C_{0(Ir)}$ a starting bulk concentration. D_{Ir} is a solid-liquid distribution coefficient of Ir and *g* is the fraction of crystallized material. Hypothetically, such equation can be written for every element, or even isotope, taking part in the crystallization (equation 6-7). If we assume that the distribution coefficients of Fe isotopes are not fully equal, this will lead to isotope fractionation.

$$C\left({}^{5x}Fe\right) = D_{5x} C_{0(5xFe)} (1-g)^{D_{5x}-1} \qquad (6-7)$$

Equation 6-7, formulated for ^{57}Fe can be divided to that for ^{54}Fe to yield the dependence of the delta notation of Fe (equation 6-8) on the crystallized fraction *g*:

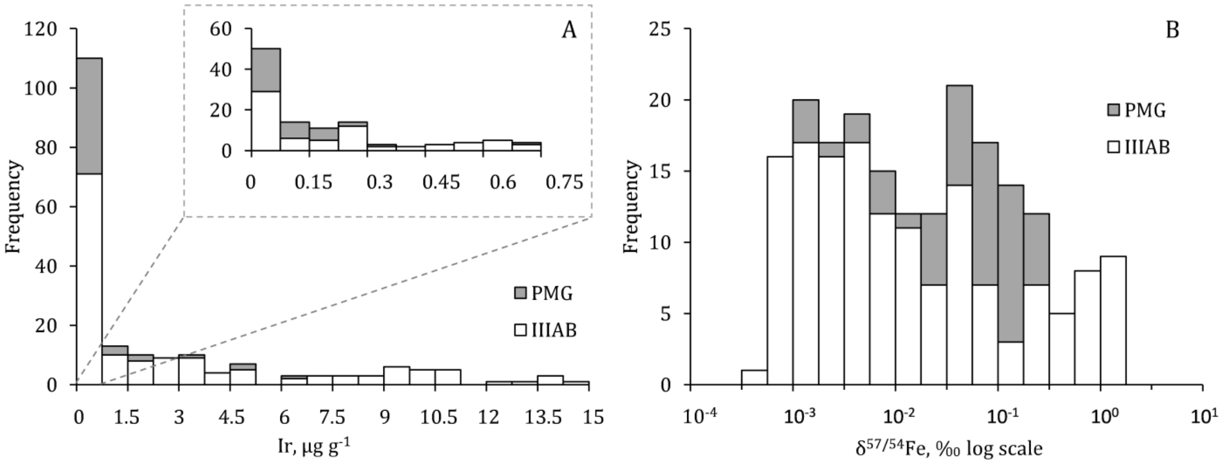

Figure 6-8. A – frequency distribution of Ir in 150 IIIAB iron meteorites and 48 main group pallasites. Data from (Danielson et al., 2009; Lauretta et al., 2006; Scott, 1977b; Scott et al., 1973; van Niekerk et al., 2007; Wasson, 1999a; Wasson and Choi, 2003). B – frequency distribution of $\delta^{57/54}$Fe, calculated using the Ir concentrations and the empirically fitted lines from figure 6-7.

$$\delta^{57/54}Fe = \left(\frac{D_{57}}{D_{54}}(1-g)^{D_{57}-D_{54}} - 1\right)1000 \qquad (6-8)$$

$\delta^{57/54}$Fe here denotes deviation of the Fe isotopic composition from the initial "bulk" value. Alternatively, equation 6-8 can be expressed versus the Ir concentration (Equation 6-9):

$$\delta^{57/54}Fe = \left(\frac{D_{57}}{D_{54}}\left(\frac{C_{Ir}}{C_{0Ir}D_{Ir}}\right)^{\frac{D_{57}-D_{54}}{D_{Ir}-1}} - 1\right)1000 \qquad (6-9)$$

Dashed lines at figure 6-7 B indicate the Ir dataset of 150 IIIAB iron meteorites (Scott et al., 1973) and the calculated Fe isotopic composition based on equation 6-9. To calculate these lines, we used the parameters of Wasson (Wasson, 1999b) and neglected the dependence of the Ir distribution coefficients on the changing composition of the crystallized melt. It was also assumed that the distribution coefficients of the Fe isotopes are close to unity. Comparison of the lines modeled at different parameters with actual measured data demonstrates that a difference between the solid-liquid distribution coefficients D_{57}-D_{54} of the two Fe isotopes within the range of 10^{-5} to 10^{-4} can adequately explain the observed trends of $\delta^{57/54}$Fe versus Ir. However, the limited precision of the isotope ratio measurements, the disturbance of bulk isotope data by kamacite/taenite sampling and the strong curvature of the trend limit more detailed modeling of the isotope fractionation due to fractional crystallization. Potentially, more precise bulk Fe isotope data of multiple fragments of Cape York, the largest IIIAB iron meteorite with large Ir concentration variations can further constrain this process.

7.3. Appendix C. Fe and Ni isotope fractionation in stony-iron meteorites. Figure 6-10 provides three-isotope plots for Fe and Ni isotope fractionation between metal and silicate in pallasites, mesosiderites and Udei Station iron meteorite. The experimental β factor is calculated for $\delta^{62/58}$Ni - $\delta^{62/58}$Ni using the approach described by Young *et al*. (2002). The β fractionation exponent calculated on the basis of the most precisely measured Ni isotope ratios is closer to equilibrium isotope fractionation control, rather than to kinetic (β = 1.942 ± 0.037, 2SD), although within ±2SD these mechanisms cannot be distinguished. The calculated ^{60}Ni/^{58}Ni – ^{62}Ni/^{58}Ni fractionation exponent for the data set of pallasites is 1.945 ± 0.044 (2SD), and 1.971 ± 0.060 (2SD) for the dataset of pallasites when Fukang metal is excluded based on the suspicion of inadequate sampling. Unfortunately, none of the calculated fractionation exponents is characterized with sufficient precision to distinguish whether the Ni fractionation mechanism in PMGs is equilibrium or kinetic in nature. $\Delta_{\text{Met-Si}}^{60/58}$ indicates the difference in terms of $\delta^{60/58}$Ni between the corresponding metal and silicate fractions of stony-iron meteorites.

7.4. Appendix D. OKUM komatiite reference material. Different to pallasites, the crusts of the Earth ($\delta^{56/54}$Fe of +0.1 ‰ relative to IRMM-014), Moon ($\delta^{56/54}$Fe of +0.09 ± 0.03 ‰) and angrite parent body ($\delta^{56/54}$Fe of +0.12 ± 0.01 ‰) are enriched in heavy Fe isotopes relative to initially chondritic compositions (Wang *et al*., 2012). This shift has been interpreted to reflect a change in the sign of the equilibrium isotope fractionation factor between silicate and native iron (Polyakov, 2009), becoming positive when increasing the pressure from the asteroid-sized pallasite parent body (~10-50 MPa) to the core-mantle boundary of the Earth (~100 GPa). Based on high-pressure synchrotron inelastic nuclear resonance X-ray scattering (INRXS), a shift in the ^{56}Fe/^{54}Fe isotope ratio between the silicate mantle and core of Earth of +0.13 ± 0.053 ‰ was predicted (Polyakov, 2009). However, the heavy Fe isotopic composition observed forthe silicate Earth is more likely the result of various magmatic differentiation processes taking place in planetary crusts rather than of primary metal core – silicate mantle differentiation (Wang *et al*., 2015). This is in agreement with the measured chondritic Fe isotopic compositions for peridotites (Craddock *et al*., 2013) and komatiites (Dauphas *et al*., 2010), indicating chondritic Fe isotopic

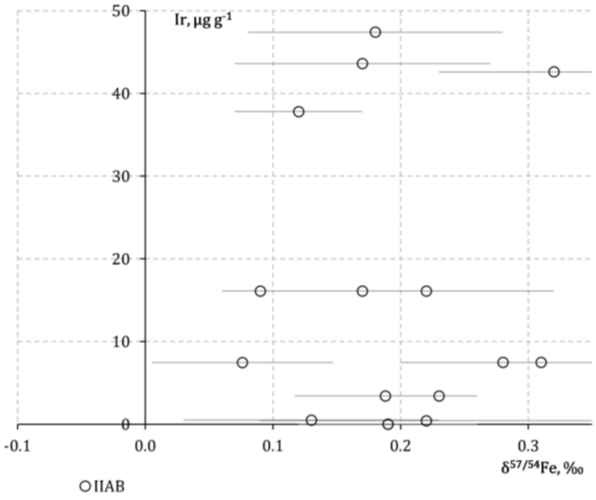

Figure 6-9. $\delta^{57/54}$Fe vs Ir concentration in metal fractions of pallasites and IIAB irons. Literature data for the Fe isotopic compositions of these meteorites are from (Zhu *et al.* 2001, Williams *et al.* 2006).

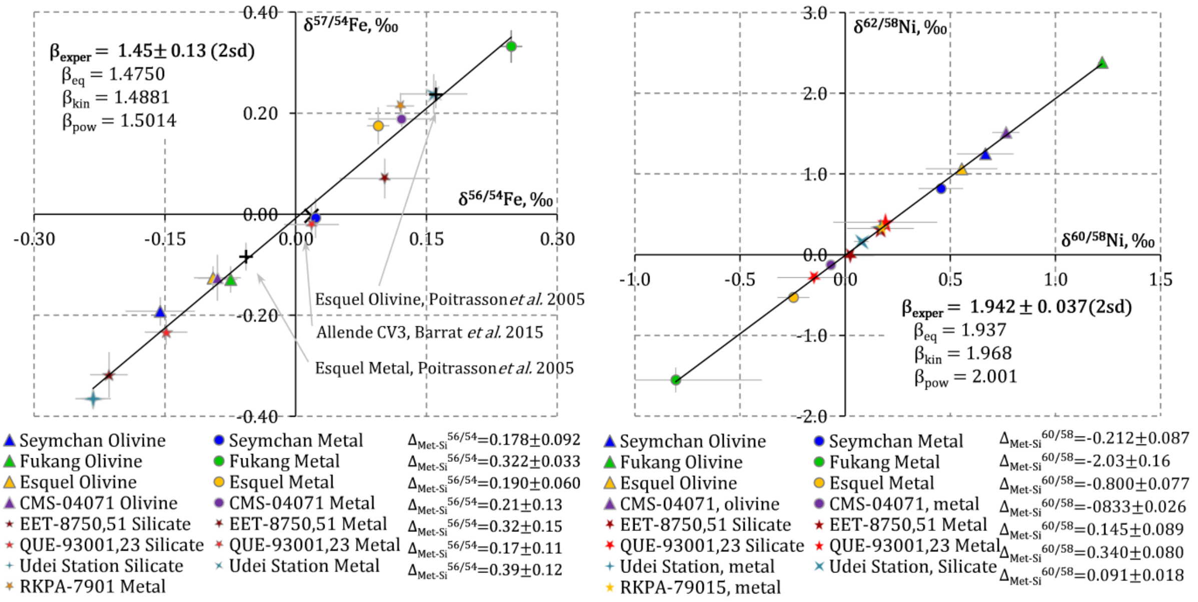

Figure 6-10. Three-isotope plots for Fe and Ni isotope fractionation between metal and silicate in pallasites, mesosiderites and Udei Station iron meteorite with silicate inclusions.

compositions for terrestrial magmas. Various high-temperature magmatic processes (partial melting/fractional crystallization) between mantle and crust have been suggested to fractionate Fe isotopes, resulting in isotopically heavier partially molten crustal basalts (Teng *et al.*, 2008; Weyer, 2008; Wang *et al.*, 2015). The controlling processes can be both kinetic (Richter *et al.*, 2009) or equilibrium in nature (Young *et al.*, 2015). In comparison to Fe, relatively little is known about Ni isotope fractionation in magmatic and crustal processes on Earth. Recent studies have mostly aimed to understand the biogeochemical circulation mechanisms and budgets of Ni (Cameron *et al.*, 2009; Cameron and Vance, 2014), the isotope fractionation mechanisms due to vegetation control and weathering (Deng *et al.*, 2014; Ratié *et al.*, 2015; Estrade *et al.*, 2015), as well as marine deposits and the processes involved in Ni sedimentation (Gall *et al.*, 2013; Porter *et al.*, 2014; Wasylenki *et al.*, 2015).

OKUM is a reference material of powdered ultramafic komatiite, certified for major and trace element mass fractions. As $\delta^{56/54}$Fe of komatiites were previously found

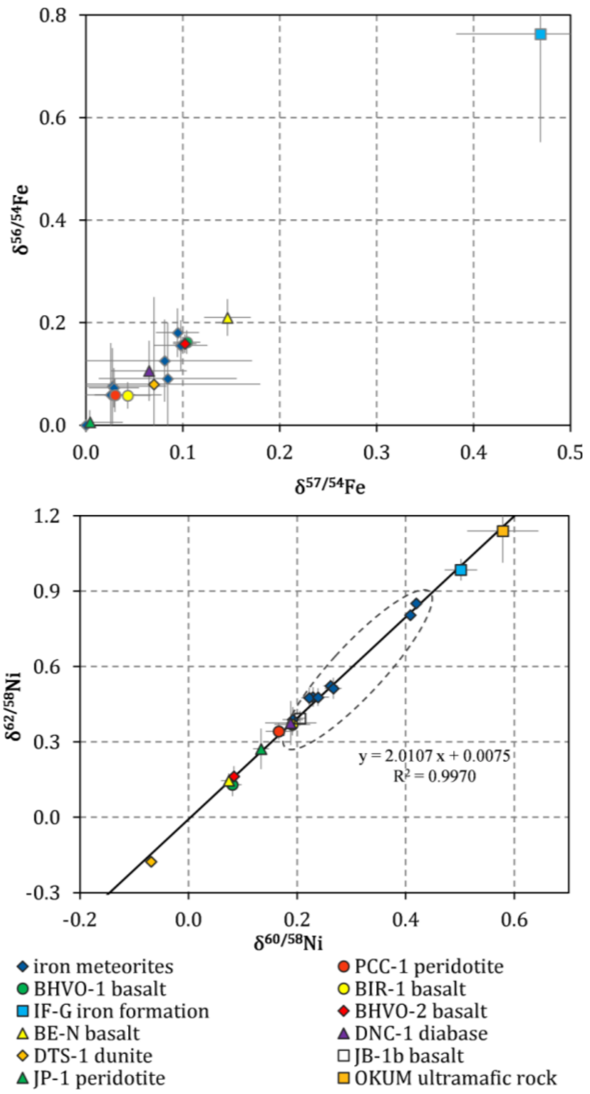

Figure 6-11. The Fe and Ni isotopic compositions of iron meteorites and selected mafic terrestrial igneous and sedimentary rocks. The Ni isotope ratio data have been previously reported (Chernonozhkin *et al.*, 2015) and the Fe isotopic composition corresponds to bulk digestions of the iron meteorites analyzed. The Fe isotopic compositions of GRMs are reported in this work or were taken from literature (Dauphas *et al.*, 2009, 2007; Fehr *et al.*, 2008; Poitrasson *et al.*, 2004; Telus *et al.*, 2012; Wang *et al.*, 2012). ►

to be near-chondritic, +0.044±0.030 ‰ on average, minor fractionation appears to take place during komatiite magma genesis (Dauphas *et al.*, 2010). Our Fe isotope ratio measurements of OKUM are also close to chondritic isotopic signatures, in agreement with Dauphas *et al*. (2010).

Previous work has reported a broad range of negative $\delta^{60/58}$Ni values (from -0.10 to -1.03 ‰) for komatiites and their mineral separates, which has been attributed to significant magmatic fractionation, *e.g.* partial melting (Gueguen *et al*., 2013). In contrast, a positive $\delta^{60/58}$Ni = +0.58 ‰ was reported for OKUM komatiite (Chernonozhkin *et al*., 2015). This Ni isotope ratio result, discordant to what is expected based on Fe isotope ratios and different from the predictions of Gueguen et al. (2013), remains enigmatic. It shows the perspectives for Ni isotope studies to further understand the fractionation mechanisms in magmatic and crustal settings.

Figure 6-11 presents an overview of literature data for stable Fe and Ni isotope ratios in terrestrial rocks (GRMs), in comparison to the Fe and Ni isotope ratio data for bulk iron meteorites (dashed circle). The Ni isotope ratio data have previously been published (Chernonozhkin *et al*., 2015), while the Fe isotope ratio data for the same GRMs were taken from literature for comparison (except for BHVO-1 and PCC-1, reported in this work). It is important to note that the composition of NIST SRM 986 Ni standard, relative to which the Ni delta-values are calculated, is not chondritic. This means that Ni in some of the terrestrial CRMs is lighter than the initial, presumably chondritic composition. The Fe and Ni isotope ratios of iron meteorites were measured from the same bulk (50-150 mg) digestions.

8. Acknowledgements

This research project has been funded by the Planet Topers, Interuniversity Attraction Poles Program initiated by the Belgian Science Policy Office (BELSPO). Steven Goderis and Marta Costas Rodríguez are postdoctoral fellows of the Research Foundation – Flanders (FWO). The support of the Hercules Foundation is acknowledged. US Antarctic meteorite samples are recovered by the Antarctic Search for Meteorites (ANSMET) program, which has been funded by NSF and NASA, and characterized and curated by the Department of Mineral Sciences of the Smithsonian Institution and Astromaterials Curation Office at NASA Johnson Space Center. The collection of iron meteorites from east Russia and northern Kazakhstan was kindly donated by Felix P. Lesnov (IGM SB RAS). The ordinary chondrites, provided by the RBINS, are part of the Antarctic meteorite collection that was recovered through the SAMBA project, also founded by BELSPO, in collaboration with the Japanese National Institute of Polar Research (NIRP). Frank Vanhaecke acknowledges Teledyne Cetac Technologies for financial support of his LA-ICP-MS research projects. Authors acknowledge the highly constructive comments supplied by two anonymous reviewers, Thomas Mueller (University of Leeds), and by the editor Nicolas Dauphas (University of Chicago). Stef Vansteenberge and Christina Makarona (VUB) are kindly acknowledged for their technical help with the MicroMill and XRF units. The authors appreciate valuable discussions with Seann McKibbin and Lidia Pittarello (VUB).

9. List of references

Alexander C. M. O. and Wang J. (2001) Iron isotopes in chondrules: Implications for the role of evaporation during chondrule formation. *Meteorit. Planet. Sci.* **36**, 419–428.

Barrat J. A., Rouxel O., Wang K., Moynier F., Yamaguchi A., Bischoff A. and Langlade J. (2015) Early stages of core segregation recorded by Fe isotopes in an asteroidal mantle. *Earth Planet. Sci. Lett.* **419**, 93–100.

Baxter D. C., Rodushkin I., Engström E. and Malinovsky D. (2006) Revised exponential model for mass bias correction using an internal standard for isotope abundance ratio measurements by multi-collector inductively coupled plasma mass spectrometry. *J. Anal. At. Spectrom.* **21**, 427–430.

Boesenberg J. S., Delaney J. S. and Hewins R. H. (2012) A petrological and chemical reexamination of Main Group pallasite formation. *Geochim. Cosmochim. Acta* **89**, 134–158.

Bogard D. D. and Garrison D. H. (1998) ^{39}Ar- ^{40}Ar ages and thermal history of mesosiderites. *Geochim. Cosmochim. Acta* **62**, 1459–1468.

Cameron V. and Vance D. (2014) Heavy nickel isotope compositions in rivers and the oceans. *Geochim. Cosmochim. Acta* **128**, 195–211.

Cameron V., Vance D., Archer C. and House C. H. (2009) A biomarker based on the stable isotopes of nickel. *Proc. Natl. Acad. Sci. U. S. A.* **106**, 10944–10948.

Chabot N. L. and Haack H. (2006) Evolution of Asteroidal Cores. In *Meteorites and the Early Solar System II* University of Arizona Press. pp. 747–771.

Chen J. H., Papanastassiou D. and Wasserburg G. (2002) Re-Os and Pd-Ag systematics in Group IIIAB irons and in pallasites. *Geochim. Cosmochim. Acta* **66**, 3793–3810.

Chernonozhkin S. M., Goderis S., Bauters S., Vekemans B., Vincze L., Claeys P. and Vanhaecke F. (2014) Evaluation of pneumatic nebulization and ns-laser ablation ICP-MS for bulk elemental analysis and 2-dimensional element mapping of iron meteorites. *J. Anal. At. Spectrom.* **29**, 1001–1016.

Chernonozhkin S. M., Goderis S., Lobo L., Claeys P. and Vanhaecke F. (2015) Development of an isolation procedure and MC-ICP-MS measurement protocol for the study of stable isotope ratio variations of nickel. *J. Anal. At. Spectrom.* **30**, 1518–1530.

Choi B., Ouyang X. and Wasson J. T. (1995) Classification and origin of IAB and IIICD iron meteorites. *Geochim. Cosmochim. Acta* **59**, 593–612.

Cook D. L., Wadhwa M., Clayton R. N., Dauphas N., Janney P. E. and Davis A. M. (2007) Mass-dependent fractionation of nickel isotopes in meteoritic metal. *Meteorit. Planet. Sci.* **42**, 2067–2077.

Cook D. L., Wadhwa M., Janney P. E., Dauphas N., Clayton R. N. and Davis A. M. (2006) High precision measurements of non-mass-dependent effects in nickel isotopes in meteoritic metal via multicollector ICPMS. *Anal. Chem.* **78**, 8477–8484.

Craddock P. R. and Dauphas N. (2011) Iron isotopic compositions of geological reference materials and chondrites. *Geostand. Geoanalytical Res.* **35**, 101–123.

Craddock P. R., Warren J. M. and Dauphas N. (2013) Abyssal peridotites reveal the near-chondritic Fe isotopic composition of the Earth. *Earth Planet. Sci. Lett.* **365**, 63–76.

Danielson L. R., Righter K. and Humayun M. (2009) Trace element chemistry of Cumulus Ridge 04071 pallasite with implications for main group pallasites. *Meteorit. Planet. Sci.* **44**, 1019–1032.

Dauphas N. (2007) Diffusion-driven kinetic isotope effect of Fe and Ni during formation of the Widmanstätten pattern. *Meteorit. Planet. Sci.* **42**, 1597–1613.

Dauphas N., Cates N. L., Mojzsis S. J. and Busigny V. (2007) Identification of chemical sedimentary protoliths using iron isotopes in the >3750 Ma Nuvvuagittuq supracrustal belt, Canada. *Earth Planet. Sci. Lett.* **254**, 358–376.

Dauphas N., Cook D. L., Sacarabany A., Fröhlich C., Davis A. M., Wadhwa M., Pourmand A., Rauscher T. and Gallino R. (2008) Iron 60 evidence for early injection and efficient mixing of stellar debris in the protosolar nebula. *The Astrophysical Journal*, **686**, 560–569.

Dauphas N., Craddock P. R., Asimow P. D., Bennett V. C., Nutman A. P. and Ohnenstetter D. (2009) Iron isotopes may reveal the redox conditions of mantle melting from Archean to Present. *Earth Planet. Sci. Lett.* **288**, 255–267.

Dauphas N., Janney P. E., Mendybaev R. A., Wadhwa M., Richter F. M., Davis A. M., van Zuilen M., Hines R. and Foley C. N. (2004) Chromatographic separation and multicollection-ICPMS analysis of iron. Investigating mass-dependent and -independent isotope effects. *Anal. Chem.* **76**, 5855–63.

Dauphas N., Marty B. and Reisberg L. (2002) Molybdenum evidence for inherited planetary scale isotope heterogeneity of the protosolar nebula. *Astrophys. J.* **565**, 640–644.

Dauphas N., Roskosz M., Alp E. E., Golden D. C., Sio C. K., Tissot F. L. H., Hu M. Y., Zhao J., Gao L. and Morris R. V. (2012) A general moment NRIXS approach to the determination of equilibrium Fe isotopic fractionation factors: Application to goethite and jarosite. *Geochim. Cosmochim. Acta* **94**, 254–275.

Dauphas N., Roskosz M., Alp E. E., Neuville D. R., Hu M. Y., Sio C. K., Tissot F. L. H., Zhao J., Tissandier L., Médard E. and Cordier C. (2014) Magma redox and structural controls on iron isotope variations in Earth's mantle and crust. *Earth Planet. Sci. Lett.* **398**, 127–140.

Dauphas N., Teng F.-Z. and Arndt N. T. (2010) Magnesium and iron isotopes in 2.7 Ga Alexo komatiites: Mantle signatures, no evidence for Soret diffusion, and identification of diffusive transport in zoned olivine. *Geochim. Cosmochim. Acta* **74**, 3274–3291.

Deng T.-H.-B., Cloquet C., Tang Y.-T., Sterckeman T., Echevarria G., Estrade N., Morel J.-L. and Qiu R.-L. (2014) Nickel and zinc isotope fractionation in hyperaccumulating and nonaccumulating plants. *Environ. Sci. Technol.* **48**, 11926–11933.

Desrousseaux A., Doukhan J. C., Leroux H. and Van Duysen J. C. (1997) An analytical electron microscope investigation of some pallasites. *Phys. Earth Planet. Inter.* **103**, 101–115.

Dohmen R., Becker H.-W. and Chakraborty S. (2007) Fe–Mg diffusion in olivine I: experimental determination between 700 and 1,200°C as a function of composition, crystal orientation and oxygen fugacity. *Phys. Chem. Miner.* **34**, 389–407.

Dohmen R. and Chakraborty S. (2007) Fe–Mg diffusion in olivine II: point defect chemistry, change of diffusion mechanisms and a model for calculation of diffusion coefficients in natural olivine. *Phys. Chem. Miner.* **34**, 409–430.

Estrade N., Cloquet C., Echevarria G., Sterckeman T., Deng T., Tang Y. and Morel J.-L. (2015) Weathering and vegetation controls on nickel isotope fractionation in surface ultramafic environments (Albania). *Earth Planet. Sci. Lett.* **423**, 24–35.

Fehr M. A., Andersson P. S., Hålenius U. and Mörth C.-M. (2008) Iron isotope variations in Holocene sediments of the Gotland Deep, Baltic Sea. *Geochim. Cosmochim. Acta* **72**, 807–826.

Franchi I. A., Greenwood R. C. and Scott E. R. D. (2013) The IIIAB-pallasite relationship revisited the oxigen isotope perspective. In *76th Annual Meteoritical Society Meeting* p. 5326.

Fukami Y., Kimura J., Irisawa K., Yokoyama T. and Hirata T. (2010) Mass-dependent fractionation of tungsten isotopes in IIIAB iron meteorites. In *Lunar Planet. Sci. XLI.* The Woodlands, Texas. #1649 (abstr.).

Gall L., Williams H. M., Siebert C., Halliday A. N., Herrington R. J. and Hein J. R. (2013) Nickel isotopic compositions of ferromanganese crusts and the constancy of deep ocean inputs and continental weathering effects over the Cenozoic. *Earth Planet. Sci. Lett.* **375**, 148–155.

Goldstein J. I., Scott E. R. D. and Chabot N. L. (2009) Iron meteorites: Crystallization, thermal history, parent bodies, and origin. *Chemie der Erde - Geochemistry* **69**, 293–325.

Goldstein J. I., Yang J. and Scott E. R. D. (2014) Determining cooling rates of iron and stony-iron meteorites from measurements of Ni and Co at kamacite–taenite interfaces. *Geochim. Cosmochim. Acta* **140**, 297–320.

Greenwood R. C., Barrat J.-A., Scott E. R. D., Haack H., Buchanan P. C., Franchi I. A., Yamaguchi A., Johnson D., Bevan A. W. R. and Burbine T. H. (2015) Geochemistry and oxygen isotope composition of main-group pallasites and olivine-rich clasts in mesosiderites: Implications for the “Great Dunite Shortage” and HED-mesosiderite connection. *Geochim. Cosmochim. Acta*. **169**, 115-136.

Greenwood R. C., Franchi I. A., Jambon A., Barrat J. A. and Burbine T. H. (2006) Oxygen isotope variation in stony-iron meteorites. *Science* **313**, 1763–1765.

Grimm R. E. and Mcsween H. Y. (1993) Heliocentric zoning of the asteroid belt by aluminum-26 heating. In *Lunar and Planetary Science Conference XXIV* pp. 577–578.

Gueguen B., Rouxel O., Ponzevera E., Bekker A. and Fouquet Y. (2013) Nickel isotope variations in terrestrial silicate rocks and geological reference materials measured by MC-ICP-MS. *Geostand. Geoanalytical Res.* **37**, 297–317.

Haack H., Bizzarro M., Backer J. A. and Rosing M. (2003) Early thermal evolution and sizes of the HED and mesosiderite parent bodies new constraints from Lu-Hf chronology. In *Lunar Planet. Sci. XXXIV.* League City, Texas. #1317(abstr.).

Hassanzadeh J., Rubin A. E. and Wasson J. T. (1990) Compositions of large metal nodules in mesosiderites: Links to iron meteorite group IIIAB and the origin of mesosiderite subgroups. *Geochim. Cosmochim. Acta* **54**, 3197–3208.

Van Heghe L., Engström E., Rodushkin I., Cloquet C. and Vanhaecke F. (2012) Isotopic analysis of the metabolically relevant transition metals Cu, Fe and Zn in human blood from vegetarians and omnivores using multi-collector ICP-mass spectrometry. *J. Anal. At. Spectrom.* **27**, 1327–1334.

Hezel D. C., Poole G. M., Hoyes J., Coles B. J., Unsworth C., Albrecht N., Smith C., Rehkämper M., Pack A., Genge M. and Russell S. S. (2015) Fe and O isotope composition of meteorite fusion crusts: possible natural analogues to chondrule formation? *Meteorit. Planet. Sci.* **50**, 229–242.

Hoefs J. (2009) *Stable Isotope Geochemistry*. 6th ed. Springer Berlin Heidelberg.

Jaoul O., Bertran-Alvarez Y., Liebermann R. C. and Price G. D. (1995) Fe-Mg interdiffusion in olivine up to 9 GPa at T = 600–900°C; experimental data and comparison with defect calculations. *Phys. Earth Planet. Inter.* **89**, 199–218.

Lazar C., Young E. D. and Manning C. E. (2012) Experimental determination of equilibrium nickel isotope fractionation between metal and silicate from 500°C to 950°C. *Geochim. Cosmochim. Acta* **86**, 276–295.

Lodders K. (2003) Solar System Abundances and Condensation Temperatures of the Elements. *Astrophys. J.* **591**, 1220–1247.

Luais B. (2007) Isotopic fractionation of germanium in iron meteorites: Significance for nebular condensation, core formation and impact processes. *Earth Planet. Sci. Lett.* **262**, 21–36.

Maréchal C. N., Télouk P. and Albarède F. (1999) Precise analysis of copper and zinc isotopic compositions by plasma-source mass spectrometry. *Chem. Geol.* **156**, 251–273.

Markowski A., Quitté G., Halliday A. and Kleine T. (2006) Tungsten isotopic compositions of iron meteorites: Chronological constraints vs. cosmogenic effects. *Earth Planet. Sci. Lett.* **242**, 1–15.

Mason B. (1967) The Woodbine meteorite, with notes on silicates in iron meteorites. *Mineral. Mag.* **36**, 120–126.

McKibbin S. J., Ireland T. R., Holden P., O’Neill H. S. C. and Mallmann G. (2016) Rapid cooling of planetesimal core-mantle reaction zones from Mn-Cr isotopes in pallasites. *Geochemical Perspect.* **2**, 68–77.

McKibbin S. J., O’Neill H. S. C., Mallmann G. and Halfpenny A. (2013) LA-ICP-MS mapping of olivine from the Brahin and Brenham meteorites: Complex elemental distributions in the pallasite olivine precursor. *Geochim. Cosmochim. Acta* **119**, 1–17.

McSween H. Y., Mittlefehldt D. W., Beck A. W., Mayne R. G. and McCoy T. J. (2011) HED Meteorites and Their Relationship to the Geology of Vesta and the Dawn Mission. *Space Sci. Rev.* **163**, 141–174.

Miyamoto M. (1997) Chemical zoning of olivine in several pallasites. *J. Geophys. Res.* **102**, 21,613–21,618.

Moynier F., Blichert-Toft J., Telouk P., Luck J.-M. and Albarède F. (2007) Comparative stable isotope geochemistry of Ni, Cu, Zn, and Fe in chondrites and iron meteorites. *Geochim. Cosmochim. Acta* **71**, 4365–4379.

Mueller T., Watson E. B., Trail D., Wiedenbeck M., Van Orman J. and Hauri E. H. (2014) Diffusive fractionation of carbon isotopes in γ-Fe: Experiment, models and implications for early solar system processes. *Geochim. Cosmochim. Acta* **127**, 57–66.

Mueller T., Watson E. B., Harrison T. M. (2010) Applications of diffusion data to high-temperature earth systems. *Reviews in Mineralogy & Geochemistry* **72**, 997-1038.

Oeser M., Dohmen R., Horn I., Schuth S. and Weyer S. (2015) Processes and time scales of magmatic evolution as revealed by Fe–Mg chemical and isotopic zoning in natural olivines. *Geochim. Cosmochim. Acta* **154**, 130–150.

O'Neil J. R. (1986) Theoretical and experimental aspects of isotopic fractionation. *Rev. Mineral.* **16**, 1–40.

Pernicka E. and Wasson J. T. (1987) Ru, Re, Os, Pt and Au in iron meteorites. *Geochim. Cosmochim. Acta* **51**, 1717–1726.

Poitrasson F., Halliday A. N., Lee D.-C., Levasseur S. and Teutsch N. (2004) Iron isotope differences between Earth, Moon, Mars and Vesta as possible records of contrasted accretion mechanisms. *Earth Planet. Sci. Lett.* **223**, 253–266.

Poitrasson F., Levasseur S. and Teutsch N. (2005) Significance of iron isotope mineral fractionation in pallasites and iron meteorites for the core–mantle differentiation of terrestrial planets. *Earth Planet. Sci. Lett.* **234**, 151–164.

Polyakov V. B. (2009) Equilibrium Iron Isotope Fractionation at Core-Mantle Boundary Conditions. *Science* **323**, 912–914.

Polyakov V. B. and Mineev S. D. (2000) The use of Mössbauer spectroscopy in stable isotope geochemistry. *Geochim. Cosmochim. Acta* **64**, 849–865.

Porter S. J., Selby D. and Cameron V. (2014) Characterising the nickel isotopic composition of organic-rich marine sediments. *Chem. Geol.* **387**, 12–21.

Powell B. N. (1969) Petrology and chemistry of mesosiderites—I. Textures and composition of nickel-iron. *Geochim. Cosmochim. Acta* **33**, 789–810.

Quitté G., Birck J.-L. and Allègre C. J. (2005) Stony-iron meteorites: History of the metal phase according to tungsten isotopes. *Geochim. Cosmochim. Acta* **69**, 1321–1332.

Rasmussen K. L., Malvin D. J., Buchwald V. F. and Wasson J. T. (1984) Compositional trends and cooling rates of group IVB iron meteorites. *Geochim. Cosmochim. Acta* **48**, 805–813.

Rasmussen K. L., Malvin D. J. and Wasson J. T. (1988) Trace Element Partitioning between Taenite and Kamacite; Relationship to the Cooling Rates of Iron Meteorites. *Meteoritics* **23**, 107–112.

Ratié G., Jouvin D., Garnier J., Rouxel O., Miska S., Guimarães E., Cruz Vieira L., Sivry Y., Zelano I., Montarges-Pelletier E., Thil F. and Quantin C. (2015) Nickel isotope fractionation during tropical weathering of ultramafic rocks. *Chem. Geol.* **402**, 68–76.

Regelous M., Elliott T. and Coath, C. D. (2008) Nickel isotope heterogeneity in the early Solar System. *Earth Planet. Sci. Lett.* **272**, 330–338.

Richter F., Dauphas N. and Teng F. (2009) Non-traditional fractionation of non-traditional isotopes: Evaporation, chemical diffusion and Soret diffusion. *Chem. Geol.* **258**, 92–103.

Richter F. M., Huss, G. R. and Mendybaev R. A. (2014) Iron and nickel isotopic fractionation across metal grains from three CBb meteorites. *45th Lunar and Planetary Science Conference*, Texas. #1346 (abstr.)

Richter F. M., Watson E. B., Mendybaev R., Dauphas N., Georg B., Watkins J. and Valley J. (2009) Isotopic fractionation of the major elements of molten basalt by chemical and thermal diffusion. *Geochim. Cosmochim. Acta* **73**, 4250–4263.

Ruzicka A. (2014) Silicate-bearing iron meteorites and their implications for the evolution of asteroidal parent bodies. *Chemie der Erde - Geochemistry* **74**, 3–48.

Ruzicka A., Boynton W. V. and Ganguly J. (1994) Olivine coronas, metamorphism, and the thermal history of the Morristown and Emery mesosiderites. *Geochim. Cosmochim. Acta* **58**, 2725–2741.

Ruzicka A. and Hutson M. (2010) Comparative petrology of silicates in the Udei Station (IAB) and Miles (IIE) iron meteorites: Implications for the origin of silicate-bearing irons. *Geochim. Cosmochim. Acta* **74**, 394–433.

Schoenberg R. and Blanckenburg F. von (2006) Modes of planetary-scale Fe isotope fractionation. *Earth Planet. Sci. Lett.* **252**, 342–359.

Schwandt C. S., Cygan R. T. and Westrich H. R. (1998) Magnesium self-diffusion in orthoenstatite. *Contrib. to Mineral. Petrol.* **130**, 390–396.

Scott E. R. D. (1972) Chemical fractionation in iron meteorites and its interpretation. *Geochim. Cosmochim. Acta* **36**, 1205–1236.

Scott E. R. D. (1977a) Composition, mineralogy and origin of group IC iron meteorites. *Earth Planet. Sci. Lett.* **37**, 273–284.

Scott E. R. D. (1977b) Geochemical relationships between some pallasites and iron meteorites. *Mineral. Mag.* **41**, 265–272.

Scott E. R. D. (1977c) Pallasites—metal composition, classification and relationships with iron meteorites. *Geochim. Cosmochim. Acta* **41**, 349–360.

Scott E. R.D., Wasson J. T. and Buchwald V. F. (1973) The chemical classification of iron meteorites—VII. A reinvestigation of irons with Ge concentrations between 25 and 80 ppm. *Geochim. Cosmochim. Acta* **37**, 1957–

1983.Shahar A., Young E. D. and Manning C. E. (2008) Equilibrium high-temperature Fe isotope fractionation between fayalite and magnetite: An experimental calibration. *Earth Planet. Sci. Lett.* **268**, 330–338.

Sio C. K. I., Dauphas N., Teng F.-Z., Chaussidon M., Helz R. T. and Roskosz M. (2013) Discerning crystal growth from diffusion profiles in zoned olivine by in situ Mg–Fe isotopic analyses. *Geochim. Cosmochim. Acta* **123**, 302–321.

Steele R. C. J., Elliott T., Coath C. D. and Regelous M. (2011) Confirmation of mass-independent Ni isotopic variability in iron meteorites. *Geochim. Cosmochim. Acta* **75**, 7906–7925.

Stewart B. W., Papanastassiou D. A. and Wasserburg G. J. (1994) Sm-Nd chronology and petrogenesis of mesosiderites. *Geochim. Cosmochim. Acta* **58**, 3487–3509.

Tang H. and Dauphas N. (2012) Abundance, distribution, and origin of 60Fe in the solar protoplanetary disk. *Earth Planet. Sci. Lett.* **359-360**, 248–263.

Tang H. and Dauphas N. (2014) ^{60}Fe–^{60}Ni chronology of core formation in Mars. *Earth Planet. Sci. Lett.* **390**, 264–274.

Tanimizu M. and Hirata T. (2006) Determination of natural isotopic variation in nickel using inductively coupled plasma mass spectrometry. *J. Anal. At. Spectrom.* **21**, 1423–1426.

Telus M., Dauphas N., Moynier F., Tissot F. L. H., Teng F.-Z., Nabelek P. I., Craddock P. R. and Groat L. A. (2012) Iron, zinc, magnesium and uranium isotopic fractionation during continental crust differentiation: The tale from migmatites, granitoids, and pegmatites. *Geochim. Cosmochim. Acta* **97**, 247–265.

Telus M., Huss G. R., Ogliore R. C., Nagashima K., Howard D. L., Newville M. G. and Tomkins A. G. (2016) Mobility of Iron and Nickel at Low Temperatures: Implications for 60Fe-60Ni Systematics of Chondrules from Unequilibrated Ordinary Chondrites. *Geochim. Cosmochim. Acta* **178**, 87–105.

Teng F.-Z., Dauphas N. and Helz R. T. (2008) Iron Isotope Fractionation During Magmatic Differentiation in Kilauea Iki Lava Lake. *Science* **320**, 1620–1622.

Tomiyama T. and Huss G. R. (2006) Minor and Trace Element Zoning in Pallasite Olivine: Modeling Pallasite Thermal History. In *Lunar Planet. Sci. XXXVII.* League City, Texas. #2132(abstr.).

Tomiyama T. and Huss G. R. (2005) Minor element behavior of pallasite olivine: understandidng pallasite thermal history and chronology. In *Lunar Planet. Sci. XXXVI.* League City, Texas. p. #2071(abstr.).

Vanhaecke F. and Moens L. (2004) Overcoming spectral overlap in isotopic analysis via single- and multi-collector ICP-mass spectrometry. *Anal. Bioanal. Chem.* **378**, 232–240.

Wang K., Jacobsen S. B., Sedaghatpour F., Chen H. and Korotev R. L. (2015) The earliest Lunar Magma Ocean differentiation recorded in Fe isotopes. *Earth Planet. Sci. Lett.* **430**, 202–208.

Wang K., Moynier F., Dauphas N., Barrat J.-A., Craddock P. and Sio C. K. (2012) Iron isotope fractionation in planetary crusts. *Geochim. Cosmochim. Acta* **89**, 31–45.

Wasson J. T. (1970a) Ni, Ga, Ge and Ir in the metal of iron-meteorites-with-silicate-inclusions. *Geochim. Cosmochim. Acta* **34**, 957–964.

Wasson J. T. (1970b) The chemical classification of iron meteorites. *Icarus* **12**, 407–423.

Wasson J. T. (1999) Trapped melt in IIIAB irons; solid/liquid elemental partitioning during the fractionation of the IIIAB magma. *Geochim. Cosmochim. Acta* **63**, 2875–2889.

Wasson J. T. and Choi B.-G. (2003) Main-group pallasites: Chemical composition, relationship to IIIAB irons, and origin. *Geochim. Cosmochim. Acta* **67**, 3079–3096.

Wasson J. T. and Kallemeyn G. (2002) the IAB iron-meteorite complex: A group, five subgroups, numerous grouplets, closely related, mainly formed by crystal segregation in rapidly cooling melts. *Geochim. Cosmochim. Acta* **66**, 2445–2473.

Wasson J. T. and Rubin A. E. (1985) Formation of mesosiderites by low-velocity impacts as a natural consequence of planet formation. *Nature* **318**, 168–170.

Wasson J. T., Schaudy R., Bild R. W. and Chou C.-L. (1974) Mesosiderites—I. Compositions of their metallic portions and possible relationship to other metal-rich meteorite groups. *Geochim. Cosmochim. Acta* **38**, 135–149.

Watson E. B. and Müller T. (2009) Non-equilibrium isotopic and elemental fractionation during diffusion-controlled crystal growth under static and dynamic conditions. *Chem. Geol.* **267**, 111–124.

Wasylenki L. E., Howe H. D., Spivak-Birndorf L. J. and Bish D. L. (2015) Ni isotope fractionation during sorption to ferrihydrite: Implications for Ni in banded iron formations. *Chem. Geol.* **400**, 56–64.

Weyer S. (2008) Geochemistry: What Drives Iron Isotope Fractionation in Magma? *Science* **320**, 1600–1601.

Weyer S., Anbar A. D., Brey G. P., Munker C., Mezger K., Woodland A. B., Münker C., Mezger K. and Woodland A. B. (2005) Iron isotope fractionation during planetary differentiation. *Earth Planet. Sci. Lett.* **240**, 251–264.

Weyrauch M., Zipfel J. and Weyer S. (2015) Ni isotope composition of zoned metal grains in CBb chondrite Hammadah al Hamra 237. *Paneth Kolloquium*, Nördlingen. #0051 (abstr.)

Williams H. M., Markowski A., Quitté G., Halliday A. N., Teutsch N. and Levasseur S. (2006) Fe isotope fractionation in iron meteorites: New insights into metal-sulphide segregation and planetary accretion. *Earth Planet. Sci. Lett.* **250**, 486–500.

Wombacher F. and Rehkamper M. (2003) Investigation of the mass discrimination of multiple collector ICP-MS using neodymium isotopes and the generalised power law. *J. Anal. At. Spectrom.* **18**, 1371–1375.

Yang C.-W., Williams D. B. and Goldstein J. I. (1996) A revision of the Fe-Ni phase diagram at low temperatures (<400 ˚C). *Journal of Phase Equilibria* **17**, 522-531.

Yang J., Goldstein J. I. and Scott E. R. D. (2010) Main-group pallasites: Thermal history, relationship to IIIAB irons, and origin. *Geochim. Cosmochim. Acta* **74**, 4471–4492.

Young E. D., Galy A. and Nagahara H. (2002) Kinetic and equilibrium mass-dependent isotope fractionation laws in nature and their geochemical and cosmochemical significance. *Geochim. Cosmochim. Acta* **66**, 1095–1104.

Young E. D., Manning C. E., Schauble E. A., Shahar A., Macris C. A., Lazar C. and Jordan M. (2015) High-temperature equilibrium isotope fractionation of non-traditional stable isotopes: Experiments, theory, and applications. *Chem. Geol.* **395**, 176–195.

Zhu X. K., Guo Y., O'Nions R. K., Young E. D. and Ash R. D. (2001) Isotopic homogeneity of iron in the early solar nebula. *Nature* **412**, 311–313.

Zhu X. K., Guo Y., Williams R. J. P., O'Nions R. K., Matthews A., Belshaw N. S., Canters G. W., de Waal E. C., Weser U., Burgess B. K. and Salvato B. (2002) Mass fractionation processes of transition metal isotopes. *Earth Planet. Sci. Lett.* **200**, 47–62.

Chapter 7

Thermal equilibration of iron meteorite and pallasite parent bodies recorded at the mineral scale by Fe and Ni isotope systematics

Stepan M. Chernonozhin, Mona Weyrauch, Steven Goderis, Seann McKibbin, Ingo Horn, Stefan Weyer, Philippe Claeys and Frank Vanhaecke

The manuscript is prepared for publication, subject for further changes and modifications.

S.Ch. designed and participated in implementing the experiment, processed the raw data, delivered and analysed the results, wrote the manuscript and took part in the discussion.

> *"I am in blood*
> *Step't in so far that, should I wade no more,*
> *Returning were as tedious as go o'er:*
> *Strange things I have in head, that will to hand;*
> *Which must be acted ere they may be scann'd."*
>
> *William Shakespeare*
> *Macbeth, Act III, Scene IV*

1. Abstract

This work reports the first laterally resolved (30-80 μm), high-precision stable Ni isotope ratio data for a variety of mineral phases (kamacite, taenite, schreibersite) composing iron meteorites and main group pallasites (PMG), obtained by a combination of femtosecond laser ablation and multi-collector inductively coupled plasma-mass spectrometry (*fs*-LA-MC-ICP-MS). Through comparison with the stable Fe isotope data for similar and other (troilite, olivine) mineral phase sections, the type of control – kinetic or equilibrium – governing isotope fractionation processes during parent body formation and modification is unraveled. No significant Fe isotope zoning was observed for olivines in main group pallasites, suggesting these were largely isotopically equilibrated. The observed faint Fe isotopic zoning is within the internal precision level of the isotope ratio measurements and likely linked to the sampling resolution. The measured Fe isotope profile does not allow a quantitative constraining of the cooling rates of PMG olivines. The narrow ranges in the Fe and Ni isotopic signatures of the troilite and schreibersite grains characterized suggest efficient thermal equilibration. Due to the complex distribution of Fe between metal, schreibersite, troilite, and silicate, the equilibrium-driven Fe isotope systematics of troilite/metal cannot be used as an isotope geothermometer. The Ni isotopic signatures of bulk metal and schreibersite correlate negatively, with isotopically lighter Ni in the metal of PMGs and isotopically heavier Ni in the metal of iron meteorites. As Ni in pallasites is mainly distributed between these two phases, an unidentified

process needs to be invoked to explain the Ni isotope ratio distribution in the metal-schreibersite system, potentially related to the fractional crystallization of the parent body core. Although the lateral resolution achieved is not sufficient to quantitatively constrain metallographic cooling rates, comparison between the determined isotope ratio profiles of Fe and Ni across kamacite-taenite interfaces and theoretical taenite sub-solidus diffusive isotope zoning suggest that the parent body cooling took place at higher (~650 ˚C) rather than lower (≤450 ˚C) temperatures.

2. Introduction

Iron meteorites are thought to sample the Fe-Ni cores of catastrophically disrupted differentiated asteroids, as most of these show fractional crystallization trends in their element abundances (Scott, 1972). Main group pallasites (PMGs) consist of nearly equal amounts of Fe-Ni metal and Fe-Mg silicate (olivine), and are consistent with the end member composition of the fractional crystallization sequence observed for IIIAB iron meteorites (Wasson, 2016). Although the formational history of PMGs is still heavily debated, these meteorites likely represent mixtures of Fe-Ni metal from the core and mantle-derived olivine from the core-mantle boundary of differentiated asteroids (Boesenberg et al., 2012; McKibbin et al., 2016, 2013). Trace element systematics and zoning in PMG olivine have been used to constrain the magmatic histories experienced by these olivines before the olivine-metal mixing event (McKibbin et al., 2013). However, as the olivine compositions largely equilibrated after their mixing with molten metal, the late-stage thermal histories of PMG might have been recorded by the metal-olivine element and isotope partitioning (Chernonozhkin et al., 2016; Poitrasson et al., 2005; Reed et al., 1979), and are potentially reflected in the PMG element and isotopic zoning (Miyamoto, 1997; Oeser et al., 2015). If the olivines of PMGs equilibrated thermally, the element and isotope olivine-metal fractionation factors existing in literature can be used to calculate equilibration temperatures, and the elemental and isotopic distributions can used as geothermometers (Hoefs, 2009). On the other hand, if a full equilibrium between the adjacent minerals was not achieved, the diffusive profiles of elements and isotope ratios from the olivine cores to the rims can be used to constrain the cooling rates of the parent body and to refine the nature of the processes taking place during the thermal evolution of the olivine through modeling (Miyamoto, 1997; Oeser et al., 2015).

Schreibersite (Fe,Ni phosphide, $(Fe,Ni)_3P$) and troilite (Fe sulfide, FeS) are two minor minerals contained in iron meteorites and PMGs, which contain a large fraction of the P and S in asteroidal metal cores. Troilite, similar to schreibersite, is believed to have a magmatic origin, exsolving from metal melts at Fe-FeS eutectic temperatures due to the incompatible nature of S and P, as fractional crystallization of the metal core proceeds in the Fe-Ni metal liquid. Troilite-metal Fe isotope fractionation factors have previously been shown to correlate with metallographic cooling rates (Williams et al., 2006). This is an indirect indication of the equilibrated nature of troilites, because closure temperatures (T_c), the main driving force of thermodynamic isotope fractionation, depend on the cooling rates (dT/dt) via Dodson's equation (Dodson, 1973; Valley, 2001):

$$T_c = \frac{R}{E ln(A\tau D_0/a^2)};\ \tau = -\frac{RT^2}{E dT/dt} \qquad (7-1)$$

In the equation 7-1 R denotes for the gas constant, E is the activation energy of the thermally activated diffusion, a is a characteristic diffusion size, A is a numerical constant, and D_0 is a preexponent of the diffusion coefficient. The observation that the troilite-metal fractionation factors depend on the cooling rates, together with thermodynamic parameters, recently determined for Fe in troilites by nuclear resonance inelastic X-ray scattering (NRIXS, Dauphas et al., 2012), might make it possible to use the Fe-FeS system as an isotope geothermometer.

After the molten Fe-Ni metal in the core is fully crystallized, the cooling of the parent body proceeds and the *fcc* crystal structure, thermodynamically stable at temperature above ~800 ^oC, starts to decay to form *bcc* Ni-poor α-iron (kamacite) and *fcc* Ni-rich γ-iron (taenite). Nickel concentration profiles across taenite lamellae of meteorites, formed via sub-solidus diffusion, form a traditional way to determine meteorites cooling rates. Later, it was shown that Fe and Ni isotopic signatures of Fe-Ni metal of iron meteorites exhibit a surprisingly large range, probably related to kamacite-taenite formation (Cook et al., 2007; Horn et al., 2006; Poitrasson et al., 2005; Weyer et al., 2005). As shown recently, diffusion drives Fe and Ni isotope fractionation, and the isotope profiles can potentially be used to constrain the cooling process of the parent body by modeling the diffusion in the metal (Dauphas, 2007).

The main goal of this work is to provide high-precision, laterally resolved Fe and Ni stable isotope ratio data for relevant accessory mineral phases in PMGs and iron meteorites, including spatially resolved isotope ratio profiles, to shed light on the cooling and crystallization histories of the meteorite parent bodies and further constrain their formation. In recent years, femtosecond laser ablation has been increasingly used in combination with MC-ICP-MS (*e.g.* Horn et al., 2006; Oeser et al., 2014; Planavsky et al., 2012). The ability of the method to carry out matrix-independent high-precision isotopic analysis without mass-dependent laser-related isotope fractionation removes the necessity of intra-element isotope fractionation correction, as is the case with nanosecond LA systems. Nanosecond laser pulse due to its longer duration interacts differently with the solid sample, leading to change of the sample aerosol formation mechanisms (Anisimov et al., 2003; Perez and Lewis, 2002; Povarnitsyn et al., 2007; Yang et al., 2006). As a result, pulses of nanosecond duration result in increased evaporation, loss of large fraction of aerosol, formed by splashing of melted sample material, and, as a result, laser-induced isotopic fractionation (Bleiner and Bogaerts, 2006; Jochum et al., 2014; Kovacs and Günther, 2008; Mao et al., 1998). This is not the case for femtosecond LA systems, which provide practically no laser-induced isotope fractionation (Jackson and Günther, 2003). The ability to use an admixed internal standard, nebulized from the solution, for internal correction for instrumental mass discrimination permits in situ measurements of stable isotope ratios, highly appreciated in geo- and cosmochemistry. In comparison to pneumatic nebulization MC-ICP-MS, which is capable of bulk analysis, application of fs-LA sampling enables the analysis of pure sub-mm scaled accessory minerals without potential mixing with other phases. Additionally, the advantage of the *in situ* sampling strategy is used in this work to provide lateral isotope ratio profiles inside olivine and schreibersite minerals to reveal their equilibration histories.

3. Experimental

3.1. Samples. Two iron meteorites (Chinga IVB ungrouped and Sikhote-Alin IIB) were obtained from the Central Siberian Geological Museum, V. S. Sobolev Institute of Geology and Mineralogy, Russia. These iron meteorites have previously been characterized for their major and trace element concentrations, while bulk and micro-drilled fractions of these meteorites have also been analyzed for their Fe and Ni isotope ratios as reported in chapters 2 and 6 (Chernonozhkin et al., 2016, 2014). A section of the PMG CMS 04071 was obtained from the Antarctic meteorite collection of the National Aeronautics and Space Administration (NASA), while PMG Esquel was purchased from a commercial vendor. The samples were characterized for their Fe and Ni element distributions using µXRF. Two-dimensional element distribution maps of the thick sections of the iron meteorites and PMGs were obtained using a Bruker M4 Tornado XRF instrument. The acquired 2D element distribution maps permit mineral phases in the targeted meteorites to be distinguished and ideal locations for high-precision isotopic analysis using laser ablation MC-ICP-MS to be selected.

3.2. Reference materials. Certified reference material (CRMs) of synthetic silicate glass of the National Institute of Standards and Technology (NIST) SRM 612 was used for daily tuning of the LA-ICP-MS instrumental parameters. The certified reference material IRMM-014 was used as external calibrator to correct for instrumental mass discrimination when measuring Fe isotope ratios in metal, troilite and schreibersite phases of meteorites. When measuring Fe isotope ratios in olivines of PMGs, MPI-DING BCR-2G was used as external calibrator. First, reference values of the latter were adapted from (Oeser et al., 2014), and later the measured values of the sample were re-calculated with respect to IRMM-014. Although no matrix effects have been observed during femtosecond laser ablation sampling, BCR-2G was preferred over IRMM-014 because the Fe concentrations of the former fit closer to those of olivines. When Fe isotope ratios were measured, the Ni certified isotopic reference material NIST SRM 986 was used as an internal standard. To determine Ni isotope ratios, steel NIST SRM 1226 with 5.42 wt% Ni was used as external calibrator to correct for instrumental mass discrimination throughout this study. The delta-notations of Ni were then recalculated with respect to NIST SRM 986. In-house isotopic reference materials include ML3B-G (flux-free basalt glass MPI-DING SRM) and high-purity Fe metal (99.995 % Fe, Puratronic, Johnson Matthey, lot No. FE495007IF2), which have previously been characterized for their Fe isotopic compositions (Horn et al., 2006; Oeser et al., 2014).

3.3. In-situ isotopic analysis. The isotope ratios of Fe and Ni were measured using a combination of a femtosecond laser ablation system and a Thermo Scientific Neptune MC-ICP-MS unit. The in-house built laser ablation system is based on a 100 femtosecond Ti-sapphire regenerative amplifier (Solstice, Spectra-Physics, Santa Clara, CA, USA) with a fundamental IR wavelength of 775 nm, which was consecutively frequency-quadrupled, thus resulting in an output laser beam with a UV wavelength of 194 nm. The final output energy is ~3.2 mJ pulse^{-1} at a fundamental wavelength of 775 nm, resulting in a pulse energy of 70 μJ at a wavelength of 194 nm. The duration of the laser pulse was determined to be 100-200 fs. The frequency of the laser pulses can be changed between 1 and 500 Hz, and was selected to be in the range 10-40 Hz during the analysis. The laser spot size and the frequency of the laser pulses were tuned before each analysis to fit the intensities of the samples and bracketing standards within 5%. For details on the LA unit design, see (Horn et al., 2006; Oeser et al., 2014). Laser sampling was performed by ablating ~400 μm long lines, typically placed parallel to the straight margin of the target mineral, while recording the transient MC-ICP-MS signals. The absence of significant laser-related instrument mass discrimination was confirmed in previous studies for olivine and metal matrix (Horn et al., 2006; Oeser et al., 2014). The laser-generated aerosol is transported by He carrier gas, admixed with Ar downstream of the LA unit. The internal standard (Ni in the case of Fe isotopic analysis and Cu in the case of Ni isotopic analysis) was added to the sample aerosol via pneumatic nebulization of a 5 μg g^{-1} solution using an ESI PFA-ST nebulizer and a quartz glass spray chamber (double-pass Scott design). The Thermo Scientific Neptune MC-ICP-MS unit at the Institut fur Mineralogie of the Leibniz Universitat Hannover (Germany) was operated in high mass resolution mode (M/ΔM = 9000) and equipped with a high-efficiency 'jet' interface. The transient signal was acquired in 180 1.049 s long cycles, 25 of which constituted measurement of the gas blank before the actual sample ablation. The instrumental mass discrimination was corrected for using a combination of internal standards, relying on the Russel law, and additionally, an external sample-standard bracketing correction. To do so, Ni or Cu standards were continuously introduced during the laser ablation of samples in standards via pneumatic nebulization for Fe and Ni isotopic analysis, respectively. Following the internal mass bias correction, the isotope ratios are reported as delta values, relative to the bracketing reference material to correct for minor drift in the instrumental parameters:

$$\delta^{x/60}Ni = \left[\frac{({}^{x}Ni/{}^{60}Ni)_{Cu\,corr,smp}}{({}^{x}Ni/{}^{60}Ni)_{Cu\,corr,NISTSRM986}} - 1\right] \cdot 1000 \qquad (7-2)$$

$$\delta^{x/54}Fe = \left[\frac{({}^{x}Fe/{}^{54}Fe)_{Ni\,corr,smp}}{({}^{x}Fe/{}^{54}Fe)_{Ni\,corr,IRMM014}} - 1\right] \cdot 1000 \qquad (7-3)$$

where *x* is 61 or 62 for Ni and 56 or 57 for Fe, and the subscripts denote that the ratios were first corrected internally assuming an Russel model. For more details on the isotope ratio measurement protocol, the instrument settings used and the correction for mass discrimination, we refer the reader to (Oeser et al., 2015, 2014; Weyrauch et al., 2015).

3.4. Electron probe microanalysis (EPMA) and micro X-ray fluorescence spectrometry (μXRF). The 2D element distribution maps of the entire thick sections of meteorites were obtained with a resolution of 25 μm under a vacuum of 20 mbar using a Bruker M4 Tornado XRF instrument at the Vrije Universiteit Brussel. This instrument is equipped with a 30 W Rh-anode X-ray source and two Silicon Drift Detector spectrometers. Quantitative EPMA of the olivines within PMGs was performed using a JEOL JXA-8500F electron probe microanalyzer at the Museum für Naturkunde Berlin. This microprobe is equipped with a field emission cathode, five wavelength dispersive spectrometers, and an energy-dispersive spectrometer. Standardization was performed using Smithsonian and Astimex natural mineral standards. For the details of the μXRF and EPMA setup and the corresponding procedures, the reader is referred to Chernonozhkin et al., (2016) and Van Roosbroek et al., (2015), respectively.

4. Results

The results of the Fe and Ni isotopic analysis are plotted in figure 7-1. The average $\delta^{56/54}$Fe results for kamacite of iron meteorites and PMGs is in agreement with the range reported in the literature for ordinary chondrites, although concentrated at the lighter side of the chondrites frequency distribution (see compilations in Barrat et al., 2015; Beard and Johnson, 2004). However, the $\delta^{56/54}$Fe variation for different kamacite grains within a single meteorite can be larger, up to 0.37 ‰ (*e.g.*, $\delta^{56/54}$Fe of -0.28 to 0.09 ‰ in Esquel kamacite). The average $\delta^{62/60}$Ni results for kamacites in Sikhote-Alin IIA and Chinga iron meteorites fall within the range of ordinary chondrites reported by Chernonozhkin et al. (2016) and Cook et al. (2007). In contrast, the average $\delta^{62/60}$Ni results for kamacite in the Udei Station IAB iron meteorite and PMGs are significantly heavier than the range reported for ordinary chondrites. Fe in taenite is isotopically heavier than in kamacite, while Ni in taenite is isotopically lighter than in kamacite. Troilite is characterized by light $\delta^{56/54}$Fe isotope signatures relative to kamacite and taenite of the host meteorite ($\delta^{56/54}$Fe of -

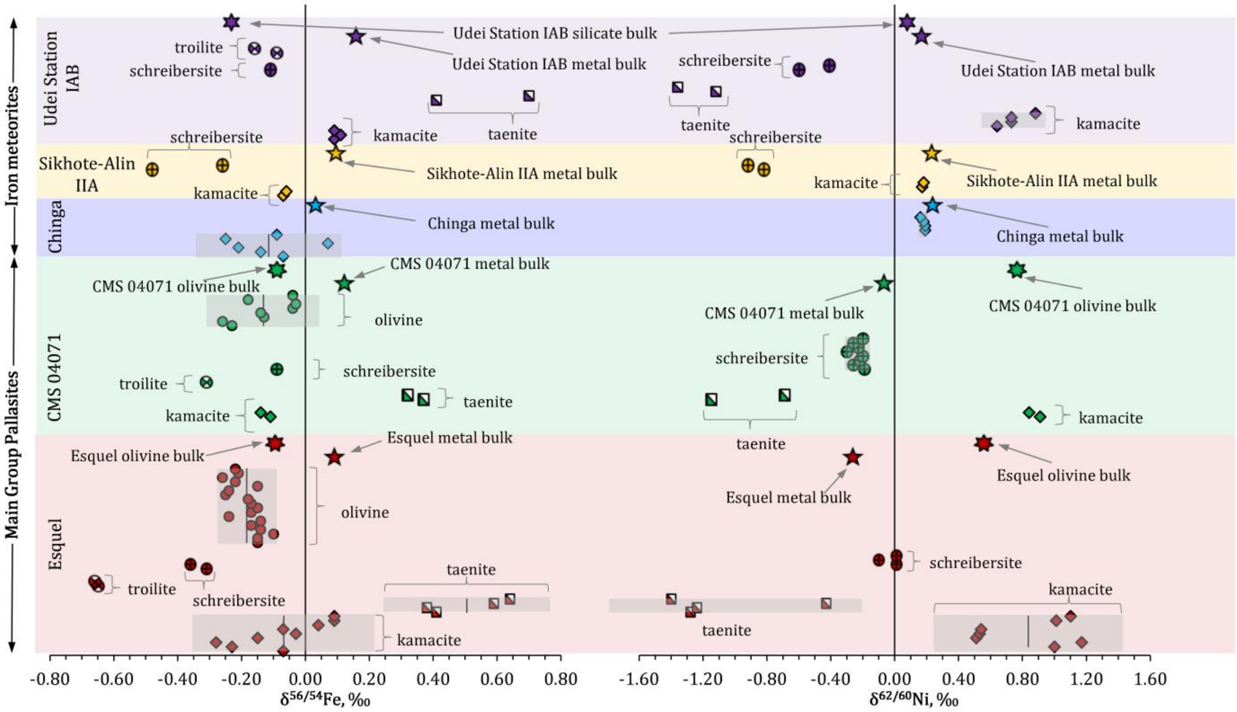

Figure 7-1. Stable isotope ratio plot for $\delta^{56/54}$Fe and $\delta^{62/60}$Ni in different mineral phases of 2 main group pallasites and 3 iron meteorites. Bulk meteorite Ni data, marked with stars, is reported as $\delta^{60/58}$Ni (Chernonozhkin et al., 2016). Given the similar mass difference between the isotope couples ^{60}Ni-^{58}Ni and ^{62}Ni-^{60}Ni and the absence of mass-independent effects, these values are similar.

0.66 to -0.09 ‰). Ni isotope ratios were not measured in troilite, because of its insufficient abundances. Schreibersite generally exhibits light $\delta^{56/54}$Fe and $\delta^{62/60}$Ni isotope signatures relative to chondrites ($\delta^{56/54}$Fe is -0.36 to -0.09 ‰, and $\delta^{62/60}$Ni is -0.64 to +0.29 ‰). Here, one should keep in mind that NIST SRM 986, used as reference for the Ni isotope ratios measurements, has shifted from chondritic isotope compositions during manufacturing by the Mond process of Ni purification (Tanimizu and Hirata, 2006). Olivines of PMGs show light $\delta^{56/54}$Fe isotopic signatures ($\delta^{56/54}$Fe of -0.1 to -0.2 ‰), at the lower end of the chondritic range (Barrat et al., 2015), slightly lighter than previously reported by (Weyer et al., 2005).

5. Discussion

5.1. Equilibrated olivines in PMG. The abundances of major and several trace elements in olivines of main group pallasites have previously been shown to be distributed nearly uniformly, with only faint zoning, observed within a few hundred micrometers of the olivine crystal edges only (Miyamoto, 1997). Such zoning is the result of a cooling that is fast enough to hinder complete diffusive homogenization, and can be used to constrain the cooling rates of olivines, provided that the diffusion coefficients are known. Using electron probe (EPMA), both normal, with increased Fe concentrations next to the olivine rim, and reversed Fe concentration patterns have been observed within a single pallasite, both providing similar estimates of the pallasite's cooling rate within 20-200 ^{o}C/yr, in the temperature range of 1100 to 600 ^{o}C (Miyamoto, 1997). However, the Fe concentration variations near the edge of PMG olivines is on the level of the instrumental precision, of the order of 1 % Fa# with Fa# = Fe / [Fe ± Mg], which deteriorates the precision of the cooling rate determination. Recently, it was shown that incomplete diffusive equilibration of olivine is accompanied by kinetically controlled Fe and Mg isotope fractionation, which, in combination with concentration zoning, provides the ability to distinguish between various processes of magmatic olivine formation, for example through crystal growth/dissolution, diffusive Fe-Mg exchange or Fe-Mg inter-diffusion (Oeser et al., 2015). At the same time, the assumption of full Fe isotopic equilibration between the olivine and metal parts of pallasites allows to determine the equilibration temperatures of these mineral phases (Poitrasson et al., 2005, Chernonozhkin et al., 2016). Figure 7-2 shows four Fe isotope profiles across the olivines of two PMG meteorites, while the most detailed Esquel olivine profile is also complemented by the Fe isotopic analysis of

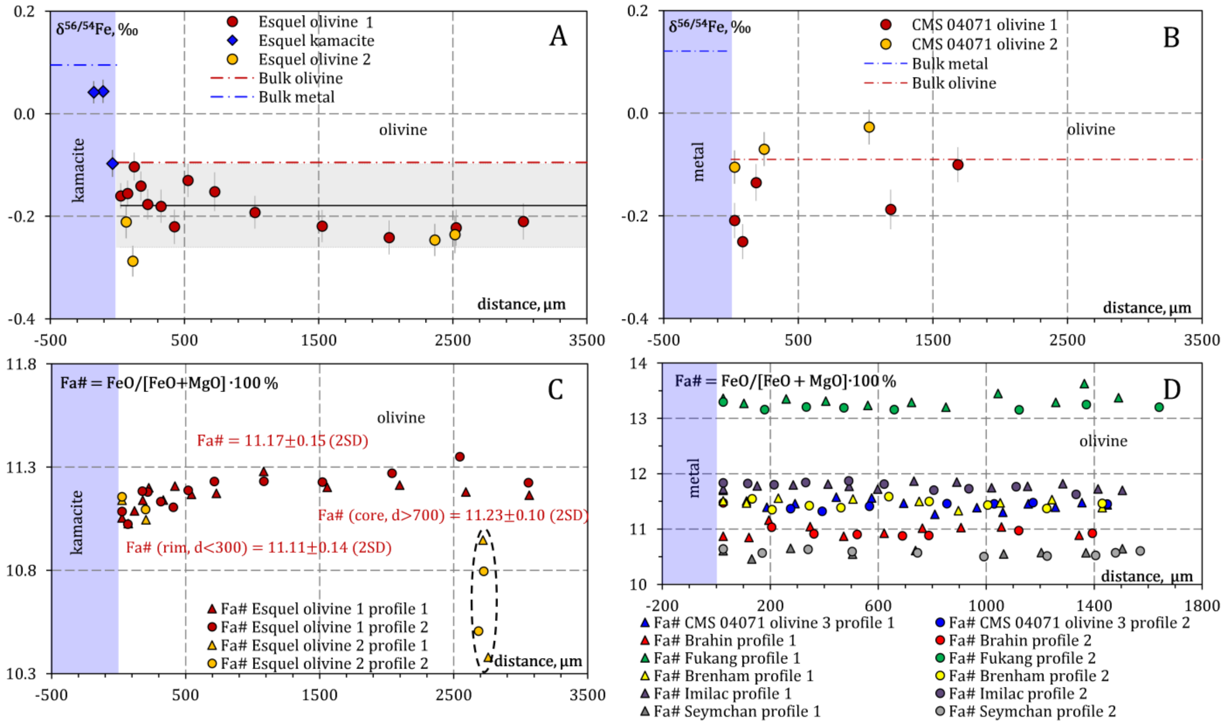

Figure 7-2. A,B – Fe isotope ratio profiles for olivines of Esquel and CMS 04071, respectively, measured next to the olivine-metal junction, versus the distance x to the olivine margin (x=0). The applied laser spot size is 40 µm in diameter for olivines and 70 µm in diameter for the metal phase, with lines ablated closely to one another (40 µm displacement for olivines and 70 µm displacement for the metal phase). The measurement results for Esquel kamacite (blue diamonds) are located adjacent to the profile for Esquel olivine 1, red circles. Error bars represent ±1 SD of a single measurement. The Fe isotope ratios for bulk olivine and metal were measured *via* pneumatic nebulization MC-ICP-MS after acid digestion of the meteorite samples and Fe chemical isolation at Ghent University, Belgium (Chernonozhkin et al., 2016). The black line and gray bar represent the mean $\delta^{56/54}$Fe with 2 standard deviations of Esquel olivine 1. Note that this is different from figure 7-1, where the mean $\delta^{56/54}$Fe of all olivine measurements is shown. C – EPMA Fa# profiles of Esquel olivine 1 and olivine 2, measured at both sides of the laser traces used for documenting the Fe isotopic profile. D – EPMA Fa# profiles of olivines of 6 other PMGs, measured next to olivine-metal rim, which show no significant zoning.

kamacite in direct contact to this olivine.

All the data points of the most detailed Esquel olivine 1 profile fall within the ±2 SD range of the olivine analyses ($\delta^{56/54}$Fe = -0.179 ± 0.081 ‰ for 14 analyses of the single Esquel olivine), which is comparable to the internal precision of the isotope ratio measurement (2 SD on the working standard over a measurement session of a single day). However, the data points are not distributed randomly compared to this average, as the five data points furthest from the olivine-metal rim are systematically light. The average of the olivine core ($\delta^{56/54}$Fe = -0.217 ± 0.018 ‰, 1 SD, five points near the core of the olivine) is significantly lighter than the average of the spots near the rim ($\delta^{56/54}$Fe = -0.158 ± 0.033 ‰, 1 SD, nine points adjacent to the olivine rim) at the 95 % significance level, $t = 3.65 > t_{12,5\%} = 2.18$. This might hint towards PMG olivine cores that are slightly lighter than the olivine rims. Possibly, insufficient lateral resolution near the rims of the olivine, where the highest magnitude of the diffusion- or overgrowth-generated Fe isotope zoning is expected, creates a sampling artefact (c.f. fig. 9-10 in (Oeser et al., 2015). However, even if faint Fe isotope zoning in pallasite olivines does occur, the magnitude and precision of the $\delta^{56/54}$Fe do not allow to constrain any information on the timing of the olivine formation process. Importantly, the (near) absence of Fe isotope zoning in Esquel olivine suggests efficient thermal equilibration of the PMG olivine and metal fractions, and suggests that the assumption of complete isotopic equilibration of Fe in the context of isotope thermometric applications is reasonable. Any influence of the 1 mm isotopically heavier (by 0.059 ‰) olivine outer layer on the bulk isotope signature of the centimeter-sized olivine can be considered negligible. Significant improvements of the analytical capabilities in terms of precision of the isotope ratio measurements and instrument sensitivity are needed to resolve the Fe isotope zoning expected based on Fe concentration profiles across PMG olivines (Miyamoto, 1997).

The $\delta^{56/54}$Fe profile of the kamacite directly next to the olivine margin indicates that the kamacite metal closely adjacent to the olivine is ~0.14 ‰ lighter than the more remote kamacite. Stable transient signals during the measurement of this individual kamacite zone with intensities similar to other kamacite locations suggest sampling of pure kamacite. Although this ratio is within the range of the Fe isotopic signatures measured for kamacite in this work, this is an interesting observation, as the variability of kamacite in FeNi-rich meteorites is constrained by diffusive kamacite-taenite exsolution during slow cooling of the meteorite parent body below 800 ˚C (Dauphas, 2007), while no taenite is located near this particular kamacite-olivine margin. The light Fe isotopic signature of the kamacite next to the olivine rim may potentially be interpreted as an effect of grain-boundary diffusion or simply terrestrial alteration.

The $\delta^{56/54}$Fe profile of the kamacite next to the olivine margin indicates that the kamacite metal closely adjacent to the olivine is 0.14 ‰ lighter than the remote kamacite material. Stable transient signal during the measurement of this individual kamacite, with intensity similar to the other kamacites suggests sampling of pure kamacite. Although this ratio is within the range of kamacite isotope signatures measured in this work, it is an interesting observation, because the variability of kamacite is constrained by diffusive kamacite-taenite exsolution during slow cooling of the meteorite parent body below 800 ^{o}C (Dauphas, 2007), while no taenite is located near the location of kamacite-olivine margin. The light Fe isotope signature of kamacite next to olivine rim may potentially be interpreted as effect of grain boundary diffusion or simply terrestrial contamination.

5.2. Schreibersite: equilibrium or diffusion control? In contrast to metal phases, the Fe and Ni isotopic signatures of schreibersite grains exhibit a smaller variability within each individual meteorite. The largest difference in $\delta^{56/54}$Fe for different schreibersite grains within an individual meteorite is found for Sikhote-Alin IIA (0.22 ‰), while the largest difference in $\delta^{62/60}$Ni is observed for Udei Station IAB (0.19 ‰, see figure 7-1). Figure 7-3 shows a ~800 µm $\delta^{62/60}$Ni profile across a large schreibersite grain in the main group pallasite CMS 04071. No Ni isotopic zoning is found within the analyzed schreibersite, with single $\delta^{62/60}$Ni measurements showing a standard deviation of 0.037 ‰, (*n*=7) and a range of ~0.10 ‰. The small dispersion of Fe and Ni isotope ratios of different schreibersite grains within a single meteorite and the absence of Ni isotopic zoning across a single large (~800 µm) schreibersite grain suggest that schreibersites have thermally equilibrated efficiently.

As a result of the kinetic control of the isotope fractionation and the diffusive fluxes of Fe and Ni towards each other during the formation of the Widmanstätten pattern (Dauphas, 2007), kamacite and taenite show a negative correlation between their $\delta^{56/54}$Fe and $\delta^{62/60}$Ni (c.f. figure 7-4). The absence of a similar negative correlation between the stable Fe and Ni isotopic signatures of schreibersites indicates that the driving process of the isotope fractionation during their formation differs from diffusion. Rather, this distribution suggests a thermodynamically controlled Fe and Ni isotope fractionation in thermally equilibrated schreibersite. Unfortunately, the Fe and Ni isotope fractionation factors (average force constants) for the schreibersite-metal system have not been studied experimentally.

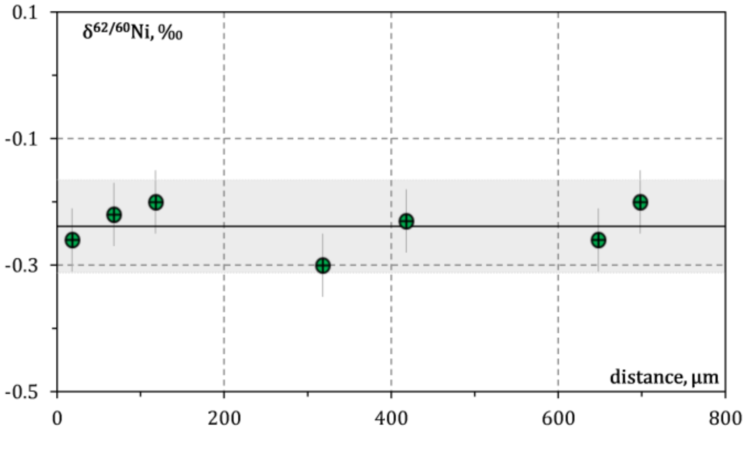

Figure 7-3. $\delta^{62/60}$Ni across a single large schreibersite grain of main group pallasite CMS 04071, adjacent to kamacite Fe-Ni metal (left side of the plot) and olivine (right side of the plot). The solid line and grey bar denote the mean $\delta^{62/60}$Ni = -0.239 ‰ with 2 standard deviation uncertainty (1 SD = 0.037 ‰, *n*=7).

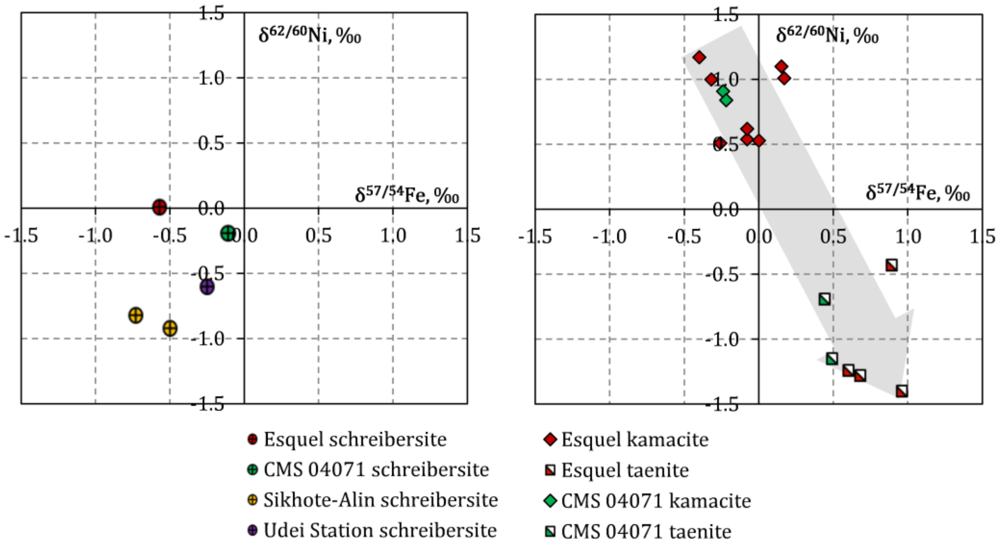

Figure 7-4. Isotope plots of $\delta^{56/54}$Fe versus $\delta^{62/60}$Ni for schreibersite grains (left) and kamacite-taenite interfaces (right).

In pallasites, Fe is distributed between Fe-Ni metal, exsolved into kamacite and taenite when the cooling of the parent body proceeded below ~800 ˚C, olivine, and the minor phases troilite and schreibersite. In the case of silicate-bearing iron meteorite, a range of mineral compositions needs to be considered in the case of the silicate inclusions. Although schreibersite is a minor phase and its isotopic equilibration probably did not change the overall Fe isotopic signature of the metal, the complexity of the Fe isotope fractionation pathways masks any clear pattern (see figure 7-5). In contrast to Fe, Ni is mainly distributed between metal and accessory schreibersite, as the Ni contents are extremely low in silicates and troilite. The Ni stable isotopic signatures of schreibersites in pallasites and iron meteorites show a distinctive trend when plotted versus bulk metal Ni isotope composition (figure 7-5). Previous studies have observed lighter Ni stable isotope ratios for the metal portions of pallasites (Cook et al., 2007, Chernonozhkin et al., 2016), while relatively heavier Ni isotope ratios have been measured for pallasite olivine (Chernonozhkin et al., 2016). Figure 7-5 indicates that the light $\delta^{60/58}$Ni of the bulk metal in pallasites compared to iron meteorites is correlated with heavier $\delta^{62/60}$Ni isotopic compositions for the pallasite schreibersites relative to iron meteorites. The nature of the process leading to Ni isotope fractionation in the PMG parent asteroid and the

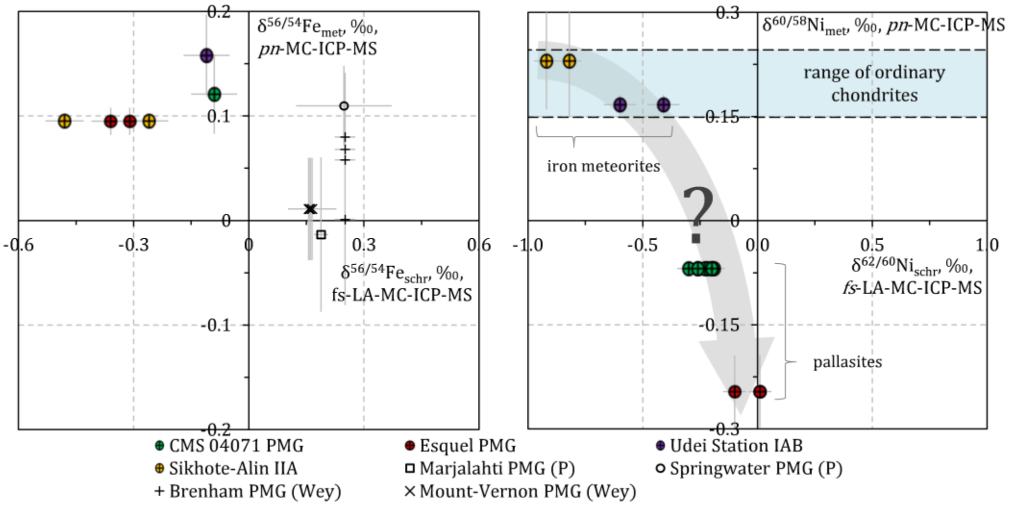

Figure 7-5. Fe and Ni isotope plots of schreibersite (measured via *fs*-LA-MC-ICP-MS) versus bulk metal, composed of troilite, schreibersite and predominantly of Fe-Ni metal (measured via pneumatic nebulization MC-ICP-MS (Chernonozhkin et al., 2016), for two PMGs and two iron meteorites. Literature data for four additional PMGs are also shown: P - (Poitrasson et al., 2005), and Wey - (Weyer et al., 2005). The bulk Ni isotopic data is expressed in $\delta^{60/58}$Ni, although the mass difference for the isotope couples ^{60}Ni-^{58}Ni and ^{62}Ni-^{60}Ni is nearly the same. The $\delta^{60/58}$Ni range for ordinary chondrites is taken from Chernonozhkin et al., 2016.

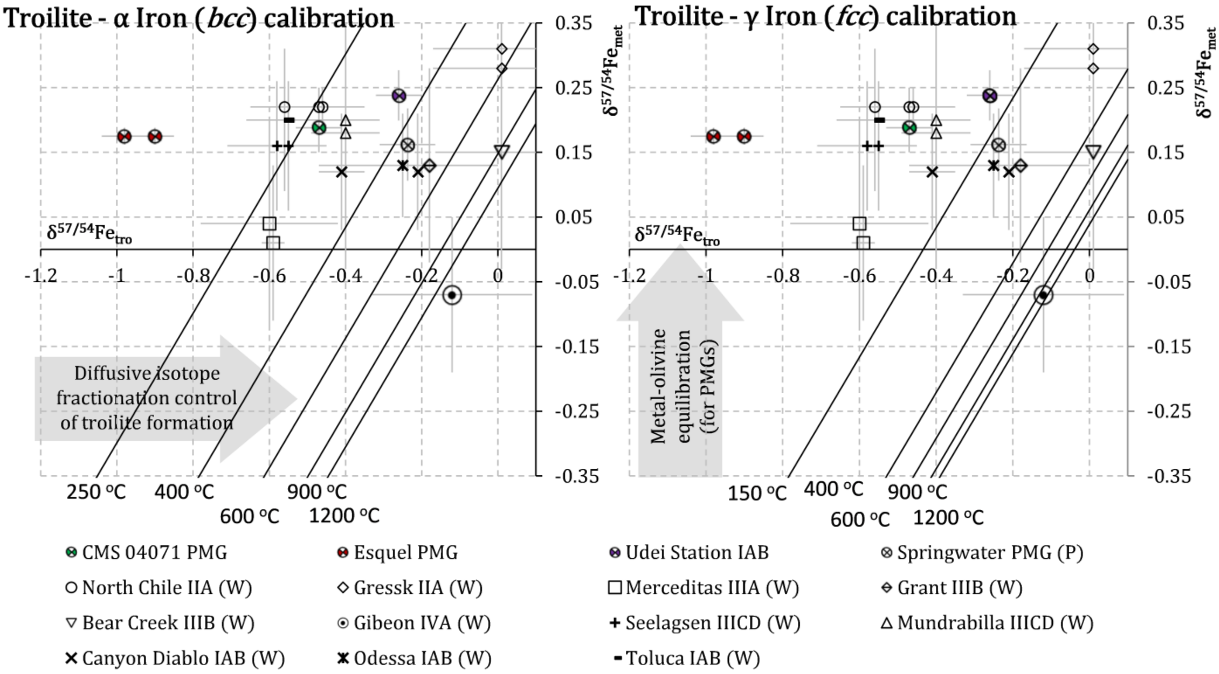

Figure 7-6. $\delta^{57/54}Fe_{metal}$ (measured via PN-MC-ICP-MS at Ghent University) versus $\delta^{57/54}Fe_{troilite}$ (measured via *fs*-LA-MC-ICP-MS at Leibnitz University Hannover) for pallasites and iron meteorites. Geothermometric isotherms at different temperatures are calibrated using parameters of NRIXS (Dauphas et al., 2012) for *bcc* α- (left) and *fcc* γ- (right) allotropic modifications of Fe-Ni metal. Literature data taken from: P - (Poitrasson et al., 2005), and W - (Williams et al., 2006).

implication of an unsampled reservoir with a heavier Ni isotopic composition, as the measured heavy Ni isotopic composition of the minor schreibersite phase cannot compensate for the light Ni isotopic composition of the bulk metal in pallasites alone, remain unclear. Possibly, the equilibrium-controlled Ni isotopic signatures were governed by differences in temperature settings in the parent bodies during schreibersite formation. Alternatively, the equilibrium-controlled Ni isotopic signatures were governed by the bonding environment that is constrained by minor element contents (e.g., S).

5.3. Assessment of troilite as Fe isotope thermometer. Troilite does not contain sufficient amounts of Ni to be analyzed for its isotopic composition via LA-MC-ICP-MS, and thus, only Fe isotope ratios were measured in troilites of iron meteorites and PMGs (Fig. 1). Two parallel measurements of a single troilite grain in the PMG Esquel yielded nearly identical $\delta^{56/54}Fe$ values, with a difference of ~0.01 ‰ only. Two different troilite grains in the Udei Station IAB iron meteorite also yielded nearly identical $\delta^{56/54}Fe$ values, with a difference of ~0.02 ‰. This reproducibility suggests that troilites in PMGs and iron meteorites are fully thermally equilibrated. The Fe isotopic signatures of troilites in iron meteorites and PMGs are light, with the absolute difference in $\delta^{56/54}Fe$ between troilite and bulk metal ($\Delta^{56/54}Fe_{M\text{-}FeS}$, fractionation factor) equal to 0.74 ‰, 0.43 ‰ and 0.25 % for Esquel, CMS 04071 and Udei Station, respectively. The largest observed $\Delta^{56/54}Fe_{M\text{-}FeS}$ is only slightly larger than the $\Delta^{56/54}Fe_{M\text{-}FeS}$ measured for IIAB, IIIAB, IAB and IIICD iron meteorites ($\Delta^{57/54}Fe_{M\text{-}FeS}$ 0.79, 0.63, 0.76 and 0.74‰, respectively; (Williams et al., 2006). This agrees with the observed positive correlation of the troilite-metal fractionation factor with the meteorite cooling rates (Williams et al., 2006), as PMGs are characterized by slower cooling rates than iron meteorites. Such correlation of the cooling rate to the isotope fractionation factor is an indication of thermodynamically driven fractionation, as the closing temperatures, and corresponding equilibrated isotope ratios, depend on the diffusive cooling rates through the Dodson equation. Experimentally determined average bonding constants for troilites (Dauphas et al., 2012), allow to predict the temperature dependence of the metal-troilite fractionation. However, the complexity of the Fe isotope distribution between multiple meteorite mineral phases (Fe-Ni metal, schreibersite, troilite, olivine in the case of PMGs, and multiple silicate phases in the case of IAB complex irons) complicates the calculation of equilibration temperatures. Indeed, the Fe isotope thermometry isotherms, calculated using the data of (Dauphas et al., 2012), yield unrealistically low equilibration temperatures, in particular for the slowest cooling PMGs, independent of the allotrope modification of the Fe-Ni metal with which

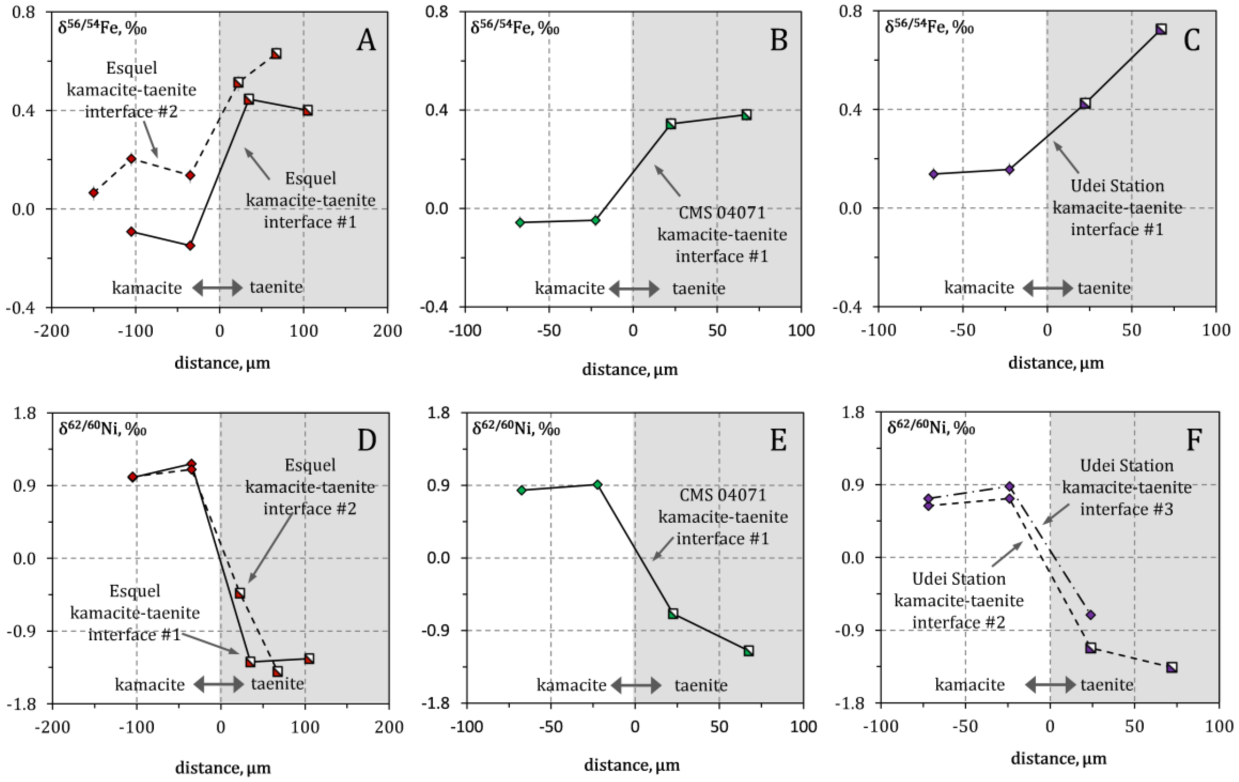

Figure 7-7. $\delta^{57/54}$Fe (A, B, C) and $\delta^{62/60}$Ni (D, E, F) profiles of kamacite and taenite, measured at the kamacite-taenite interfaces of Esquel PMG (A, D), CMS 04071 PMG (B, E), and Udei Station IAB iron (C, F). The Fe and Ni isotopic signatures were measured at nearly the same locations, via *fs*-LA-MC-ICP-MS at the Leibnitz University Hannover. Laser line scans were positioned parallel to the mineral interfaces without gaps between neighboring lines. The Ni isotope ratio profiles were positioned as close as possible to where the Fe isotope ratio profile were measured in the case of Esquel and CMS 04071. In the case of Udei Station, the $\delta^{57/54}$Fe and $\delta^{62/60}$Ni were measured at different kamacite-taenite interfaces, because of spatial limitations.

the troilites are assumed to equilibrate with (figure 7-6). Based on metal-troilite eutectic temperatures, the expected crystallization temperatures are of the order of 1300 ˚C, (Boesenberg et al., 2012; McKibbin et al., 2013). As such, the Fe isotopic signatures of troilites and bulk metal do not reveal realistic time and temperature constraints on the parent body evolution.

5.4. Kamacite-taenite diffusive isotope profiles. Previous work has demonstrated that the Fe and Ni isotopic compositions of kamacite (*bcc* α-iron, Ni-poor) and taenite (*fcc*, γ-iron, Ni-rich) are kinetically governed by sub-solidus diffusion during formation of the Widmanstätten pattern, when kamacite and taenite form during cooling of the parent body below ~800 ˚C (Dauphas, 2007). Using nanosecond LA-MC-ICP-MS, Košler et al. (2005) obtained kamacite-taenite fractionation factors $\Delta^{56/54}\text{Fe}_{\text{kam-tae}}$ of 2.92 ‰ and 1.42 ‰ for IAB Canyon Diablo and IIIAB Horh Uul, respectively. In contrast, Horn et al. (2006) found a considerably smaller $\Delta^{56/54}\text{Fe}_{\text{kam-tae}}$ value of 0.3 ‰ for the IAB Toluca iron meteorite using *fs*-LA-MC-ICP-MS. Similary, Chernonozhkin et al. (2016) presented $\Delta^{56/54}\text{Fe}_{\text{kam-tae}}$ values of 0.088 ‰ and 0.063 ‰ for the IAB Canyon Diablo and IAB Campo del Cielo silicate-bearing iron meteorites, respectively, and $\Delta^{56/54}\text{Fe}_{\text{kam-tae}}$ values of 0.16 ‰ and 0.19 ‰ for the IIIAB Henbury and IVA Gibeon iron meteorites, respectively. These values were obtained by combining micro-drilling with pneumatic nebulization MC-ICP-MS. Here, profiles of $\delta^{56/54}$Fe and $\delta^{62/60}$Ni across kamacite-taenite interfaces were determined with a laser beam diameter of 45 to 70 µm in the Udei Station iron meteorite and in the Esquel and CMS 04071 PMGs (figure 7-7). The largest measured kamacite-taenite fractionation factors for Fe, $\Delta^{56/54}\text{Fe}_{\text{kam-tae}}$, are 0.779 ‰, 0.565 ‰ and 0.82 ‰, while the largest measured kamacite-taenite fractionation factors for Ni, $\Delta^{62/60}\text{Ni}_{\text{kam-tae}}$, are 2.57 ‰, 2.06 ‰, and 2.24 ‰ for Esquel PMG, CMS 04071 PMG and IAB Udei Station, respectively. The $\delta^{56/54}$Fe and $\delta^{62/60}$Ni are negatively correlated in Fe-Ni metal (figure 7-4). This negative correlation and the overall larger fractionation factors for Ni compared to Fe, with a similar difference between the nuclide masses, agree with a diffusive control on the isotope fractionation (Dauphas, 2007). Except for the Esquel PMG profile (#1, figure 7-7 A, D), larger absolute Fe and Ni isotopic signatures are found with increasing distance from the kamacite-taenite interface (closer to the core of the lamellae), with smaller absolute differences in the taenite adjacent to the interface. Based on the modeling of the diffusion isotope ratio profiles (cf. figures 7 and 9 of Dauphas, (2007), these measured isotope ratio patterns place some constraints on the temperatures at which the isotope ratio profiles formed, as the measured $\delta^{56/54}$Fe and $\delta^{62/60}$Ni profiles are not likely to form at temperatures of 450 ˚C or lower, when the most extreme isotopic signatures are predicted near the kamacite-taenite edge. However, significant improvements in the lateral resolution are needed to quantitatively compare these experimental results with theoretically predicted diffusion-driven isotope profiles.

Unexpectedly, six measurements along parallel lines in Chinga metal reveal a $\Delta^{56/54}$Fe fractionation factor of 0.32 ‰, while laterally-resolved Ni isotopic signatures in the same section of Chinga metal show no significant differences, with a $\Delta^{62/60}$Ni of 0.03 ‰. Sub-solidus diffusion between kamacite and taenite cannot explain this pattern, as Chinga is an ataxite, previously classified as a IVB member, but currently ungrouped according to the meteoritical bulletin (Agafonov et al., 1997; Chernonozhkin et al., 2014). µXRF mapping of this meteorite confirms that this meteorite does not contain any taenite lamellae and that the major constituting elements are homogeneously distributed. As such, the fractionation factor observed for Fe could indicate a currently unidentified process driving Fe isotope fractionation.

6. Conclusions

Stable isotope ratios of Fe and Ni were measured *in situ* in various major and minor mineral phases of iron meteorites and main group pallasites (PMG) with high precision using a combination of femtosecond laser ablation and multi-collector ICP-mass spectrometry (*fs*-LA-MC-ICP-MS). Next to Fe-Ni metal and silicate fractions, individual sub-mm sized phosphide and sulphide grains were characterized for their Fe and Ni isotopic compositions. Isotope profiles across individual PMG olivines and troilite, as well as across rims of Fe-Ni metal lamellas were measured with a spatial resolution of 30 to 80 µm. In general, these laterally resolved Fe-Ni stable isotope ratio signatures indicate efficient thermal equilibration of the refractory mineral phases formed at higher temperatures (olivine, troilite, schreibersite), with predominantly equilibrium-driven isotope fractionation between these phases. In contrast, kamacite and taenite, exsolved from FeNi metal below ~800 ˚C, exhibit diffusive Fe and Ni isotope ratio profiles, confirming kinetically driven isotope fractionation. The narrow range in Fe and Ni isotope ratios measured for troilites and schreibersites suggests efficient thermal equilibration. Due to the complex distribution of Fe between metal, schreibersite, troilite and/or silicate, the Fe isotope ratios of troilites/metal that are governed by equilibrium-driven fractionation cannot be used for geothermometric reconstructions. The Ni isotopic signatures of bulk metal and schreibersite correlate negatively, with isotopically lighter Ni in the metal phase of PMGs and isotopically heavier Ni in the metal phase of iron meteorites. As Ni in PMGs is mainly distributed between these two phases and kinetic control is unlikely, the effect of an unidentified process needs to be invoked to explain these Ni stable isotopic signatures in the metal-schreibersite system. The driving force of this fractionation may be the change of the temperature and different Fe-P-Ni bulk contents during fractional crystallization in iron meteorite and PMG parent bodies, when different types of schreibersites are crystallized in different stability fields of the metal-schreibersite phase diagram (Yoshikawa and Matsueda, 1992). Olivines of main group pallasites are largely isotopically equilibrated, with only a hint of Fe isotopic zoning observed, which is insufficient to quantitatively constrain the cooling histories or processes of magmatic evolution, such as growth/dissolution. On the other hand, efficient Fe isotope equilibration of the olivine permits the use of Fe isotope ratios in the olivine-bulk metal system for isotope geothermometry purposes. Similarly, metallographic cooling rates cannot be quantitatively constrained as the lateral resolution of diffuse Fe-Ni isotope profiles across kamacite-taenite interfaces remains insufficient (~10 µm resolution is needed according to Dauphas, 2007). However, as the laterally resolved Fe and Ni isotopic signatures across the measured profiles are larger further from the kamacite-taenite interface, the cooling of the parent bodies must have occurred at higher (~650 ˚C) rather than lower (≤450 ˚C) temperatures based on comparison with the theoretically calculated kamacite-taenite sub-solidus diffusive isotope profiles.

7. List of references

Agafonov, L. V., Kuzhuget, K.S., Oidup, C.K., Ivanova, G.M., 1997. Mineral composition of the Chinge meteorite. Dokl. Akad. Nauk. (in Russ. 352, 201–503.

Anisimov, S.I., Zhakhovskii, V. V., Inogamov, N.A., Nishihara, K., Oparin, A.M., Petrov, Y. V., 2003. Destruction of a solid film under the action of ultrashort laser pulses. J. Exp. Theor. Phys. Lett. 77, 606–610.

Barrat, J.A., Rouxel, O., Wang, K., Moynier, F., Yamaguchi, A., Bischoff, A., Langlade, J., 2015. Early stages of core segregation recorded by Fe isotopes in an asteroidal mantle. Earth Planet. Sci. Lett. 419, 93–100. doi:10.1016/j.epsl.2015.03.026

Beard, B.L., Johnson, C.M., 2004. Fe Isotope Variations in the Modern and Ancient Earth and Other Planetary Bodies. Rev. Mineral. Geochemistry 55, 319–357. doi:10.2138/gsrmg.55.1.319

Bleiner, D., Bogaerts, A., 2006. Multiplicity and contiguity of ablation mechanisms in laser-assisted analytical micro-sampling. Spectrochim. Acta Part B At. Spectrosc. 61, 421–432. doi:10.1016/j.sab.2006.02.007

Boesenberg, J.S., Delaney, J.S., Hewins, R.H., 2012. A petrological and chemical reexamination of Main Group pallasite formation. Geochim. Cosmochim. Acta 89, 134–158. doi:10.1016/j.gca.2012.04.037

Chernonozhkin, S.M., Goderis, S., Bauters, S., Vekemans, B., Vincze, L., Claeys, P., Vanhaecke, F., 2014. Evaluation of pneumatic nebulization and ns-laser ablation ICP-MS for bulk elemental analysis and 2-dimensional element mapping of iron meteorites. J. Anal. At. Spectrom. 29, 1001–1016. doi:10.1039/c3ja50387a

Chernonozhkin, S.M., Goderis, S., Costas-Rodríguez, M., Claeys, P., Vanhaecke, F., 2016. Effect of parent body evolution on equilibrium and kinetic isotope fractionation: a combined Ni and Fe isotope study of iron and stony-iron meteorites. Geochim. Cosmochim. Acta 186, 168–188. doi:10.1016/j.gca.2016.04.050

Cook, D.L., Wadhwa, M., Clayton, R.N., Dauphas, N., Janney, P.E., Davis, A.M., 2007. Mass-dependent fractionation of nickel isotopes in meteoritic metal. Meteorit. Planet. Sci. 42, 2067–2077. doi:10.1111/j.1945-5100.2007.tb01008.x

Dauphas, N., 2007. Diffusion-driven kinetic isotope effect of Fe and Ni during formation of thereadthrough Widmanstätten pattern. Meteorit. Planet. Sci. 42, 1597–1613. doi:10.1111/j.1945-5100.2007.tb00593.x

Dauphas, N., Roskosz, M., Alp, E.E., Golden, D.C., Sio, C.K., Tissot, F.L.H., Hu, M.Y., Zhao, J., Gao, L., Morris, R.V., 2012. A general moment NRIXS approach to the determination of equilibrium Fe isotopic fractionation factors: Application to goethite and jarosite. Geochim. Cosmochim. Acta 94, 254–275. doi:10.1016/j.gca.2012.06.013

Dodson, M.H., 1973. Closure temperature in cooling geochronological and petrological systems. Contrib. to Mineral. Petrol. 40, 259–274. doi:10.1007/BF00373790

Hoefs, J., 2009. Stable Isotope Geochemistry, 6th ed. Springer-Verlag, Berlin Heidelberg.

Horn, I., von Blanckenburg, F., Schoenberg, R., Steinhoefel, G., Markl, G., 2006. In situ iron isotope ratio determination using UV-femtosecond laser ablation with application to hydrothermal ore formation processes. Geochim. Cosmochim. Acta 70, 3677–3688. doi:10.1016/j.gca.2006.05.002

Jackson, S.E., Günther, D., 2003. The nature and sources of laser induced isotopic fractionation in laser ablation-multicollector-inductively coupled plasma-mass spectrometry. J. Anal. At. Spectrom. 18, 205–212. doi:10.1039/b209620j

Jochum, K.P., Stoll, B., Weis, U., Jacob, D.E., Mertz-Kraus, R., Andreae, M.O., 2014. Non-Matrix-Matched Calibration for the Multi-Element Analysis of Geological and Environmental Samples Using 200 nm Femtosecond LA-ICP-MS: A Comparison with Nanosecond Lasers. Geostand. Geoanalytical Res. 38, 265–292. doi:10.1111/j.1751-908X.2014.12028.x

Košler, J., Pedersen, R.B., Kruber, C., Sylvester, P.J., 2005. Analysis of Fe isotopes in sulfides and iron meteorites by laser ablation high-mass resolution multi-collector ICP mass spectrometry. J. Anal. At. Spectrom. 20, 192–199. doi:10.1039/B412169D

Kovacs, R., Günther, D., 2008. Influence of transport tube materials on signal response and drift in laser ablation-inductively coupled plasma-mass spectrometry. J. Anal. At. Spectrom. 23, 1247–1252. doi:10.1039/b803789b

Mao, X.L., Ciocan, A.C., Russo, R.E., 1998. Preferential Vaporization during Laser Ablation Inductively Coupled Plasma Atomic Emission Spectroscopy. Appl. Spectrosc. 52, 913–918.

McKibbin, S.J., Ireland, T.R., Holden, P., O'Neill, H.S.C., Mallmann, G., 2016. Rapid cooling of planetesimal core-mantle reaction zones from Mn-Cr isotopes in pallasites. Geochemical Perspect. 2, 68–77. doi:10.7185/geochemlet.1607

McKibbin, S.J., O'Neill, H.S.C., Mallmann, G., Halfpenny, A., 2013. LA-ICP-MS mapping of olivine from the Brahin and Brenham meteorites: Complex elemental distributions in the pallasite olivine precursor. Geochim. Cosmochim. Acta 119, 1–17. doi:10.1016/j.gca.2013.05.031

Miyamoto, M., 1997. Chemical zoning of olivine in several pallasites. J. Geophys. Res. 102, 21,613–21,618. doi:10.1029/97JE01852

Oeser, M., Dohmen, R., Horn, I., Schuth, S., Weyer, S., 2015. Processes and time scales of magmatic evolution as revealed by Fe–Mg chemical and isotopic zoning in natural olivines. Geochim. Cosmochim. Acta 154, 130–150. doi:10.1016/j.gca.2015.01.025

Oeser, M., Weyer, S., Horn, I., Schuth, S., 2014. High-Precision Fe and Mg Isotope Ratios of Silicate Reference Glasses Determined In Situ by Femtosecond LA-MC-ICP-MS and by Solution Nebulisation MC-ICP-MS. Geostand.

Geoanalytical Res. 38, 311–328. doi:10.1111/j.1751-908X.2014.00288.x

Perez, D., Lewis, L.J., 2002. Ablation of solids under femtosecond laser pulses. Phys. Rev. Lett. 89, 255504–1–255504–4. doi:10.1103/PhysRevLett.89.255504

Planavsky, N., Rouxel, O.J., Bekker, A., Hofmann, A., Little, C.T.S., Lyons, T.W., 2012. Iron isotope composition of some Archean and Proterozoic iron formations. Geochim. Cosmochim. Acta 80, 158–169. doi:10.1016/j.gca.2011.12.001

Poitrasson, F., Levasseur, S., Teutsch, N., 2005. Significance of iron isotope mineral fractionation in pallasites and iron meteorites for the core–mantle differentiation of terrestrial planets. Earth Planet. Sci. Lett. 234, 151–164. doi:10.1016/j.epsl.2005.02.010

Povarnitsyn, M.E., Itina, T.E., Sentis, M., Khishchenko, K. V., Levashov, P.R., 2007. Material decomposition mechanisms in femtosecond laser interactions with metals. Phys. Rev. B 75, 235414–1–235414–5. doi:10.1103/PhysRevB.75.235414

Reed, S.J.B., Scott, E.R.D., Long, J.V.P., 1979. Ion microprobe analysis of olivine in pallasite meteorites for nickel. Earth Planet. Sci. Lett. 43, 5–12. doi:10.1016/0012-821X(79)90150-X

Scott, E.R.D., 1972. Chemical fractionation in iron meteorites and its interpretation. Geochim. Cosmochim. Acta 36, 1205–1236. doi:10.1016/0016-7037(72)90046-4

Tanimizu, M., Hirata, T., 2006. Determination of natural isotopic variation in nickel using inductively coupled plasma mass spectrometry. J. Anal. At. Spectrom. 21, 1423–1426. doi:10.1039/b609543g

Valley, J.W., 2001. Stable Isotope Thermometry at High Temperatures. Rev. Mineral. Geochemistry 43, 365–413. doi:10.2138/gsrmg.43.1.365

Van Roosbroek, N., Debaille, V., Pittarello, L., Goderis, S., Humayun, M., Hecht, L., Jourdan, F., Spicuzza, M.J., Vanhaecke, F., Claeys, P., 2015. The formation of IIE iron meteorites investigated by the chondrule-bearing Mont Dieu meteorite. Meteorit. Planet. Sci. 50, 1173–1196. doi:10.1111/maps.12463

Wasson, J.T., 2016. Formation of the Treysa quintet and the main-group pallasites by impact-generated processes in the IIIAB asteroid. Meteorit. Planet. Sci. 51, 773–784. doi:10.1111/maps.12635

Weyer, S., Anbar, A.D., Brey, G.P., Munker, C., Mezger, K., Woodland, A.B., Münker, C., Mezger, K., Woodland, A.B., 2005. Iron isotope fractionation during planetary differentiation. Earth Planet. Sci. Lett. 240, 251–264. doi:10.1016/j.epsl.2005.09.023

Weyrauch, M., Zipfel, J., Weyer, S., 2015. Ni isotope composition of zoned metal grains in CBb chondrite Hammadah al Hamra 237, in: Paneth Kolloquium Nördlingen. p. #0051.

Williams, H.M., Markowski, A., Quitté, G., Halliday, A.N., Teutsch, N., Levasseur, S., 2006. Fe isotope fractionation in iron meteorites: New insights into metal-sulphide segregation and planetary accretion. Earth Planet. Sci. Lett. 250, 486–500. doi:10.1016/j.epsl.2006.08.013

Yang, J., Zhao, Y., Zhu, X., 2006. Transition between nonthermal and thermal ablation of metallic targets under the strike of high-fluence ultrashort laser pulses. Appl. Phys. Lett. 88, 094101–1–094101–3. doi:10.1063/1.2168513

Yoshikawa, M., Matsueda, H., 1992. Texture, chemical composition and genesis of schreibersite in iron meteorite. Jour. Fac. Sci., Hokkaido Univ., Ser IV 23, 255–280.

Chapter 8

Summary and conclusions

In this work, inductively coupled plasma – mass spectrometry (ICP-MS) based analytical methods for trace element and isotopic (Fe, Ni) analysis of meteoritic material, including both bulk analysis via pneumatic nebulization of dissolved samples and *in situ* analysis via laser ablation (LA) micro-sampling, have been developed and carefully evaluated. The LA-ICP-MS based methods for trace element determination proposed in this work are attractive for cosmochemical applications due to their ability to provide quantitative, accurate and precise spatially-resolved information on trace to major elements in meteoritic material at low spatial resolution and non-respect of matrix effects. The quantitative 2D element distribution maps thus obtained are highly useful to provide insight into the processes experienced by the meteorite parent bodies, as they provide information on features, such as (1) the equilibration conditions of the system, reflected in the elemental composition of the mineral phases, (2) solid-state diffusion between adjacent minerals composing meteorites and (3) the crystal chemistry constraining element substitution in mineral lattices. In order to acquire quantitative 2D element distribution maps, specific challenges, related to the nature of laser-solid interaction during the laser sampling, had to be overcome. A significant effect of the matrix on the analytical results, especially when analysing metal materials, has been demonstrated. Careless use of 2D intensity distribution maps without proper correction for these matrix effects can lead to biased interpretations. The quantification procedure with application of a matrix-matched external standards and proper internal standardization is required to correct for these, sometimes severe, matrix effects. When matrix-matched standards are not available (*e.g.*, flux-free molten natural rock glas reference materials for analysis of silicate samples), application of well-characterized samples for external calibration (*i.e.* of homogeneous ataxites or hexahedrites for analysis of iron meteorites) has been shown to provide accurate results, on condition that sufficiently large total ablated areas have been considered. Internal standardization based on sum normalization to 100 % of the major elements has been demonstrated suitable for quantification of 2D maps of both alloys (Fe-Ni metal of iron meteorites) and silicates (olivine of pallasites). The added value of a combined approach for 2D elemental mapping, in which μXRF has been applied to realize large-scale major element distribution maps, after which LA-ICP-MS has been used for 2D quantitative multi-element mapping of smaller areas of meteoritic material, has been demonstrated. In the context of the interpretation of the large data sets of laterally resolved multi-element concentrations generated by LA-ICP-MS, multivariate analysis has been shown to be a powerful tool to bring trends to light within and between the maps at the mineral and parent body scale, potentially revealing genetic links between meteorites within their parent body and providing valuable information on the fractionation of the elements in the parent bodies of meteorites.

In this work, new data on element concentrations and their lateral distribution in multiple meteorites, valuable for understanding and further interpretation of the processes in the early Solar System has also been presented. *E.g.* in chapter 2 reliable concentrations of PGEs and other elements in Darinskoe IIC and several other iron meteorites that were poorly characterized so far have been presented. Meteorites of the IIC group are rare (only 8 known members), and before this study, Darinskoe IIC was the least studied member of the group. Unique information on the lateral distribution of the trace elements within the Darinskoe IIC iron meteorite has been provided. A dataset of bulk compositions for 14 major to trace elements in 7 pallasite olivines has been provided in chapter 3, and for the first time the 2D LA-ICP-MS element distribution maps in olivines of PMGs have been presented. The element concentrations in these maps indicate complex relations and are often correlated, which cannot be explained by simple diffusion gradients acquired during cooling of the olivine following metal-olivine mixing. Rather, the element distributions in pallasite olivines reflect a superposition of multiple contributions: (1) primary features, inherited from the olivine formation in the parent body mantle, (2) anisotropic diffusion in polycrystalline olivine, (3) charge-balancing of substituting elements, as in the case of correlated Cr-Al distributions in all pallasite olivines studied, and (4) late-stage shock events and terrestrial weathering. Additionally, in this work is has been demonstrated that the accuracy of bulk element analysis of pallasite olivines is jeopardized by presense of the ubiquitous inclusions, potentially leading to biased interpretations of the conditions at which olivine and metal equilibrated. An approach to discriminate these inclusions and to calculate the bulk element concentrations within “pure” olivine has been developed.

The second aspect of this work is the development and evaluation of analytical methods for high-precision isotopic analysis of Ni and Fe via MC-ICP-MS for cosmochemical applications. The last decade stable isotopic analysis of Fe via MC-ICP-MS received considerable attention in cosmo- and geosciences due to its ability to trace magmatic, metamorphic and sedimentary processes and biological cycling. While the stable isotope ratio variations of Fe in geo- and cosmochemical processes are relatively well understood, the stable isotopic variations of Ni are yet to further an understanding of the underlying fractionation processes. Ni isotopic analysis is an attractive tool for geo- and cosmochemistry as the result of the nearly similar chemical properties of Ni and Fe, but with Fe exhibiting an extra redox change (3+ → 2+) in nature, which creates the possibility to trace redox-related processes. It is also known that due to the siderophile character of Ni, the condensation events in the Solar Nebula are imprinted in C-chondrite metal as light (and zoned) Ni stable isotope signatures, which may also be preserved in some groups of differentiated meteorites. As such, variation of Ni stable isotope ratios in these mereorites may be used as a tool to trace mixing of the components in the Solar Nebula. In order to guaranty accurate and precise isotopic analysis of Ni for geo- and cosmochemical applications, a chemical isolation method for Ni, based on sequential ion exchange column chromatography steps, and a multicollector (MC) ICP-MS measurement protocol have been developed, as described in chapter 4 of the present work. The challenge, critical for high-precision isotopic analysis of Ni via MC-ICP-MS, is successfully overcoming matrix effects, spectral interferences caused by matrix elements of the silicate material (*e.g.*, Mg, Ti, Cr, Zn), and on-column isotope fractionation of the target element. The optimized Ni isolation method, described in chapter 4, involves three chromatographic separation steps and the separation factors attained are sufficient to avoid spectral interferences to a large extent. At the same time, the isolation protocol developed has been proven to avoid the effect of artificial on-column fractionation on the final results. The models of instrumental mass discrimination correction, relying on an admixed internal standard, have been carefully evaluated in order to avoid any instrumental isotope fractionation. The overall precision of the mass-dependent results is equivalent to or better than those of other methods reported, including double-spiking techniques, and sufficient to distinguish between the stable isotopic signatures of Ni in various geological materials. In chapter 5, more light has been shed onto the sources of instrumental mass discrimination and spectral interference formation in MC-ICP-MS Fe isotopic analysis *via* application of cold plasma conditions. The present work has demonstrated that when all other parameters are the same, cold plasma conditions are associated with a nearly twice lower extent of instrumental discrimination for Fe than under hot plasma conditions. It has been shown that cold plasma conditions can efficiently resolve interferences due to the occurrence of $^{40}Ar^{16}O^+$ and $^{40}Ar^{14}N^+$ (but not that due to the presence of $^{40}Ar^{16}O^1H^+$), and once $^{40}Ar^{16}O^+$ and $^{40}Ar^{14}N^+$ interferences on Fe isotopes are fully removed, low mass resolution can be used, providing a gain of intensity at the cost of losing the possibility to monitor the ^{57}Fe isotope. It has been demonstrated that although application of a high-efficiency ‘jet’ interface provides higher ion transmission efficiency, it significantly enhances the level of spectral interference for Fe isotopes, so that none of these interferences can fully be removed under cold plasma conditions. When the high-transmission ‘jet’ interface is used, no effect of mitigated instrumental mass discrimination is found for Fe when switching to cold plasma conditions. In addition to bulk Fe, Ni isotopic analysis, *in situ* high-precision stable isotope signatures of Fe and Ni in major and accessory mineral phases of iron meteorites and main group pallasites (PMG) have been presented in chapter 7, recorded *in situ* using femtosecond LA micro-sampling combined with MC-ICP-MS with a spatial resolution of 30-80 µm. This allow (1) to measure stable isotope signatures of major elements of accessory minerals, unaccessible by pneumatic nebulization MC-ICP-MS, (2) to measure lateral isotopic profiles on the margins of adjucent minerals, invaluable for diffusion reconstructions.

Finally, the protocol developed for isotopic analysis of Ni in combination with that of Fe has been applied in the present work to a range of chondrites, iron and stony-iron meteorites, which has shed more light onto the formation and evolution of differentiated meteorite parent bodies. As these meteorites represent the deep interiors of their parent bodies, i.e. cores and core – mantle boundaries of the differentiated asteroids, building blocks of the discrete planetary accretion, this study is of potential implication to the processes on our own planet. Bulk and spatially resolved stable isotopic signatures of Fe and Ni in meteoritic material provide insight into (1) the thermal histories of the iron and stony-iron meteorites parent bodies, including applications of isotopic thermometers, (2) sub-solidus diffusive equilibration of the minerals during slow meteorite parent body cooling, (3) the interaction between the metal core and silicate mantle of differentiated asteroids, and (4) the process of the fractional crystallization in the cores of iron and stony-iron meteorite parent bodies. In the case of mesosiderites, light Ni and Fe isotopic signatures have been observed in the silicate portions relative to the heavier, near-chondritic signatures of the corresponding metal phases. These compositions likely result from diffusion of Ni and Fe from the metal into the silicate portion of these meteorites, following the mixing between an impactor and the original parent body. It has been shown that Fe isotopes of the PMG and in the IIIAB parent bodies' metal core(s) are fractionated in the process of fractional crystallization of the metal core. Unlike Fe, Ni isotope ratios do not indicate fractionation coupled to the fractional crystallization of the parent body core. The metal and olivine portions of pallasites show resolvable Fe isotope fractionation, which cannot be explained by a single equilibration event on the PMG parent body due to mass balance constraints. The Fe isotope fractionation in olivine – metal system has been interpreted in terms of isotope thermometry of the parent body. The equilibration temperatures thus obtained for different pallasites indicate a wide temperature range (255-340˚C to 1100-1300˚C), not expected for PMG equilibrium formation on the relatively thin core – mantle border of their parent body. Unless these temperatures are not a result of inadequate sampling of inhomogeneous metal phases of PMG, this finding suggests that the wide range of the equilibration temperatures is a result of violent impact mixing and rather represents re-equilibration at different depths in the parent body (potentially, secondary parent body re-accreted after impact). Unexpectedly, Ni shows an isotope fractionation factor between metal and olivine in pallasites that is reversed compared to that of Fe, with lighter isotopic compositions for the metal phase and heavier compositions for the corresponding olivine. By using *in situ fs*-LA-MC-ICP-MS analysis of accessory minerals of iron and stony iron meteorites, it has been demonstrated that light Ni isotopic signatures in PMG are not a result of inhomogeneity in the solar nebula, but rather represent isotope fractionation in the metal – schreibersite system. The Ni isotopic signatures of bulk metal and schreibersite correlate negatively, with isotopically lighter Ni in the metal of PMGs and isotopically heavier Ni in the metal of iron meteorites. As Ni in pallasites is mainly distributed between these two phases, the driving force of this fractionation must be the change of the thermal settings or different Fe-P-Ni bulk contents during fractional crystallization in iron meteorite and PMG parent bodies, when different types of schreibersites are crystallized in different stability fields of the metal-schreibersite phase diagram. In general, laterally resolved Fe-Ni stable isotope signatures (spatial resolution of 30-80 µm) highlight efficient thermal equilibration of PMGs mineral phases formed at higher temperatures (olivine, troilite, schreibersite), and the isotope fractionation between the phases is equilibrium-driven. Olivines of PMG are largely isotopically equilibrated, with only a hint of Fe isotopic zoning, which is insufficient to quantitatively constrain the cooling histories or processes of magmatic evolution, such as growth/dissolution. At the same time, kamacite-taenite Fe-Ni metal, formed at below ≈ 800 ˚C displays diffusive Fe and Ni isotope ratio profiles, confirming previous suggestions of a kinetically driven isotope fractionation. It has been demonstrated that metal-rich achondritic materials such as iron and stony-iron meteorites exhibit wider ranges of isotope fractionation for Ni than for Fe. The stable isotope signatures of Fe and Ni have been interpreted to reflect the slower cooling rates experienced by the magmatic iron meteorites. Comparison of the magnitude of kamacite-taenite isotope fractionation of Fe and Ni measured in situ via *fs*-LA-MC-ICP-MS with the magnitudes predicted theoretically has allowed to broadly constrain cooling rates of Esquel, CMS 04071 PMGs and Udei Station IAB between ~25 and 500 ˚C/Myr.

Future prospects

As more and more new members of rare achondrite meteorite groups (*e.g.*, ureilites, angrites) are found in Antarctica and arid deserts every year, elemental and stable isotopic analysis of these achondrites, including unique meteorites, *via* ICP-MS based techniques will significantly advance our understanding of the formation of the Solar System. Application of LA-ICP-MS to differentiated achondritic material can provide element contents and their lateral distributions for large sets of single minerals in a fast manner. In combination with multivariate analysis, the datasets thus acquired can reveal general trends that exist at the mineral scale in these rare objects, and open new window of opportunity to study the magmatic processes at the differentiated asteroid parent body. Although most achondrite meteorite groups have been studied for their bulk Fe isotopic signatures, the isotopic variability among their constituent mineral phases is yet to be measured, either relying on *in situ* LA, microdrilling or mineral separation. In this work, it has been shown how the Fe isotopic signatures of adjacent phases in iron and stony iron meteorites yield valuable constraints on the thermal history of meteorite parent bodies, with melting/crystallization or diffusive equilibration taking place in the cores and at the core-mantle boundaries of these bodies. Similarly, the phase-specific Fe isotopic signatures of other groups of differentiated and primitive achondrites can yield similar constraints on the equilibration conditions (or discover the disequilibria of the mineral assembledge) of crust and mantle processes in other differentiated asteroids, enhancing our understanding of their formation and evolution in the early Solar System. On the other hand, this work has demonstrated that the combined stable isotope signatures of Ni and Fe at mineral scale can better resolve the formation processes of meteorite parent bodies, than single element (Fe) isotopic signatures alone at bulk scale. In the future, multiple stable isotope systems should be studied in conjunction with Fe. Here, the case could potentially be made for isotopic analysis of elements with chemical properties different from those of Fe, *e.g.*, of lithophile Mg or of chalcophile Zn. As such, our understanding of the early Solar System will increase sufficiently with an the increased resolution of the processes, provided by simultaneous application of multiple stable isotope systems at a mineral scale.

Acknowledgements

> *If I have seen further, it is by standing on the shoulders of giants.*
>
> *Isaac Newton*

Writing a PhD dissertation is a big step, and this is not accomplishable without support from many people. This support is received in variety of different ways – from scientific advice from elder fellows to the right questions asked by a colleague or student. First of all I want to thank Prof. Frank Vanhaecke for giving me this opportunity to join his in all senses state of the art lab. You were always helping me with right remark and piece of advice, at the same time giving me freedom to choose the direction, and letting me to grow as a scientist. But a state of the art lab is not just a set of expensive equipement, but a team of people, whom you accurately featured in order to create highly friendly atmosphere and scientifically cumulative environment. These are the talents of the promoter any PhD student can wish, and I do appreciate this. I sincerely say similar words to Prof. Philippe Claeys, who let me to join his lab at VUB and directed me to grow in the field of cosmochemistry. I especially appreciate your discerning idea to study Ni isotopes at the very beginning of my PhD, which, at the end, led to the fruitful outcomes. I also want to thank here Prof. Stefan Weyer from Leibnitz University Hannover for letting me to perform *in situ* isotope ratio measurements in his lab as well as for plenty of constructive comments on cosmochemical implications. Many thanks for Prof. Laszlo Vincze for giving me an opportunity to expand my horizons with a field of XRF analysis.

With pleasure I express my gratitude towards the Interuniversity Attraction Poles Program initiated by the BELSPO for funding this research. This project would not be possible without everyone who in any way took part in provision of meteorite samples: Cecilia Satterwhite and Kevin Righter (NASA), Marleen deCeukelaire (RBINS), Catherine Corrigan (Smithsonian Institution), Felix Lesnov (V.S. Sobolev IGM SB RAS), Eric Twelker (meteoritemarket.com) and Seann McKibbin (VUB). I also want to acknowledge the kind help of Prof. Karel Strijckmans, Chantal and Tine which they provided me in multiple administrative and bureaucratic related issues.

I would like to acknowledge all my co-authors for their involvement, constructive suggestions and for taking time to read these (extremely tedious) texts. I really enjoyed time spent in discussions on various topics, thank you for that. I also want to thank all the A&MS members for being ready to help me every time I needed advice or technical assistance, as well as for the higly cheerful and scientifically cumulative atmosphere. I will always remember our discussions and the spirit of commonwealth: Marta, Lara, Jefferson, Charo, Andrey, Winfried, Stijn, Thibaut, Ehab, Asha, Kris, Lana, Sanwang, Yulia, Ana, Veerle, Balázs, Lieve, Karen, Edu, Sara: thank you, dear friends. Special thanks for Andrey for supporting me at the early stages of my stay in the lab. Harry, Jorge, Roger: this PhD would clearly not be possible without your magic touch. I also want to acknowledge Philip for his friendly help with computer related issues. I also appreciate time spent working with numerous people in other labs: Bart, Jan and Stephen from XMI group at UGent, Seann, Lidia, Alicia, Christina and Stef from Earth System Sciences research unit at VUB, Mona from Leibnitz University Hannover.

Last but not least, I want to say many thanks for Steven Goderis, truly the key person in this project. There are no words to express my gratitude towards your patient assistance, advices, and thoughtful read through all the papers and this manuscript. I especially appreciate your brilliant talent to inspire people around you, the feature of great mentor and scientist. *"Quand tu veux construire un bateau, ne commence pas par rassembler du bois, couper des planches et distribuer du travail, mais reveille au sein des hommes le desir de la mer grande et large."*

Кроме того, я хотел бы горячо поблагодарить моих родителей и мою семью за их бесконечную поддержку и веру в меня, которые я чувствовал даже на расстоянии 5000 км. Наконец, эта работа не состоялась бы без внимания и заботы моей жены, Настя, спасибо тебе!